TECHNISCHE UNIVERSITÄT MÜNCHEN

Fakultät Chemie

Fachgebiet Organische Chemie

On a new visualization tool for quantum systems and on a time-optimal control problem for quantum gates

Ariane Garon

Vollständiger Abdruck der von der Fakultät für Chemie der Technischen Universität München zur Erlangung des akademischen Grades eines

Doktors der Naturwissenschaften

genehmigten Dissertation.

Vorsitzender:		Univ.-Prof. Dr. B. Reif
Prüfer der Dissertation:	1.	Univ.-Prof. Dr. S. J. Glaser
	2.	Assoc. Prof. Dr. D. Sugny, Université de Bourgogne /Frankreich
	3.	Univ.-Prof. Dr. R. Westermann

Die Dissertation wurde am 25.02.2014 bei der Technischen Universität München eingereicht und durch die Fakultät für Chemie am 31.03.2014 angenommen.

To my parents.

Declaration

I hereby declare that parts of this Thesis are already published/submitted or planned to be submitted in scientific journals:

Time-optimal trajectories on SU(2), A. Garon, S. J. Glaser and D. Sugny, Submitted to Acta Applicandae Mathematicae (2014).

Visualization of single- and multi-spin systems, A. Garon, R. Zeier, S. J. Glaser, *in preparation.*

Time-optimal control of SU(2) quantum operations, A. Garon, S. J. Glaser and D. Sugny, Phys. Rev. A, **88**, 043422 (2013).

Eidesstattliche Versicherung

Ich versichere, dass ich die von mir vorgelegte Dissertation selbständig angefertigt, die benutzten Quellen und Hilfsmittel vollständig angegeben und die Stellen der Arbeit, die anderen Werken im Wortlaut oder dem Sinn nach entnommen sind, in jedem Einzelfall als Entlehnung kenntlich gemacht habe; dass diese Dissertation noch keiner anderen Fakultät oder Universität zur Prüfung vorgelegen hat; dass sie abgesehen von unten angegebenen Teilpublikationen noch nicht veröffentlicht worden ist sowie, dass ich eine solche Veröffentlichung vor Abschluss des Promotionsverfahrens nicht vornehmen werde. Die Bestimmungen dieser Promotionsordnung sind mir bekannt. Die von mir vorgelegte Dissertation ist von Herrn Prof. Dr. S. J. Glaser betreut worden.

Publikationsliste

- *Visualization for multi-spin operators*, A. Garon, S. J. Glaser and R. Zeier. In preparation.
- *Time-optimal trajectories on SU(2)*, A. Garon, S. J. Glaser and D. Sugny. Submitted to Acta Applicandae Mathematicae (2014).
- *Time-optimal control of SU(2) quantum operations*, A. Garon, S. J. Glaser and D. Sugny. *Phys. Rev. A*, **88**, 043422, 2013.
- *Combinatorial properties of double square tiles*, A. Blondin-Massé, A. Garon and S. Labbé, Theoret. Comp. Sc. (TCS) 502, pp.98-117, 2013.
- *Two infinite families of polyominoes that tile the plane by translation in two distinct ways*, A. Blondin-Massé, A. Garon and S. Labbé. (GASCom), Theoret. Comp. Sc. (TCS)412, pp.4778-4786, 2011.
- *Generation of double squares tiles*, A. Blondin-Massé, A. Garon and S. Labbé. Random Generation of Combinatorial Structures International Conference Proceedings (GASCom), Montreal (Canada) 2010.
- *Equations on palindromes and circular words*, A. Blondin-Massé, S. Brlek, A. Garon and S. Labbé, Theoret. Comp. Sc. (TCS)412, pp.2922-2930, 2010.
- *Every polyomino yields at most two squares tilings*, A. Blondin-Massé, S. Brlek, A. Garon and S. Labbé. Lattice Path, Combinatorics and Applications International Conference Proceedings, Sienna (Italy) 2010.
- *Christoffel and Fibonacci Tiles*, A. Blondin-Massé, S. Brlek, A. Garon and S. Labbé. Discrete Geometry for Computer Imagery International Conference (DGCI), Montréal (Canada) Springer LNCS5810, pp. 67 to 78, 2009.

- *Palindromes and local periodicity*, A. Blondin-Massé, S. Brlek, A. Garon and S. Labbé, International Conference on Words Proceedings (126), Salerno (Italy), 2009.
- *Combinatorial properties of f-palindromes in the Thue-Morse sequence*, A. Blondin-Massé, S. Brlek, A. Garon and S. Labbé, Pure Mathematics and Applications (PU.M.A), 2008.

Abstract

Since the foundations of quantum physics have been laid, our knowledge of it never ceased to grow and this field of science naturally split into diverse specialized branches. The first part of this thesis focuses on a problem which concerns all branches of quantum physics, which is the visualization of quantum systems. The non-intuitive aspect of quantum physics justifies a shared desire to visualize quantum systems. In the present work, we develop a method to visualize *any* operators in these systems, including in particular state operators (density matrices), Hamiltonians and propagators. The method, referred to as DROPS (**D**iscrete **R**epresentation of spin **OP**erator**S**), is based on a generalization of Wigner representations, presented in this document. The resulting visualization of an operator A is called its DROPS representation or visualization. We demonstrate its intuitive character by illustrating a series of concepts in nuclear magnetic resonance (NMR) spectroscopy for systems consisting of two spin-1/2 particles. The second part of this thesis is concerned with a problem of optimal control which finds applications in the fields of NMR spectroscopy, medical imagery and quantum computing, to cite a few. The problem of creating a propagator in the shortest amount of time is considered, and the results are extended to solve the closely related problem of creating rotations in the smallest amount of time. The approach used here differs from the previous results on the subject by solving the problem using the Pontryagin's maximum principle and by its detailed consideration of singular controls and trajectories.

Zusammenfassung

Das Wissen über die Quantenphysik ist seit der Gründung dieser Wissenschaft kontinuierlich gewachsen und unterteilt sich heute in eine Vielzahl verschiedener Fachgebiete. Die vorgestellte Arbeit beschäftigt sich mit den zwei Themengebieten der Spin-Visualisierung und der Spin-Kontrolle.

Die Visualisierung eines Quantenzustandes ist eine Problemstellung, die alle Fachgebiete der Quantenphysik betrifft. Ein solches System aus Quanten bildlich aufzuarbeiten stellt das allgemeine Bedürfnis dar, die in der Quantenphysik herrschenden nicht intuitiven Sachverhalte zu vermitteln. Es wurde eine Methode entwickelt, die einzelnen Operatoren des Quantensystems zu veranschaulichen. Es wurden hier unter anderem die Zustandsoperatoren (Dichtematrix) sowie die Zustandsfunktion und die Hamilton-Operatoren berücksichtigt. Die als DROPS (Discrete Representation of spin OPeratorS) bezeichnete Methode ist eine Verallgemeinerung der Winger-Darstellungsmethode. Die resultierende visuelle Darstellung eines Operators wird zur entsprechenden DROPS-Darstellung. Die Systematik dieser Visualisationsmethode wird anhand einer Auswahl an Beispielen aus der Kernresonanzspektroskopie für zwei Spin-1/2-Teilchen vorgeführt.

Der zweite Schwerpunkt der Arbeit beschäftigt sich mit der optimalen Steuerung von Spins. Als Beispiele für eine Anwendung seien hier nur die Kernresonanzspektroskopie, bildgebende Verfahren in der Medizintechnik und der Quantencomputer zu nennen. Die Arbeit untersucht, wie ein Propagator in der kürzest möglichen Zeit erzeugt werden kann. Die Resultate dieser Untersuchung werden auf das eng verwandte Problem der Rotationserzeugung in der kürzest möglichen Zeit übertragen. Der hier gewählte Ansatz unterscheidet sich von der herkömmlichen Herangehensweise, indem er das Maximumsprinzip nach Pontrjagin benutzt sowie singuläre Kontrollen und Trajektorien detailliert berücksichtigt.

Acknowledgments

I would like to express my deep gratitude to my advisor Pr. Dr. Steffen Glaser, for his patience, guidance, enthusiastic encouragements and useful criticisms for this research work. I particularly appreciated the open mind with which he both received and expressed new ideas. His lively passion for science, that he generously shares everyday, has been an illuminating source of inspiration.

I am particularly grateful to my second advisor Dr. Dominique Sugny, for his unwavering trust and support during the last two years of my PhD. With him, every discussion has been a generating source of energy, ideas and motivation.

Thanks to Pr. Dr. Olivier Collin and Pr. Dr. Vestislav Apostolov, for giving me advice and support since the beginning of this project. I thank them for writing so many reference letters for me, and sharing with me some of their experiences whenever I was doubting on aspects of my academic projects.

The Glaser group would not be what it is without the shiny presence of Frau Martha Fill and Dr. Raimund Marx. I would like to thank them for helping out every time they could, for guiding me through the numerous mysterious university procedures and for joyfully animating our group meetings.

In addition, a thank you to my colleagues, former and actual ones, for being such a good company during the last three years. Particular thanks to Robert Fisher, Corey O'Meara, Franz Schilling, Yun Zhang and Thi-Thoa Nguyen for giving me advice and for their constant support.

I would like to offer my special thanks to my former colleague, badminton fellow and friend Manoj Nimbalkar, without whom this project would never have taken place. I thank him for introducing me to Pr. Dr. Glaser, but principally for being such a supportive friend.

Thanks to my little red bike, which has been my main "idea generator", negative energy killer, and who never let me down.

All my friends, met in Canada or in Germany, for being there and encouraging me during the last three years. A special thank you to Uwe Sander and Cyril Guinet.

I wish to acknowledge my good friend, and former colleague, Etienne Plante, for his amazing authenticity and honesty, making him such a valuable source of advice and such an interesting person to discuss with. I want to thank him for teaching me concepts of physics, for sharing with me his discoveries, for initiating me to the "rafales", for patiently reviewing each sentence of this thesis and for his endless encouragements.

I would like to thank my family, for encouraging me since the beginning of this project.

I would like to especially thank my father, who made several back and forth trips to the airport to pick me up, but more importantly to bring me support until the end in the difficult parting moments. And I would like to thank my mother, who every weekend brought me so much positive and creative energy.

I would like to thank my soul mate Yannick Assenat, for his unconditional love and for bringing me such a great amount of positive energy every day of my life. He is the one who always finds the good words to bring me light in the difficult times. This project required sacrifices from both of us, and I could never be thankful enough for not only willingly accepting them, but also turning them into everyday interesting challenges.

Contents

Introduction

The world we experience every day is the macroscopic world. Until the 19th century, theoretical physics was principally concerned with this world, that classical physics succeeded to describe with a good fidelity. However, as time went by and technology developed, physicists had the possibility to observe the world in its finest details. The discovery of a small particle, named electron (by J. J. Thomson in 1897), marked the beginning of a revolution in the History of physics, opening the doors to a world to be discovered: the quantum universe of atomic and subatomic systems. Indeed, it became indisputable that well established laws of classical physics could not explain what would become quantum mechanics and many accepted concepts had to be questioned. The uncertainty principle of Heisenberg, stating that it is not possible to simultaneously know, with 100% certitude, both the position and the velocity of a quantum particle, furnishes a striking example of the separation between classical physics and this new quantum reality. The name of the theory is a legacy of the discovery of the *quantified* nature of the energy by Max Planck in 1918, which furnished the key argument for the need to revise our conception of physics.

Quantum mechanics is a field of physics in itself, which possesses its own laws and its own ideas. The interpretation of some of these concepts is still a subject of debate [1]. Some of the prime examples would be the concepts of wave-particle duality [2], Schrödinger's cat [3] and entanglement [4]. The concept of operator, which plays a central role in the theory, also challenges our classical preconceptions of physics. Of course, operators describe transformations on the systems and follow, in this case, our intuitive understanding of what "to operate on" means. But the states of systems (using the density matrix formalism [5]) as well as measurements also are described by operators. One of the advantages of the operator formalism is that quantum mechanics can be described and manipulated using the reliable apparatus of linear algebra. A drawback of this formalism is however that most objects are represented by matrices (operators in linear algebra) and that it is more often than not difficult to give a tangible meaning to these matrices.

In the case of systems consisting of one spin-1/2 particle, a solution to remedy this situation is to represent operators (in this case 2×2 matrices) as vectors [6]. This visualization tool has found numerous applications [7–9], not only because of its "visual" nature, but also because this representation also conveys the physical meaning of the operators. For instance, the vector representing density matrices (called the Bloch vector) defines the magnetization vector whose components are physically measurable.

Clearly, such a meaningful visualization tool is highly desirable for communication purposes and to help developing intuition about systems we can neither *see* nor directly interact with in daily life. This common interest in developing intuition by visualization already led to many ideas of possible representations of complex systems [9–14] to which

the Bloch vector representation is not applicable. However, most of the attempts so far have failed to simultaneously satisfy the two fundamental criteria generally expected from a visualization tool. That is, either the visualization tool is not bijective (*i.e.* to each operator must correspond a unique picture and distinct operators must have distinct pictures) or it fails at establishing an intuitive connection between the visual representations of operators and their physical nature. The first part of this thesis presents a new visualization tool which satisfies the above two criteria. It is based on the representation of operators by Wigner functions [9, 13, 14], an idea which appeared already in the literature in [11, 12, 15–17]. Although the potential of Wigner functions to represent systems has been acknowledged [18, 19], so far their concrete use to represent systems with multiple particles seems to have appeared in literature only for two particles [15]. In **Chapter 2**, we lay down the foundation of a general visualization method, called DROPS visualization, which can be applied to *any* quantum system. The visualization principle relies on the decomposition of the operator space in a basis of irreducible spherical tensors [20–22]. A particular basis, the LiSA basis, is presented for systems consisting of n identical spins and its explicit derivation is given for systems of k spin-1/2 particles, with $k = 1, 2, 3$. In **Chapter 3**, we make explicitly use of the LiSA basis to illustrate concepts in the field of nuclear magnetic resonance spectroscopy.

The second part of this thesis tackles a problem raised by modern applications of quantum physics: the control of quantum systems. Manipulating a quantum system by an external field to achieve a given task remains a goal of primary interest in a variety of domains [23]. In applications such as imagery [7], the quantum systems under concern are molecules in the studied body and their control leads to the creation of signals converted into images. In the field of quantum computing [24], control of systems is required to transmit and store information which can later be retrieved. In **Chapter 4** of this thesis, we address a control problem on one spin-1/2 systems. The problem consists of creating any unitary transformation (an operator) in the shortest possible time, where the interaction of the system with an external magnetic field is used to control the system. The control field is constrained to lie in the xy plan, which restricts its freedom of action on the system and makes the problem challenging. We must certainly point out that this problem has already been studied in the past [25–30], but our approach differs by making use of the Pontryagin maximum principle to find an explicit coordinate-parametrization of the optimal trajectories. We then apply the results obtained to address the related time-optimal control problem of creating rotations. In our study, we take into consideration all the controls which can potentially be time-optimal, including in particular singular controls. All the results are mathematically proven to be correct.

In order to present the results in a continuous flow, supporting information which is not necessary to understand the general ideas is gathered into appendices at the end of each chapter. Such information includes technical proofs, additional examples, numerical tables and complementary notes on some theoretical concepts.

Visualization of multi-spin operators

2.1 Introduction

The ability to visualize complex information in a meaningful way plays an important role in understanding and communicating abstract concepts and ideas. Furthermore, visualization techniques also provide powerful intuitive approaches to think about problems and to create innovative solutions. In quantum mechanics, the state of a system of coupled spins or quantum bits (qubits) is mathematically captured by the density operator [5], which has a complex matrix representation that in general is hard to visualize. Other important but similarly abstract and unwieldy operators include Hamiltonian operators (representing the energy terms of the quantum system) and unitary transformation operators (representing *e.g.* the time evolution of spin systems or logical quantum gates in quantum information processing). For the special case of a quantum mechanical two-level system, such as an isolated spin-1/2 particle in an external magnetic field, Feynman, Vernon and Hellwarth showed in a seminal paper [6] that these operators (and the corresponding complex 2×2 matrices) can always be mapped to three-dimensional vectors with real components. In this approach, the density operator, the Hamilton operator and unitary transformation operators are represented by the Bloch vector, the field vector and rotation vectors, respectively. This mapping has made it possible to visualize and to design experiments for many applications, ranging from magnetic resonance imaging [7, 8] and spectroscopy [8] to quantum optics [9]. Unfortunately, this powerful approach cannot be directly applied to systems with three or more energy levels, such as systems consisting of two or more coupled spins or quantum bits (qubits). In this communication, we present a versatile and physically motivated representation and visualization technique for arbitrary operators in coupled spin systems, which in fact reduces to the simple vector representation for the special case of uncoupled spin-1/2 particles. Hence it may be viewed as a generalization of the representation based on the mapping by Feynman et al. [6].

Hitherto, a number of approaches have been used to illustrate the density operator of coupled spin systems. However, they all have severe limitations and shortcomings. In the most direct (and least intuitive) approach, the real and imaginary parts of the individual matrix elements of the operator of interest is simply displayed in the form of a three-dimensional bar chart. This graphical representation is commonly used in the field of quantum information theory to display the density operator, *e.g.* the results of state tomography for a set of qubits [31]. In NMR spectroscopy, density operators are sometimes represented as annotated energy level diagrams, where populations are represented by circles on energy levels and coherences by lines between energy levels [32]. However, this representation is practical only for simple cases with a small number

of non-zero matrix elements and does not directly reflect the properties of operators under rotations. Another commonly used pictorial representation of the density operator is based on the vector representation of single-transition operators [8], which however provide limited intuition if a large number of non-zero density matrix elements exist and behave in a non-intuitive way under simple non-selective spin rotations.

For single, uncoupled spins, the Wigner representation [9, 13, 14] provides an elegant basis for the visualization of the density operator [11, 12, 16]. In contrast to the Bloch vector approach, this representation is not limited to spin-1/2 particles but is also applicable to higher spins and is based on a mapping of tensor operators to spherical harmonics. Although no formal mapping was given, it is remarkable that some selected density operator terms of a spin-1 particle were depicted in the same spirit by Pines et al. already in 1976, alluding to the love of chemists for thinking of atomic and molecular orbitals [33]. Although the possibility of a potential generalization of the Wigner representation for coupled spin systems was suggested about three decades ago [18, 19], such a representation is in general non-trivial and to our knowledge has not been explicitly worked out. More recently, some authors were even skeptical whether it was possible at all to generate a Wigner-type representation of operators for systems consisting of coupled spins [12]. However, as shown in the following, physically meaningful Wigner representations can be constructed for systems consisting of an arbitrary number of spins. For the special case of two coupled spins, a particular Wigner-type representation has already been introduced by Jessen et al. [15]. Here, we present a new class of Wigner-type representations for general systems consisting of coupled spin systems. This approach not only provides an efficient way to visualize arbitrary operators but also reflects characteristic features, such as transformation properties and the rank of localization or correlations that is associated with a given operator.

For arbitrary spin systems, the available ranks of freedom in the construction of the underlying mapping between operators and functions are presented and criteria for choosing a unique map are given. For the case of up to three coupled spin-1/2 particles, the explicit mapping is presented and possible extensions to larger spin systems or to coupled systems of particles with larger spin quantum number are discussed. The power of this mapping is demonstrated for a number of illustrative examples. We expect that this intuitive visualization technique will find many applications in the visualization of states or operators in all fields where coupled spins or qubits are of interest, including nuclear and electron magnetic resonance spectroscopy as well as quantum information theory.

2.2 Visualization

The visualization of abstract objects such as quantum mechanical operators can be realized by designing a map between these abstract objects and three-dimensional functions that can be displayed as concrete objects in three-dimensional space. For example, the state a quantum mechanical two-level system can be mapped to the Bloch vector, which can be visualized as a three-dimensional arrow. To be of maximum usefulness, this mapping should ideally have the following desirable properties: It should be bijective and physically intuitive. (A) Bijectivity means that every operator corresponds to a unique function and vice versa. (B) A physically intuitive representation should preserve system symmetries with respect to fundamental transformations such as linear combinations, rotations and permutations.

It is well known that there exists a natural mapping between irreducible tensor components T_{jm} (which form an operator basis) and spherical harmonics Y_{jm} [20–22]. More details about the definition of spherical tensors and their relationship with the spherical harmonics can be found in Appendix 2.10.1 and the representation of the latter adopted in this work is illustrated in Fig. 2.9. In the case of a single spin with arbitrary spin number I, all the tensors in the basis have distinct ranks j, and any operator A can be represented by a unique spherical function f_A using the straightforward mapping [12, 13, 17]

$$A = \sum_{j,m} c_{jm} \mathrm{T}_{jm} \Leftrightarrow f_A(\theta, \phi) = \sum_{j,m} c_{jm} \mathrm{Y}_{jm}(\theta, \phi) \tag{2.1}$$

with integers $0 \leq j \leq 2\mathrm{I}$, $-j \leq m \leq j$. This mapping has been exploited in the generalized Wigner representation [13]. However, extending this idea to systems consisting of several spins is not trivial and there were even doubts whether it was possible at all [12].

Here, we introduce a general approach to extend this idea in a systematic way to systems consisting of an arbitrary number of spins. The procedure is be illustrated explicitly for the example of three coupled spin-1/2 particles.

In the general case, the tensor operator basis contains multiple operators with the same rank j and order m. Consequently, the direct mapping as in (2.1) would not be bijective, as distinct operators would be mapped to the same function. This requires finding a way to distinguish the representations for the tensors of identical rank j: $\mathrm{T}_j^{(\ell)} \neq \mathrm{T}_j^{(\ell')}$. For instance, the tensor basis for a system consisting of two spin-1/2 particles contains three distinct tensors of rank $j = 1$. [8]

A simple solution to the uniqueness problem would be to view the system as a one-particle system of higher spin number $\mathrm{I}' > \mathrm{I}$ and using relation (2.1) in order to have a visualization as a single three-dimensional function on a sphere. However, such a solution would provide little intuitive insight as there would not be a one-to-one correspondence between the transformation properties of operators and their visualization (desirable property (A)).

A much more natural and intuitive solution can be found if the representation of a given operator is not restricted to a single 3-dimensional object (corresponding to a single spherical function) but comprises a set L of objects (corresponding to a set of spherical functions $f_A^{(\ell)}$ where $\ell \in L$):

$$A = \sum_{\ell \in L} A^{(\ell)} \Leftrightarrow \bigcup_{\ell \in L} f_A^{(\ell)}(\theta, \phi) \tag{2.2}$$

with

$$A^{(\ell)} = \sum_{j,m} c_{jm}^{(\ell)} \mathrm{T}_{jm}^{(\ell)} \Leftrightarrow f_A^{(\ell)}(\theta, \phi) = \sum_{j,m} c_{jm}^{(\ell)} \mathrm{Y}_{jm}(\theta, \phi). \tag{2.3}$$

Here, $\ell \in L$ labels different sets of tensor operators. The definition of these sets is a matter of choice (*vide infra*), the only restriction being that all tensors in a given set have distinct rank j. In the following, such a **D**iscrete **R**epresentation of spin **OP**erator**S** is called a DROPS visualization for short and we refer to each individual object $f_A^{(\ell)}$ in such a representation as a *droplet*. To fix ideas, this is illustrated in Fig. 2.1, which shows an example of such a DROPS visualization. It consists of $|L| = 11$ droplets and represents a random operator A for a system consisting of three spin-1/2 particles.

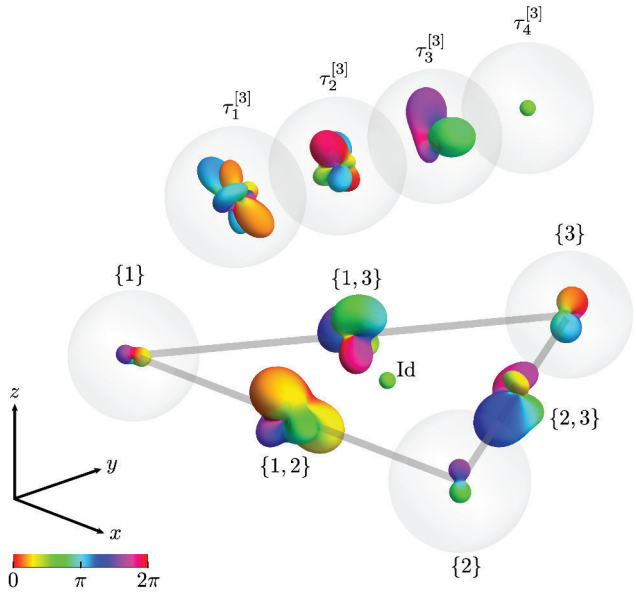

Figure 2.1: DROPS visualization of a random 8×8 matrix A corresponding to an operator for a quantum system consisting of $n = 3$ qubits (spin-1/2 particles). The DROPS visualization is defined by the tensor product basis and its DROPS mapping presented in Section 2.10.10. Each droplet is a linear combination of spherical harmonics corresponding to a specific $f_A^{(\ell)}$ in Eq. (2.3). The labels ℓ of the droplets are defined in Fig. 2.2.

2.2.1 Complete Wigner representation

In the framework of Wigner representations, it is generally assumed that each operator A corresponds to a unique *single* function f_A. In Appendix 2.10.2, we show that the *set* of functions $\{f_A^{(\ell)}\}_{\ell \in L}$ Eq. (2.2) defines a complete (or "true" [34]) Wigner representation of multiple-spin systems. By "complete", we mean here that any operator A can be recovered from the values of $f_A^{(\ell)}$. The additional four fundamental criteria [35, 36] that must be fulfilled by the original single mapping f can be generalized in a straightforward way to the set of functions $\{f^{(\ell)}\}_{\ell \in L}$ (details in the Appendix 2.10.2) making the proposed representation complete, coherent and intuitive.

2.2.2 Tensor bases and number of droplets

Given a matrix space $\mathrm{Mat}(N)$ together with a representation (action) of SU(2) on this space, one can always find an orthonormal irreducible tensor basis B of $\mathrm{Mat}(N)$

$$\mathrm{B} = \bigcup_{q=1}^{Q} \mathrm{T}_{j_q}, \tag{2.4}$$

where $\mathrm{T}_j := \{\mathrm{T}_{jm}\}_{m \in \{-j \ldots j\}}$ [1] denotes the set of all the $2j+1$ components of the tensor. The set of ranks $\{j_q\}_{q \in \{1 \ldots Q\}}$ in a basis of the form (2.4) is unique but the

[1] For instance, a tensor T_2 of rank $j = 2$ corresponds to a set of five components, for $-2 \leq m \leq 2$: $\mathrm{T}_2 = \{\mathrm{T}_{2,-2}, \mathrm{T}_{2,-1}, \mathrm{T}_{2,0}, \mathrm{T}_{2,1}, \mathrm{T}_{2,2}\}$. Each component T_{jm} is an operator in the system and accordingly, a tensor T_j is a set of $2j+1$ matrices.

tensors themselves are not uniquely defined. Indeed, the set of all irreducible spherical tensors of identical rank j in B forms a vector space [37] and as being so, there is an infinite number of orthonormal generating tensors for this space that can be chosen to appear in (2.4). This freedom in the choice of the tensors in (2.4) allows one to choose tensors having some desired properties and/or preserving specific symmetries. These additional characteristics for the tensors can be used to label them in a structured way and define a natural DROPS mapping (2.3).

Note that the (unique) explicit list $\{j_q\}_{q\in\{1\ldots Q\}}$ of ranks in any basis B defines a lower and an upper bound for the possible number of droplets in a DROPS visualization. The upper bound corresponding to a DROPS mapping for which all tensors in the basis have a distinct label, that is $|L| = Q$ in (2.2). The lower bound corresponds to the maximum number M of tensors having identical rank $j_{q_1} = \cdots = j_{q_M}$ in (2.4) since a necessary condition to have a bijectve DROPS visualization is to ensure that all tensors of the same rank are mapped to distinct droplets (*i.e.* have distinct labels $\ell_{q_1} \neq \cdots \neq \ell_{q_M}$ in (2.3)).

For the specific case of three spin-1/2 particles for instance, the list of ranks in the basis (2.4) is $\{j_q\}_{q\in\{1\ldots Q=20\}} = \{3,2,2,2,2,2,1,1,1,1,1,1,1,1,0,0,0,0,0\}$ (*c.f.* Fig. 2.2) and consequently, the maximum and minimum number of droplets in a DROPS mapping based on (2.3) are respectively $|L| = 20$ and $|L| = 9$, where 9 is the number of tensors of ranks $j = 1$ in the above list of ranks $\{j_q\}$.

In the following, we present a specific DROPS visualization for this system where the tensors in the basis B are taken to preserve linearity and subsystems as well as permutation symmetries in the case of the trilinear tensors. The resulting DROPS visualization is characterized by 11 droplets and their corresponding labels are found in the last column of Fig. 2.2.

2.2.3 The LiSA tensor basis

Here, we focus on the most common situation typically found in the field of quantum information processing and magnetic resonance spectroscopy where spins are distinguishable. In order to define the final set L of tensor operators (each corresponding to one droplet $f_A^{(\ell)}$), we proceed in three steps (see Fig. 2.2). First, tensors are partitioned according to their linearity or particle number k, *i.e.* the number of spins (or pseudo spins) involved with $1 \leq k \leq n$. Second, they are further split according to the set of involved spins $\{s_1, ..., s_k\}$. For example, for $n = 3$ and particle number $k = 2$, these sets are $\{1,2\}$, $\{1,3\}$ and $\{2,3\}$ (see Fig. 2.2). Third, if, for a given subsystem, several tensors of the same rank j exist, the tensors (or linear combinations of them) for this subsystem can be partitioned further according to their symmetry species with respect to the permutation group S_k acting only on the particles involved in the tensor subsystem (see the tensors for the subsystem $\{1,2,3\}$ in Fig. 2.2). In this case, each droplet can be uniquely labeled by a standard Young tableau $\tau_i^{[k]}$ [37, 38].

This procedure provides a unique set L of labels ℓ (see Equation (2.3)). For the specific case of three spin-1/2 particles, the j values for the trilinear terms are $\{0,1,1,1,2,2,3\}$ and the set L consists of the following 11 elements: Id, $\{1\}$, $\{2\}$, $\{3\}$, $\{1,2\}$, $\{1,3\}$, $\{2,3\}$, $\tau_1^{[3]}$, $\tau_2^{[3]}$, $\tau_3^{[3]}$, $\tau_4^{[3]}$ (see Fig. 2.2), each of which corresponds to a single droplet in Fig. 2.1. For the specific case of $n \leq 5$ spin-1/2 particles, this procedure provides a tensor basis [39] with defined linearity, spin subsystem, and permutation symmetry, which we refer to as the LiSA basis, where LiSA stands for **Li**nearity, **S**ubsystem

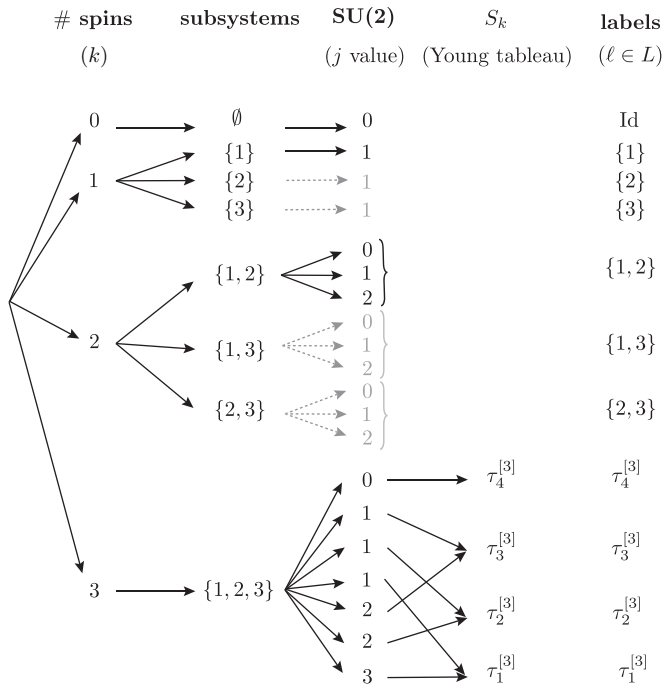

Figure 2.2: Properties and labels of the tensors of the LiSA basis for a system consisting of three spin-1/2 particles. Each tensor is k-linear (# **spins**) and involves a specific subsystem of the global system (**subsystems**). They are moreover chosen to be of a specific symmetry species corresponding to a standard Young tableau $\tau_i^{[k]}(S_k)$. The final tensors are grouped (**labels**) into droplets according to the subsystem they involve and for the trilinear tensors also according to their symmetry species.

and **A**dditional criteria such as permutation symmetry in the present case. For larger systems, additional criteria can be used in order to uniquely label the elements of a tensor basis. In the Discussion, alternative groupings using the same basis is also be discussed. In Appendix 2.10.10, we present two alternative tensor bases and suggest a DROPS visualization for each of them.

2.3 Idea of the construction

Although general algorithms and explicit formulas for irreducible tensor operators are known, all necessary tensor operators can be derived by combining iteratively the operators T_0 and T_1 for one qubit basis and symmetrizing the tensors obtained by applying the theory of group projectors [19, 37, 40]. The mathematical grounds concerning the permutation group and its representations used to derive this basis are presented in details in Appendix 2.10.4 and the explicit construction of the LiSA basis for systems consisting of three spin-1/2 particles in Appendix 2.10.5.

For a general system consisting of n spin-1/2 particles, the construction of the LiSA tensor basis is performed in three steps. **(I)** The first step consists in constructing recursively the k-linear symmetrized tensors $\mathrm{T}_j(\tau_i^{[k]})$ of the k-particle systems for all $k \in \{0, 1, \ldots, n\}$. **(II)** In the second step, each of these tensors is multiplied by a unique phase factor $\mathrm{e}^{i\phi}$, the choice of which is discussed in the next section. **(III)** These tensors

(constructed for k-particle systems of dimension 2^k) are finally embedded in the global system of dimension 2^n.

The main part of the construction consists in step (I). Proceeding recursively, the particles are included one at a time by combining the elements of the product basis $\mathrm{T}_j(\tau_i^{[k-1]}) \otimes \mathrm{T}_1(\tau_1^{[1]})$. The explicit form of the tensor $\mathrm{T}_1(\tau_1^{[1]})$ for a single qubit can be found in Appendix 2.10.5 [2]. Referring to the Clebsch-Gordan decomposition [20–22], each product $\mathrm{T}_j(\tau_i^{[k-1]}) \otimes \mathrm{T}_1$ can be decomposed as a direct sum of irreducible tensors with ranks running from $|j-1|$ to $j+1$ [8, 22, 41], namely

$$\mathrm{T}_j(\tau_i^{[k-1]}) \otimes \mathrm{T}_1(\tau_1^{[1]}) = \mathrm{T}_{|j-1|} \oplus \ldots \oplus \mathrm{T}_{j+1}, \tag{2.5}$$

where the explicit tensor components $\mathrm{T}_{j'm}$ are calculated using Wigner coefficients [37, 41]. The tensors $\mathrm{T}_{j'}$ so constructed form all together a k-linear tensor basis (2.4) for the new system which could already form a basis for an alternative DROPS visualization (see the section Discussion). The complete symmetrized tensors are obtained by symmetrizing these k-linear tensors with respect to permutations using the projectors $P_{\tau_i^{[k]}}$ introduced in Appendix 2.10.4. That is,

$$\mathrm{T}_{j'}(\tau_i^{[k]}) := cP_{\tau_i^{[k]}}\left(\mathrm{T}_{j'}\right),$$

where $c > 0$ is a normalization constant. The LiSA basis is obtained from these k-linear symmetrized tensors after performing steps (II) and (III).

2.3.1 Uniqueness and sign freedom

The irreducible spherical tensors previously constructed satisfy the relation $\mathrm{T}_{jm} = (-1)^{p-m}\mathrm{T}^\dagger_{jm}$ where p is an arbitrary integer [22]. Here, we adopt the phase convention of Schwinger [42] which is to set

$$p = 0. \tag{2.6}$$

A direct consequence of (2.6) is that the $m = 0$ tensor components T_{j0} are Hermitian. The considered spherical tensor operators are then uniquely defined up to a sign. Although the choice of sign is completely arbitrary, it can make a notable difference in the resulting visualization mapping. The specific choice of signs leading to the LiSA basis proposed here is motivated by the physical intuition behind Cartesian product operators (see Fig. 2.10). The reader may refer to Appendix 2.10.7 for the justification of the present choice.

2.4 Result: DROPS visualization of three spins-1/2

Once the LiSA basis is built, all the tools are available to represent arbitrary operators for systems consisting of n spin-1/2 particles in this basis. In order to visualize an operator in this system, we decompose it as its unique linear combination of the elements of the LiSA basis and use the mapping of Eq. (2.3). Recall that a tensor T_j of rank j is a basis which consists of $2j+1$ matrices T_{jm}, one for each $m \in \{-j, \ldots, j\}$. The structure of

[2] The tensors for a system consisting of a single particle are necessarily symmetrized according to particle permutations, that is, $\mathrm{T}_1(\tau_1^{[1]}) := \mathrm{T}_1$.

the LiSA basis and the associated DROPS visualization of operators are now illustrated explicitly for the case of three spin-1/2 particles. The justification for the present tensor labeling is discussed in Appendix 2.10.6.

There are three linear tensors $\mathrm{T}_{1m}^{\{s_1\}}$, one corresponding to each spin $s_1 \in \{1,2,3\}$, and in Fig. 2.1 the corresponding three droplets are placed at the corners of an equilateral triangle in the x-y plane. For each subsystem $\{s_1,s_2\} \in \{\{1,2\},\{1,3\},\{2,3\}\}$ consisting of two spins, there are three bilinear tensors of *distinct* ranks $j=0,1,2$ (see Fig. 2.2) which therefore can be combined in a single droplet. Each $\{s_1,s_2\}$-droplet is conveniently plotted on the corresponding s_1-s_2 edge of the triangle. There are seven trilinear tensors: one tensor of rank $j=0$, three of rank $j=1$, two of rank $j=2$ and one of rank $j=3$ (see Fig. 2.2). Since some of these tensors share the same rank j, they cannot all be part of the same droplet and the second identification level specified by their symmetry species can be taken into account to regroup them into different droplets. The four symmetry species for 3-linear spherical tensors are summarized in Eq. (2.12) of Appendix 2.10.4 and in Fig. 2.1 the corresponding droplets are plotted above the other ones. Finally, the droplet of the tensor $\mathrm{T}_{0,0}^{\emptyset}$ (corresponding to the identity operator) is plotted in the center of the triangle in Fig. 2.1.

2.5 Properties of the LiSA DROPS visualization

2.5.1 Topological information

As each droplet involves a unique subset of particles, they can be arranged on the global DROPS picture according to the natural topology of the system. Hence, the three-dimensional arrangement of the droplets implicitly conveys additional information in an intuitive way. In particular, it is immediately apparent which spins are involved in a given visualized operator. Furthermore, subsystems can be visualized merely by restricting the global DROPS visualization to the only droplets involving the particles of interest. The arrangement of the droplets on an equilateral triangle as in Fig. 2.1 could be modified to match specific features to be emphasized in a given application. For example, the droplets representing the linear operators could be positioned at the location of the corresponding nuclear spins in a specific molecular geometry or each side length of the triangle could be scaled according to the strength of the coupling constant J_{ij} in the Hamiltonian, providing an additional element of information in the visualization.

2.5.2 Visualization of general operators

The DROPS representation is completely general and hence can be applied to arbitrary operators. It is not limited to Hermitian operators (such as Hamiltonians and density operators) and can also be used to visualize non-Hermitian operators. Examples of such operators of practical interest include (a) unitary operators representing time-evolution operators (propagators) or quantum gates; (b) parts of the density operator corresponding to specific coherence orders, such as the raising and lowering operators for a given spin or *e.g.* a term representing +3 quantum coherence in a spin system. The simultaneous display of *e.g.* density operators and propagators (or Hamiltonians) can be helpful in understanding the evolution of a quantum system in concrete experimental building blocks as the crucial information about what drives the system can be seen (see

Fig. 2.8 where this is illustrated for the example of a standard experiment in nuclear magnetic resonance spectroscopy).

2.5.3 Color information

In order to visualize complex functions on the sphere $f(\theta,\phi) := r(\theta,\phi)\cdot \mathrm{e}^{i\alpha(\theta,\phi)}$ (*i.e.* linear combination of spherical harmonics), the convention adopted in the present text is to represent the radial part $r(\theta,\phi)$ by the shape of the graph for r and the phase $\alpha(\theta,\phi)$ by a color derived from the mapping shown in Fig. 2.1. The representation of spherical harmonics illustrated in Fig. 2.9 is derived from this representation. A commonly used alternative way to display complex functions on a sphere is to represent the phase and the radial part $r(\theta,\phi)$ of the function by color and brightness, respectively (see [15] for an example of use of this alternative representation in a visualization context).

The definition of the mapping (2.3) together with property (2.6) has as a direct consequence that each droplet in the DROPS visualization of a Hermitian matrix is a real-valued function and consequently, Hermitian matrices are the ones and only ones corresponding to purely red (phase $\alpha = 0$) and/or blue (phase $\alpha = \pi$) DROPS pictures. This feature is clearly visible for the visualization of the Hamiltonians and density operators in Fig. 2.8 or Cartesian operators in Fig. 2.3. More generally, if the matrix component corresponding to a specific droplet is Hermitian up to a *constant* phase factor $e^{i\alpha}$, the droplet will also be 2-colored, with colors corresponding to the angles $\{\alpha, \alpha+\pi\}$ in the color mapping given in Fig. 2.1. See for example the different droplets of the unitary propagators in Fig. 2.8.

2.5.4 Cartesian product operators

Cartesian product operators are widely used as a convenient orthogonal basis in spin physics [8] (see Appendix 2.10.3). They are Hermitian and consequently, as discussed above, their DROPS visualization involves only red and blue colors (see Fig. 2.3). Moreover, as they are k-linear (with well-defined integer k) and correspond to a well-defined subsystem of spins, their DROPS visualization requires only droplets associated with the corresponding subsystem.

The LiSA visualization of a linear Cartesian product operator $I_{k\eta}$ consists of two spheres with opposite algebraic signs which are aligned in the direction of the axis $\eta \in \{x,y,z\}$ (see Fig. 2.3 and Fig. 2.5). In fact, it is easy to show that for an arbitrary Cartesian operator A the droplet representing the linear spin-k term is colinear and proportional to the three-dimensional vector whose components are given by the projection of A onto the operators I_{kx}, I_{ky} and I_{kz}, respectively. In particular, if A corresponds to a density operator, the positive (red) pole of the spin-k droplet can be associated with the tip of the spin-k Bloch vector (corresponding to a magnetization or polarization vector in NMR and optics, respectively [8] and [9, 11]). In the context of quantum information and entanglement measurements, it is interesting to point out that the spin-k Bloch vector is identical to the Bloch vector of the reduced density operator that is obtained by taking the partial trace over the remaining spins. If A is a Hamiltonian, the positive pole corresponds to the tip of a field vector (*e.g.* a magnetic field in the case of NMR). Hence, the DROPS representation can be regarded as a natural generalization of the well known and widely used vector picture. However, the DROPS representation is limited neither to linear nor to Cartesian operators. For characteristic

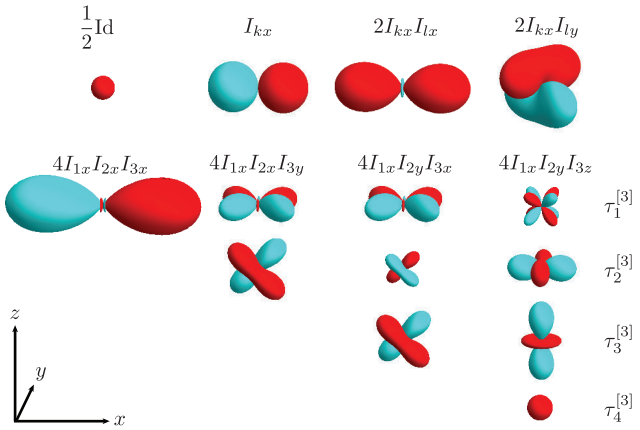

Figure 2.3: Characteristic droplets of Cartesian product operators. The Cartesian product operator $4I_{1y}I_{2x}I_{3x}$, omitted here, has the same visualization as $4I_{1x}I_{2y}I_{3x}$ up to an inversion of colors for the τ_3-component. The red and blue colors refer to positive and negative values of the droplet functions $f^{(\ell)}(A)$, respectively. In order to visualize any other Cartesian product operator, it suffices to rotate the actual droplets along the desired directions.

non-linear Cartesian product operators, the corresponding DROPS representations are summarized in Fig. 2.3 and Fig. 2.5.

It is interesting to take a closer look at the DROPS representation of operators of the form $2I_{k\eta_1}I_{l\eta_2}$, which play a central role in the Cartesian product operator formalism commonly used in NMR spectroscopy. For example, an operator with $\eta_1 = x$ and $\eta_2 = z$ corresponds to anti-phase coherence [8]. The corresponding droplet for such an operator has an uncommon shape that is not encountered in the typical representation of the standard spherical harmonics or of atomic orbitals. It consists of two bean-shaped lobes with opposite sign (see Fig. 2.10 - 2.4) and the long axes of these lobes are orthogonal to each other. Its graphical decomposition in terms of the bilinear double- and zero-quantum operators $(DQ_y)_{kl}$ and $(ZQ_y)_{kl}$ is shown in Fig. 2.4. In the LiSA representation, the long axis of the positive lobe is oriented in the $\vec{\eta}_1 + \vec{\eta}_2$ direction and the center of the positive lobe is displaced in the $\vec{\eta}_3$ direction relative to the center of the droplet, where the direction of $\vec{\eta}_3 = \vec{\eta}_1 \times \vec{\eta}_2$ is given by the right-hand rule. The DROPS representation captures all the properties of the operators under global rotations and permutation of particles. For example, when both spins k and ℓ are rotated by 180° around the x axis, the anti-phase operator $2I_{kx}I_{lz}$ is transformed to $-2I_{kx}I_{lz}$ and the corresponding droplet also performs a corresponding rotation around the x axis, resulting in the same shape as before but with inverted signs, as expected.

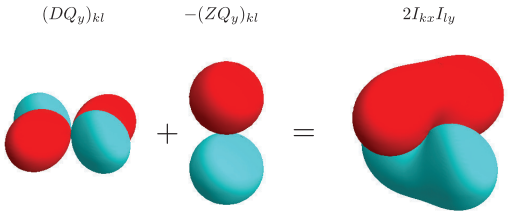

Figure 2.4: Decomposition of the bilinear Cartesian product operator $2I_{kx}I_{ly}$ in terms of the double-quantum operator $(DQ_y)_{kl} = I_{kx}I_{ly} + I_{ky}I_{lx}$ and the zero-quantum operator $(ZQ_y)_{kl} = -I_{kx}I_{ly} + I_{ky}I_{lx}$ [8].

Note that in the proposed LiSA visualization, bilinear operators of the form $2I_{k\eta}I_{l\eta}$ and trilinear operators $4I_{1\eta}I_{2\eta}I_{2\eta}$ are represented by symmetric and antisymmetric elongated shapes along the η direction (*c.f.* Fig. 2.3).

2.5.5 Multiple quantum coherences

Operators A_p of defined multiple quantum order p play an important role in NMR spectroscopy. They are invariant under global z rotations up to a phase factor [8]

$$\exp(-i\alpha \sum_{k=1}^{n} I_{kz})\, A_p\, \exp(i\alpha \sum_{k=1}^{n} I_{kz}) = A_p \exp(-ip\alpha). \tag{2.7}$$

This property is nicely captured in the DROPS representation, for example the operators displayed on the right side of Fig. 2.5 have defined coherence order p and they are invariant under rotations up to a phase factor. The operators displayed on the left side of Fig. 2.5 correspond to mixtures of multiple quantum orders $\pm p$. These operators as well as their corresponding DROPS representations are invariant under global z rotations by integer multiples of $\alpha = 2\pi/|p|$. For example the operator $(DQ_x)_{kl}$ has coherence order $p = \pm 2$ and is invariant under a z rotation of 180°. In the next Chapter, we take advantage of this property to visualize the concepts of phase cycling and gradient pulses arising in the design of NMR experiments.

2.5.6 Hamiltonians

As discussed above, Hamiltonians $\mathscr{H}$ of quantum systems are Hermitian operators that correspond to real spherical functions in the DROPS representation (*c.f.* Fig. 2.8). Typically, the Hamiltonian consists of linear terms of the form $\mathscr{H}_{\text{lin}} := 2\pi \sum_{k=1}^{3} \vec{\omega}_k \cdot \vec{I}_k$ (where $\vec{\omega}_k$ is a vector and $\vec{I}_k := [I_{kx}, I_{ky}, I_{kz}]$), which represent *e.g.* magnetic fields, and bilinear terms of the form $\mathscr{H}_{\text{bil}} = 2\pi \sum_{kl} c_{kl}(aI_{kx}I_{lx} + aI_{ky}I_{ly} + bI_{kz}I_{lz})$, which correspond to spin-spin couplings. It is common practice to visualize the linear terms as three-dimensional field vectors $\vec{\omega}_k$. In fact, the droplets corresponding to the linear terms of the Hamiltonian in the DROPS representation are colinear to these field vectors, which make the representation consistent with the conventional picture. However, so far there was no general way to visualize arbitrary coupling terms of the Hamiltonian. It is an important feature of the DROPS visualization that it also provides a natural representation of bilinear (or even higher order) coupling terms. This is illustrated in Fig. 2.6, which shows the following four characteristic coupling terms.

The case $a = 0$ and $b = 1$ corresponds to an *Ising*-ZZ or *Heisenberg-Ising model* [44, 45], which is also called *weak coupling* [8] or *longitudinal coupling* [46]. Note that in the LiSA DROPS convention this is represented by a *longitudinally* elongated droplet (*c.f.* $\mathscr{H}_{\text{long}}$ in Fig. 2.6). The case $a = 1$ and $b = 1$ corresponds to the *Heisenberg*-XXX *model*, which is also called *strong coupling* or *isotropic coupling* [8]. In the LiSA visualization, it is represented by an *isotropic* spherical droplet (*c.f.* $\mathscr{H}_{\text{iso}}$ in Fig. 2.6). The case $a = 1$ and $b = 0$ corresponds to the *Heisenberg*-XX *model*, also called *planar coupling* [46, 47], which in the LiSA visualization is represented by a *planar* disc-shaped droplet in x-y plane (*c.f.* $\mathscr{H}_{\text{plan}}$ in Fig. 2.6). The case $a = 1$ and $b = -2$ corresponds to a *dipolar coupling* [8] (*c.f.* $\mathscr{H}_{\text{dip}}$ in Fig. 2.6).

Note that the LiSA mapping can also represent more general coupling terms, such as the *anisotropic Heisenberg*-XYZ *model* as well as trilinear coupling terms. Hence, with

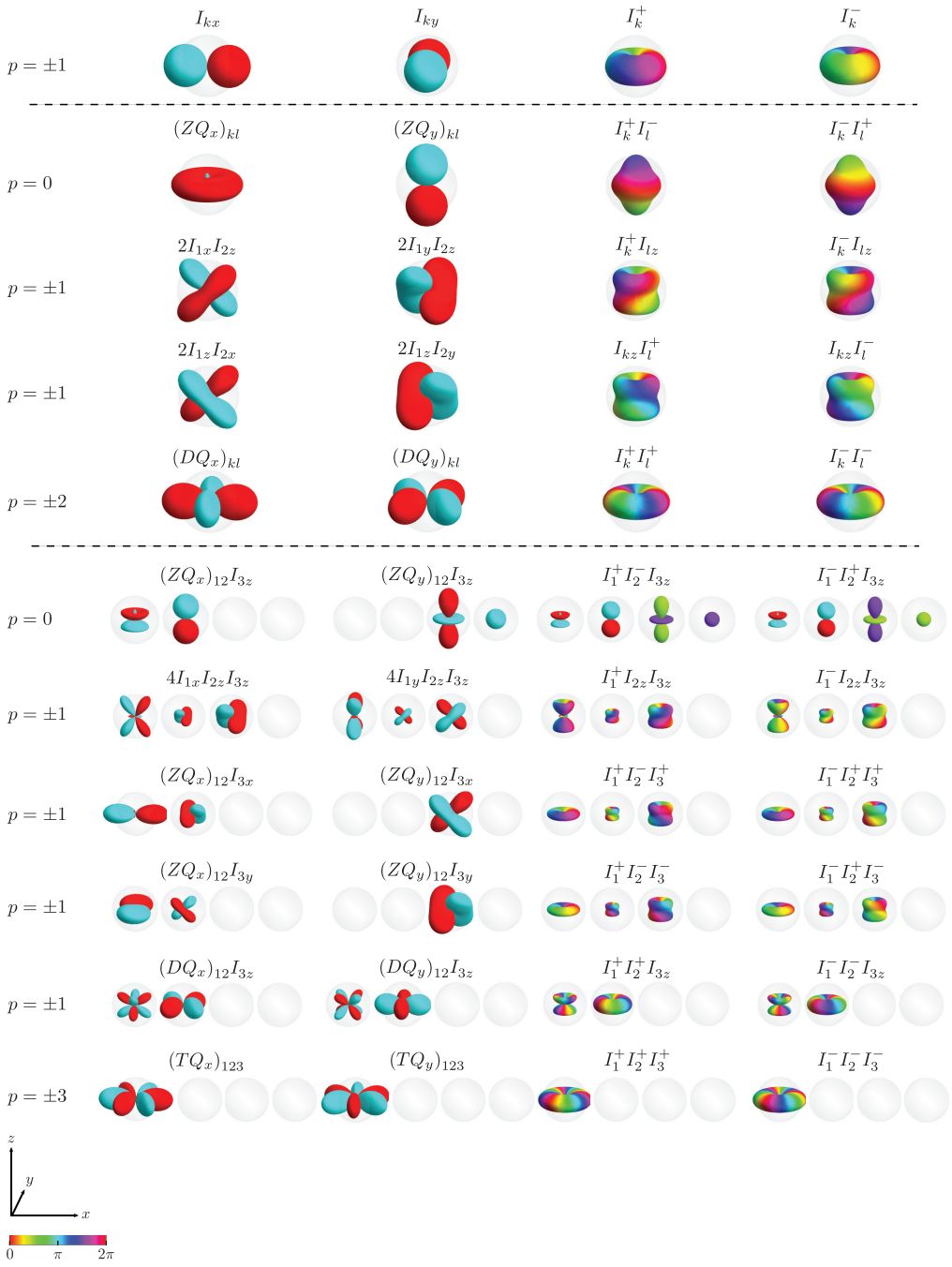

Figure 2.5: DROPS visualization in the LiSA basis of some characteristic multiple quantum coherences for a system consisting of three spin-1/2 particles. The operators are classified according to their linearity and their coherence order $p \in \mathbb{N}$. For visualization purposes, the empty droplets in the DROPS representation of the linear and bilinear operators are not displayed, and neither are the linear and bilinear empty droplets in the DROPS representation of trilinear operators. The four trilinear droplets are ordered from left to right according to the natural order in the symmetry defining each droplet, *i.e.* from $\tau_1^{[3]}$ to $\tau_4^{[3]}$ (see Fig. 2.1 and (2.12)). The above pictures correspond to the DROPS visualization of the tensors after normalization (note that the droplets for the trilinear operators have been scaled down, as indicated by the size of the spheres). The definition of the zero-, double- and triple-quantum operators $(ZQ_\eta)_{kl}$, $(DQ_\eta)_{kl}$ and $(TQ_\eta)_{kl}$, for $\eta \in \{x, y\}$, which are commonly used in the field of NMR spectroscopy can be found *e.g.* in [8, 43].

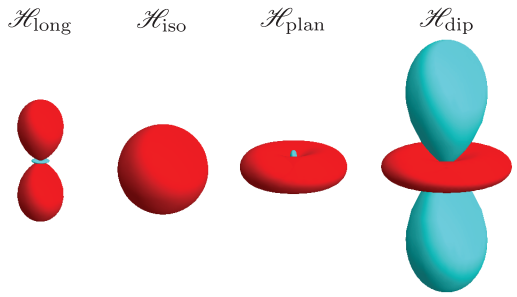

Figure 2.6: Visualization of characteristic terms of coupling Hamiltonians. In $\mathscr{H}_{\text{long}}$ (corresponding to the *Ising*-ZZ or *Heisenberg-Ising model*), the terms are proportional to $I_{kz}I_{lz}$. In $\mathscr{H}_{\text{iso}}$ (corresponding to the *Heisenberg*-XXX *model*), they are proportional to $I_{kx}I_{lx}+I_{ky}I_{ly}+I_{kz}I_{lz}$. In $\mathscr{H}_{\text{plan}}$ (corresponding to the *Heisenberg*-XX *model*), the terms are proportional to $I_{kx}I_{lx}+I_{ky}I_{ly}$ and in $\mathscr{H}_{\text{dip}}$ they are proportional to $I_{kx}I_{lx}+I_{ky}I_{ly}-2I_{kz}I_{lz}$. See the text in the subsection Hamiltonians for more details.

the explicit LiSA mapping for up to three spins presented here, it is straightforward to visualize the Hamiltonian terms of systems with an arbitrary number of spins or qubits, such as the well-known Kitaev honeycomb lattice [48], if the largest coupling terms are trilinear.

As discussed in Appendix 2.10.7, tensors are *a priori* defined only up to an arbitrary sign and the sign choice we made in the definition of the bilinear LiSA tensors is motivated by the resulting intuitive form of the bilinear coupling terms (*c.f.* Fig. 2.10).

2.6 Examples

The LiSA visualization is further illustrated in the present chapter by two chosen examples, for which more details can be found in Appendix 2.10.8. Note that Chapter 3 of this thesis is completely devoted to applications and illustrations of the LiSA DROPS visualization of quantum systems.

The first example (*c.f.* Fig. 2.7) shows the DROPS representation of entangled pure states of two qubits (Bell states) and three qubits (W and GHZ states), as well as the representation of a separable two-qubit state. It is interesting to note that the *concurrence* C, which measures the rank of bipartite entanglement in a pure two-qubit state, is directly visible in the DROPS representation: as pointed out above, the droplets representing the linear terms of the density operator are directly proportional to the Bloch vectors of the reduced density operators, which are obtained by taking the partial trace over the remaining spin. For two qubits in a pure state, the lengths of the two reduced Bloch vectors corresponding to the first and second qubits are identical (*c.f.* Fig. 2.7) and if this length is denoted R, the *concurrence* is simply given by $C=\sqrt{1-R^2}$ [49] (see also [50, p. 168] or [51, p. 50]).

The second example (Fig. 2.8)) illustrates the operators of interest (density operators of mixed states, Hamiltonians, propagators, effective Hamiltonian and effective propagator) for the analysis of a non-trivial experiment in NMR spectroscopy. The pulse sequence consists of two 90° pulses separated by a delay, and is designed to excite triple-quantum coherences starting from the thermal density operator in the high-temperature limit [8].

The reader can also find in Appendix 2.10.8 an overview of the concatenated

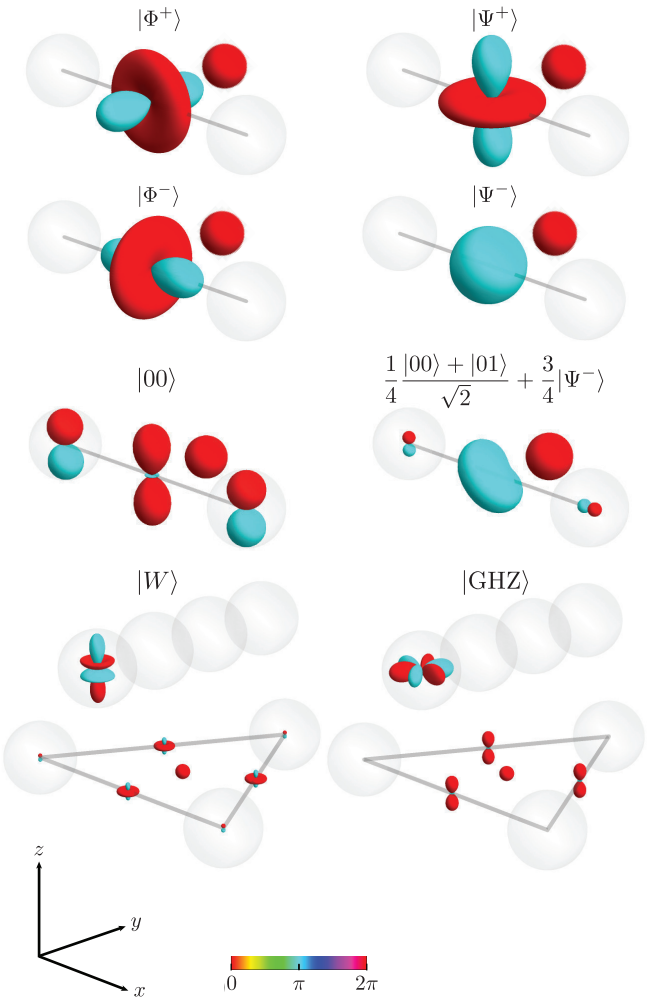

Figure 2.7: LiSA representation of characteristic entangled and separable pure states for two and three qubits (spin-1/2 particles). The first six DROPS pictures represent states in a system consisting of two qubits. The four Bell states $\left|\phi^{\pm}\right\rangle = \frac{1}{\sqrt{2}}(|00\rangle \pm |11\rangle)$ and $\left|\psi^{\pm}\right\rangle = \frac{1}{\sqrt{2}}(|01\rangle \pm |10\rangle)$ correspond to maximally entangled states of two qubits. For comparison, a separable state ($|00\rangle$) and a partially entangled two-bit state ($\frac{1}{4}\frac{|00\rangle+|01\rangle}{\sqrt{2}} + \frac{3}{4}\left|\psi^{-}\right\rangle$) are depicted in the third row. In the last row, the Werner state $|W\rangle = \frac{1}{\sqrt{3}}(|100\rangle + |010\rangle + |001\rangle)$ and the Greenberger-Horne-Zeilinger state $|\mathrm{GHZ}\rangle = \frac{1}{\sqrt{2}}(|000\rangle + |111\rangle)$ are shown, which correspond to two different entangled quantum states of three qubits.

INEPT experiment, which is designed to transfer magnetization between two indirectly-coupled spins.

2.7 Generalization

The method given in Section 2.3 to construct symmetrized tensors for n identical qubits can be generalized in a straightforward way to systems with n identical spin-I particles. The tensor basis of a spin-I particle has the form $\{\mathrm{T}_0, \mathrm{T}_1, \cdots, \mathrm{T}_{2\mathrm{S}}\}$. When the k^{th} spin is added to the system, all the tensor products $\mathrm{T}_j(\tau_i^{[k-1]}) \otimes \mathrm{T}_1$, $\mathrm{T}_j(\tau_i^{[k-1]}) \otimes \mathrm{T}_2$, ...,

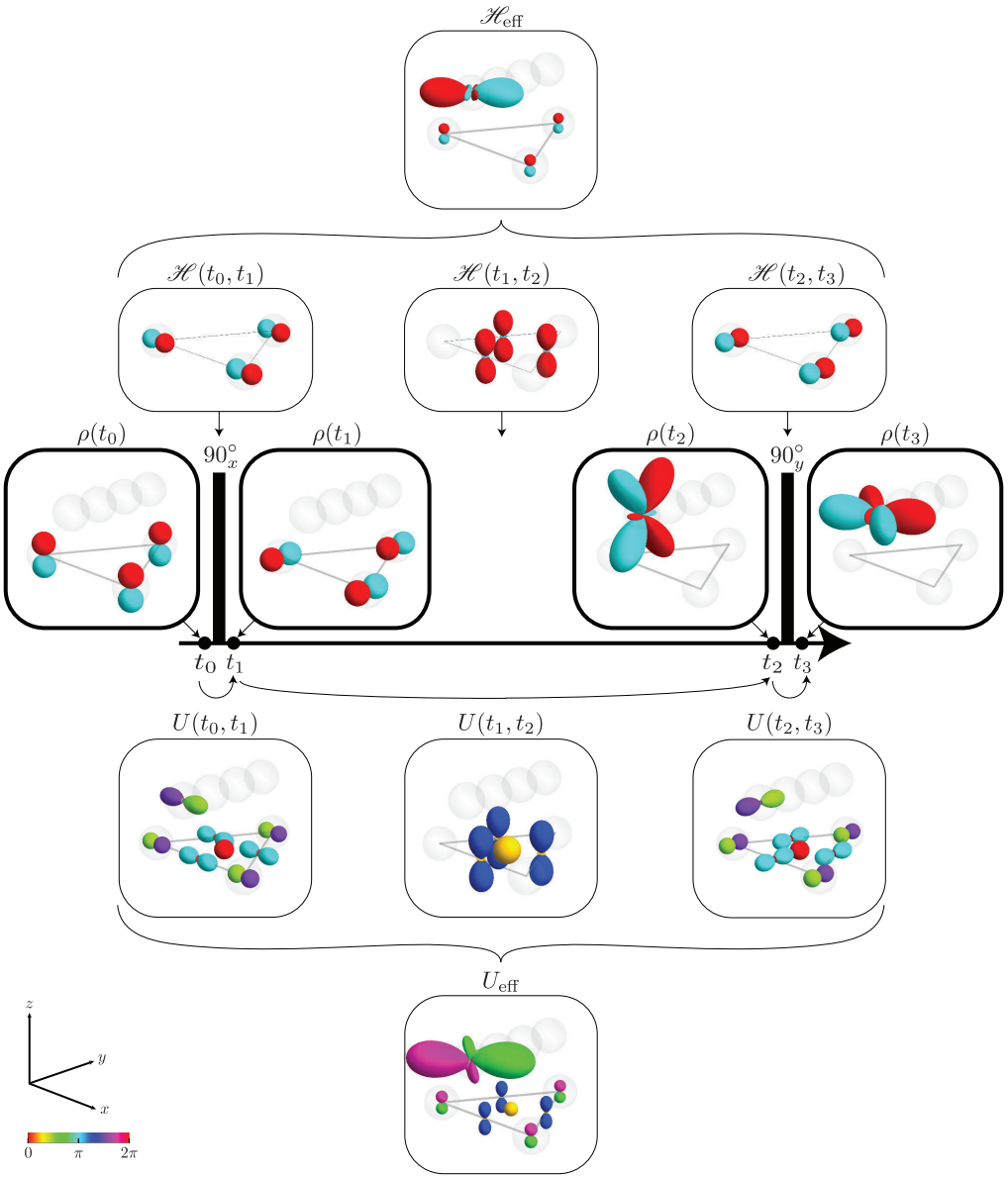

Figure 2.8: Experimental NMR pulse sequence to create triple-quantum coherences starting from the thermal equilibrium density operator in the high-temperature limit [8]. The pulse sequence consists of a 90° pulse (with phase x) followed by a delay $(t_2 - t_1)$ and a second 90° pulse (with phase y). The density operators $\rho(t_i)$ for this experiment are depicted in the middle row. The Hamiltonians $\mathscr{H}(t_i, t_{i+1})$ (scaled to the same norm for display) are shown in the upper row and the effective Hamiltonian [8] of the experiment is shown at the top. In the lower row, DROPS representations of the propagators associated with the individual time steps are displayed and the effective propagator is shown at the bottom (see Appendix 2.10.8 for details).

$\mathrm{T}_j(\tau_i^{[k-1]}) \otimes \mathrm{T}_{2S}$ (see Eq. 2.15) have to be taken into account in order to generate a complete tensor basis in Step (III). Then Steps (II) and (III) remain the same. Note that already for systems consisting of two spins $\mathrm{I} > 1/2$, some of the tensors in the LiSA basis need an additional parameter κ to be uniquely defined. That is, the linearity, spin

sub-system and symmetry type of a tensor are not necessarily sufficient to distinguish all the tensors.

In the case of systems with distinct spin numbers I_1, I_2,..., symmetrization can be applied to each subsystem of particles having identical symmetry species. Additional symmetries, such as those in the Hamiltonian, can be taken into account in order to simplify the DROPS pictures involved in the visualized operators.

2.8 Discussion

In general, the visualization of spin operators (and the corresponding generalized Wigner representation) requires several spherical functions, each representing a group of tensors. As discussed above, in the LiSA representation introduced here the tensors are grouped according to their particle number, spin subsets and permutation symmetry (see Fig. 2.2).

Note that the tensor operators derived from the Clebsch-Gordan decomposition (2.15) already form a tensor basis for the operator space such that a DROPS representation for operators could also be defined based on these operators, *i.e.* without symmetrizing. The recursive construction of these tensors furnishes a natural grouping according to their parents since the tensors on the right of (2.15) have identical parents and distinct rank j (see Appendix 2.10.10). It is important however to remember that the basis so constructed is of course strongly dependent on the different coupling schemes between the spins in the system [52].

Even if the tensors in the LiSA basis are taken to have a defined symmetry species, they also depend on the coupling order of the spins. Indeed, the trilinear symmetry species considered here are such that tensor operators are always either symmetric or anti-symmetric with respect to permutation of spins 1 and 2, whereas permutations involving spin 3 may not preserve the tensors (*c.f.* the tensors of symmetry species $\tau_2^{[3]}$ and $\tau_3^{[3]}$). Hence, for the visualization of experiments where two particles are indistinguishable, it is of advantage to label them "spin 1" and "spin 2", exploiting this symmetry. The visualization of experiments where two or more spins are indistinguishable can also be further simplified by also symmetrizing the linear and bilinear basis operators over the relevant permutation group. The use of such a symmetry-adapted basis makes it possible to reduce the number of droplets in the DROPS representation, because the subset of droplets with the wrong symmetry will always be empty. For example, in an I_2S spin system [**?**, 8], where the Hamiltonian and the density operator are both symmetric with respect to permutation of spins one and two, the number of droplets can be reduced from eleven to seven. For a spin system where the Hamiltonian and the density operator are symmetric with respect to permutations of all three spins, the number of droplets can be further reduced to four (see Appendix 2.10.9 for more details).

There are many alternative choices of tensor operator bases (with many possible DROPS visualizations for each of them, depending on how they are combined). The best choice depends on the system under study and the questions asked [53, 54]. Multipole operators [19, 52] are also commonly used spherical tensor operators due to their close relation with state vectors. These tensors do not have a defined linearity (*i.e.* particle number) but they are characterized by the angular momentum transition they perform on the states and which can then be used as criterion to group the tensors. It is interesting to note that the Wigner representation introduced in [15] for the special case of two coupled spins, where at least one of the two spins is a spin-1/2 particle, is in

fact identical to the DROPS visualization based on multipole operators. The interested reader will find in Appendix 2.10.10 more information about multipole operators and also a suggestion of DROPS representation using these operators in the case of systems consisting of three spin-1/2 particles.

In the definition of the DROPS visualization given by Eqs. (2.2) and (2.3), the $2j+1$ components T_{jm} of a tensor T_j are part of the same droplet. Note that it is also possible to represent each (or some) of the tensor components T_{jm} by different droplets, in order to highlight the presence or absence of certain coherence orders m in the system (albeit at the cost of an increased number of droplets).

2.9 Conclusion

In this chapter, we presented a general method to visualize operators in single- and multiple-spin systems, based on a generalization of Wigner representations. We presented a possible DROPS representation for systems consisting of identical spin-1/2 particles, based on the choice of a suitable symmetric tensors basis for the operator space. A corresponding visualization has been proposed and its multiple advantages have been pointed out. This work presents a multitude of possible extensions, from varying the possible tensor bases to considering systems increasing in complexity. The determination of the best adapted DROPS representation depending on the process to be visualized is certainly an interesting question. A more challenging aspect of the DROPS representation is to eventually describe physical processes by studying the dynamics on the droplets only, *i.e.* studying the dynamics between the different Wigner functions $\{f^{(\ell)}_{A(t)}\}$ defining a DROPS representation.

2.10 Appendices

The reader will find in this appendix further details left aside in the main text about the mathematical concepts related to the construction of the LiSA basis as well as the explicit and detailed construction of the LiSA basis for a system consisting of three spin-1/2 particles.

Appendix 2.10.1 briefly surveys the irreducible representations of SU(2) and presents the spherical harmonics and the irreducible spherical tensors as being such irreducible representations.

Appendix 2.10.2 inserts DROPS representations in the context of phase-space distributions and presents them as a rigorous generalization of conventional phase-space representations.

In **Appendix 2.10.3** is presented the Cartesian product operators, which we recall from a widely used standard basis in the field of NMR spectroscopy [8].

Appendix 2.10.4 is dedicated to the symmetric group S_n and its representations. It is divided in logical steps toward the main goal of defining the projectors necessary to symmetrize the tensors in the LiSA basis. The action of these projectors on operators is then presented in order to finally define the concept on tensors with defined symmetry species.

Appendix 2.10.5 presents the explicit construction of the LiSA basis for a system consisting of three spin-1/2 particles.

Appendix 2.10.6 presents and justifies the short-hand notation used to denote tensors in the LiSA basis for a systems consisting of three spin-1/2 particles.

Appendix 2.10.7 shows the motivation of the (*a priori* arbitrary) sign choice made here in defining the final tensors.

Appendix 2.10.8 gives more details on the examples presented in the main text in Section 2.6.

Appendix 2.10.9 discusses the possibility of further symmetrizing the tensors to simplify the DROPS pictures for systems with indistinguishable particles.

Appendix 2.10.10 presents two other possible tensor bases and suggests a DROPS visualization for each of them in the case of a system of three spin-1/2 particles.

Finally, **Appendix 2.10.11** surveys the explicit transformations between the LiSA tensor operator basis and the Cartesian product operator basis.

2.10.1 Spherical harmonics and irreducible spherical tensors for spin-1/2 systems

Irreducible representations of $\mathfrak{su}(2)$

Consider the algebra $\mathfrak{su}(2)$ and let J denote one of its elements. Suppose that the elements of $\mathfrak{su}(2)$ act linearly on a given vector space V and let $R(\mathrm{J})$ denote the associated (matrix) transformation on V. A subspace W of V which is invariant under the action of all $R(\mathrm{J})$ and having itself no proper invariant subspace is called an *irreducible representation* of $\mathfrak{su}(2)$. Given $j \in \frac{1}{2}\mathbb{Z}$ such that the dimension of W equals $d = 2j + 1$, a

standard basis of W consists of elements $\{|j,m\rangle\}_{-j\leq m\leq j}$ which satisfy:

$$\begin{array}{rcl} R(\mathrm{J}_\pm)\,|j,m\rangle &=& \sqrt{j(j+1)-m(m\pm 1)}\;|j,m\pm 1\rangle\,, \\ R(\mathrm{J}_z)\,|j,m\rangle &=& m\;|j,m\rangle\,, \end{array} \tag{2.8}$$

where $\mathrm{J}_+ := \left(\begin{smallmatrix} 0 & 1 \\ 0 & 0 \end{smallmatrix}\right)$, $\mathrm{J}_- := \left(\begin{smallmatrix} 0 & 0 \\ 1 & 0 \end{smallmatrix}\right)$ and $\mathrm{J}_z := \frac{1}{2}\left(\begin{smallmatrix} 1 & 0 \\ 0 & -1 \end{smallmatrix}\right)$. If two invariant subspaces W and W' have the same dimension, an extra parameter κ is needed to distinguish their standard basis: $|\kappa,j,m\rangle \neq |\kappa',j,m\rangle$.

Spherical harmonics

Consider the vector space $V_1 := \mathcal{L}^2$ of square integrable complex functions on the sphere. An element $\mathrm{J} \in \mathfrak{su}(2)$ acts on a spherical function $f(\theta,\phi) \in V_1$ by rotation according to $R_1(\mathrm{J})f(\theta,\phi) := f(\mathcal{R}^{-1}(\theta,\phi))$, where $\mathcal{R} = \mathrm{e}^{\mathrm{J}} \in \mathrm{SO}(3)$ is the rotation having J as a generator. The existence of $\mathcal{R}$ is guaranteed by the well-known relation $\mathfrak{su}(2) \cong \mathfrak{so}(3)$ [55]. For each natural number $j \in \mathbb{Z}$, there is a unique irreducible representation of dimension $2j+1$ and its standard basis is the set of $2j+1$ *spherical harmonics* $\mathrm{Y}_{jm}(\theta,\phi)$ with $m \in \{-j,\ldots,j\}$ [56–59]. Spherical harmonics satisfy relations (2.8) according to the actions $R_1(\mathrm{J}_\pm) := \exp(\pm i\phi)[\pm\partial/(\partial\theta) + i\cot(\theta)\partial/(\partial\phi)]$ and $R_1(\mathrm{J}_z) := -i\partial/(\partial\phi)$. The first spherical harmonics are depicted in Fig. 2.9.

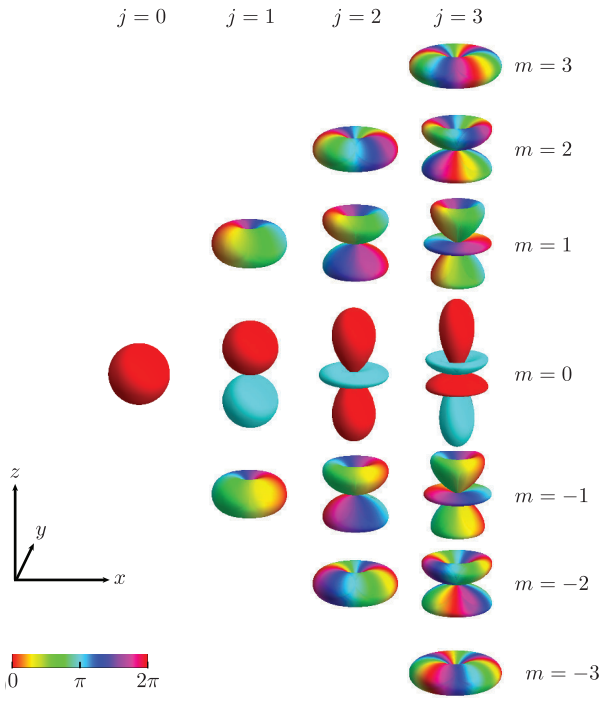

Figure 2.9: The spherical harmonics $\mathrm{Y}_{jm}(\theta,\phi) = r\exp(i\alpha)$ up to $j = 3$. The radial part $r(\theta,\phi)$ of the spherical harmonics is given by the shape of the graph and the phase $\alpha(\theta,\phi)$ by a color derived from the color bar at the bottom.

Irreducible spherical tensors

Consider now the vector space $V_2 := \mathrm{Mat}(2^n, \mathbb{C})$ of $2^n \times 2^n$ matrices with complex entries. This vector space corresponds to all possible operators acting on an n-qubit quantum system. The action of $\mathrm{J} \in \mathfrak{su}(2)$ on a matrix $M \in \mathrm{Mat}(2^n, \mathbb{C})$ is defined through the Lie bracket [60] (cf. p. 90 in [56])

$$M \xmapsto{R_2(\mathrm{J})} [\varphi_{\frac{1}{2}}^{\otimes n}(\mathrm{J}),\ M\ ], \tag{2.9}$$

where $\varphi_{\frac{1}{2}}(\mathrm{J}) \in \mathrm{Mat}(2, \mathbb{C})$ denotes the 2-dimensional matrix representation of J and $\varphi_{\frac{1}{2}}^{\otimes n}(\mathrm{J}) := [\varphi_{\frac{1}{2}}(\mathrm{J}) \otimes \mathrm{Id} \otimes \cdots \otimes \mathrm{Id}] + [\mathrm{Id} \otimes \varphi_{\frac{1}{2}}(\mathrm{J}) \otimes \mathrm{Id} \otimes \cdots \otimes \mathrm{Id}] + \ldots + [\mathrm{Id} \otimes \cdots \otimes \mathrm{Id} \otimes \varphi_{\frac{1}{2}}(\mathrm{J})] \in \mathrm{Mat}(2^n, \mathbb{C})$, with Id the 2×2 identity matrix. In particular, the matrices $\varphi_{\frac{1}{2}}(\mathrm{J}_+) := \left(\begin{smallmatrix} 0 & 1 \\ 0 & 0 \end{smallmatrix}\right)$, $\varphi_{\frac{1}{2}}(\mathrm{J}_-) := \left(\begin{smallmatrix} 0 & 0 \\ 1 & 0 \end{smallmatrix}\right)$ and $\varphi_{\frac{1}{2}}(\mathrm{J}_z) := \frac{1}{2}\left(\begin{smallmatrix} 1 & 0 \\ 0 & -1 \end{smallmatrix}\right)$ correspond to the matrices $I_+ := I_x + iI_y$, $I_- := I_x - iI_y$ and I_z of a system consisting of a single spin-1/2 [8], where I_x, I_y and I_z are Hermitian and are called Cartesian single spin-1/2 operators.

Given $j \in \mathbb{Z}$, the standard basis of an irreducible representation of dimension $2j+1$ for the action (2.9) defines the components $\{\mathrm{T}_{jm}\}_{-j \leq m \leq j}$ of an *irreducible spherical tensor operator* of rank j, denoted T_j. By definition, the components T_{jm} satisfy (2.8). For $n > 1$, distinct irreducible spherical tensor operators will have identical rank j (for example, for a system consisting of two spin-1/2 particles, there exist three distinct tensors of rank $j = 1$, *i.e.* three distinct invariant subspaces of $\mathrm{Mat}(2^2, \mathbb{C})$ of dimension $2j + 1 = 3$). Using the fact that the linear combination of irreducible spherical tensor operators of identical rank j is still an irreducible spherical tensor operator of rank j, tensor operators $\mathrm{T}_j(\kappa)$ can be chosen to satisfy additional properties κ which are then used as parameters to distinguish them.

2.10.2 Multiple-spin Wigner representation

Wigner representations of systems are a particular case of "representation distributions" as initially defined in [35]. A representation distribution on the sphere is a mapping

$$\begin{array}{rccc} \Delta: & S^2 & \to & X \\ & (\theta, \phi) & \mapsto & \Delta(\theta, \phi) \end{array}$$

from the sphere to the operator space of the system X. In the case where the operator space can be generated by a tensor basis $\{\mathrm{T}_j\}$ where all the ranks j are distinct, the operator Δ can, for instance, take the form

$$\Delta(\theta, \phi) := \sum_{j,m} \mathrm{T}_{j,m} \mathrm{Y}^*_{j,m}(\theta, \phi).$$

The Wigner function associated with an operator A is then [35, 36]

$$f_A(\theta, \phi) := \mathrm{Tr}[\Delta^\dagger(\theta, \phi) A] = \sum_{j,m} \mathrm{Tr}[\mathrm{T}^\dagger_{j,m} A] \mathrm{Y}_{j,m}(\theta, \phi), \tag{2.10}$$

which corresponds to a direct mapping as in (2.1). The function $f_A(\theta, \phi)$ then satisfies the Stratonovich-Weyl (SW) correspondence, that we summarize under the form presented in [36]:

1. (Linearity) $A \to f_A(\theta, \phi)$ is a one-to-one linear map,

2. (Standardization)
$$\int_{S^2} f_A(\theta,\phi)d\mu = \mathrm{Tr}(A),$$

3. (Covariance)
$$f_{\mathcal{R}(A)}(\theta,\phi) = f_A(\mathcal{R}^{-1}(\theta,\phi)),$$

4. (Traciality)
$$\int_{S^2} f_A(\theta,\phi) f_B(\theta,\phi)d\mu = \mathrm{Tr}(AB),$$

where $d\mu := \sin\theta \; d\theta d\phi$.

The first condition implies that the map given in Eq. (2.10) is linear and bijective. The second condition establishes the connection between the operator framework and the state-phase representation theory. The third condition constrains the mapping (2.10) to be consistent with the rotational symmetry of the space (see Appendix 2.10.1 for more details about the action of rotations on both operators and functions defined on the sphere.) The last condition assures that the tracing properties of operators are consistent with the product of Wigner functions.

We now show how these conditions can be generalized to DROPS representations, which consist of mapping the operator A on a set of functions $\{f_A^{(\ell)}(\theta,\phi)\}_{\ell\in L}$ as defined by the Eqs. (2.2) and (2.3) and that we recall here:

$$A = \sum_{\ell\in L} A^{(\ell)} \leftrightarrow \bigcup_{\ell\in L} f^{(\ell)}(A),$$

with
$$A^{(\ell)} = \sum_{j,m} c_{jm}^{(\ell)} \mathrm{T}_{jm}^{(\ell)} \leftrightarrow f_A^{(\ell)}(\theta,\phi) = \sum_{j',m'} c_{j'm'}^{(\ell)} \mathrm{Y}_{j'm'}(\theta,\phi).$$

For such sets of functions, the previous criteria are adapted as follows:

1. (Linearity) $A \to f_A^{(\ell)}(\theta,\phi)$ are linear maps and the correspondence of A with the corresponding *ordered* k-tuple $\leftrightarrow \left(f_A^{(\ell_1)}(\theta,\phi), f_A^{(\ell_2)}(\theta,\phi), \ldots, f_A^{(\ell_k)}(\theta,\phi)\right)$ is one-to-one,

2. (Standardization)
$$\sum_{\ell\in L} \int_{S^2} f_A^{(\ell)}(\theta,\phi) f_{\mathrm{Id}}^{(\ell)}(\theta,\phi)d\mu = \mathrm{Tr}(A),$$

3. (Covariance)
$$f_{\mathcal{R}(A)}^{(\ell)}(\theta,\phi) = f_A^{(\ell)}(\mathcal{R}^{-1}(\theta,\phi)), \quad \text{for all } \ell \in L,$$

4. (Traciality)
$$\sum_{\ell\in L} \int_{S^2} f_A^{(\ell)}(\theta,\phi) f^{(\ell)}{}_B(\theta,\phi)d\mu = \mathrm{Tr}(AB).$$

We want to show that the DROPS representation of operators satisfies these generalized criteria. The first condition follows directly from the definition of the DROPS mapping. The second condition is a special case of the fourth one, which we prove afterwards. Here, a summation over all droplet functions appear (in comparison to the criterion previously encountered),as well a the Wigner function for the identity on the left side of the equality. The third relation is a direct extension of the initial Covariance criterion and uses the rotational properties of spherical tensor operators. This criterion is satisfied since, by definition, the components $\{T_{j,m}\}_{-j\leq m\leq j}$ of the same tensor define an invariant subspace under rotations and since all these components are part of the same droplet. The last condition is the only one which requires more careful verifications. To verify it, we develop both sides of the equality and show that they lead to the same expression. To simplify the expressions, the dependence of the spherical harmonics on the variables θ and ϕ is dropped.

The left-hand side of the equality is developed as:

$$\sum_{\ell\in L}\int_{S^2} f_A^{(\ell)}(\theta,\phi){f^{(\ell)}}_B(\theta,\phi)d\mu = \sum_{\ell\in L}\int_{S^2}\sum_{jm}\mathrm{Tr}[\mathrm{T}^{\dagger(\ell)}_{jm}A]\mathrm{Y}_{jm}\cdot\sum_{j'm'}\mathrm{Tr}[\mathrm{T}^{\dagger(\ell)}_{j'm'}B]\mathrm{Y}_{j'm'}d\mu$$

(orthonormality of spherical harmonics and property $\mathrm{Y}_{j,m}=(-1)^{-m}\mathrm{Y}^{\dagger}_{j,-m}$

$$=\sum_{\ell\in L}\sum_{jm}\mathrm{Tr}[\mathrm{T}^{\dagger(\ell)}_{jm}A]\cdot\mathrm{Tr}[\mathrm{T}^{\dagger(\ell)}_{j,-m}B](-1)^{-m}$$

(tensor normalization and property $\mathrm{T}_{jm}=(-1)^{-m}\mathrm{T}^{\dagger}_{j,-m}$

$$=\sum_{\ell\in L}\sum_{jm}\mathrm{Tr}[\mathrm{T}^{\dagger(\ell)}_{jm}A]\cdot\mathrm{Tr}[\mathrm{T}^{\dagger(\ell)}_{j,m}B].$$

On the right-hand side,

$$\mathrm{Tr}(AB)=\mathrm{Tr}\left(\sum_{\ell\in L}A^{(\ell)}\sum_{\ell'\in L}B^{(\ell')}\right)$$

(linearity of the trace)

$$=\sum_{\ell\in L}\sum_{\ell'\in L}\mathrm{Tr}\left(A^{(\ell)}B^{(\ell')}\right)$$

(orthogonality of the operator spaces corresponding to different droplets)

$$=\sum_{\ell\in L}\mathrm{Tr}\left(A^{(\ell)}B^{(\ell)}\right)$$

(decomposition of $A^{(\ell)}$ and $B^{(\ell)}$)

$$=\sum_{\ell\in L}\mathrm{Tr}\left(\sum_{jm}\mathrm{Tr}[\mathrm{T}^{\dagger(\ell)}_{jm}A]\mathrm{T}^{(\ell)}_{jm}\cdot\sum_{j'm'}\mathrm{Tr}[\mathrm{T}^{\dagger(\ell)}_{j'm'}B]\mathrm{T}^{(\ell)}_{j'm'}\right)$$

(linearity of the trace)

$$=\sum_{\ell\in L}\sum_{jm}\sum_{j'm'}\mathrm{Tr}[\mathrm{T}^{\dagger(\ell)}_{jm}A]\mathrm{Tr}[\mathrm{T}^{\dagger(\ell)}_{j'm'}B]\mathrm{Tr}(\mathrm{T}^{(\ell)}_{jm}\mathrm{T}^{(\ell)}_{j'm'})$$

(tensor normalization and property $\mathrm{T}_{j,m}=(-1)^{-m}\mathrm{T}^{\dagger}_{j,-m}$)

$$=\sum_{\ell\in L}\sum_{jm}\mathrm{Tr}[\mathrm{T}^{\dagger(\ell)}_{jm}A]\mathrm{Tr}[\mathrm{T}^{\dagger(\ell)}_{j,-m}B](-1)^{m}$$

$$\overset{(\text{property } \mathrm{T}_{j,m} = (-1)^{-m}\mathrm{T}^{\dagger}_{j,-m})}{=} \sum_{\ell\in L}\sum_{jm} \mathrm{Tr}[\mathrm{T}^{\dagger(\ell)}_{jm} A]\mathrm{Tr}[\mathrm{T}^{(\ell)}_{j,m} B]. \blacksquare$$

The ensemble of distributions $\{\Delta^{(\ell)}\}$

$$\Delta^{(\ell)}(\theta,\phi) := \sum_{j,m} \mathrm{T}^{(\ell)}_{j,m} \mathrm{Y}^{*}_{j,m}(\theta,\phi),$$

together with their associated Wigner functions

$$f^{(\ell)}_{A}(\theta,\phi) := \mathrm{Tr}[\Delta^{(\ell)\dagger}(\theta,\phi)A] = \sum_{j,m} \mathrm{Tr}[\mathrm{T}^{(\ell)\dagger}_{j,m} A]\mathrm{Y}_{j,m}(\theta,\phi), \tag{2.11}$$

then define a complete and consistent representation of the operator space X.

2.10.3 Cartesian product operators for an n qubits system

We briefly introduce the Cartesian product operators which are commonly used in nuclear magnetic resonance [8, 32]. They are Hermitian and they form a complete basis of the operator space for systems consisting of spin-1/2 particles. For a single-spin-1/2 system, the Cartesian operators I_η, $\eta \in \{x, y, z\}$ have been defined in Appendix 2.10.1 and correspond (up to a factor 1/2) to the Pauli matrices. I_0 is the identity matrix. The Cartesian product operators for an n-spin-1/2 system are defined by first embedding the one-spin operators I_η with $\eta \in \{x, y, z\}$ into the global system by choosing a position $p \in \{1, \ldots, n\}$ and defining the n-spin operators $I^{[n]}_{p\eta} := \bigotimes_{k=1}^{n} I_{a_k}$ (or $I_{p\eta}$ for short), where $a_k{=}\eta$ for $k{=}p$ and $a_k{=}0$ otherwise. The Cartesian product operator basis [8] for an n-spin-1/2 system is now given by all the elements of the form $2^{d-1}\prod_{k=1}^{d} I_{p_k\eta_k}$ for which $d, p_k \in \{1, \ldots, n\}$, $\ell_k < p_{k+1}$ for $k < d$, and $\eta_k \in \{x, y, z\}$. For instance, in a system consisting of 3 spin-1/2 particles, the symbols I_{2x}, $2I_{1z}I_{3_y}$ and $4I_{1x}I_{2x}I_{3y}$ all correspond to valid Cartesian product operators. Note that Cartesian product operators are in general neither irreducible nor components of a tensor operator.

2.10.4 Symmetrizers, projectors and symmetry species

The following presentation follows Chapter 5 of [40] (alternatively, see [19, 37], or [61] for a general survey of projection theory.)

Standard Young tableaux

A standard Young tableau of size k is the left-justified arrangement of k boxes labeled from 1 to k such that 1) each row has more or the same number of boxes than the ones below and 2) the numbers in the boxes increase from left to right and from top to bottom. For instance, the four standard Young tableaux of size $k = 3$ are

$$\tau^{[3]}_1 = \begin{array}{|c|c|c|}\hline 1 & 2 & 3 \\ \hline \end{array}, \quad \tau^{[3]}_2 = \begin{array}{|c|c|}\hline 1 & 2 \\ \hline 3 \\ \cline{1-1} \end{array}, \quad \tau^{[3]}_3 = \begin{array}{|c|c|}\hline 1 & 3 \\ \hline 2 \\ \cline{1-1} \end{array}, \quad \tau^{[3]}_4 = \begin{array}{|c|}\hline 1 \\ \hline 2 \\ \hline 3 \\ \hline \end{array}. \tag{2.12}$$

Total order on standard Young tableaux

The subscript i in $\tau_i^{[k]}$ refers to the natural total order defined on standard Young tableaux of size k. Let $\lambda(\tau_i^{[k]})$ denote the word made of the number of boxes in each line from top to bottom in $\tau_i^{[k]}$ and and $w(\tau_i^{[k]})$ denote the k-letter word obtained by reading the numbers in $\tau_i^{[k]}$ from left to right and from top to bottom. The words $\lambda(\tau_i^{[k]})$ and $w(\tau_i^{[k]})$ are respectively called the *shape* and the *filling pattern* of $\tau_i^{[k]}$. For instance, the shape of $\tau_3^{[3]}$ in (2.12) is $\lambda(\tau_3^{[3]}) = 21$ and its filling pattern is $w(\tau_3^{[3]}) = 132$. Then $\tau_i^{[k]} < \tau_{i'}^{[k]}$ if either $\lambda(\tau_i^{[k]}) > \lambda(\tau_{i'}^{[k]})$ or if $\lambda(\tau_i^{[k]}) = \lambda(\tau_{i'}^{[k]})$ and $w(\tau_i^{[k]}) < w(\tau_{i'}^{[k]})$ where the inequalities hold for the alphabetical order. The index i corresponds to the position of the Young tableau relative to this total order (see (2.12)).

Permutation group S_k and its real algebra $\widetilde{S}_k$

The symmetric group S_k [37, 62–67] is a finite group consisting of $k!$ different permutations $\sigma \in S_k$ which map labels $i \in \{1, \ldots, k\}$ to positions $\sigma(i) \in \{1, \ldots, k\}$, where $\sigma(i_1) \neq \sigma(i_2)$ for $i_1 \neq i_2$. One way to express a permutation σ is to write $\sigma = \left(\begin{smallmatrix} 1 & 2 & \cdots & k \\ \sigma(1) & \sigma(2) & \cdots & \sigma(k) \end{smallmatrix}\right)$, where the labels are written in the upper row and the position they are assigned to in the lower row. The more standard notation used in the present work is to write the permutation in disjoint cycles $\sigma = c_1 c_2 \ldots c_p$, where a cycle $c = (i_1 i_2 \ldots i_q) \in S_k$ maps label i_1 to position i_2, label i_2 to position i_3, etc. and finally, label i_q to position i_1. Any permutation can be uniquely decomposed as a product of disjoint cycles. The adjacent transpositions, called *transpositions* for short, are the cycles $(i\ i+1)$ which exchange the position of 2 consecutive labels. The group multiplication for $\sigma_1, \sigma_2 \in S_k$ is given by the composition $(\sigma_2 \circ \sigma_1)(i) := \sigma_2(\sigma_1(i))$.

The *real algebra* $\widetilde{S}_k$ consists in all the real linear combinations of permutations σ in S_k. That is, $\widetilde{x} \in \widetilde{S}_k$ can be decomposed (not uniquely) as $\widetilde{x} = \sum_{\sigma \in S_k} x_\sigma \sigma$ with $x_\sigma \in \mathbb{R}$. Given two elements $\widetilde{x}, \widetilde{y} \in \widetilde{S}_k$, the sum is naturally defined as $\widetilde{x} + \widetilde{y} = \sum_{\sigma \in S_k} (x_\sigma + y_\sigma)\sigma$ and the product as $\widetilde{x} \cdot \widetilde{y} = \sum_{\sigma' \in S_k} \sum_{\sigma \in S_k} (x_{\sigma'} \cdot y_\sigma)(\sigma' \circ \sigma)$.

Symmetrizers [37, 40]

Given a standard Young Tableau τ of size k, let $h_\tau \in \widetilde{S}_k$ denote the sum of all permutations not mixing the labels of different lines of τ and $v_\tau \in \widetilde{S}_k$ denote the "alternated" sum of all permutations not mixing the labels of different columns in τ. The sign of a permutation σ in the alternated sum v_τ is $(-1)^{|\sigma|}$ where $|\sigma|$ is the number of transpositions $(i\ i+1)$ necessary to construct σ starting from the identity element e. Taking for instance $\tau := \tau_2^{[3]}$ (see Eq. (2.12)), one verifies that $h_\tau = e + (12)$ and $v_\tau = e - (13)$. The product $e_\tau := c_\tau(h_\tau \cdot v_\tau) \in \widetilde{S}_k$ defines the *irreducible symmetrizer* associated with τ. The normalization factor c_τ is taken such that $\sum_{\tau_i^{[k]}} e_{\tau_i^{[k]}} = e$ (the identity element) where the sum is taken over all the standard Young tableaux of size k.

For instance, the symmetrizers corresponding to the four standard Young tableaux of size 3 in Eq. (2.12) are

$$e_{\tau_1^{[3]}} = \frac{e + (12) + (23) + (31) + (123) + (321)}{6} \tag{2.13a}$$

$$e_{\tau_2^{[3]}} = \frac{e + (12) - (31) - (321)}{3} \tag{2.13b}$$

$$e_{\tau_3^{[3]}} = \frac{e + (31) - (12) - (123)}{3} \tag{2.13c}$$

$$e_{\tau_4^{[3]}} = \frac{e - (12) - (23) - (31) - (123) - (321)}{6} \tag{2.13d}$$

and one directly verifies that $e_{\tau_1^{[3]}} + e_{\tau_2^{[3]}} + e_{\tau_3^{[3]}} + e_{\tau_4^{[3]}} = e$.

Projectors

Let $\tau_q^{[k]}, \tau_{q+1}^{[k]}, \ldots, \tau_{q+d}^{[k]}$ be the ordered list of Young tableaux having identical shape λ (the fact that the sequence of indices $q, \ldots, q+d$ is unbroken follows from the definition of the total order on Young tableaux of size k introduced earlier) and consider $\tau_i^{[k]}$ with $q \leq i \leq q+d$. The *projector* $P_{\tau_i^{[k]}}$ is an element of the algebra $\widetilde{S}_k$ and is defined recursively from $e_{\tau_q^{[k]}}$, the symmetrizer associated with the smallest standard Young tableau of shape λ.

Basic case: $i = q$. The projector associated with the first Young tableau is equal to its symmetrizer, that is $P_{\tau_i^{[k]}} := e_{\tau_i^{[k]}}$.

General case: $i > q$. There exists $i' \in \{q, \ldots, i-1\}$ such that the Young tableau $\tau_{i'}^{[k]}$ differs from $\tau_i^{[k]}$ only by the position of two boxes $\boxed{a}$ and $\boxed{b}$ with consecutive labels ($b = a + 1$) and for which the projector $P_{\tau_{i'}^{[k]}}$ has already been defined. Let δ denote the number of boxes in the hook path [37] joining the boxes $\boxed{a}$ and $\boxed{b}$ in $\tau_i^{[k]}$ (excluding the starting box $\boxed{a}$) and define $A = \frac{1}{\delta}$ and $B = \frac{\sqrt{\delta^2 - 1}}{\delta}$. Then

$$P_{\tau_i^{[k]}} := \left(\frac{(a\ b) + A}{B} \right) P_{\tau_{i'}^{[k]}} \in \widetilde{S}_k, \tag{2.14}$$

where $(a\ b) \in S_k$ is a transposition. To make this construction more concrete, let us construct the four projectors in S_3 used to symmetrize trilinear tensors in a system consisting of three spin-1/2.

- $\tau_1^{[3]} = \begin{array}{|c|c|c|}\hline 1 & 2 & 3 \\ \hline \end{array}$ is the only standard Young tableau of shape $\lambda = 3$. Since it is (necessarily) the smallest Young tableau of this shape, $P_{\tau_1^{[3]}} = e_{\tau_1^{[3]}}$ and one can refer to Eq. (2.13) for its explicit expression.
- $\tau_2^{[3]} = \begin{array}{|c|c|}\hline 1 & 2 \\ \hline 3 \\ \cline{1-1} \end{array}$ and $\tau_3^{[3]} = \begin{array}{|c|c|}\hline 1 & 3 \\ \hline 2 \\ \cline{1-1} \end{array}$ are the two Young tableaux of shape $\lambda = 21$. The smallest of these two Young tableaux is $\tau_2^{[3]}$ and consequently, $P_{\tau_2^{[3]}} = e_{\tau_2^{[3]}}$ (see Eq. (2.13) for its explicit expression). Now, $\tau_3^{[3]}$ differs from $\tau_2^{[3]}$ by the exchange of the two boxes of consecutive labels $a = 2$ and $b = 3$. The length of the hook path joining the boxes $\boxed{2}$ and $\boxed{3}$ in $\tau_3^{[3]}$ (excluding the starting box $\boxed{2}$) is $\delta = 2$ and we define $A = \frac{1}{2}$ and $B = \frac{\sqrt{3}}{2}$. According to Equation (2.14), we obtain

$$P_{\tau_3^{[3]}} := \left(\frac{(23) + A}{B} \right) P_{\tau_2^{[3]}}$$

$$
\begin{aligned}
&= \left(\frac{(23) + \frac{1}{2}}{\frac{\sqrt{3}}{2}} \right) e_{\tau_2^{[3]}} \\
&= \left(\frac{(23) + \frac{1}{2}}{\frac{\sqrt{3}}{2}} \right) \frac{e + (12) - (31) - (321)}{3} \\
&= \frac{1}{\sqrt{3}} \left(\frac{e - (12) - (31) + 2(23) + (321) - 2(123)}{3} \right).
\end{aligned}
$$

- Finally, $\tau_4^{[3]} = \begin{array}{|c|}\hline 1 \\ \hline 2 \\ \hline 3 \\ \hline \end{array}$ is the only standard Young tableau of shape $\lambda = 111$. Since it is the smallest Young tableau of this shape, then $P_{\tau_4^{[3]}} = e_{\tau_4^{[3]}}$ ant its expression is given in Eq. (2.13).

Action of permutations on operators

The action of a permutation $\sigma \in S_k$ on operators is defined via the Cartesian product operator basis. A permutation σ acts on a Cartesian product operator by permuting its particle labels according to σ. For instance, $(321)(I_{1x}I_{2y}I_{3z}) = I_{3x}I_{1y}I_{2z} \equiv I_{1y}I_{2z}I_{3x}$. This action extends naturally by linearity to the group algebra $\widetilde{S}_k$ and then to the decomposition of any operator with respect to the Cartesian product operator basis.

Symmetry species

Given a standard Young tableau τ, a tensor T_j is said to be of *symmetry species* τ if each of its components is left invariant (up to a constant c) under the action of the projector P_τ associated with τ, that is, $P_\tau(\mathrm{T}_{jm}) = c\ \mathrm{T}_{jm}\ \forall m \in \{-j, \ldots, j\}$. The particular cases $\tau = \begin{array}{|c|c|c|c|}\hline 1 & 2 & \cdot\cdot & k \\ \hline \end{array}$ and $\tau = \begin{array}{|c|}\hline 1 \\ \hline 2 \\ \hline : \\ \hline k \\ \hline \end{array}$ correspond respectively to the symmetric and antisymmetric k-linear tensors.

For instance, one verifies directly on the tensor component

$$\mathrm{T}_{2,0}(\tau_2^{[3]}) := \sqrt{2}(-I_{xzy} + I_{yzx} - I_{zxy} + I_{zyx})$$

that $P_{\tau_2^{[3]}} \left(\mathrm{T}_{2,0}(\tau_2^{[3]}) \right) = \mathrm{T}_{2,0}(\tau_2^{[3]})$, where $P_{\tau_2^{[3]}}$ was deduced in a previous paragraph of the present appendix.

2.10.5 Explicit construction of the LiSA tensor basis of a three-spin-1/2 system

The irreducible representations of $\mathfrak{su}(2)$ on the space $V_2 = \mathrm{Mat}(2^n, \mathbb{C})$ $(n = 3)$ considered are carefully chosen such that their basis elements are labeled

$$\mathrm{T}_{j,m}^{\{s_1,\ldots,s_k\}}(\tau_i^{[k]})$$

where j and m are defined as before, $\tau_i^{[k]}$ is a standard Young tableau of length k giving the symmetry species of the tensor and $\{s_1, \ldots, s_k\}$ denotes the particles involved in the tensor. The parameter k specifies the linearity of the tensor. The construction of the basis elements is performed in three steps:
(I) Recursive construction of symmetrized k-linear operators for the systems consisting of k spin-1/2 particles, for $k = 0, 1, 2, 3$;
(II) Phase correction by an element in $\{1, -1, i, -i\}$ of the tensors obtained in **(I)**, where the imaginary factor ensures that condition (2.6) is satisfied and the choice of the sign $\pm$ is motivated in Appendix 2.10.7;
(III) Embedding of the k-linear symmetrized tensors **(II)** in the entire system, where a copy of the k-linear symmetrized tensors corresponds to each k-particle subsystem $\{s_1, \ldots, s_k\}$ (see [38] for an alternative way to define symmetrized tensors).

Step (I)

- k=0: The tensor $\mathrm{T}_0(\tau_1^{[0]})$ is simply the 2×2 identity matrix and the symbol $\tau_1^{[0]}$ denotes the empty Young tableau.

- k=1: There is one 1-linear tensor operator $\mathrm{T}_1(\tau_1^{[1]})$ whose components are the only matrices to be computed using Eq. (2.8). They can be found in any reference book on spins such as [8] for example. They are necessarily already symmetrized since there is only one Young tableau with one box, namely $\tau_1^{[1]} = \ydiagram{1}$. The explicit tensor components are

$$\mathrm{T}_{1,-1}(\tau_1^{[1]}) = \begin{pmatrix} 0 & 0 \\ 1 & 0 \end{pmatrix}, \mathrm{T}_{1,0} \ (\tau_1^{[1]}) = \begin{pmatrix} \frac{1}{\sqrt{2}} & 0 \\ 0 & -\frac{1}{\sqrt{2}} \end{pmatrix}, \mathrm{T}_{11}(\tau_1^{[1]}) = \begin{pmatrix} 0 & -1 \\ 0 & 0 \end{pmatrix}.$$

- k=2: The three 2-linear tensors are built using the Clebsch-Gordan decomposition $\mathrm{T}_1(\tau_1^{[1]}) \otimes \mathrm{T}_1(\tau_1^{[1]}) = \mathrm{T}_0 \oplus \mathrm{T}_1 \oplus \mathrm{T}_2$. The two standard Young tableaux $\tau_i^{[2]}$ of size 2, their associated symmetrizers $e_{\tau_i^{[2]}}$ and projectors $P_{\tau_i^{[2]}}$ are constructed according to Appendix 2.10.4 and have the explicit form

$$e_{\tau_1^{[2]}} = \frac{e + (12)}{2} = P_{\tau_1^{[2]}} \ \text{ for } \ \tau_1^{[2]} = \ydiagram{2}, \qquad e_{\tau_2^{[2]}} = \frac{e - (12)}{2} = P_{\tau_2^{[2]}} \ \text{ for } \ \tau_2^{[2]} = \ydiagram{1,1}.$$

  The tensors T_j are already symmetrized since there is only one standard Young tableau of each shape λ. In particular,

$$\mathrm{T}_0(\tau_1^{[2]}) := \mathrm{T}_0, \quad \mathrm{T}_1(\tau_2^{[2]}) := \mathrm{T}_1, \quad \mathrm{T}_2(\tau_1^{[2]}) := \mathrm{T}_2.$$

  Recall that these tensors correspond to 2-linear tensors in a 2-spin-1/2 system and are elements of $\mathrm{Mat}(2^2, \mathbb{C})$.

- k=3: There are seven non-symmetrized 3-linear tensors which are obtained from the Clebsch-Gordan decomposition for the tensor product of the 2-linear tensors previously found and the 1-linear one:

$$\begin{aligned}
&\mathrm{T}_0(\tau_1^{[2]}) \otimes \mathrm{T}_1(\tau_1^{[1]}) = {\mathrm{T}_1}' \\
&\mathrm{T}_1(\tau_2^{[2]}) \otimes \mathrm{T}_1(\tau_1^{[1]}) = {\mathrm{T}_0}'' \oplus {\mathrm{T}_1}'' \oplus {\mathrm{T}_2}'' \\
&\mathrm{T}_2(\tau_1^{[2]}) \otimes \mathrm{T}_1(\tau_1^{[1]}) = {\mathrm{T}_1}''' \oplus {\mathrm{T}_2}''' \oplus {\mathrm{T}_3}'''.
\end{aligned}$$

  The four standard Young tableaux of size 3 and their associated symmetrizers are summarized in (2.13). The associated projectors have been computed in Appendix 2.10.4. The symmetrized and normalized tensors are:

$$\begin{aligned}
\mathrm{T}_0(\tau_4^{[3]}) &:= P_{\tau_4^{[3]}}\left({\mathrm{T}_0}''\right), \\
\mathrm{T}_1(\tau_1^{[3]}) &:= \frac{3}{\sqrt{5}} P_{\tau_1^{[3]}}\left({\mathrm{T}_1}'\right), \\
\mathrm{T}_1(\tau_2^{[3]}) &:= \frac{3}{2} P_{\tau_2^{[3]}}\left({\mathrm{T}_1}'\right), \\
\mathrm{T}_1(\tau_3^{[3]}) &:= \frac{3}{2} P_{\tau_3^{[3]}}\left({\mathrm{T}_1}'\right), \\
\mathrm{T}_2(\tau_2^{[3]}) &:= P_{\tau_2^{[3]}}\left({\mathrm{T}_2}''\right), \\
\mathrm{T}_2(\tau_3^{[3]}) &:= P_{\tau_3^{[3]}}\left({\mathrm{T}_2}''\right), \\
\mathrm{T}_3(\tau_1^{[3]}) &:= P_{\tau_1^{[3]}}\left({\mathrm{T}_3}'''\right),
\end{aligned}$$

  and are elements of $\mathrm{Mat}(8, \mathbb{C})$ with appropriate normalization factors.

Note that since n-linear tensors in systems consisting of $n \leq 5$ spin-1/2 particles [39] are uniquely defined by their rank j and symmetry species $\tau_i^{[n]}$, the outcome of the action of a projector $P_{\tau_i^{[n]}}$ is independent of the tensors to which they are applied. For more general spin systems, the action of a projector on two distinct tensors of rank j may result in distinct tensors with identical symmetry species.

Step (II)

We only exhibit here the sign change applied to the current tensors, the choice of which is further discussed in Appendix 2.10.7. The new tensors (with their proper signs) are denoted by the subscript $[\ ]_{\mathbf{(II)}}$ and are obtained by scalar multiplication of those in step **(I)**, denoted with the subscript $[\ ]_{\mathbf{(I)}}$. Recall that the presence of a complex factor i is uniquely decided by the relation 2.6.

$$\begin{aligned}
&\left[\mathrm{T}_1(\tau_1^{[1]})\right]_{\mathbf{(II)}} = \left[\mathrm{T}_1(\tau_1^{[1]})\right]_{\mathbf{(I)}} \\
&\begin{bmatrix} \mathrm{T}_0(\tau_1^{[2]}) \\ \mathrm{T}_1(\tau_2^{[2]}) \\ \mathrm{T}_2(\tau_1^{[2]}) \end{bmatrix}_{\mathbf{(II)}} = \mathrm{diag}(1, -i, -1) \begin{bmatrix} \mathrm{T}_0(\tau_1^{[2]}) \\ \mathrm{T}_1(\tau_2^{[2]}) \\ \mathrm{T}_2(\tau_1^{[2]}) \end{bmatrix}_{\mathbf{(I)}}
\end{aligned}$$

$$\begin{bmatrix} \mathrm{T}_0(\tau_4^{[3]}) \\ \mathrm{T}_1(\tau_1^{[3]}) \\ \mathrm{T}_1(\tau_2^{[3]}) \\ \mathrm{T}_1(\tau_3^{[3]}) \\ \mathrm{T}_2(\tau_2^{[3]}) \\ \mathrm{T}_2(\tau_3^{[3]}) \\ \mathrm{T}_3(\tau_1^{[3]}) \end{bmatrix}_{\textbf{(II)}} = \mathrm{diag}(-i,-1,1,1,-i,-i,1) \begin{bmatrix} \mathrm{T}_0(\tau_4^{[3]}) \\ \mathrm{T}_1(\tau_1^{[3]}) \\ \mathrm{T}_1(\tau_2^{[3]}) \\ \mathrm{T}_1(\tau_3^{[3]}) \\ \mathrm{T}_2(\tau_2^{[3]}) \\ \mathrm{T}_2(\tau_3^{[3]}) \\ \mathrm{T}_3(\tau_1^{[3]}) \end{bmatrix}_{\textbf{(I)}}$$

Step (III)

- $k = 0$**.** The embedding of $\mathrm{T}_0(\tau_1^{[0]}) = \mathrm{Id}_2 \in \mathrm{Mat}(2, \mathbb{C})$ is performed by considering $\mathrm{Id}_8 \in \mathrm{Mat}(2^3, \mathbb{C})$:

$$\mathrm{T}_0^{\emptyset}(\tau_1^{[0]}) := \mathrm{T}_0(\tau_1^{[0]}) \otimes \mathrm{Id}_2 \otimes \mathrm{Id}_2 = \mathrm{Id}_8.$$

- $k = 1$**.** The embedding of $\mathrm{T}_1(\tau_1^{[1]}) \in \mathrm{Mat}(2, \mathbb{C})$ for the spin $\{1\}$ subsystem is performed by taking the tensor product with the identity Id_2 on the two unaffected particles, here $\{2\}$ and $\{3\}$. Explicitly:

$$\mathrm{T}_1^{\{1\}}(\tau_1^{[1]}) := \mathrm{T}_1(\tau_1^{[1]}) \otimes \mathrm{Id}_2 \otimes \mathrm{Id}_2.$$

  The remaining 1-linear tensors can simply be obtained from $\mathrm{T}_1^{\{1\}}(\tau_1^{[1]})$ (just computed) by permuting the particle labels (the action of permutations on operators is defined in Appendix 2.10.4):

$$\mathrm{T}_1^{\{2\}}(\tau_1^{[1]}) := (12)\left(\mathrm{T}_1^{\{1\}}(\tau_1^{[1]})\right),$$
$$\mathrm{T}_1^{\{3\}}(\tau_1^{[1]}) := (13)\left(\mathrm{T}_1^{\{1\}}(\tau_1^{[1]})\right).$$

- $k = 2$**.** The embedding of $\mathrm{T}_j(\tau_i^{[2]}) \in \mathrm{Mat}(2^2, \mathbb{C})$ for the subsystem consisting of spins $\{1, 2\}$ is performed by taking the tensor product with the identity Id_2 for the unaffected particle $\{3\}$:

$$\mathrm{T}_j^{\{1,2\}}(\tau_i^{[2]}) := \mathrm{T}_j(\tau_i^{[2]}) \otimes \mathrm{Id}_2.$$

  The 2-linear tensors for the remaining 2-particle subsystems $\{1, 3\}$ and $\{2, 3\}$ can be obtained from $\mathrm{T}_j^{\{1,2\}}(\tau_i^{[2]})$ by permutation of the particle labels:

$$\mathrm{T}_j^{\{1,3\}}(\tau_i^{[2]}) := (23)\left(\mathrm{T}_j^{\{1,2\}}(\tau_i^{[2]})\right),$$
$$\mathrm{T}_j^{\{2,3\}}(\tau_i^{[2]}) := (12)\left(\mathrm{T}_j^{\{1,3\}}(\tau_i^{[2]})\right)$$

- $k = 3$**.** Since the 3-linear tensors $\mathrm{T}_j(\tau_i^{[3]}) \in \mathrm{Mat}(8, \mathbb{C})$ already involve all the spins of the global system, there is no embedding to perform and one can directly write

$$\mathrm{T}_j^{\{1,2,3\}}(\tau_i^{[3]}) := \mathrm{T}_j(\tau_i^{[3]}).$$

2.10.6 Labeling

The linear and bilinear ($k = 1, 2$) tensors are uniquely defined by their rank j and the subsystem they involve and consequently, the symmetry species is superfluous in their labeling. To avoid redundancy, the symmetry parameter can be dropped when referring to them:

$$\mathrm{T}^{\{s_1\}}_{j,m} := \mathrm{T}^{\{s_1\}}_{j,m}(\tau_1^{[1]}) \quad \text{and} \quad \mathrm{T}^{\{s_1,s_2\}}_{j,m} := \mathrm{T}^{\{s_1,s_2\}}_{j,m}(\tau_i^{[2]}).$$

Another shorthand notation can be used when referring to n-linear tensors in an n-particle system. Indeed, since these tensors involve all the particles, there is no need to carry the sequence of spins involved and they can therefore be uniquely denoted

$$\mathrm{T}_{j,m}(\tau_i^{[n]}) := \mathrm{T}^{\{1,2,\ldots,n\}}_{j,m}(\tau_i^{[n]}).$$

2.10.7 Motivation of the sign choice

We already discussed the fact that normalized tensors of the LiSA basis fulfilling (2.6) are defined up to a sign, the choice of which is arbitrary. We present here the choice made for the introduced LiSA basis. The sign of the linear tensors has been chosen such

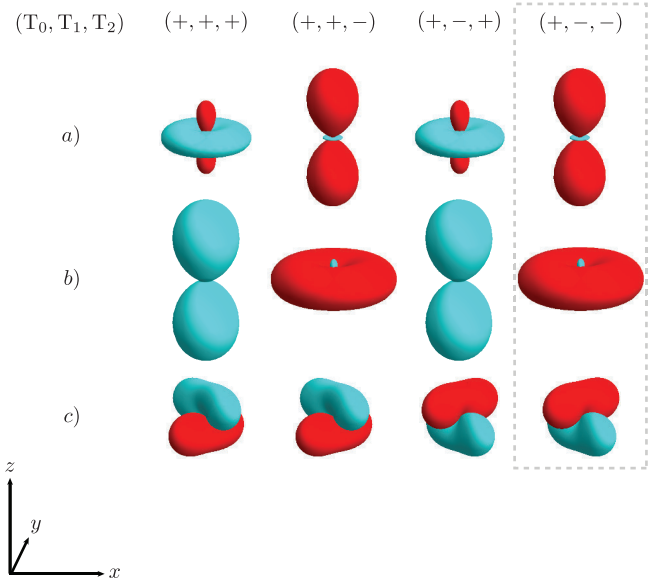

Figure 2.10: Different sign choice for the bilinear tensors $\mathrm{T}^{\{k,l\}}_j$ of rank $j = 0, 1, 2$. For the different sign choices, the resulting visualization of the operators *a)* $2I_{kz}I_{lz}$, *b)* $2I_{kx}I_{lx} + 2I_{ky}I_{ly}$ and *c)* $2I_{kx}I_{ly}$ is displayed (the red and blue colors refer to positive and negative values of the droplet function $f^{(\{k,l\})}(A)$, respectively). In the standard LiSA basis proposed here, signs are chosen according to the last column $(+,-,-)$.

that the $\{k\}$ droplet representing the linear Cartesian operators $I_{k\eta}$, $\eta \in \{x, y, z\}$, is consistent with its Bloch vector representation. That is, the positive lobe of the LiSA representation of $I_{k\eta}$ is pointing in the η direction (see Fig. 2.3).

The sign of the bilinear tensors has been chosen in order to be consistent with the different coupling Hamiltonians together with the operators of the form $2I_{k\eta_1}I_{l\eta_2}$

(which include the anti-phase operators). Figure 2.10 a) and b) shows that there are two possible shapes (up to a global -1 factor) for the longitudinal and planar Hamiltonian terms respectively. Choosing the signs $+1$ and -1 for the tensors T_0 and T_2 results in an elongated shape for the longitudinal Hamiltonian droplets and a planar shape for the planar Hamiltonian droplets. The sign -1 for the tensor T_1 has been chosen such that the center of the positive lobe in the droplet representing $2I_{k\eta_1}I_{l\eta_2}$ (Fig. 2.10 c)) is displaced in the $\vec{\eta}_3$-direction relative to the center of the droplet, where $\vec{\eta}_3 = \vec{\eta}_1 \times \vec{\eta}_2$ is given by the right-hand rule (c.f. Figs. 2.10 and 2.4).

All but two the signs of the trilinear tensors have simply been inherited from the bilinear ones, recalling that the trilinear tensors are derived from the Clebsch-Gordan decomposition of the tensor product of a bilinear tensor with a linear one. The only tensors for which the sign has been chosen opposite to the one of their bilinear tensor parent are the totally symmetric tensors $\mathrm{T}_1(\tau_1^{[3]})$ and $\mathrm{T}_3(\tau_1^{[3]})$. This choice has been made such that the positive lobe of the droplet involved in the visualization of the fully symmetric Cartesian tensor $4I_{1\eta}I_{2\eta}I_{1\eta}$ points in the η direction (see Fig. 2.3).

2.10.8 Examples

Concurrence example

The first example shown in Fig. 2.7 displays the DROPS representation of entangled pure states of two qubits (Bell states) and three qubits (W and GHZ states) as well as the representation of a separable two-qubit state.

Consider an operator A acting on a two-qubit system. This operator can be decomposed as

$$A = A^{(\{1\})} + A^{(\{2\})} + A^{(\{1,2\})} + A^{(\mathrm{Id})}$$

using the LiSA mapping corresponding to Eq. (2.3). Since $A^{(\{1\})}$ acts on the first spin only, we can write

$$A^{(\{1\})} = A_1 \otimes \mathrm{Id},$$

where Id denotes the identity matrix on spin two and similarly,

$$A^{(\{2\})} = \mathrm{Id} \otimes A_2.$$

The matrices A_k correspond to the reduced operators for the corresponding spin k, and can also be recovered by tracing out A with respect to the complementary spin. The trace of A_k^2 furnishes a measurement of entanglement in the full operator A and for operators representing pure states, $C := \sqrt{1 - \mathrm{Tr}(A_1^2)} = \sqrt{1 - \mathrm{Tr}(A_2^2)}$ is called the *concurrence* of the state. In particular, writing $A_k = a_{kx}I_{kx} + a_{ky}I_{ky} + a_{kz}I_{kz}$, then the concurrence is $C = \sqrt{1 - a_{kx}^2 - a_{ky}^2 - a_{kz}^2}$.

On the other hand, we have that the droplet corresponding to $a_{kx}I_{kx} + a_{ky}I_{ky} + a_{kz}I_{kz}$ has the form of two spheres of opposite sign which delineate an axis pointing in the direction $a_{kx}\vec{1}_x + a_{ky}\vec{1}_y + a_{kz}\vec{1}_z$. More precisely, the length of the droplet (defined by the line joining the opposite sides of the positive and negative spheres) is $R = \sqrt{\frac{6}{\pi}(a_{kx}^2 + a_{ky}^2 + a_{kz}^2)}$, that is, $C = \sqrt{1 - \frac{\pi}{6}R^2}$ and we see that the bigger the droplets are (value of R), the lower the concurrence value is.

Creation of triple-quantum coherences experiment

The example shown in Fig. 2.8 represents an experiment commonly used in NMR spectroscopy, which is designed to create triple-quantum coherences from the polarization of three coupled spin-1/2 [8]. The building blocks of the experiment are summarized in Fig. 2.8 using the LiSA visualization. Recall that triple-quantum coherences consist of combinations of tensor operators of rank $j = 3$ and order $m = \pm 3$. At the initial time t_0, the system is in thermal equilibrium, which corresponds in the high-temperature limit to the density matrix

$$\rho(t_0) = I_{1x} + I_{2x} + I_{3x} = \sqrt{2}(\mathrm{T}_{10}^{\{1\}} + \mathrm{T}_{10}^{\{2\}} + \mathrm{T}_{10}^{\{3\}})$$

(where for simplicity only the traceless part of the density operator is considered here).

A first 90° pulse (with phase x) is applied to the system with an amplitude of 10 kHz for a time $t_1 - t_0 = 25\mu$s and flips the three magnetization vectors into the transverse plane. The corresponding linear control Hamiltonian is

$$\mathscr{H}(t_0, t_1) = 2\pi\ 10^4\mathrm{Hz}\ (I_{1x} + I_{2x} + I_{3x})$$

and the density operator of the system at time t_1 is

$$\begin{aligned}\rho(t_1) &= -I_{1y} - I_{2y} - I_{3y} \\ &= -i(\mathrm{T}_{1,-1}^{\{1\}} + \mathrm{T}_{1,1}^{\{1\}}) - i(\mathrm{T}_{1,-1}^{\{2\}} + \mathrm{T}_{1,1}^{\{2\}}) - i(\mathrm{T}_{1,-1}^{\{3\}} + \mathrm{T}_{1,1}^{\{3\}}).\end{aligned}$$

The next step consists in letting the coupling Hamiltonian act on the system in order to create trilinear terms in the density operator. The coupling Hamiltonian, applied for a time $t_2 - t_1 = 50$ ms, is longitudinal (*c.f.* Fig. 2.6) and has the explicit form

$$\mathscr{H}(t_1, t_2) = 2\ \pi\ 10^4\mathrm{Hz}\ (I_{1z}I_{2z} + I_{1z}I_{3z} + I_{2z}I_{3z}).$$

At time t_2, the system is in the state $\rho(t_2) = 4I_{1y}I_{2z}I_{3z} + 4I_{1z}I_{2y}I_{3z} + 4I_{1z}I_{2z}I_{3y} \cong$

$$0.78(\mathrm{T}_{1,-1}(\tau_1^{[3]}) + \mathrm{T}_{1,1}(\tau_1^{[3]})) + 1.55i(\mathrm{T}_{3,-1}(\tau_1^{[3]}) + \mathrm{T}_{3,1}(\tau_1^{[3]})).$$

Finally, a second 90° pulse (with phase y) is applied in order to create density operator terms of order $m = \pm 3$. The corresponding linear control Hamiltonian

$$\mathscr{H}(t_2, t_3) = 2\ \pi\ 10^4\mathrm{Hz}\ (I_{1y} + I_{2y} + I_{3y})$$

is applied for a time $t_3 - t_2 = t_1 - t_0$. At time t_3, the density operator of the system is

$$\begin{aligned}\rho(t_3) &= 4I_{1y}I_{2x}I_{3x} + 4I_{1x}I_{2y}I_{3x} + 4I_{1x}I_{2x}I_{3y} \\ &\cong 0.78[(\mathrm{T}_{1,-1}(\tau_1^{[3]}) + \mathrm{T}_{1,1}(\tau_1^{[3]})] \\ &- 0.39i[(\mathrm{T}_{3,-1}(\tau_1^{[3]}) + \mathrm{T}_{3,1}(\tau_1^{[3]})] \\ &+ 1.5i[(\mathrm{T}_{3,-3}(\tau_1^{[3]}) + \mathrm{T}_{3,3}(\tau_1^{[3]})].\end{aligned}$$

At this point, the desired triple-quantum coherence term $\mathrm{T}_{3,-3}(\tau_1^{[3]}) + \mathrm{T}_{3,3}(\tau_1^{[3]})$ has been created. Note that the shape of the droplet corresponding to the term $\tau_1^{[3]}$ of $\rho(t_3)$ in Fig. 2.8 also clearly exhibits the (partial) content of triple-quantum coherence (*c.f.* term $(TQ_x)_{123}$ in Fig. 2.5). The remaining undesired terms of the density operator can be

removed by applying a triple quantum filter [8] to $\rho(t_3)$ (not shown for simplicity). The density operators $\rho(t_i)$ for this experiment are depicted in the middle row of Fig. 2.8.

The Hamiltonians $\mathscr{H}(t_i, t_{i+1})$ (scaled to the same norm for display) are shown in the upper row and the real effective Hamiltonian is [8]

$$\begin{aligned}\mathscr{H}_{\text{eff}} = &-18.1\text{Hz}(I_{1z} + I_{2z} + I_{3z})\\ &- 24.2\text{Hz}(I_xI_xI_x + I_yI_yI_y + I_zI_zI_z)\\ &- 72.5\text{Hz}(I_xI_xI_y + I_xI_yI_x + I_yI_xI_x)\\ &- 72.5(\text{Hz}I_yI_yI_x + I_yI_xI_y + I_xI_yI_y)\end{aligned}$$

of the experiment is shown at the top. In the lower row, DROPS representations of the propagators

$$\begin{aligned}U(t_0, t_1) = &\ 0.35\ \text{Id} - 0.71i(I_{1x} + I_{2x} + I_{3x})\\ &- 1.41(I_{1x}I_{2x} + I_{1x}I_{3x} + I_{2x}I_{3x}) + 2.83I_{1x}I_{2x}I_{3x},\\ U(t_1, t_2) = &\ 0.35(1+i)\ \text{Id} - 1.41(1+i)(I_{1z}I_{2z} + I_{1z}I_{3z} + I_{2z}I_{3z}),\end{aligned}$$

and

$$\begin{aligned}U(t_2, t_3) = &\ 0.35\ \text{Id} - 0.71i(I_{1y} + I_{2y} + I_{3y})\\ &- 1.41(I_{1y}I_{2y} + I_{1y}I_{3y} + I_{2y}I_{3y}) + 2.83I_{1y}I_{2y}I_{3y},\end{aligned}$$

associated with the individual time steps are displayed and the effective propagator

$$\begin{aligned}U_{\text{eff}} = &\ 0.18(1+i)\ \text{Id} - 0.35(1+i)(I_{1z} + I_{2z} + I_{3z})\\ &- 0.71(1+i)(I_{1z}I_{2z} + I_{1z}I_{3z} + I_{2z}I_{3z})\\ &- 1.41(1-i)(I_xI_xI_x + I_yI_yI_y - I_zI_zI_z)\\ &- 1.41(1-i)(I_xI_xI_y + I_xI_yI_x + I_yI_xI_x)\\ &- 1.41(1-i)(I_yI_yI_x + I_yI_xI_y + I_xI_yI_y)\end{aligned}$$

is shown at the bottom of Fig. 2.8.

Concatenated INEPT experiment

The concatenated INEPT experiment is designed to transfer the magnetization between two indirectly coupled spins, say spins one and three, via their coupling with the intermediary spin two. Considering a homonuclear system, we consider the internal Hamiltonian driving the system to be

$$\mathscr{H}_0 = \mathscr{H}_J = 2\pi J(I_{1z}I_{2z} + I_{2z}I_{3z}).$$

The pulse sequence achieving the desired transfer is illustrated in Fig. 2.11. Note that since the spins are identical, the pulses applied are not selective and affect all spins. However, to lighten the picture, only the components which have an effect on the system are identified.

At initial time, the state of the system is $\rho(t_0) = I_{1z}$ and a first 90°_y pulse is applied to create transverse magnetization: $\rho(t_1) = I_{1x}$. The system then evolves freely for a time duration $\tau = \frac{1}{2J}$ such that at time $t_2 = t_1 + \tau$, all the magnetization has been converted into anti-phase magnetization [68] $\rho(t_2) = 2I_{1y}I_{2z}$. A 90°_x pulse is then applied

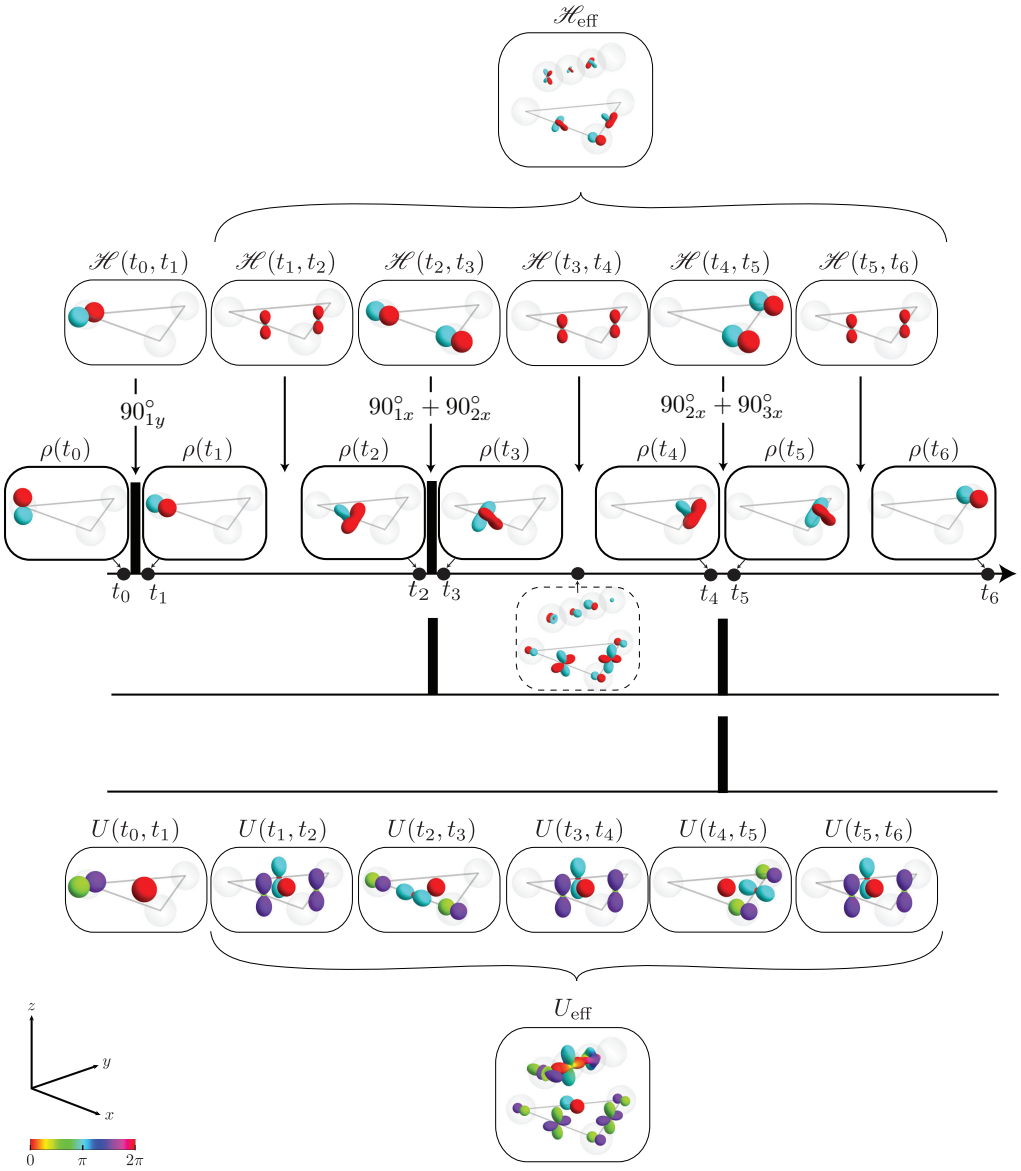

Figure 2.11: Concatenated INEPT experiment, designed to transfer the magnetization between indirectly coupled spins. Here spins one and three are coupled to (the intermediate) spin two, with the same coupling constant J. The coupling Hamiltonian corresponds to $\mathscr{H}(t_k, t_{k+1})$ for $k = 1, 3, 5$. The DROPS visualizations of the states $\rho(t_k)$ at critical times t_i are depicted directly above the pulse sequence. The constant Hamiltonian for each period (t_k, t_{k+1}) are illustrated above the density matrices and the effective Hamiltonian is depicted at the top of the picture. The propagators for each period (t_k, t_{k+1}) are illustrated below the pulse sequence and the effective propagator lies at the bottom of the picture.

and transform the anti-phase magnetization into $\rho(t_3) = -2I_{1z}I_{2y}$. Then the system freely evolves for a time τ such that the anti-phase magnetization between spins one and two evolves into anti-phase magnetization between spins two and three: $\rho(t_4) = 2I_{2y}I_{3z}$. A last 90°_x pulse is applied, followed by a delay, such that the state of the system becomes $\rho(t_5) = -2I_{2z}I_{3y}$ and finally $\rho(t_6) = I_{3x}$.

2.10.9 Further symmetrizations

By construction, each k-linear tensor operator in the LiSA basis involves a subset of exactly k particles $\{s_1, \ldots, s_k\}$ and is thus symmetrized with respect to the permutation subgroup $S_k \subseteq S_n$. For systems with indistinguishable particles, it is advantageous to further symmetrize the tensor operators with respect to the identical particles, using the projector machinery presented in Appendix 2.10.4. Indeed, the resulting tensor operators which are not fully symmetric with respect to the indistinguishable particles can then be left aside. This new symmetrization then results in decreasing the number of droplets necessary to represent operators in systems with indistinguishable particles.

Consider for example the LiSA basis for a system consisting of $n = 3$ spin-1/2 particles and assume that we have an I_2S system, *i.e.* the first two particles are indistinguishable. The symmetrization of the LiSA basis with respect to particles $\{1, 2\}$ creates the following 40 operators (grouped into 12 tensor operators) fully symmetric in $\{1, 2\}$: $\frac{1}{2}(\mathrm{T}_1^{\{1\}} + \mathrm{T}_1^{\{2\}})$, $\mathrm{T}_1^{\{3\}}$, $\mathrm{T}_j^{\{1,2\}}$ $(j = 0, 2)$, $\frac{1}{2}(\mathrm{T}_j^{\{1,3\}} + \mathrm{T}_j^{\{2,3\}})$ $(j = 0, 1, 2)$, $\mathrm{T}_j(\tau_1^{[3]})$ $(j = 1, 3)$, $\mathrm{T}_j(\tau_2^{[3]})$ $(j = 1, 2)$ and the identity $\mathrm{T}_0^{\emptyset}(\tau_1^{[0]})$. In particular, operators fully symmetric with respect to particles $\{1, 2\}$ can be represented with seven droplets.

Suppose now that all three particles are indistinguishable. The symmetrization of the LiSA basis with respect to particles $\{1, 2, 3\}$ creates the following 20 operators (grouped into 6 tensor operators) fully symmetric in the three particles: $\frac{1}{3}(\mathrm{T}_1^{\{1\}} + \mathrm{T}_1^{\{2\}} + \mathrm{T}_1^{\{3\}})$, $\frac{1}{3}(\mathrm{T}_j^{\{1,2\}} + \mathrm{T}_j^{\{1,3\}} + \mathrm{T}_j^{\{2,3\}})$ $(j = 0, 2)$, $\mathrm{T}_j(\tau_1^{[3]})$ $(j = 1, 3)$ and the identity $\mathrm{T}_0^{\emptyset}(\tau_1^{[0]})$. That is, operators fully symmetric with respect to particles $\{1, 2, 3\}$ can be represented with four droplets only.

2.10.10 Two alternative tensor bases

We present two alternative tensor bases and suggest a DROPS mapping for each of them. To clarify the discussion, the construction of each basis is illustrated for a system consisting of three spin-1/2 particles.

Tensor product basis

The tensor product operators naturally appear when constructing a tensor basis by successively adding particles to the system. To simplify the discussion, we consider that all the spins are identical. Proceeding recursively, the particles are included one at a time taking all the products $\mathrm{T}_j^{(\ell)}[k-1] \otimes \mathrm{T}_{j'}^{(j')}[1]$, where $\mathrm{T}_j^{(\ell)}[k]$ are the operators in the tensor product basis for the subsystem consisting of the first k particles. In particular, $\mathrm{T}_{j'}^{(j')}[1]$ denotes the tensors in the basis for one particle.

Referring to the Clebsch-Gordan decomposition [20–22], each product $\mathrm{T}_j^{(\ell)}[k-1] \otimes \mathrm{T}_{j'}^{(j')}[1]$ can be decomposed as a direct sum of irreducible tensors with ranks running from $|j - j'|$ to $j + j'$ [8, 22, 41], namely

$$\mathrm{T}_j^{(\ell)}[k-1] \otimes \mathrm{T}_{j'}^{(j')}[1] = \mathrm{T}_{|j-j'|}^{(\ell'')} \oplus \ldots \oplus \mathrm{T}_{j+j'}^{(\ell'')}, \tag{2.15}$$

where the explicit tensor components $\mathrm{T}_{j'm}^{(j'')}$ are calculated using Wigner coefficients [37, 41]. The labels (ℓ'') are also recursively defined by $(\ell'') := (\ell, j', \kappa)$ where the

additional parameter κ further distinguishes tensors associated with identical rank j and couple (ℓ, j'). The tensors $\mathrm{T}_{j'}^{(\ell'')}$ so constructed form all together a k-linear tensor basis (2.4) for the new system.

Example: Three-spin-1/2 system

The tensor basis for one spin-1/2 particle is $\mathrm{B}_1 = \{\mathrm{T}_0^{(0)}, \mathrm{T}_1^{(1)}\}$, where $\mathrm{T}_0^{(0)}$ is proportional to the 2×2 identity matrix. Adding one particle leads to four combinations:

$$\begin{aligned}
&\mathrm{T}_0^{(0)} \otimes \mathrm{T}_0^{(0)} = \mathrm{T}_0^{(0,0)},\\
&\mathrm{T}_0^{(0)} \otimes \mathrm{T}_1^{(1)} = \mathrm{T}_1^{(0,1)},\\
&\mathrm{T}_1^{(1)} \otimes \mathrm{T}_0^{(0)} = \mathrm{T}_1^{(1,0)},\\
&\mathrm{T}_1^{(1)} \otimes \mathrm{T}_1^{(1)} = \mathrm{T}_0^{(1,1)} \oplus \mathrm{T}_1^{(1,1)} \oplus \mathrm{T}_2^{(1,1)},
\end{aligned}$$

and the tensor product basis for systems consisting of two spin-1/2 particles is $\mathrm{B}_2 = \{\mathrm{T}_0^{(0,0)}, \mathrm{T}_1^{(0,1)}, \mathrm{T}_1^{(1,0)}, \mathrm{T}_0^{(1,1)}, \mathrm{T}_1^{(1,1)}, \mathrm{T}_2^{(1,1)}\}$. Adding one more particle then leads to 12 such tensor products, schematically represented by $\mathrm{B}_3 = \mathrm{B}_2 \otimes \mathrm{B}_1$, and results in the following tensors:

$$\begin{aligned}
&\mathrm{T}_0^{(0,0)} \otimes \mathrm{T}_0^{(0)} = \mathrm{T}_0^{(0,0,0)},\\
&\mathrm{T}_1^{(0,1)} \otimes \mathrm{T}_0^{(0)} = \mathrm{T}_1^{(0,1,0)},\\
&\mathrm{T}_1^{(1,0)} \otimes \mathrm{T}_0^{(0)} = \mathrm{T}_1^{(1,0,0)},\\
&\mathrm{T}_0^{(1,1)} \otimes \mathrm{T}_0^{(0)} = \mathrm{T}_0^{(1,1,0)},\\
&\mathrm{T}_1^{(1,1)} \otimes \mathrm{T}_0^{(0)} = \mathrm{T}_1^{(1,1,0)},\\
&\mathrm{T}_2^{(1,1)} \otimes \mathrm{T}_0^{(0)} = \mathrm{T}_2^{(1,1,0)},\\
&\mathrm{T}_0^{(0,0)} \otimes \mathrm{T}_1^{(1)} = \mathrm{T}_1^{(0,0,1)},\\
&\mathrm{T}_1^{(0,1)} \otimes \mathrm{T}_1^{(1)} = \mathrm{T}_0^{(0,1,0)} \oplus \mathrm{T}_1^{(0,1,0)} \oplus \mathrm{T}_2^{(0,1,0)},\\
&\mathrm{T}_1^{(1,0)} \otimes \mathrm{T}_1^{(1)} = \mathrm{T}_0^{(1,0,0)} \oplus \mathrm{T}_1^{(1,0,0)} \oplus \mathrm{T}_2^{(1,0,0)},\\
&\mathrm{T}_0^{(1,1)} \otimes \mathrm{T}_1^{(1)} = \mathrm{T}_1^{(1,1,1,\kappa_1)},\\
&\mathrm{T}_1^{(1,1)} \otimes \mathrm{T}_1^{(1)} = \mathrm{T}_0^{(1,1,1,\kappa_2)} \oplus \mathrm{T}_1^{(1,1,1,\kappa_2)} \oplus \mathrm{T}_2^{(1,1,1,\kappa_2)},\\
&\mathrm{T}_2^{(1,1)} \otimes \mathrm{T}_1^{(1)} = \mathrm{T}_1^{(1,1,1,\kappa_3)}, \oplus \mathrm{T}_2^{(1,1,1,\kappa_3)} \oplus \mathrm{T}_3^{(1,1,1,\kappa_3)}.
\end{aligned}$$

Note that since the single particle operator $\mathrm{T}_0^{(0)}$ is proportional to the identity matrix, the labels of the tensors (except for the κ_i) give the linearity of the tensor as well as the subsystems the operator is acting on. For instance, the tensors $\mathrm{T}_j^{(1,0,1)}$ are bilinear and involve particles one and three only. These "subsystem" and "linearity" features are always present, regardless of the system under concern. We insisted to list all the tensors to underline the requirement of three additional parameters κ_1, κ_2 and κ_3 in the labeling of three-linear tensors $\mathrm{T}_j^{(1,1,1,\kappa_i)}$. Tensors obtained from the same product, *i.e.* having the same parents, are associated with the same κ_i value. In order to define

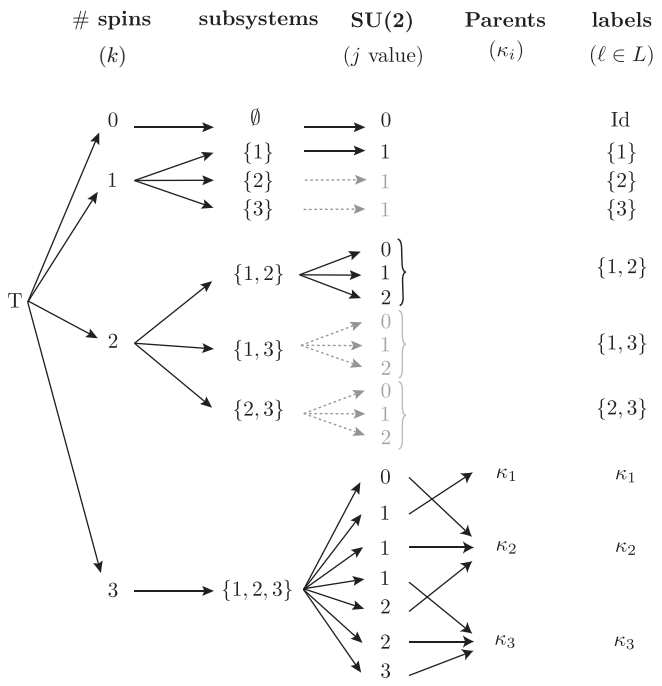

Figure 2.12: Properties and labels of the tensors in the tensor product basis for a system consisting of three spin-1/2 particles. Each tensor is k-linear (**# spins**) and involves a specific subsystem of the global system (**subsystems**). An additional parameter κ_i referring to the parents (**Parents**) is required to distinguish trilinear operators. The final tensors are grouped (**labels**) into droplets according to the subsystem they involve and for the trilinear tensors also according to their parents.

a DROPS visualization based on the tensor product basis, each tensor must finally be assigned to a label ℓ in a label set $L = \{\ell\}$ to group them into droplets according to Eq. (2.3). Using the "subsystem" and "linearity" properties of the basis, the labels used to recursively construct the basis may also be replaced by the spins involved in the operator. A possible labeling is illustrated in Fig. 2.12, where for instance the recursively defined label $(1, 0, 1)$ is identified with the DROPS label $\ell = \{1, 3\}$. Trilinear operators are labeled according to their parents only. An example of DROPS visualization for a random 8×8 matrix using the tensor product basis is shown in Fig. 2.13. The non-physical nature of the parents parameters κ_i is the principal motivation in defining the LiSA tensor basis, which assigns physically meaningful labels to the trilinear operators.

Multipole tensor basis

The multipole tensor basis [21] is defined from the atomic coherent states $\{|j, m, \kappa\rangle\}$ of the system, where κ distinguishes states having identical total angular momentum j and z angular momentum component m. Given j and κ fixed, $|j, \kappa\rangle := \{|j, m, \kappa\rangle\}_{-j \leq m \leq j}$ denotes the ordered *coherent state set* having angular momentum j and labeled by κ. We can write the state basis of any spin system as a union $B = \bigcup_{j,\kappa} |j, \kappa\rangle$ of coherent state sets. In such a basis, components of the multipole tensors, denoted $T_{j,m}(|j_1, \kappa_1\rangle \to |j_2, \kappa_2\rangle)$, transform the elements of the set $|j_1, \kappa_1\rangle$ into elements of the

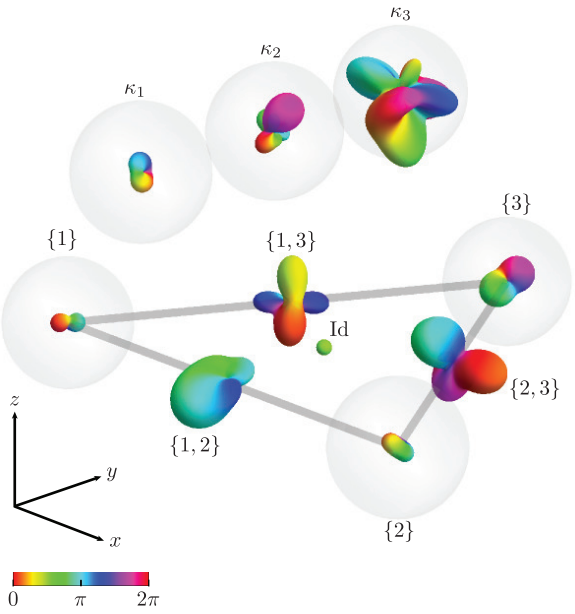

Figure 2.13: DROPS visualization of a random 8×8 matrix A corresponding to an operator for a quantum system consisting of $n = 3$ qubits (spin-1/2). The DROPS visualization is defined by the tensor product basis and its DROPS mapping presented in Fig. 2.12. Each droplet is a linear combination of spherical harmonics corresponding to a specific $f_A^{(\ell)}$ in Eq. (2.3). The labels ℓ of the droplets are defined in Fig. 2.12.

set $|j_2, \kappa_2\rangle$ according to the Clebsch decomposition:

$$T_{j,m}(|j_1, \kappa_1\rangle \to |j_2, \kappa_2\rangle) := \sqrt{\tfrac{2j+1}{2j_2+1}} \sum_{m_1} \langle j_2, m_2 | j, m | j_1, m_1 \rangle \, |j_2, m_2, \kappa_2\rangle \, \langle j_1, m_1, \kappa_1| \tag{2.16}$$

where $\langle j_2, m_2 | j, m | j_1, m_1 \rangle$ is a conventional representation for Clebsch-Gordan coefficients [8,22,41]. Note that the multipole tensor operators transforming $|j_1, \kappa_1\rangle \to |j_2, \kappa_2\rangle$ have ranks $|j_1 - j_2| < j < j_1 + j_2$ and since the angular momentum values j_1, j_2 are either all integers or all half-integers, the tensor ranks j are integers as expected.

A natural DROPS representation for the multipole operators groups into a single droplet all the tensor operators corresponding to the same "coherent state set" transition $|j_1, \kappa_1\rangle \to |j_2, \kappa_2\rangle$. If we refer to the formal mapping given by Eqs. (2.2) and (2.3) defining a DROPS representation, the labels $\ell \in L$ for this representation consist of all the possible transitions $|j_1, \kappa_1\rangle \to |j_2, \kappa_2\rangle$.

Example for a $n = 3$ spin-1/2 system. We first have to construct the coherent states for the system, which is done recursively by adding one particle at a time. For a system consisting of $n = 1$ spin-1/2 particle, the coherent state basis is simply

$$B_1 = |1/2\rangle = \{|1/2, 1/2\rangle, |1/2, -1/2\rangle\}.$$

For $n = 2$, the state basis is $B_2 = |1\rangle \cup |0\rangle$ obtained from the Clebsch decomposition $B_1 \otimes B_1$:

$$|1/2\rangle \otimes |1/2\rangle = |0\rangle \oplus |1\rangle,$$

corresponding to the singlet and triplet states respectively. Note that no additional label κ is needed since the ranks of the two coherent state sets are distinct. Finally, for the $n = 3$ spins system, the basis consists of the three coherent state sets $B_3 = |3/2, \kappa_1\rangle \cup |1/2, \kappa_1\rangle \cup |1/2, \kappa_2\rangle$ obtained from the Clebsch decomposition $B_2 \otimes B_1$:

$$|1\rangle \otimes |1/2\rangle = |1/2, \kappa_1\rangle \oplus |3/2, \kappa_1\rangle\,, \tag{2.17}$$

$$|0\rangle \otimes |1/2\rangle = |1/2, \kappa_2\rangle\,, \tag{2.18}$$

where $\kappa_1 = 1$ and $\kappa_2 = 0$ identify the parents from which a tensor is obtained.

The next step is to construct the tensors associated with each of the nine transitions $|j_1, \kappa_1\rangle \to |j_2, \kappa_2\rangle$ using Eq. (2.16). For each possible transition, we list here the ranks of the tensors obtained by this construction:

Transitions	**Ranks** j
$\|3/2, \kappa_1\rangle \to \|3/2, \kappa_1\rangle$	$0, 1, 2, 3$
$\|1/2, \kappa_1\rangle \to \|1/2, \kappa_1\rangle$	$0, 1, 2$
$\|1/2, \kappa_2\rangle \to \|1/2, \kappa_2\rangle$	$0, 1, 2$
$\|3/2, \kappa_1\rangle \to \|1/2, \kappa_1\rangle$	$1, 2$
$\|1/2, \kappa_1\rangle \to \|3/2, \kappa_1\rangle$	$1, 2$
$\|3/2, \kappa_1\rangle \to \|1/2, \kappa_2\rangle$	$1, 2$
$\|1/2, \kappa_2\rangle \to \|3/2, \kappa_1\rangle$	$1, 2$
$\|1/2, \kappa_1\rangle \to \|1/2, \kappa_2\rangle$	$0, 1$
$\|1/2, \kappa_2\rangle \to \|1/2, \kappa_1\rangle$	$0, 1$

Figure 2.14 illustrates the grouping of these tensors into droplets, which defines a possible DROPS representation of operators acting on three spin-1/2 particles. An example of DROPS representation for a random operator A is illustrated in Fig. 2.15.

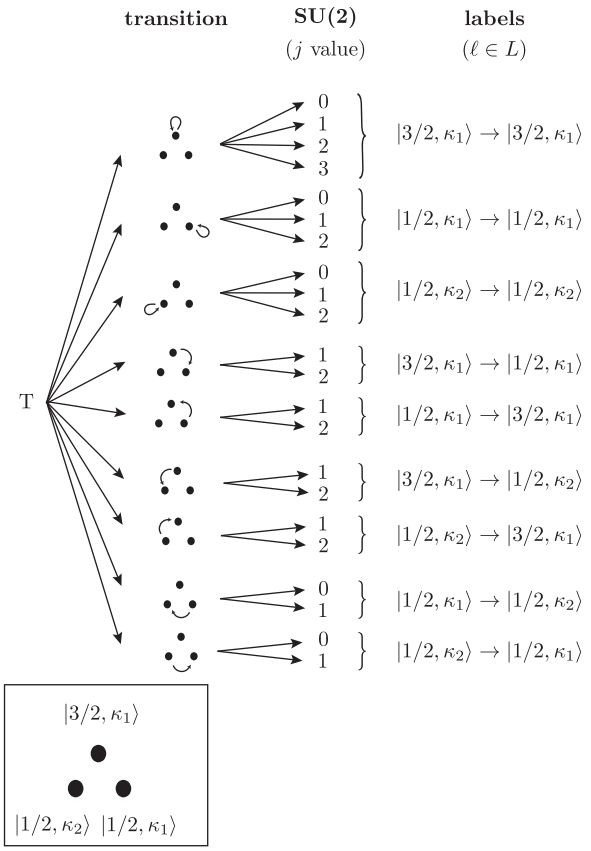

Figure 2.14: Properties and labels of the multipole tensors in the basis for a system consisting of three spin-1/2 particles. Each tensor is associated with a defined transition $|j_1, \kappa_1\rangle \to |j_2, \kappa_2\rangle$ which is graphically illustrated here (**transition**). The tensors are grouped (**labels**) into droplets according to these transitions.

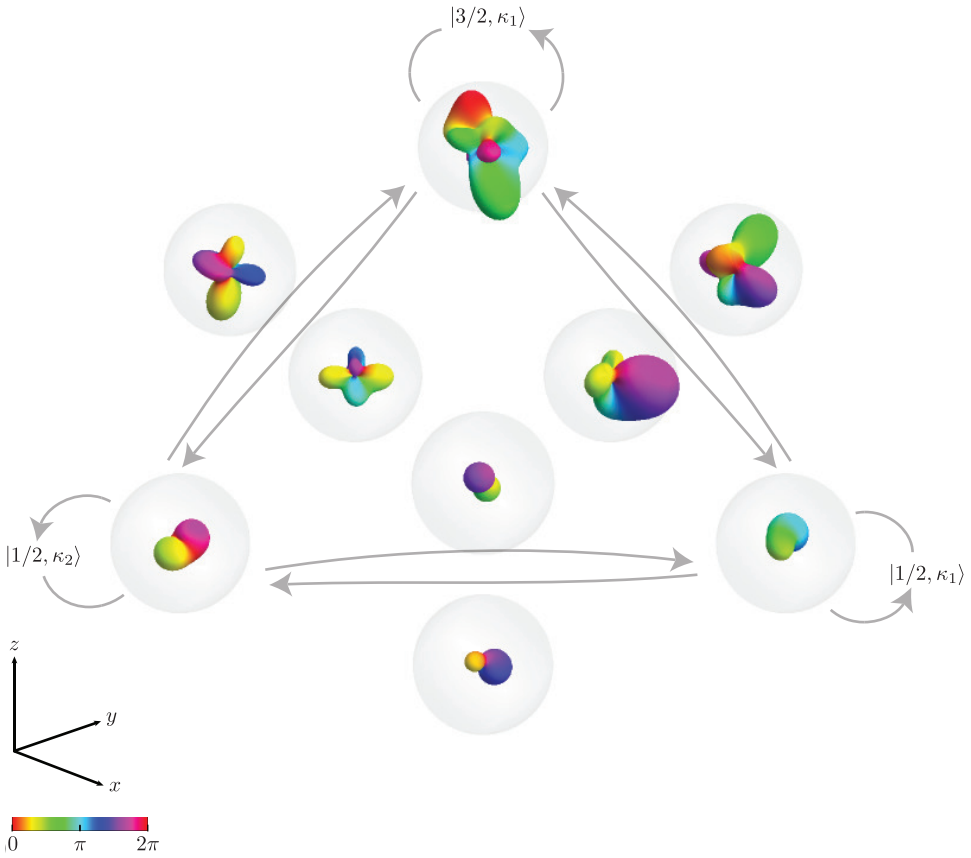

Figure 2.15: DROPS visualization of a random 8×8 matrix A corresponding to an operator for a quantum system consisting of $n = 3$ qubits (spin-1/2). The DROPS visualization is defined by the multipole tensors basis and its DROPS mapping presented in Section 2.10.10. Each droplet is a linear combination of spherical harmonics corresponding to a specific $f_A^{(\ell)}$ in Eq. (2.3). The labels ℓ of the droplets are defined in Fig. 2.14.

2.10.11 From the LiSA basis to the Cartesian product operator bases

The explicit transformations between the LiSA tensor operator basis and the Cartesian product operator basis are given in Fig. 2.16 to Fig. 2.19. Figure 2.16 shows the transformations between the linear operators and Fig. 2.17 the transformations between the bilinear operators. The decomposition of the trilinear tensor operator components in terms of the Cartesian product operators is given in Fig. 2.18 and reciprocally, the decomposition of the trilinear Cartesian product basis operators in terms of the LiSA tensor operator components is given in Fig. 2.19. In order to lighten the expressions, the shorthand notation for Cartesian operators $I_{abc} := I_a I_b I_c$ is used in the decomposition of trilinear operators.

$$\begin{pmatrix} \mathrm{T}^{\{k\}}_{1,-1} \\ \mathrm{T}^{\{k\}}_{1,0} \\ \mathrm{T}^{\{k\}}_{1,1} \end{pmatrix} = \begin{pmatrix} \frac{1}{2} & -\frac{i}{2} & 0 \\ 0 & 0 & \frac{1}{\sqrt{2}} \\ -\frac{1}{2} & -\frac{i}{2} & 0 \end{pmatrix} \begin{pmatrix} I_{kx} \\ I_{ky} \\ I_{kz} \end{pmatrix}$$

$$\begin{pmatrix} I_{kx} \\ I_{ky} \\ I_{kz} \end{pmatrix} = \begin{pmatrix} 1 & 0 & -1 \\ i & 0 & i \\ 0 & \sqrt{2} & 0 \end{pmatrix} \begin{pmatrix} \mathrm{T}^{\{k\}}_{1,-1} \\ \mathrm{T}^{\{k\}}_{1,0} \\ \mathrm{T}^{\{k\}}_{1,1} \end{pmatrix}$$

Figure 2.16: Transformation between the LiSA linear tensor operator components and the linear Cartesian product basis operators.

$$\begin{pmatrix} \mathrm{T}^{\{k,\ell\}}_{0,0} \\ \mathrm{T}^{\{k,\ell\}}_{1,-1} \\ \mathrm{T}^{\{k,\ell\}}_{1,0} \\ \mathrm{T}^{\{k,\ell\}}_{1,1} \\ \mathrm{T}^{\{k,\ell\}}_{2,-2} \\ \mathrm{T}^{\{k,\ell\}}_{2,-1} \\ \mathrm{T}^{\{k,\ell\}}_{2,0} \\ \mathrm{T}^{\{k,\ell\}}_{2,1} \\ \mathrm{T}^{\{k,\ell\}}_{2,2} \end{pmatrix} = \begin{pmatrix} \frac{1}{\sqrt{6}} & 0 & 0 & 0 & \frac{1}{\sqrt{6}} & 0 & 0 & 0 & \frac{1}{\sqrt{6}} \\ 0 & 0 & \frac{i}{2\sqrt{2}} & 0 & 0 & \frac{1}{2\sqrt{2}} & -\frac{i}{2\sqrt{2}} & -\frac{1}{2\sqrt{2}} & 0 \\ 0 & \frac{1}{2} & 0 & -\frac{1}{2} & 0 & 0 & 0 & 0 & 0 \\ 0 & 0 & \frac{i}{2\sqrt{2}} & 0 & 0 & -\frac{1}{2\sqrt{2}} & -\frac{i}{2\sqrt{2}} & \frac{1}{2\sqrt{2}} & 0 \\ \frac{1}{2\sqrt{2}} & -\frac{i}{2\sqrt{2}} & 0 & -\frac{i}{2\sqrt{2}} & -\frac{1}{2\sqrt{2}} & 0 & 0 & 0 & 0 \\ 0 & 0 & \frac{1}{2\sqrt{2}} & 0 & 0 & -\frac{i}{2\sqrt{2}} & \frac{1}{2\sqrt{2}} & -\frac{i}{2\sqrt{2}} & 0 \\ -\frac{1}{2\sqrt{3}} & 0 & 0 & 0 & -\frac{1}{2\sqrt{3}} & 0 & 0 & 0 & \frac{1}{\sqrt{3}} \\ 0 & 0 & -\frac{1}{2\sqrt{2}} & 0 & 0 & -\frac{i}{2\sqrt{2}} & -\frac{1}{2\sqrt{2}} & -\frac{i}{2\sqrt{2}} & 0 \\ \frac{1}{2\sqrt{2}} & \frac{i}{2\sqrt{2}} & 0 & \frac{i}{2\sqrt{2}} & -\frac{1}{2\sqrt{2}} & 0 & 0 & 0 & 0 \end{pmatrix} \begin{pmatrix} 2I_{kx}I_{lx} \\ 2I_{kx}I_{ly} \\ 2I_{kx}I_{lz} \\ 2I_{ky}I_{lx} \\ 2I_{ky}I_{ly} \\ 2I_{ky}I_{lz} \\ 2I_{kz}I_{lx} \\ 2I_{kz}I_{ly} \\ 2I_{kz}I_{lz} \end{pmatrix}$$

$$\begin{pmatrix} 2I_{kx}I_{lx} \\ 2I_{kx}I_{ly} \\ 2I_{kx}I_{lz} \\ 2I_{ky}I_{lx} \\ 2I_{ky}I_{ly} \\ 2I_{ky}I_{lz} \\ 2I_{kz}I_{lx} \\ 2I_{kz}I_{ly} \\ 2I_{kz}I_{lz} \end{pmatrix} = \begin{pmatrix} \sqrt{\frac{2}{3}} & 0 & 0 & 0 & \frac{1}{\sqrt{2}} & 0 & -\frac{1}{\sqrt{3}} & 0 & \frac{1}{\sqrt{2}} \\ 0 & 0 & 1 & 0 & \frac{i}{\sqrt{2}} & 0 & 0 & 0 & -\frac{i}{\sqrt{2}} \\ 0 & -\frac{i}{\sqrt{2}} & 0 & -\frac{i}{\sqrt{2}} & 0 & \frac{1}{\sqrt{2}} & 0 & -\frac{1}{\sqrt{2}} & 0 \\ 0 & 0 & -1 & 0 & \frac{i}{\sqrt{2}} & 0 & 0 & 0 & -\frac{i}{\sqrt{2}} \\ \sqrt{\frac{2}{3}} & 0 & 0 & 0 & -\frac{1}{\sqrt{2}} & 0 & -\frac{1}{\sqrt{3}} & 0 & -\frac{1}{\sqrt{2}} \\ 0 & \frac{1}{\sqrt{2}} & 0 & -\frac{1}{\sqrt{2}} & 0 & \frac{i}{\sqrt{2}} & 0 & \frac{i}{\sqrt{2}} & 0 \\ 0 & \frac{i}{\sqrt{2}} & 0 & \frac{i}{\sqrt{2}} & 0 & \frac{1}{\sqrt{2}} & 0 & -\frac{1}{\sqrt{2}} & 0 \\ 0 & -\frac{1}{\sqrt{2}} & 0 & \frac{1}{\sqrt{2}} & 0 & \frac{i}{\sqrt{2}} & 0 & \frac{i}{\sqrt{2}} & 0 \\ \sqrt{\frac{2}{3}} & 0 & 0 & 0 & 0 & 0 & \frac{2}{\sqrt{3}} & 0 & 0 \end{pmatrix} \begin{pmatrix} \mathrm{T}^{\{k,l\}}_{0,0} \\ \mathrm{T}^{\{k,l\}}_{1,-1} \\ \mathrm{T}^{\{k,l\}}_{1,0} \\ \mathrm{T}^{\{k,l\}}_{1,1} \\ \mathrm{T}^{\{k,l\}}_{2,-2} \\ \mathrm{T}^{\{k,l\}}_{2,-1} \\ \mathrm{T}^{\{k,l\}}_{2,0} \\ \mathrm{T}^{\{k,l\}}_{2,1} \\ \mathrm{T}^{\{k,l\}}_{2,2} \end{pmatrix}$$

Figure 2.17: Transformation between the LiSA bilinear tensor operator components and the linear Cartesian product basis operators.

$$
\begin{aligned}
\mathrm{T}_{0,0}(\tau_4) = &\ \tfrac{2}{\sqrt{3}}\left[(I_{xyz} - I_{xzy} - I_{yxz} + I_{yzx} + I_{zxy} - I_{zyx})\right] \\
\mathrm{T}_{1,-1}(\tau_1) = &\ \tfrac{2}{\sqrt{15}}\left[3I_{xxx} - 3iI_{yyy} - i(I_{xxy} + I_{xyx} + I_{yxx}) + (I_{xyy} + I_{yxy} + I_{yyx}) + (I_{xzz} + I_{zxz} + I_{zzx})\right. \\
&\left. -i(I_{yzz} + I_{zyz} + I_{zzy})\right] \\
\mathrm{T}_{1,0}(\tau_1) = &\ \sqrt{\tfrac{8}{15}}\left[(I_{xxz} + I_{xzx} + I_{zxx}) + (I_{yyz} + I_{yzy} + I_{zyy}) + 3I_{zzz}\right] \\
\mathrm{T}_{1,1}(\tau_1) = &\ -\tfrac{2}{\sqrt{15}}\left[i(I_{xxy} + I_{xyx} + I_{yxx}) + (I_{xyy} + I_{yxy} + I_{yyx}) + (I_{xzz} + I_{zxz} + I_{zzx})\right. \\
&\left. +i(I_{yzz} + I_{zyz} + I_{zzy}) + 3I_{xxx} + 3iI_{yyy}\right] \\
\mathrm{T}_{1,-1}(\tau_2) = &\ \tfrac{1}{\sqrt{3}}\left[-i(I_{yxx} + I_{xyx} - 2I_{xxy}) - i(I_{yzz} + I_{zyz} - 2I_{zzy}) + (I_{xyy} + I_{yxy} - 2I_{yyx})\right. \\
&\left. +(I_{xzz} + I_{zxz} - 2I_{zzx})\right] \\
\mathrm{T}_{1,0}(\tau_2) = &\ \sqrt{\tfrac{2}{3}}\left[-2(I_{xxz} + I_{yyz}) + (I_{zxx} + I_{xzx}) + (I_{zyy} + I_{yzy})\right] \\
\mathrm{T}_{1,1}(\tau_2) = &\ \tfrac{1}{\sqrt{3}}\left[(-I_{xyy} - I_{yxy} + 2I_{yyx}) + (-I_{xzz} - I_{zxz} + 2I_{zzx}) + i(-I_{yxx} - I_{xyx} + 2I_{xxy})\right. \\
&\left. +i(-I_{yzz} - I_{zyz} + 2I_{zzy})\right] \\
\mathrm{T}_{1,-1}(\tau_3) = &\ \left[(I_{xyy} - I_{yxy}) + (I_{xzz} - I_{zxz}) - i(I_{yxx} - I_{xyx}) - i(I_{yzz} - I_{zyz})\right] \\
\mathrm{T}_{1,0}(\tau_3) = &\ \sqrt{2}\left[(I_{zxx} - I_{xzx}) + (I_{zyy} - I_{yzy})\right] \\
\mathrm{T}_{1,1}(\tau_3) = &\ -\left[(I_{xyy} - I_{yxy}) + (I_{xzz} - I_{zxz}) + i(I_{yxx} - I_{xyx}) + i(I_{yzz} - I_{zyz})\right] \\
\mathrm{T}_{2,-2}(\tau_2) = &\ \tfrac{1}{\sqrt{3}}\left[(I_{yzx} + I_{zyx}) + (I_{xzy} + I_{zxy}) - 2(I_{xyz} + I_{yxz}) - (2iI_{xxz} - iI_{xzx} - iI_{zxx})\right. \\
&\left. +(2iI_{yyz} - iI_{yzy} - iI_{zyy})\right] \\
\mathrm{T}_{2,-1}(\tau_2) = &\ \tfrac{1}{\sqrt{3}}\left[-(2I_{xxy} - I_{xyx} - I_{yxx}) - i(2I_{yyx} - I_{yxy} - I_{xyy}) + (2iI_{zzx} - iI_{zxz} - iI_{xzz})\right. \\
&\left. +(2I_{zzy} - I_{zyz} - I_{yzz})\right] \\
\mathrm{T}_{2,0}(\tau_2) = &\ \sqrt{2}\left[(I_{yzx} + I_{zyx}) - (I_{xzy} + I_{zxy})\right] \\
\mathrm{T}_{2,1}(\tau_2) = &\ \tfrac{1}{\sqrt{3}}\left[(2I_{xxy} - I_{xyx} - I_{yxx}) - (2I_{zzy} - I_{zyz} - I_{yzz}) + i(2I_{zzx} - I_{zxz} - I_{xzz})\right. \\
&\left. -i(2I_{yyx} - I_{yxy} - I_{xyy})\right] \\
\mathrm{T}_{2,2}(\tau_2) = &\ \tfrac{1}{\sqrt{3}}\left[-(2I_{xyz} - I_{xzy} - I_{zxy}) - (2I_{yxz} - I_{yzx} - I_{zyx}) + i(2I_{xxz} - I_{xzx} - I_{zxx})\right. \\
&\left. -i(2I_{yyz} - I_{yzy} - I_{zyy})\right] \\
\mathrm{T}_{2,-2}(\tau_3) = &\ \left[(I_{zxy} - I_{xzy}) + (I_{zyx} - I_{yzx}) + i(I_{zxx} - I_{xzx}) + i(I_{yzy} - I_{zyy})\right] \\
\mathrm{T}_{2,-1}(\tau_3) = &\ \left[(I_{yxx} - I_{xyx}) + i(I_{xyy} - I_{yxy}) + i(I_{zxz} - I_{xzz}) + (I_{zyz} - I_{yzz})\right] \\
\mathrm{T}_{2,0}(\tau_3) = &\ \sqrt{\tfrac{2}{3}}\left[-(2I_{xyz} + I_{xzy} - I_{zxy}) + (2I_{yxz} + I_{yzx} - I_{zyx})\right] \\
\mathrm{T}_{2,1}(\tau_3) = &\ \left[(I_{xyx} - I_{yxx}) + (I_{yzz} - I_{zyz}) + i(I_{xyy} - I_{yxy}) + i(I_{zxz} - I_{xzz})\right] \\
\mathrm{T}_{2,2}(\tau_3) = &\ \left[(I_{zxy} - I_{xzy}) + (I_{zyx} - I_{yzx}) + i(I_{xzx} - I_{zxx}) + i(I_{zyy} - I_{yzy})\right] \\
\mathrm{T}_{3,-3}(\tau_1) = &\ \left[(I_{xxx} - iI_{yyy}) - i(I_{xxy} + I_{xyx} + I_{yxx}) - (I_{xyy} + I_{yxy} + I_{yyx})\right] \\
\mathrm{T}_{3,-2}(\tau_1) = &\ \sqrt{\tfrac{2}{3}}\left[(I_{xxz} + I_{xzx} + I_{zxx}) - (I_{yyz} + I_{yzy} + I_{zyy})\right. \\
&\left. -i(I_{xyz} + I_{xzy} + I_{yxz} + I_{yzx} + I_{zxy} + I_{zyx})\right] \\
\mathrm{T}_{3,-1}(\tau_1) = &\ \tfrac{1}{\sqrt{15}}\left[-3(I_{xxx} - iI_{yyy}) + i(I_{xxy} + I_{xyx} + I_{yxx}) - (I_{xyy} + I_{yxy} + I_{yyx})\right. \\
&\left. +4(I_{xzz} + I_{zxz} + I_{zzx}) - 4i(I_{yzz} + I_{zyz} + I_{zzy})\right] \\
\mathrm{T}_{3,0}(\tau_1) = &\ -\tfrac{2}{\sqrt{5}}\left[(I_{xxz} + I_{xzx} + I_{zxx}) + (I_{yyz} + I_{yzy} + I_{zyy}) - 2I_{zzz}\right] \\
\mathrm{T}_{3,1}(\tau_1) = &\ \tfrac{1}{\sqrt{15}}\left[3(I_{xxx} + iI_{yyy}) + i(I_{xxy} + I_{xyx} + I_{yxx}) + (I_{xyy} + I_{yxy} + I_{yyx})\right. \\
&\left. -4(I_{xzz} + I_{zxz} + I_{zzx}) - 4i(I_{yzz} + I_{zyz} + I_{zzy})\right] \\
\mathrm{T}_{3,2}(\tau_1) = &\ \sqrt{\tfrac{2}{3}}\left[(I_{xxz} + I_{xzx} + I_{zxx}) - (I_{yyz} + I_{yzy} + I_{zyy})\right. \\
&\left. +i(I_{xyz} + I_{xzy} + I_{yxz} + I_{yzx} + I_{zxy} + I_{zyx})\right] \\
\mathrm{T}_{3,3}(\tau_1) = &\ \left[(I_{xxx} + iI_{yyy}) - i(I_{xxy} + I_{xyx} + I_{yxx}) + (I_{xyy} + I_{yxy} + I_{yyx})\right]
\end{aligned}
$$

Figure 2.18: Decomposition of the trilinear LiSA tensor operators in terms of the Cartesian product operators.

$$
\begin{aligned}
4I_{xxx} = {} & \tfrac{1}{10}\left[2\sqrt{15}\,(\mathrm{T}_{1,-1}(\tau_1)-\mathrm{T}_{1,1}(\tau_1))-\sqrt{15}\,(\mathrm{T}_{3,-1}(\tau_1)-\mathrm{T}_{3,1}(\tau_1))+5\,(\mathrm{T}_{3,-3}(\tau_1)-\mathrm{T}_{3,3}(\tau_1))\right]\\
4I_{xxy} = {} & \tfrac{1}{30}\left[2i\sqrt{15}\,(\mathrm{T}_{1,-1}(\tau_1)+\mathrm{T}_{1,1}(\tau_1))-i\sqrt{15}\,(\mathrm{T}_{3,-1}(\tau_1)+\mathrm{T}_{3,1}(\tau_1))+15i\,(\mathrm{T}_{3,-3}(\tau_1)+\mathrm{T}_{3,3}(\tau_1))\right.\\
& \left.-10i\sqrt{3}\,(\mathrm{T}_{1,-1}(\tau_2)+\mathrm{T}_{1,1}(\tau_2))-10\sqrt{3}\,(\mathrm{T}_{2,-1}(\tau_2)-\mathrm{T}_{2,1}(\tau_2))\right]\\
4I_{xxz} = {} & \sqrt{\tfrac{2}{15}}\mathrm{T}_{1,0}(\tau_1)-\tfrac{1}{\sqrt{5}}\mathrm{T}_{3,0}(\tau_1)+\tfrac{1}{\sqrt{6}}\mathrm{T}_{3,-2}(\tau_1)+\mathrm{T}_{3,2}(\tau_1)-\sqrt{\tfrac{2}{3}}\mathrm{T}_{1,0}(\tau_2)\\
& +\tfrac{i}{\sqrt{3}}\,(\mathrm{T}_{2,-2}(\tau_2)-\mathrm{T}_{2,2}(\tau_2))\\
4I_{xyx} = {} & \tfrac{1}{30}\left[2i\sqrt{15}\,[\mathrm{T}_{1,-1}(\tau_1)+\mathrm{T}_{1,1}(\tau_1)]-i\sqrt{15}\,[\mathrm{T}_{3,-1}(\tau_1)+\mathrm{T}_{3,1}(\tau_1)]+15i\,[\mathrm{T}_{3,-3}(\tau_1)+\mathrm{T}_{3,3}(\tau_1)]\right.\\
& +5i\sqrt{3}\,[\mathrm{T}_{1,-1}(\tau_2)+\mathrm{T}_{1,1}(\tau_2)]+5\sqrt{3}\,[\mathrm{T}_{2,-1}(\tau_2)-\mathrm{T}_{2,1}(\tau_2)]\\
& \left.-15i\,[\mathrm{T}_{1,-1}(\tau_3)+\mathrm{T}_{1,1}(\tau_3)]-15\,[\mathrm{T}_{2,-1}(\tau_3)-\mathrm{T}_{2,1}(\tau_3)]\right]\\
4I_{xyy} = {} & \tfrac{1}{30}\left[2\sqrt{15}\,[\mathrm{T}_{1,-1}(\tau_1)-\mathrm{T}_{1,1}(\tau_1)]-\sqrt{15}\,[\mathrm{T}_{3,-1}(\tau_1)-\mathrm{T}_{3,1}(\tau_1)]-15\,[\mathrm{T}_{3,-3}(\tau_1)-\mathrm{T}_{3,3}(\tau_1)]\right.\\
& +5\sqrt{3}\,[\mathrm{T}_{1,-1}(\tau_2)-\mathrm{T}_{1,1}(\tau_2)]-5i\sqrt{3}\,[\mathrm{T}_{2,-1}(\tau_2)+\mathrm{T}_{2,1}(\tau_2)]+15\,[\mathrm{T}_{1,-1}(\tau_3)-\mathrm{T}_{1,1}(\tau_3)]\\
& \left.-15i\,[\mathrm{T}_{2,-1}(\tau_3)+\mathrm{T}_{2,1}(\tau_3)]\right]\\
4I_{xyz} = {} & \tfrac{1}{2\sqrt{3}}\left[i\sqrt{2}\,[\mathrm{T}_{3,-2}(\tau_1)-\mathrm{T}_{3,2}(\tau_1)]-2\sqrt{2}\mathrm{T}_{2,0}(\tau_3)-2\,[\mathrm{T}_{2,-2}(\tau_2)+\mathrm{T}_{2,2}(\tau_2)]+2\mathrm{T}_{0,0}(\tau_4)\right]\\
4I_{xzx} = {} & \tfrac{1}{30}\left[2\sqrt{30}\,[\mathrm{T}_{1,0}(\tau_1)]-6\sqrt{5}\,[\mathrm{T}_{3,0}(\tau_1)]+5\sqrt{6}\,[\mathrm{T}_{3,-2}(\tau_1)+\mathrm{T}_{3,2}(\tau_1)]\right.\\
& \left.+5\sqrt{6}\mathrm{T}_{1,0}(\tau_2)-5i\sqrt{3}\,[\mathrm{T}_{2,-2}(\tau_2)-\mathrm{T}_{2,2}(\tau_2)]-15\sqrt{2}\mathrm{T}_{1,0}(\tau_3)+15i\,[\mathrm{T}_{2,-2}(\tau_3)-\mathrm{T}_{2,2}(\tau_3)]\right]\\
4I_{xzy} = {} & \tfrac{1}{6}\left[i\sqrt{6}\,[\mathrm{T}_{3,-2}(\tau_1)-\mathrm{T}_{3,2}(\tau_1)]-3\sqrt{2}\mathrm{T}_{2,0}(\tau_2)+\sqrt{3}\,[\mathrm{T}_{2,-2}(\tau_2)+\mathrm{T}_{2,2}(\tau_2)]\right.\\
& \left.-3\,[\mathrm{T}_{2,-2}(\tau_3)+\mathrm{T}_{2,2}(\tau_3)]-\sqrt{6}\mathrm{T}_{2,0}(\tau_3)-2\sqrt{3}\mathrm{T}_{0,0}(\tau_4)\right]\\
4I_{xzz} = {} & \tfrac{1}{30}\left[2\sqrt{15}\,[\mathrm{T}_{1,-1}(\tau_1)-\mathrm{T}_{1,1}(\tau_1)]+4\sqrt{15}\,[\mathrm{T}_{3,-1}(\tau_1)-\mathrm{T}_{3,1}(\tau_1)]+5\sqrt{3}\,[\mathrm{T}_{1,-1}(\tau_2)-\mathrm{T}_{1,1}(\tau_2)]\right.\\
& \left.+5i\sqrt{3}\,[\mathrm{T}_{2,-1}(\tau_2)+\mathrm{T}_{2,1}(\tau_2)]+15\,[\mathrm{T}_{1,-1}(\tau_3)-\mathrm{T}_{1,1}(\tau_3)]+15i\,[\mathrm{T}_{2,-1}(\tau_3)+\mathrm{T}_{2,1}(\tau_3)]\right]\\
4I_{yxx} = {} & \tfrac{1}{30}\left[2i\sqrt{15}\,[\mathrm{T}_{1,-1}(\tau_1)+\mathrm{T}_{1,1}(\tau_1)]-i\sqrt{15}\,[\mathrm{T}_{3,-1}(\tau_1)+\mathrm{T}_{3,1}(\tau_1)]+15i\,[\mathrm{T}_{3,-3}(\tau_1)+\mathrm{T}_{3,3}(\tau_1)]\right.\\
& +5i\sqrt{3}\,[\mathrm{T}_{1,-1}(\tau_2)+\mathrm{T}_{1,1}(\tau_2)]+5\sqrt{3}\,[\mathrm{T}_{2,-1}(\tau_2)-\mathrm{T}_{2,1}(\tau_2)]+15i\,[\mathrm{T}_{1,-1}(\tau_3)+\mathrm{T}_{1,1}(\tau_3)]\\
& \left.+15\,[\mathrm{T}_{2,-1}(\tau_3)-\mathrm{T}_{2,1}(\tau_3)]\right]\\
4I_{yxy} = {} & \tfrac{1}{30}\left[2\sqrt{15}\,[\mathrm{T}_{1,-1}(\tau_1)-\mathrm{T}_{1,1}(\tau_1)]-\sqrt{15}\,[\mathrm{T}_{3,-1}(\tau_1)-\mathrm{T}_{3,1}(\tau_1)]-15\,[\mathrm{T}_{3,-3}(\tau_1)-\mathrm{T}_{3,3}(\tau_1)]\right.\\
& +5\sqrt{3}\,[\mathrm{T}_{1,-1}(\tau_2)-\mathrm{T}_{1,1}(\tau_2)]-5i\sqrt{3}\,[\mathrm{T}_{2,-1}(\tau_2)+\mathrm{T}_{2,1}(\tau_2)]-15\,[\mathrm{T}_{1,-1}(\tau_3)-\mathrm{T}_{1,1}(\tau_3)]\\
& \left.+15i\,[\mathrm{T}_{2,-1}(\tau_3)+\mathrm{T}_{2,1}(\tau_3)]\right]\\
4I_{yxz} = {} & -\tfrac{1}{2\sqrt{3}}\left[-i\sqrt{2}\,[\mathrm{T}_{3,-2}(\tau_1)-\mathrm{T}_{3,2}(\tau_1)]+2\,[\mathrm{T}_{2,-2}(\tau_2)+\mathrm{T}_{2,2}(\tau_2)]-2\sqrt{2}\mathrm{T}_{2,0}(\tau_3)+2\mathrm{T}_{0,0}(\tau_4)\right]\\
4I_{yyx} = {} & \tfrac{1}{30}\left[2\sqrt{15}\,[\mathrm{T}_{1,-1}(\tau_1)-\mathrm{T}_{1,1}(\tau_1)]-\sqrt{15}\,[\mathrm{T}_{3,-1}(\tau_1)-\mathrm{T}_{3,1}(\tau_1)]-15\,[\mathrm{T}_{3,-3}(\tau_1)-\mathrm{T}_{3,3}(\tau_1)]\right.\\
& \left.-10\sqrt{3}\,[\mathrm{T}_{1,-1}(\tau_2)-\mathrm{T}_{1,1}(\tau_2)]+10i\sqrt{3}\,[\mathrm{T}_{2,-1}(\tau_2)+\mathrm{T}_{2,1}(\tau_2)]\right]\\
4I_{yyy} = {} & \tfrac{1}{10}i\left[2\sqrt{15}\,[\mathrm{T}_{1,-1}(\tau_1)+\mathrm{T}_{1,1}(\tau_1)]-\sqrt{15}\,[\mathrm{T}_{3,-1}(\tau_1)+\mathrm{T}_{3,1}(\tau_1)]-5\,[\mathrm{T}_{3,-3}(\tau_1)+\mathrm{T}_{3,3}(\tau_1)]\right]\\
4I_{yyz} = {} & \tfrac{1}{30}\left[2\sqrt{30}\mathrm{T}_{1,0}(\tau_1)-6\sqrt{5}\mathrm{T}_{3,0}(\tau_1)-5\sqrt{6}\,[\mathrm{T}_{3,-2}(\tau_1)+\mathrm{T}_{3,2}(\tau_1)]-10\sqrt{6}\mathrm{T}_{1,0}(\tau_2)\right.\\
& \left.-10i\sqrt{3}\,[\mathrm{T}_{2,-2}(\tau_2)-\mathrm{T}_{2,2}(\tau_2)]\right]\\
4I_{yzx} = {} & \tfrac{1}{6}\left[i\sqrt{6}\,[\mathrm{T}_{3,-2}(\tau_1)-\mathrm{T}_{3,2}(\tau_1)]+3\sqrt{2}\mathrm{T}_{2,0}(\tau_2)+\sqrt{3}\,[\mathrm{T}_{2,-2}(\tau_2)+\mathrm{T}_{2,2}(\tau_2)]+\sqrt{6}\mathrm{T}_{2,0}(\tau_3)\right.\\
& \left.-3\,[\mathrm{T}_{2,-2}(\tau_3)+\mathrm{T}_{2,2}(\tau_3)]+2\sqrt{3}\mathrm{T}_{0,0}(\tau_4)\right]\\
4I_{yzy} = {} & \tfrac{1}{30}\left[2\sqrt{30}\mathrm{T}_{1,0}(\tau_1)-6\sqrt{5}\,[\mathrm{T}_{3,0}(\tau_1)]-5\sqrt{6}\,[\mathrm{T}_{3,-2}(\tau_1)+\mathrm{T}_{3,2}(\tau_1)]+5\sqrt{6}\mathrm{T}_{1,0}(\tau_2)\right.\\
& \left.+5i\sqrt{3}\,[\mathrm{T}_{2,-2}(\tau_2)-\mathrm{T}_{2,2}(\tau_2)]-15\sqrt{2}\mathrm{T}_{1,0}(\tau_3)-15i\,[\mathrm{T}_{2,-2}(\tau_3)-\mathrm{T}_{2,2}(\tau_3)]\right]\\
4I_{yzz} = {} & \tfrac{1}{30}\left[2i\sqrt{15}\,[\mathrm{T}_{1,-1}(\tau_1)+\mathrm{T}_{1,1}(\tau_1)]+4i\sqrt{15}\,[\mathrm{T}_{3,-1}(\tau_1)+\mathrm{T}_{3,1}(\tau_1)]+5i\sqrt{3}\,[\mathrm{T}_{1,-1}(\tau_2)+\mathrm{T}_{1,1}(\tau_2)]\right.\\
& \left.-5\sqrt{3}\,[\mathrm{T}_{2,-1}(\tau_2)-\mathrm{T}_{2,1}(\tau_2)]+15i\,[\mathrm{T}_{1,-1}(\tau_3)+\mathrm{T}_{1,1}(\tau_3)]-15\,[\mathrm{T}_{2,-1}(\tau_3)-\mathrm{T}_{2,1}(\tau_3)]\right]\\
4I_{zxx} = {} & \tfrac{1}{30}\left[2\sqrt{30}\mathrm{T}_{1,0}(\tau_1)-6\sqrt{5}\mathrm{T}_{3,0}(\tau_1)+5\sqrt{6}\,[\mathrm{T}_{3,-2}(\tau_1)+\mathrm{T}_{3,2}(\tau_1)]+5\sqrt{6}\mathrm{T}_{1,0}(\tau_2)\right.\\
& \left.-5i\sqrt{3}\,[\mathrm{T}_{2,-2}(\tau_2)-\mathrm{T}_{2,2}(\tau_2)]+15\sqrt{2}\mathrm{T}_{1,0}(\tau_3)-15i\,[\mathrm{T}_{2,-2}(\tau_3)-\mathrm{T}_{2,2}(\tau_3)]\right]\\
4I_{zxy} = {} & \tfrac{1}{6}\left[+i\sqrt{6}\,[\mathrm{T}_{3,-2}(\tau_1)-\mathrm{T}_{3,2}(\tau_1)]+\sqrt{3}\,[\mathrm{T}_{2,-2}(\tau_2)+\mathrm{T}_{2,2}(\tau_2)]-3\sqrt{2}\mathrm{T}_{2,0}(\tau_2)\right.\\
& \left.+3\,[\mathrm{T}_{2,-2}(\tau_3)+\mathrm{T}_{2,2}(\tau_3)]+\sqrt{6}\mathrm{T}_{2,0}(\tau_3)2\sqrt{3}\mathrm{T}_{0,0}(\tau_4)\right]\\
4I_{zxz} = {} & \tfrac{1}{30}\left[2\sqrt{15}\,[\mathrm{T}_{1,-1}(\tau_1)-\mathrm{T}_{1,1}(\tau_1)]+4\sqrt{15}\,[\mathrm{T}_{3,-1}(\tau_1)-\mathrm{T}_{3,1}(\tau_1)]+5\sqrt{3}\,[\mathrm{T}_{1,-1}(\tau_2)-\mathrm{T}_{1,1}(\tau_2)]\right.\\
& \left.+5i\sqrt{3}\,[\mathrm{T}_{2,-1}(\tau_2)+\mathrm{T}_{2,1}(\tau_2)]-15\,[\mathrm{T}_{1,-1}(\tau_3)-\mathrm{T}_{1,1}(\tau_3)]-15i\,[\mathrm{T}_{2,-1}(\tau_3)+\mathrm{T}_{2,1}(\tau_3)]\right]\\
4I_{zyx} = {} & \tfrac{1}{6}\left[+i\sqrt{6}\,[\mathrm{T}_{3,-2}(\tau_1)-\mathrm{T}_{3,2}(\tau_1)]+\sqrt{3}\,[\mathrm{T}_{2,-2}(\tau_2)+\mathrm{T}_{2,2}(\tau_2)]+3\sqrt{2}\mathrm{T}_{2,0}(\tau_2)\right.\\
& \left.+3\,[\mathrm{T}_{2,-2}(\tau_3)+\mathrm{T}_{2,2}(\tau_3)]-\sqrt{6}\mathrm{T}_{2,0}(\tau_3)-2\sqrt{3}\mathrm{T}_{0,0}(\tau_4)\right]\\
4I_{zyy} = {} & \tfrac{1}{30}\left[2\sqrt{30}\mathrm{T}_{1,0}(\tau_1)-6\sqrt{5}\mathrm{T}_{3,0}(\tau_1)-5\sqrt{6}\,[\mathrm{T}_{3,-2}(\tau_1)+\mathrm{T}_{3,2}(\tau_1)]+5\sqrt{6}\mathrm{T}_{1,0}(\tau_2)\right.\\
& \left.+5i\sqrt{3}\,[\mathrm{T}_{2,-2}(\tau_2)-\mathrm{T}_{2,2}(\tau_2)]+15\sqrt{2}\mathrm{T}_{1,0}(\tau_3)+15i\,[\mathrm{T}_{2,-2}(\tau_3)-\mathrm{T}_{2,2}(\tau_3)]\right]\\
4I_{zyz} = {} & \tfrac{1}{30}\left[2i\sqrt{15}\,[\mathrm{T}_{1,-1}(\tau_1)+\mathrm{T}_{1,1}(\tau_1)]+4i\sqrt{15}\,[\mathrm{T}_{3,-1}(\tau_1)+\mathrm{T}_{3,1}(\tau_1)]+5i\sqrt{3}\,[\mathrm{T}_{1,-1}(\tau_2)+\mathrm{T}_{1,1}(\tau_2)]\right.\\
& \left.-5\sqrt{3}\,[\mathrm{T}_{2,-1}(\tau_2)-\mathrm{T}_{2,1}(\tau_2)]-15i\,[\mathrm{T}_{1,-1}(\tau_3)+\mathrm{T}_{1,1}(\tau_3)]+15\,[\mathrm{T}_{2,-1}(\tau_3)-\mathrm{T}_{2,1}(\tau_3)]\right]\\
4I_{zzx} = {} & \tfrac{1}{5\sqrt{3}}\left[\sqrt{5}\,[\mathrm{T}_{1,-1}(\tau_1)-\mathrm{T}_{1,1}(\tau_1)]+2\sqrt{5}\,[\mathrm{T}_{3,-1}(\tau_1)-\mathrm{T}_{3,1}(\tau_1)]-5\,[\mathrm{T}_{1,-1}(\tau_2)-\mathrm{T}_{1,1}(\tau_2)]\right.\\
& \left.-5i\,[\mathrm{T}_{2,-1}(\tau_2)+\mathrm{T}_{2,1}(\tau_2)]\right]\\
4I_{zzy} = {} & \tfrac{1}{5\sqrt{3}}\left[i\sqrt{5}\,[\mathrm{T}_{1,-1}(\tau_1)+\mathrm{T}_{1,1}(\tau_1)]+2i\sqrt{5}\,[\mathrm{T}_{3,-1}(\tau_1)+\mathrm{T}_{3,1}(\tau_1)]-5i\,[\mathrm{T}_{1,-1}(\tau_2)+\mathrm{T}_{1,1}(\tau_2)]\right.\\
& \left.+5\,[\mathrm{T}_{2,-1}(\tau_2)-\mathrm{T}_{2,1}(\tau_2)]\right]\\
4I_{zzz} = {} & \tfrac{1}{\sqrt{5}}\left[\sqrt{6}\mathrm{T}_{1,0}(\tau_1)+2\mathrm{T}_{3,0}(\tau_1)\right]
\end{aligned}
$$

Figure 2.19: Decomposition of trilinear Cartesian product operators in terms of LiSA tensor operators.

Applications of the LiSA DROPS visualization

3.1 Introduction

The previous chapter was devoted to the general presentation of the DROPS visualization of quantum systems and the visualization using the LiSA basis was pointed out as presenting many interesting features. Some examples of applications have already been briefly discussed. In the present chapter, we propose to show how the LiSA DROPS visualization can be applied to help understanding fundamental concepts in theoretical and experimental nuclear magnetic resonance spectroscopy. Spin systems with spin-1/2 particles are considered, since they are the most encountered systems in NMR spectroscopy. In general, one- and two-particle systems will be complex enough to properly translate the ideas into insightful DROPS figures. To get familiar with the DROPS visualization, the first part of the chapter illustrates the most basic concepts whereas more complex ideas involving coherences are saved for the end of the chapter. Since the scope of this chapter is to illustrate how DROPS visualization may help understanding the presented concepts, each of these concepts is only briefly introduced. The reader may always consult [8] if seeking more details.

3.1.1 Visualization of two-spin systems

The DROPS visualizations encountered in the previous chapter were involving three spin-1/2 particles and 11 droplets were needed to represent general operators. In the case of systems with two spin-1/2 particles, only four droplets are needed, *i.e.* the droplets $\{1\}$, $\{2\}$, $\{1,2\}$ and $\{\mathrm{Id}\}$ which each represent the corresponding sub-system. An example of DROPS visualization of a two-spin system is illustrated in Fig. 3.1 (on the right) together with its equivalent representation when seen as a sub-system of a three-spin-1/2 system (on the left). The labels of the droplets are generally not shown when no confusion may arise, to lighten the DROPS pictures and ease their understanding.

3.2 Time evolution

3.2.1 General formulation

The time evolution of a system on a time interval $[t_0, t_f]$ designates the states taken by the system at any time t in the interval. Since the state of a system at a time t can be

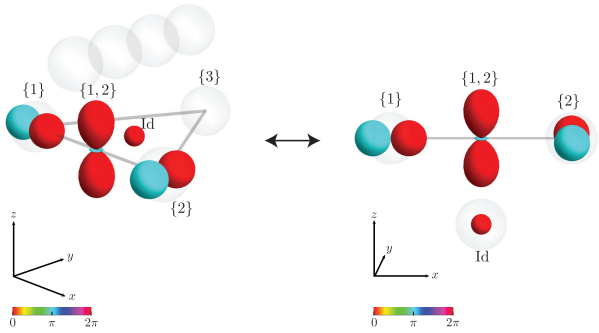

Figure 3.1: DROPS visualization of the operator $A = I_{1x} + I_{2y} + 2I_{1z}I_{2z} + \frac{1}{4}\mathrm{Id}$. The picture on the left represents the operator as part of a three-spin-1/2 system. The picture on the right shows the same operator as acting on a system consisting of two spin-1/2 particles only. The two DROPS visualizations are equivalent.

uniquely represented by a density matrix $\rho(t)$, studying the time evolution of a system amounts to studying the evolution of $\rho(t)$ for all $t \in [t_0, t_f]$. The time evolution of $\rho(t_0)$ under the action of a Hamiltonian $\mathscr{H}$ for a time t is schematically represented by

$$\rho(t_0) \xrightarrow{\mathscr{H}t} \rho(t_1),$$

where $\rho(t_1)$ is the density matrix of the system at time $t_1 := t_0 + t$. The systems considered in the present work are closed [69], that is there is no dissipation or no loss of information. In this case, the dynamics of the system is governed by the Liouville-von Neumann equation:

$$\dot{\rho} = -i[\mathscr{H}, \rho], \tag{3.1}$$

where $[A, B] := AB - BA$ denotes the commutator of A and B. For a constant Hamiltonian $\mathscr{H}$, the above equation is easy to solve and its solution is:

$$\rho(t_1) = U\rho(t_0)U^{-1}, \tag{3.2}$$

where $U = \mathrm{e}^{-i\mathscr{H}t}$ corresponds to the time-evolution operator and is called the *propagator*. In order to use Eq. (3.2), the time interval $[t_0, t_f]$ is generally split into sub-intervals on which the Hamiltonian is constant (or can be well approximated by a constant Hamiltonian). The time evolution of the system can then be computed by subsequently applying Eq. (3.2) on each sub-interval.

Note that Eq. (3.2) is linear. That is, if we decompose ρ_0 as a sum of operators $\rho_0 = \sum_i A_i$, then at time t_1 the following relation is satisfied: $\rho(t_1) = U\rho(t_0)U^{-1} = \sum_i UA_iU^{-1}$. Therefore, it is possible to consider the time evolution of density operator components A_i.

3.2.2 Cartesian operators and the sandwich formula

Cartesian product operators form a complete orthogonal basis of spin-1/2 systems and have already been formally presented in Appendix 2.10.3 of Chapter 2. We recall that for one-spin-1/2 systems, they are

$$\tfrac{1}{2}\mathrm{Id} = \begin{pmatrix} 1/2 & 0 \\ 0 & 1/2 \end{pmatrix}, I_x = \begin{pmatrix} 0 & 1/2 \\ 1/2 & 0 \end{pmatrix}, I_y = \begin{pmatrix} 0 & -i/2 \\ i/2 & 0 \end{pmatrix}, I_z = \begin{pmatrix} 1/2 & 0 \\ 0 & -1/2 \end{pmatrix}.$$

For a two-spin-1/2 system, they are formed by taking all the possible tensor products of the one-spin operators:

$$\tfrac{1}{2}\mathrm{Id},\quad I_{1\eta_1},\quad I_{2\eta_2},\quad 2I_{1\eta_1}I_{2\eta_2},$$

where $\eta_1, \eta_2 \in \{x, y, z\}$ and the additional factors ($\frac{1}{2}$ and 2 for instance) ensure that the operators all have the same norm. For one- and two-spin systems, the DROPS visualizations of Cartesian product operators involve a single droplet and are illustrated in Fig. 2.3 of Chapter 2.

Cartesian operators have a very interesting commutation property. Indeed, any two Cartesian operators C_1 and C_2 either commute (*i.e.* $[C_1, C_2] = 0$) or satisfy a cyclic relation with a third cartesian operator C_3 [8, 70]:

$$[C_1, C_2] = iC_3, \tag{3.3a}$$
$$[C_2, C_3] = iC_1, \tag{3.3b}$$
$$[C_3, C_1] = iC_2. \tag{3.3c}$$

Using these relations, the time evolution of a Cartesian operator $\rho(t_0) = C_1$ under a Hamiltonian $\mathscr{H} = C_2$ has the following direct solution:

$$C_1 \overset{C_2 t}{\longrightarrow} = \begin{cases} C_1 & \text{if } [C_1, C_2] = 0 \\ C_1\cos(a_2 t) - C_3\sin(a_2 t) & \text{if } [C_1, C_2] = iC_3 \neq 0 \end{cases} \tag{3.4}$$

which is also known as the *sandwich formula* [70].

3.2.3 Grasping the dynamics

For all pairs of Cartesian operators C_1, C_2 (excluding the identity operator which commutes with every operator), the Cartesian operator C_3 satisfying $[C_1, C_2] = iC_3$ appearing in the evolution formula in Eq. (3.4) has been visualized and presented into a table form in Fig. 3.3. We proceed to show how, with such a table, the time evolution of any operator $\rho(t_0) = a_1C_1$ under the action of a constant Hamiltonian $\mathscr{H} = a_2C_2$ can be grasped by only considering the DROPS pictures for C_1 and C_3. The dynamics is discussed in terms of DROPS pictures only, but the technical derivation of the time-evolution operators can be found in chapter 2 of [8].

Before that, we present in Fig. 3.2 the DROPS visualization of each Cartesian operator (except for the identity) in the system. The operators are presented according to their orientation axis (which was also discussed in the section 2.5.4 of Chapter 2).

The orientation of a linear operator $I_{k\eta}$ is defined from its characteristic droplet by the two points corresponding to the center of mass of the negative and positive lobes. Its direction is given by the positive center of mass and coincides with the axis $\vec{1}_\eta$. Similarly, the orientation of a mixed bilinear operator $2I_{1\eta_1}I_{2\eta_2}$, $\eta_1 \neq \eta_2$, is determined by the center of mass of its negative and positive lobes. Its direction $\vec{1}_{\eta_3}$, given by the positive center of mass, corresponds to the vector product $\vec{1}_{\eta_3} := \vec{1}_{\eta_1} \times \vec{1}_{\eta_2}$. Finally, the orientation of symmetric bilinear operators $2I_{1\eta}I_{2\eta}$ corresponds to the axis defined by the two positive lobes of the bilinear droplet. In this case, no direction can be specified since both principal lobes of the droplet are positive.

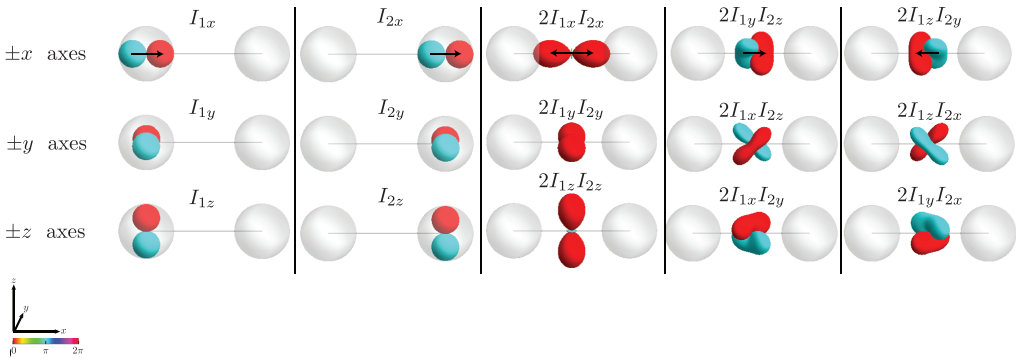

Figure 3.2: DROPS visualization of Cartesian operators in a two-spin system. The first and second columns show the linear operators acting on the first and second spins respectively. The third column shows the symmetric bilinear operators of the form $2I_{1\eta}I_{2\eta}$ and the two rightmost columns show the mixed bilinear operators $2I_{1\eta_1}I_{2\eta_2}$ with $\eta_1 \neq \eta_2$. Operators oriented in the $\pm x$, $\pm y$ and $\pm z$ directions are arranged on the first, second and third rows respectively. As an example, the orientation and direction of the operators in the first row are indicated with arrows.

Non-commuting Cartesian operators

Let $\rho(t_0) = C_1$ and $\mathscr{H} = C_2$ be two non-commuting Cartesian operators, *i.e.* the evolution $C_1 \overset{C_2 t}{\longrightarrow} C_1(t)$ is not trivial. At time $t = 0$, the visualization of $\rho(t_0)$ corresponds to the picture of C_1, which is found on the leftmost column of Fig. 3.3. As the time goes, the operator becomes $\rho(t) = C_1\cos(t) - C_3\sin(t)$ and there are four possible evolution schemes.

- If C_1 and C_2 act on one and the same single spin, the evolution of the DROPS picture corresponds to a rotation of the C_1 droplet about the axis defined by the cross product $\vec{1}_{C_1} \times \vec{1}_{C_2}$. This correspondence is well defined due to the direct relation between droplets representing single-spin operators and their corresponding Bloch vector (see section 2.5.4 of Chapter 2).
- If C_1 is linear and C_2 is bilinear, then C_3 is also bilinear and the time evolution $\rho(t)$ corresponds to a volume transfer between the non-empty linear droplet of C_1 and the bilinear droplet of $-C_3$.
- Conversely, if C_1 is bilinear and C_2 is linear, then C_3 is also bilinear and the time evolution $\rho(t)$ corresponds to a shape change in the bilinear droplet.
- If C_1 and C_2 are both bilinear, then C_3 is linear and the time evolution $\rho(t)$ corresponds to a volume transfer between the bilinear droplet for C_1 and the linear droplet for C_3.

Considering a small variation of the previous system, where $\rho(t_0) = a_1C_1$ and $\mathscr{H} = a_2C_2$, the above evolution schemes remain similar up to a size change of the droplets or a speed variation of the volume transfer.

Commuting Cartesian operators

The DROPS representation of commuting operators C_1 and C_2 can also be classified into categories defined from their DROPS pictures only. We briefly summarize them

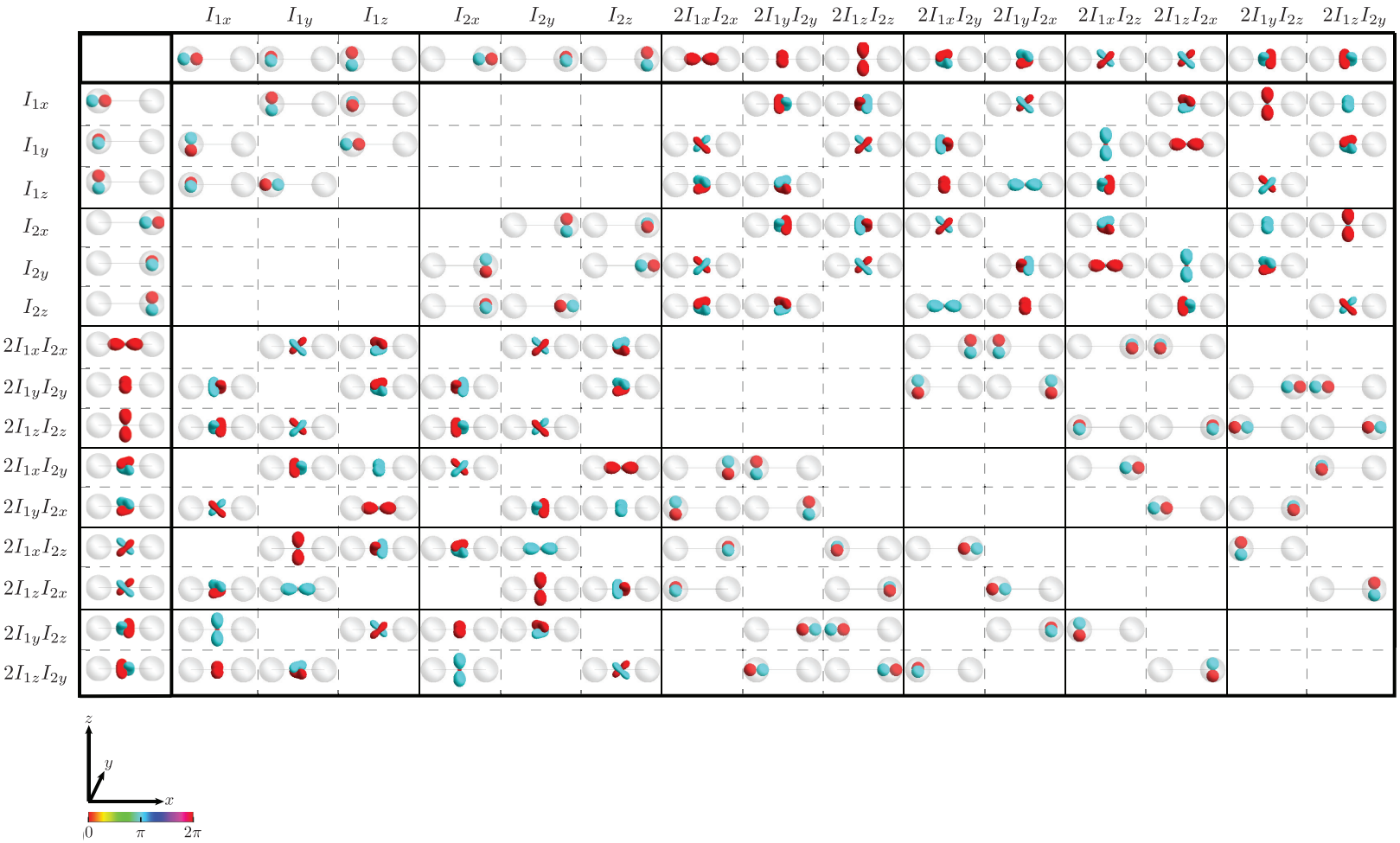

Figure 3.3: DROPS visualization of Cartesian operators C_1 (leftmost column) and C_2 (topmost row) for two-spin systems and of the operator C_3 satisfying $[C_1, C_2] = iC_3$ (in the table).

here.

- Two linear operators acting on different spins always commute. That is, if the two droplets involved in the DROPS picture of C_1 and C_2 are not "connected" to each other.
- The symmetric bilinear operators $2I_{1x}I_{2x}$, $2I_{1y}I_{2y}$, $2I_{1z}I_{2z}$ commute with each other. Moreover, symmetric operators commute with any operator having a parallel droplet axis. For instance, $2I_{1x}I_{2x}$ commutes with $I_{1,x}, I_{2,x}, 2I_{1y}I_{2z}$ and $2I_{1z}I_{2y}$.
- Mixed bilinear operators $2I_{1\eta_1}I_{2\eta_2}$, $\eta_1 \neq \eta_2$, for which the droplet axes are parallel, commute. That is, $[2I_{1x}I_{2y}, 2I_{1y}I_{2x}] = [2I_{1x}I_{2z}, 2I_{1z}I_{2x}] = [2I_{1y}I_{2z}, 2I_{1z}I_{2y}] = 0$.
- Two non-parallel mixed operators commute if and only if both of them either delineate a positive axis in $\{x, y, z\}$ or a negative axis in $\{-x, -y, -z\}$. For instance, since $2I_{1x}I_{2y}$ is oriented in the $+z$ direction and $2I_{1z}I_{2x}$ is oriented in the $+y$ direction, then $[2I_{1x}I_{2y}, 2I_{1z}I_{2x}] = 0$. Conversely, since $2I_{1x}I_{2y}$ is oriented in the $+z$ direction and $2I_{1x}I_{2z}$ is oriented in the $-y$ direction, then $[2I_{1x}I_{2y}, 2I_{1x}I_{2z}] \neq 0$.
- A linear operator acting on spin 1 oriented in the η-direction commute with a mixed bilinear operator oriented in the η'-direction if and only if the vector product $\vec{1}_\eta \times \vec{1}_{\eta'}$ is pointing in a positive direction in $\{x, y, z\}$. Consider for instance I_{1x}, which is oriented in the $+x$ direction, and $2I_{1x}I_{2z}$, which is oriented in the $-y$ direction. Since $\vec{1}_x \times \vec{1}_{-y} = \vec{1}_{+z}$ is pointing in a direction in $\{x, y, z\}$, then $[I_{1x}, 2I_{1x}I_{2z}] = 0$.
- On the other hand, a linear operator acting on spin 2 oriented in the η-direction commutes with a mixed bilinear operator oriented in the η'-direction if and only if the vector product $\vec{1}_\eta \times \vec{1}_{\eta'}$ is pointing in a negative direction in $\{-x, -y, -z\}$.

Since it is always possible to decompose operators into a linear combination of Cartesian operators, the dynamics of Cartesian operators presented above may be of great help to quickly visualize experiments.

3.3 Hamiltonians and pulse sequences

We now present the typical Hamiltonians encountered in NMR spectroscopy and visualize their effects on given initial density operators. The global Hamiltonian of a system at a given time can be decomposed as

$$\mathscr{H} = \mathscr{H}_{\text{cs}} + \mathscr{H}_J + \mathscr{H}_{\text{rf}}, \tag{3.5}$$

where $\mathscr{H}_{\text{cs}}$ is the *chemical shift Hamiltonian*, $\mathscr{H}_J$ is the *coupling Hamiltonian* and $\mathscr{H}_{\text{rf}}$ is the *pulse Hamiltonian* used to control the system and to design experiments. The internal Hamiltonian $\mathscr{H}_0 = \mathscr{H}_{\text{cs}} + \mathscr{H}_J$ designates the part of the Hamiltonian which is intrinsic to the system as opposed to the rf-Hamiltonian $\mathscr{H}_{\text{rf}}$, which we may steer.

3.3.1 The chemical shift Hamiltonians $\mathscr{H}_{\text{cs}}$

The chemical shift Hamiltonians are of the form [8]

$$\mathscr{H}_{\text{cs}} = 2\pi(\nu_1 I_{1z} + \nu_2 I_{2z})$$

and their visualization corresponds to two droplets on spins one and two of length proportional to ν_1 and ν_2 respectively. They are both pointing in the $\pm z$ direction, according to the sign of ν_i. In Fig. 3.4, two examples of chemical shift Hamiltonians are illustrated for the case (a) $\nu_1 = \nu_2$ and (b) $2\nu_1 = \nu_2$.

The effect of $\mathscr{H}_{\text{cs}}$ alone on linear operators is simple: the droplet corresponding to spin one rotates about the z axis with angular velocity ν_1 and similarly for spin two. The bilinear droplet will also rotate when $\nu_1 = \nu_2$, *i.e.* when the two spins precess with the same velocity (see Fig. 3.4 (a)). If $\nu_1 \neq \nu_2$ however, it may also change its shape as illustrated in Fig. 3.4 (b).

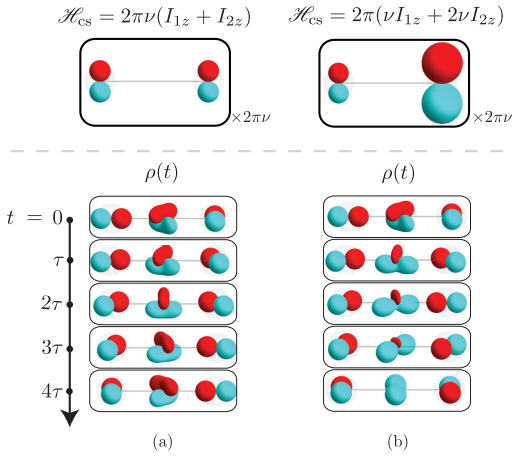

Figure 3.4: Illustration of the chemical shift Hamiltonians $\mathscr{H}_{cs} = 2\pi(\nu_1 I_{1z} + \nu_2 I_{2z})$ for a two-spin system. Given $\nu_1 = \nu$, the cases (a) $\nu_2 = \nu$ and (b) $\nu_2 = 2\nu$ are considered. On the top row lies the DROPS visualization of the corresponding Hamiltonians, which have been scaled down by a factor of $\frac{1}{2\pi\nu}$. Below the dashed line, we visualized the time evolution of $\rho(0) = I_{1x} + I_{2y} + 2I_{1x}I_{2y}$ under the corresponding Hamiltonians at equally distributed time points, where $\tau = \frac{1}{8\nu}$.

3.3.2 The coupling Hamiltonians $\mathscr{H}_J$

The spin-spin coupling Hamiltonians for a two-spin system are of the form

$$\mathscr{H}_{\text{cs}} = 2\pi J(aI_{1x}I_{2x} + aI_{1y}I_{2y} + bI_{1z}I_{2z})$$

and have already been discussed in Section 2.5.6 of Chapter 2. We simply summarize in Fig. 3.5) the shape of these characteristic Hamiltonians for the most encountered values of the parameters a and b and visualize the evolution of an initial density operator $\rho(t_0) = I_{1x}$ under the action of these Hamiltonians. The detailed time evolution of $\rho(0) = I_{1x}$ under these different coupling Hamiltonians can be found in Appendix 3.8.1.

3.3.3 The pulse Hamiltonians $\mathscr{H}_{\text{rf}}$

Experiments in nuclear magnetic resonance spectroscopy are designed to manipulate systems to find out information about their structure. For example, some experiments are designed to determine which spins are coupled together while others aim at finding their spin-spin coupling constants (see [71] for a compilation of classical experiments). An external radio-frequency (rf) magnetic field $\vec{B}_{\text{rf}}$ is used to control the system and

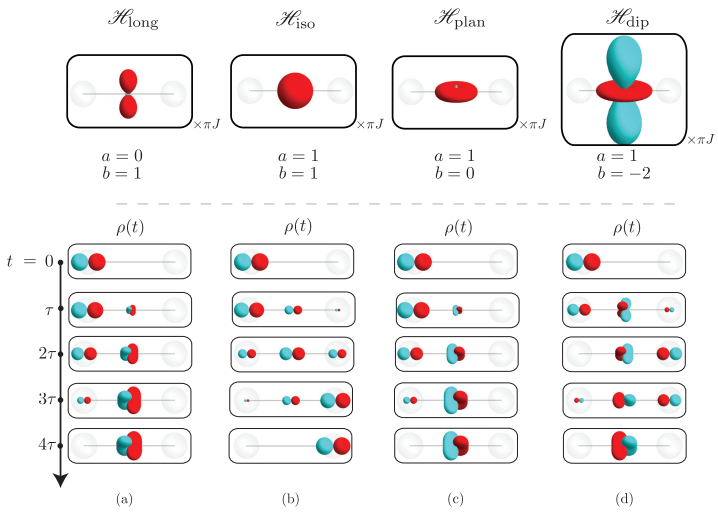

Figure 3.5: On the top row, DROPS visualization of typical coupling Hamiltonians $\mathscr{H}_J = 2\pi J(aI_{1x}I_{2x} + aI_{1y}I_{2y} + bI_{1z}I_{2z})$ for the coefficient values (a) $a = 0$, $b = 1$, (b) $a = 1$, $b = 1$, (c) $a = 1$, $b = 0$ and (d) $a = 1$, $b = -2$. The pictures are scaled down by a factor of $1/\pi J$. Below the dashed line, we visualized the time evolution of $\rho(0) = I_{1x}$ under the corresponding coupling Hamiltonians at equally distributed time points, where $\tau = 1/8J$.

the presence of this field during a certain amount of time is called a *pulse*. For the moment, we will consider rectangular pulses only, *i.e.* pulses created by an rf-field which is constant in space and time [70].

In this work, we consider that pulses are selective, *i.e.* they can act independently on each spin. The total pulse Hamiltonian is then the sum of the single-spin pulses:

$$\mathscr{H}_{\text{rf}} = \mathscr{H}_{\text{rf}}^{(1)} + \mathscr{H}_{\text{rf}}^{(2)}$$

for a two-spin system. We also consider that we are in the conditions under which the rotating-wave approximation is a valid representation of the system [8]. Under this assumption, the Hamiltonian corresponding to a pulse acting on the spin k and whose field is pointing in the $\vec{1}_{\theta^{(k)}} := \cos\theta^{(k)}\vec{1}_x + \sin\theta^{(k)}\vec{1}_y$ direction has the form

$$\mathscr{H}_{\text{rf}}^{(k)} = 2\pi\nu_x^{(k)} I_{kx} + 2\pi\nu_y^{(k)} I_{ky}, \tag{3.6}$$

with

$$\begin{cases} \nu_x^{(k)} & := \nu_{\text{rf}}^{(k)} \cos\theta^{(k)}, \\ \nu_y^{(k)} & := \nu_{\text{rf}}^{(k)} \sin\theta^{(k)}, \end{cases}$$

where the frequency

$$\nu_{\text{rf}}^{(k)} := \frac{-\gamma^{(k)}|\vec{B}_{\text{rf}}|}{2\pi} \tag{3.7}$$

is proportional to the amplitude of the external field multiplied by the gyromagnetic ratio $\gamma^{(k)}$ of spin k [8,68]. In this work, we consider systems for which $\gamma^{(1)} \cong \gamma^{(2)}$ and denote $\nu_{\text{rf}} := \nu_{\text{rf}}^{(1)} \cong \nu_{\text{rf}}^{(2)}$. Examples of DROPS representations for pulse Hamiltonians are illustrated in Fig. 3.7. The pulse Hamiltonians are, like the chemical shift Hamiltonians, linear. The action of the former is then similar to the action of the latter, rotating the droplets for spins one and two about the axes $\vec{1}_{\theta^{(1)}}$ and $\vec{1}_{\theta^{(2)}}$. Likewise, the bilinear droplet also rotates if $\vec{1}_{\theta^{(1)}} = \vec{1}_{\theta^{(2)}}$.

3.3.4 90° and 180° pulses

In many experiments, the pulses used to manipulate systems are defined to perform 90° or 180° rotations about an axis in the transverse plane. We define below the 90° pulse, but the reasoning also holds for 180° pulses by simply changing the rotation angle everywhere.

A 90° pulse on spin k about the axis $\vec{1}_\theta$, also designated as a $90^\circ_{\vec{1}_\theta}$ pulse, is determined by the time duration of the pulse: t_{90°. This duration is defined such that the propagator associated with the pulse (see Eq. (3.2)) takes the form:

$$U_{90^\circ_{\vec{1}_\theta}} := \mathrm{e}^{-i\mathscr{H}_{\mathrm{rf}}t_{90^\circ}} = \mathrm{e}^{-i\pi/2[\cos\theta I_{kx}+\sin\theta I_{ky}]}.$$

That is, $t_{90^\circ} = \frac{1}{2\pi\nu_{\mathrm{rf}}} \times \frac{\pi}{2}$, where we recall that ν_{rf} is proportional to the rf-field amplitude (see Eq. (3.7)). Similarly, the time duration to perform a 180° rotation is $t_{180^\circ} = \frac{1}{2\pi\nu_{\mathrm{rf}}} \times \pi$. Since the times t_{90° and t_{180° depend on the constant ν_{rf} only, they are independent of the rotation axis and of the identity k of the spin.

A global pulse designates a family of simultaneous pulses acting identically on all spins of the system. For instance, the Hamiltonian corresponding to a global 90°_x pulse in a two-spin system is $\mathscr{H}_{\mathrm{rf}} = 2\pi\nu_{\mathrm{rf}}(I_{1x} + I_{2x})$.

3.3.5 Pulse sequences

A pulse sequence is a sequence of pulses and delays, where a delay is a time period during which the system evolves freely. It is common practice to represent a pulse sequence with a diagram as shown in Fig. 3.6. Conventionally, the black and white rectangles represent 90° and 180° pulses respectively.

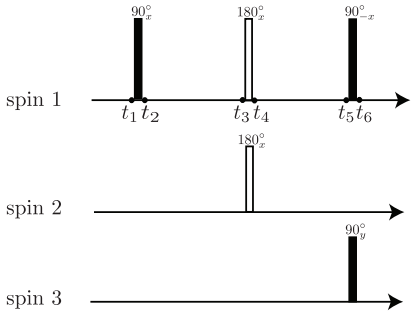

Figure 3.6: An example of pulse sequence for a system with three particles.

Illustration

The DROPS visualizations of Hamiltonians corresponding to some chosen pulses are depicted in Fig. 3.7. Since rf-Hamiltonians are linear operators, the bilinear droplet (see the upper part of the figure) in the visualization of $\mathscr{H}_{\mathrm{rf}}$ is necessarily empty. To give insight into the effect of these Hamiltonians on density matrices, the DROPS visualizations of some chosen density matrices at initial time t_1 and final time t_2 are depicted in the figure. As expected, the linear droplets for $\rho(t_1) = I_{1x} + I_{2x}$ (first line of the table) are rotated according to the pulses' name (*e.g.* 90° rotation of spins 1 and 2

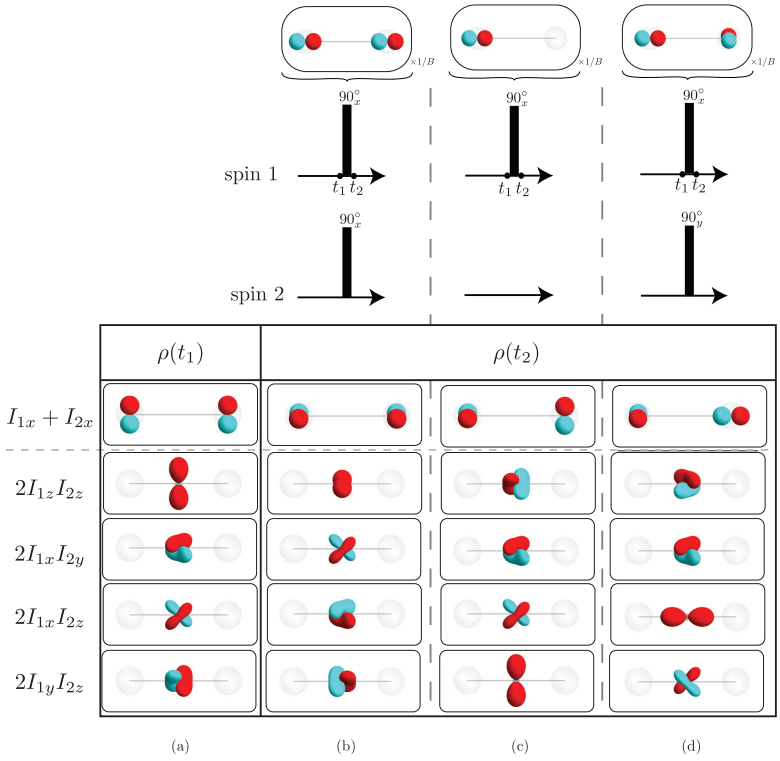

Figure 3.7: The upper part of the figure shows some chosen pulses and the DROPS visualization of their corresponding Hamiltonian. As indicated, the DROPS pictures have been scaled down by a factor of $\frac{1}{2\pi\nu_{\mathrm{rf}}}$, where ν_{rf} is a constant proportional to the rf-field amplitude and the gyromagnetic ratio (see Eqs. (3.6) and (3.7)). The lower part of the figure shows the effect ($\rho(t_2)$) of the above pulses (columns (b), (c) and (d)) on the density matrices $\rho(t_1)$ illustrated in column (a). The linear density matrices and the bilinear ones are parted by the horizontal dotted line.

about the x-axis for the first Hamiltonian). Concerning the bilinear density matrices, a global rotation is also performed when both spins are acted upon by an identical pulse, as shown in column (b). When the pulses are not identical (columns (c) and (d)), the bilinear droplet does not necessarily rotate and may change its shape.

3.4 Decoupling and refocusing pulse sequences

The decoupling and refocusing pulse sequences are well-known pulse sequences appearing as parts of numerous NMR spectroscopy experiments. In this section, we describe three of these sequences and their effects. They are illustrated for two different initial density matrices $\rho(t_0) = I_{1x}$ and $\rho(t_0) = I_{1y}$ in Figs. 3.8 and 3.9 respectively, where for both cases the time evolution in the presence of the three different internal Hamiltonians $\mathscr{H}_{\mathrm{cs}} = \mathscr{H}_{\mathrm{cs}}^{(1)} + \mathscr{H}_{\mathrm{cs}}^{(2)}$, $\mathscr{H}_J$ and $\mathscr{H}_{\mathrm{cs}}^{(1)} + \mathscr{H}_{\mathrm{cs}}^{(2)} + \mathscr{H}_J$ is shown. Note that for these illustrative examples, since the initial states involve the first spin only, one could replace $\mathscr{H}_{\mathrm{cs}}$ by $\mathscr{H}_{\mathrm{cs}}^{(1)}$ without affecting the time evolution of the state. However, in order to stay as general as possible, we keep working with the full chemical shift Hamiltonian $\mathscr{H}_{\mathrm{cs}} = \mathscr{H}_{\mathrm{cs}}^{(1)} + \mathscr{H}_{\mathrm{cs}}^{(2)}$.

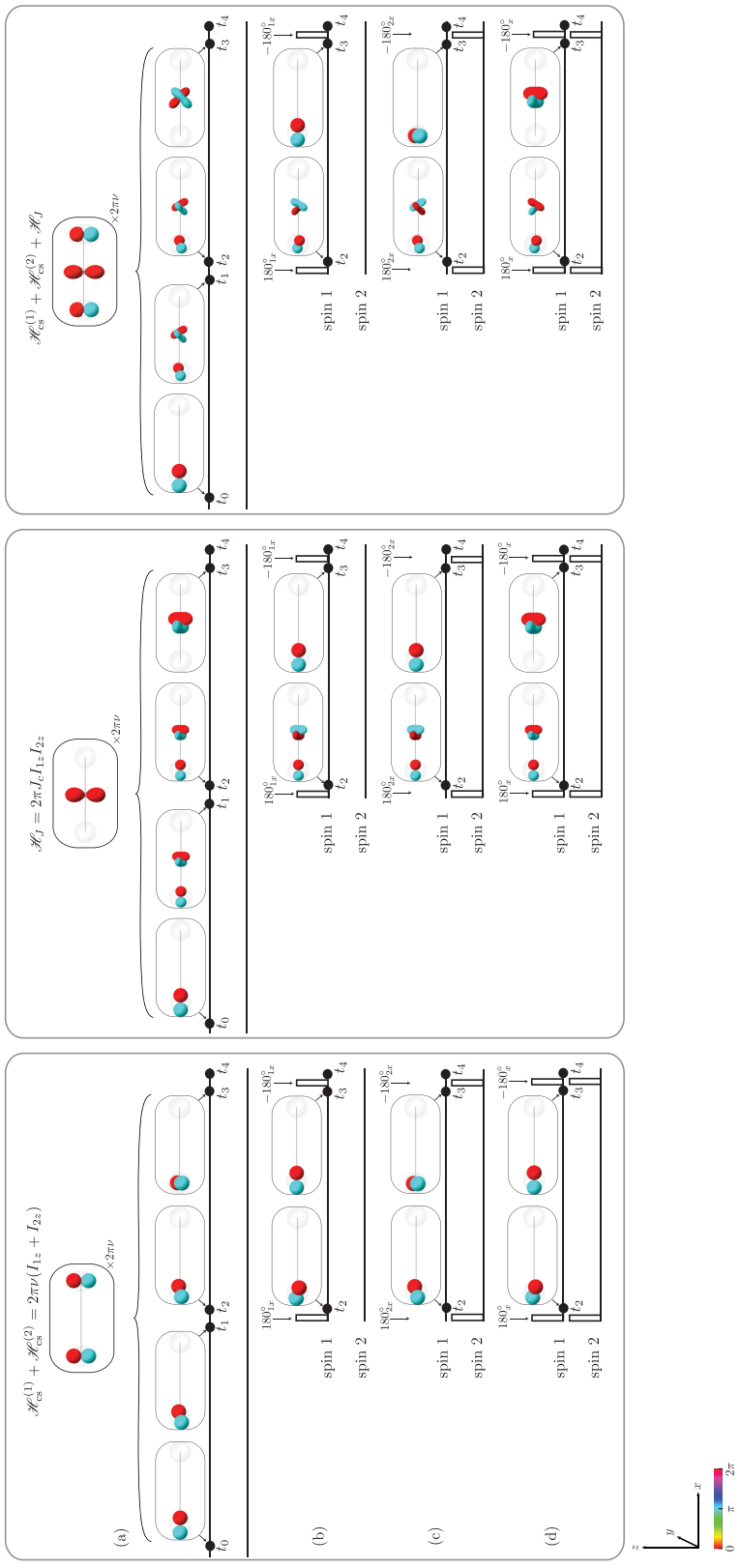

Figure 3.8: Illustration of decoupling and refocusing pulse sequences on an initial density matrix $\rho(t_0) = I_{1x}$ in the presence of the three different internal Hamiltonians $\mathscr{H}_{\rm cs}$, $\mathscr{H}_J$ and $\mathscr{H}_{\rm cs} + \mathscr{H}_J$ (columns from left to right respectively). All the pulses perform $\pm 180^\circ$ rotations about the x axis. From bottom to top are illustrated the effect of the (d) refocusing, (c) decoupling of spin two, (b) decoupling of spin one pulse sequences and (a) the free evolution (no pulse) of $\rho(t_0)$ at five different times t_i, $0 \leq i \leq 4$. Since for this example $\rho(t_4) = \rho(t_3)$, the DROPS visualization of $\rho(t_4)$ is not illustrated to lighten the picture. The chemical shifts for the two spins are equal to ν and the coupling J_c satisfies $J_c = 2\nu$. The total time of the pulse is $\tau = \frac{1}{2J} = \nu/4$ and $t_1 - t_0 \sim t_3 - t_2 = \frac{\tau}{2}$. The pictures corresponding to the DROPS visualization of the internal Hamiltonians have been scaled down by a factor of $1/2\pi\nu$.

Figure 3.9: Illustration of the decoupling and refocusing pulse sequences on an initial density matrix $\rho(t_0) = I_{1y}$. See the caption of Fig. 3.8 for more details.

For comparison purposes, the free evolution of $\rho(t_0) = I_{1x}$ and $\rho(t_0) = I_{1y}$ in the presence of the internal Hamiltonians $\mathscr{H}_{\rm cs}^{(1)} + \mathscr{H}_{\rm cs}^{(2)}$, $\mathscr{H}_J$ and $\mathscr{H}_{\rm cs}^{(1)} + \mathscr{H}_{\rm cs}^{(2)} + \mathscr{H}_J$ are illustrated in row (a) of Fig. 3.8 and 3.9. In these figures, the chemical shifts of the two spins are taken to be identical, *i.e.* $\nu_1 = \nu_2$, such that the chemical shift Hamiltonian takes the form $\mathscr{H}_{\rm cs}^{(1)} + \mathscr{H}_{\rm cs}^{(2)} = 2\pi\nu(I_{1z} + I_{2z})$, where $\mathscr{H}_{\rm cs}^{(k)} = 2\pi\nu I_{kz}$. The coupling Hamiltonian considered is longitudinal and the coupling constant J_c is related to the chemical shifts by $J_c = 2\nu$. That is, $\mathscr{H}_J = 2\pi J_c I_{1z} I_{2z} = 2\pi\nu \cdot 2I_{1z} I_{2z}$.

The refocusing pulse sequence, illustrated in the last row (d) of Figs. 3.8 and 3.9, consists of two opposite global 180° pulses and two delays of same duration $\frac{\tau}{2} = t_1 - t_0 = t_3 - t_2$ before the pulses. The sequence is designed such that the linear components of $\rho(t_2)$ present after the first pulse propagates backward during the second delay $\frac{\tau}{2}$ to be finally refocused by the last pulse. On the other hand, the bilinear term evolves during the sequence without being affected. As a result, the state $\rho(t_4)$ is identical to the state obtained from the free evolution of $\rho(t_0)$ in the absence of chemical shifts. In Figs. 3.8 and 3.9, we can actually *see* the effect of the refocusing sequence in the presence of different Hamiltonians. Under $\mathscr{H}_{\rm cs}$ (first column), the final state $\rho(t_4)$ is identical to the initial state as the effect of the total Hamiltonian is completely canceled. The final states generated by the refocusing sequence in the presence of the Hamiltonians $\mathscr{H}_J$ and $\mathscr{H}_{\rm cs} + \mathscr{H}_J$ (middle and last columns) are identical, the terms generated by $\mathscr{H}_{\rm cs}$ being canceled at the final time.

The decoupling pulse sequence, illustrated in row (c) of Figs. 3.8 and 3.9, consists of two delays of same duration $\frac{\tau}{2}$ which precede two opposite 180° pulses on spin two. This time, the components obtained from $\rho(t_0)$ due to the presence of $\mathscr{H}_J$ and $\mathscr{H}_{\rm cs}^{(2)}$ during the first delay and pulse are the ones which are propagated backward and refocused by the second delay and pulse. This sequence is understood as the decoupling of spin two. Indeed, when the initial state involves spin one only, as in our two principal examples, the fact that the sequence undoes the effect of $\mathscr{H}_{\rm cs}^{(2)}$ is not visible and the decoupling effect is the only one visible. Looking at Figs. 3.8 and 3.9, let us first consider the coupling Hamiltonian $\mathscr{H}_J$ only (second column of Fig. 3.8). We can see that the final state created by the sequence is identical to the initial state, canceling out the terms created by $\mathscr{H}_J$ and preserving $\mathscr{H}_{\rm cs}^{(1)} \equiv \mathscr{H}_{\rm cs}$ in this case. For an internal Hamiltonian $\mathscr{H}_{\rm cs} \equiv \mathscr{H}_{\rm cs}^{(1)}$ (first column), we see that the sequence has no effect on the time evolution of the system, comparing with the free evolution of the system (row 1). Finally, as expected, the final state created under $\mathscr{H}_{\rm cs} + \mathscr{H}_J$ (last column) is identical to the one with the Hamiltonian $\mathscr{H}_{\rm cs} \equiv \mathscr{H}_{\rm cs}^{(1)}$.

Similar to the sequence (c) which decouples spin two, row (b) shows the decoupling sequence of spin one. The sequence is designed to cancel the effect of $\mathscr{H}_J$ and $\mathscr{H}_{\rm cs}^{(1)}$. That is, for an initial state involving spin two only, the final state is the same as the one created by the chemical shift Hamiltonian only since in this case, $\mathscr{H}_{\rm cs} \equiv \mathscr{H}_{\rm cs}^{(2)}$ and its effect is the only one which is visible at final time. In our principal examples however, $\mathscr{H}_{\rm cs} \equiv \mathscr{H}_{\rm cs}^{(1)}$ such that the components created by both the chemical shift and coupling Hamiltonians are propagated backward and refocused. That is, the net effect of the pulse on $\rho(t_0)$ is the disappearance of any sign of time evolution, as we can see on row (b) of Figs. 3.8 and 3.9. As expected, under all three Hamiltonians $\mathscr{H}_{\rm cs}$, $\mathscr{H}_J$ and $\mathscr{H}_{\rm cs} + \mathscr{H}_J$, the state created at the final time is identical to the initial state, the terms created by both $\mathscr{H}_{\rm cs} \equiv \mathscr{H}_{\rm cs}^{(1)}$ and $\mathscr{H}_J$ being canceled at final time.

Another way to understand the effect of the above decoupling and refocusing pulse

sequences is to represent each of them by a constant Hamiltonian under which the final state $\rho(t_4)$ reached by $\rho(t_0)$ would be identical. Such a representation is illustrated in Fig. 3.10.

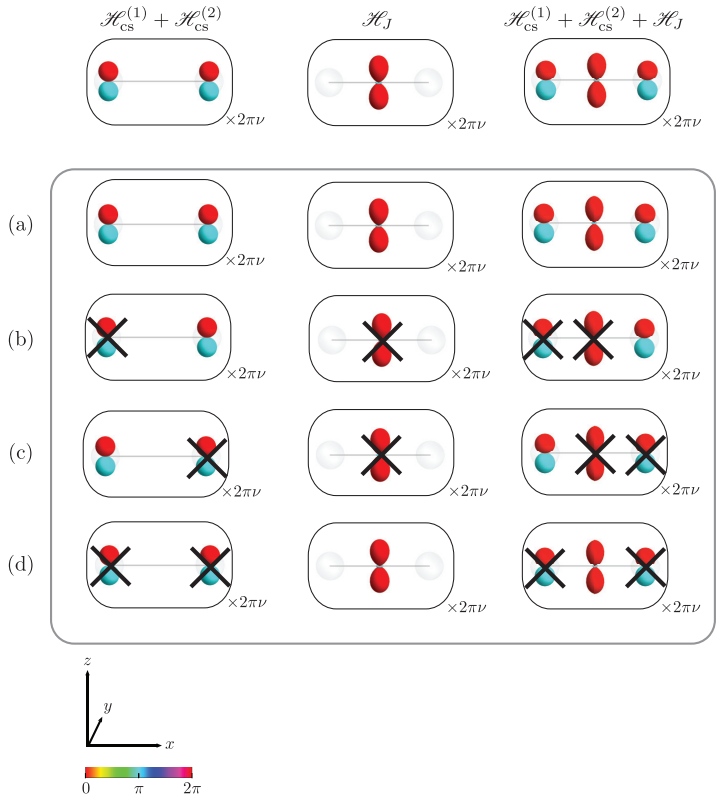

Figure 3.10: Schematic representation of the global effect of the pulse sequences presented in Figs. 3.8 and 3.9 at final time t_4.

This figure reinterprets the sequences of Figs. 3.8 and 3.9, representing each system (consisting to an internal Hamiltonian and a pulse sequence) by a constant Hamiltonian known as an *effective* Hamiltonian (further discussed in the next Section). Since the aim of these sequences is to simulate Hamiltonians without their chemical shift term $\mathscr{H}_{\mathrm{cs}}$ (for the refocusing sequence) or without their coupling term $\mathscr{H}_J$ and one chemical shift term $\mathscr{H}_{\mathrm{cs}}^{(k)}$ (for the decoupling sequences), the constant Hamiltonians then consist of the full Hamiltonians deprived of the corresponding terms. Accordingly, the Hamiltonians representing the refocusing pulse sequence (row (d)) have no chemical shift terms whereas the ones simulating the decoupling pulse sequences (rows (b,c)) have only one chemical shift term.

3.5 Average Hamiltonian theory

3.5.1 Effective Hamiltonian

We can schematically represent a pulse sequence P by a sequence of n constant Hamiltonians $\mathscr{H}_i$ each applied for a time τ_i

$$P = \{(\mathscr{H}_1, \tau_1), (\mathscr{H}_2, \tau_2), \cdots, (\mathscr{H}_n, \tau_n)\}.$$

The total time of the pulse sequence is $\tau_{\rm tot} := \sum_{1\le i\le n} \tau_i$. The time evolution on an initial state $\rho(t_0)$ is graphically represented by

$$\rho(t_0) \overset{\mathscr{H}_1\tau_1}{\longrightarrow} \rho(\tau_1) \overset{\mathscr{H}_2\tau_2}{\longrightarrow} \rho(\tau_1+\tau_2) \overset{\mathscr{H}_3\tau_3}{\longrightarrow} \cdots \overset{\mathscr{H}_n\tau_n}{\longrightarrow} \rho(\tau_{\rm tot})$$

where the state at each stage is calculated via Eq. (3.2). That is,

$$\begin{array}{rcl} \rho(\tau_1) & = & U_1\rho(t_0)U_1^{-1} \\ \rho(\tau_1+\tau_2) & = & U_2U_1\rho(t_0)U_1^{-1}U_2^{-1} \\ \vdots & & \vdots \\ \rho(\tau_{\rm tot}) & = & U_n\ldots U_2U_1\rho(t_0)U_1^{-1}U_2^{-1}\ldots U_n^{-1} \end{array}$$

where $U_i := \mathrm{e}^{-i\mathscr{H}_i\tau_i}$. Since each propagator U_i is an element of the group SU(2), the product $U_n\ldots U_2U_1$ is also an element of this group and we define the effective propagator $U_{\rm eff}$ as

$$U_{\rm eff} = U_n\ldots U_2U_1.$$

The global transformation performed by the above pulse sequence P is then

$$\rho(t_0) \overset{\mathscr{H}_{\rm eff}\cdot\tau_{\rm tot}}{\longrightarrow} U_{\rm eff}\cdot\rho(t_0)\cdot U_{\rm eff}^{-1}, \tag{3.8}$$

where the *effective Hamiltonian* [8,72] $\mathscr{H}_{\rm eff}$ can be any constant Hamiltonian satisfying $\mathrm{e}^{-i\mathscr{H}_{\rm eff}\cdot\tau_{\rm tot}} = U_{\rm eff}$. The effective Hamiltonian, which is obtained by taking the matrix logarithm of $U_{\rm eff}$:

$$\mathscr{H}_{\rm eff} = \frac{i}{\tau_{\rm tot}}\log(U_{\rm eff}), \tag{3.9}$$

is indeed not uniquely defined since the logarithm is a multivalued function. The choice of $\mathscr{H}_{\rm eff}$ is made by means of simplicity and continuity criteria [73, 74]. In the present work, we choose $\mathscr{H}_{\rm eff}$ to be a traceless solution of Eq. (3.9).

The effective propagator and Hamiltonian are insightful when one is only interested in the global transformation $U_{\rm eff}$ created by a sequence of total duration $\tau_{\rm tot}$, regardless of the way this result is achieved. The decoupling and refocusing pulse sequences introduced in Section 3.4 are good examples of such situations, since the pulses are designed to perform a certain transformation at final time t_4, independently of the initial state and the intermediate stages of the sequence.

3.5.2 Illustration (decoupling and refocusing pulse sequences)

In Fig. 3.11, effective Hamitonians $\mathscr{H}_{\rm eff}$ corresponding to the pulse sequences presented in Figs. 3.8 and 3.9 under different internal Hamiltonians are illustrated. The effective Hamiltonians corresponding to (a) the free evolution are identical to the internal Hamiltonians but are nevertheless also visualized for comparison purposes.

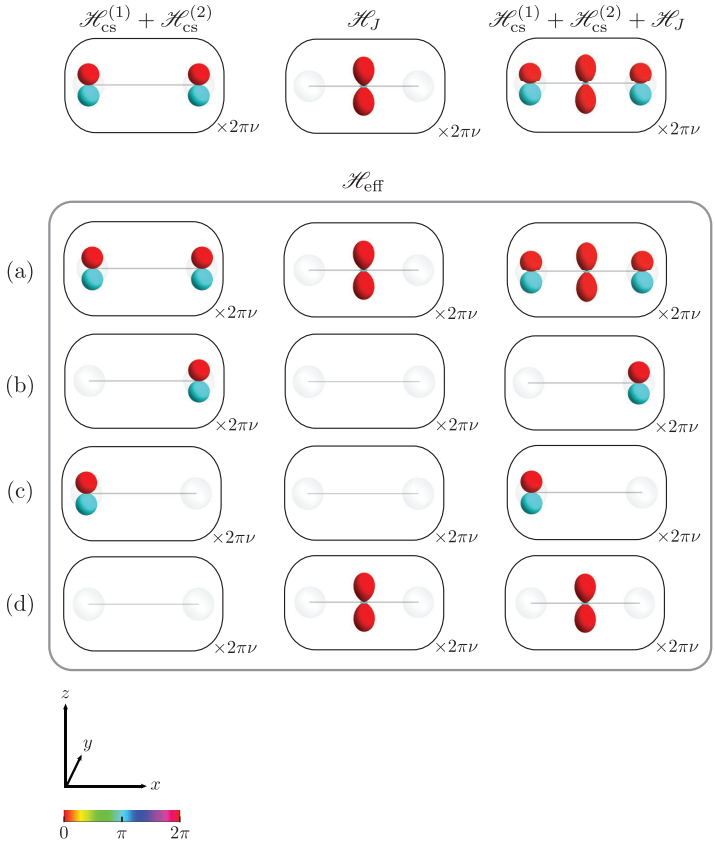

Figure 3.11: Effective Hamiltonians corresponding to the pulse sequences presented in Figs. 3.8 and 3.9. The total duration of the pulse is $\tau_{\rm tot} = \frac{1}{2J}$, the two chemical shifts are identical $\nu_1 = \nu_2 = \nu$, *i.e.* $\mathscr{H}_{\rm cs}^{(k)} = 2\pi\nu I_{kz}$. The coupling Hamiltonian is longitudinal and the coupling constant J_c is related to the chemical shifts by $J_c = 2\nu$. That is, $\mathscr{H}_J = 2\pi J_c I_{1z} I_{2z} = 2\pi\nu \cdot 2I_{1z} I_{2z}$.

The effect of the effective Hamiltonians for the refocusing pulse (row (d)) is clear when looking at the effective Hamiltonians since the DROPS representation of these Hamiltonians has no linear term. In the first case ($\mathscr{H} = \mathscr{H}_{\rm cs}$), we forthwith deduce that the final state must be identical to the initial one since $\rho(t_0)$ does not evolve at all. The fact that the effective Hamiltonians $\mathscr{H}_{\rm eff}$ for the internal Hamiltonians $\mathscr{H}_J$ and $\mathscr{H}_J + \mathscr{H}_{\rm cs}$ are identical bears witness to the fact that the pulse effectively cancels the effect of the chemical shift Hamiltonian only.

The effect of the decoupling pulse of row (c) corresponds to the internal Hamiltonian deprived of its bilinear and linear in spin-two components. The only possible evolution arises when the initial state involves the first spin and when there is a chemical shift Hamiltonian (first and last columns), in which case the linear droplet on the first spin embodies the precession of the spin. In the case where there is no chemical shift Hamiltonian $\mathscr{H}_{\rm cs}$ (column 2), the effective Hamiltonian $\mathscr{H}_{\rm eff}$ is zero and corresponds to the identity transformation $U_{\rm eff} = {\rm Id}$. That is, whatever the initial state is, it does not evolve under this Hamiltonian.

Similarly to the decoupling sequence (c), the effective Hamiltonians corresponding to the decoupling sequence (b) concur with the linear droplet in spin two of the

corresponding internal Hamiltonians. In particular, any initial state involving spin one only, as in the two examples illustrated in Figs. 3.8 and 3.9, does not evolve at all under these Hamiltonians.

It is interesting to compare the computed effective Hamiltonians illustrated in Fig. 3.11 with the schematic representation of the sequences we made in Fig. 3.10. Although the latter has been intuitively deduced from the effect of the pulse at final time only, it is noticeable that the two representations coincide. Recalling that there are many possible effective Hamiltonians leading to the same transformation U_{eff} and that the choice of a particular one should be based on simplicity and continuity, the fact that one succeeded in deducing the form of $\mathscr{H}_{\text{eff}}$ without calculations is a good indication that the calculated effective Hamiltonians in Fig. 3.11 meet these criteria.

3.5.3 Average Hamiltonian and toggling frame

Let $P = \{(\mathscr{H}_1, \tau_1), (\mathscr{H}_2, \tau_2), \cdots, (\mathscr{H}_n, \tau_n)\}$ represent a generic pulse of total duration $\tau_{\text{tot}} := \sum_{1 \leq i \leq n} \tau_i$. The Magnus expansion of an effective Hamiltonian $\mathscr{H}_{\text{eff}}$ leads to the decomposition

$$\mathscr{H}_{\text{eff}} = \mathscr{H}_{\text{eff}}^{(0)} + \mathscr{H}_{\text{eff}}^{(1)} + \mathscr{H}_{\text{eff}}^{(2)} + \cdots, \tag{3.10}$$

where [8]

$$\begin{aligned}
\mathscr{H}_{\text{eff}}^{(0)} &= \frac{1}{\tau_{\text{tot}}}(\mathscr{H}_1\tau_1 + \cdots + \mathscr{H}_n\tau_n) \\
\mathscr{H}_{\text{eff}}^{(1)} &= -\frac{9}{2\tau_{\text{tot}}}([\mathscr{H}_2\tau_2, \mathscr{H}_1\tau_1] + [\mathscr{H}_3\tau_3, \mathscr{H}_1\tau_1] + [\mathscr{H}_3\tau_3, \mathscr{H}_2\tau_2] + \ldots) \\
&\vdots
\end{aligned}$$

The zeroth-order term $\mathscr{H}_{\text{eff}}^{(0)}$ is the *average* Hamiltonian of the sequence and is denoted $\overline{\mathscr{H}}$. Clearly, when all the constant Hamiltonians $\mathscr{H}_i$ commute, the effective Hamiltonian equals the average Hamiltonian, *i.e.* $\mathscr{H}_{\text{eff}} = \overline{\mathscr{H}}$. When it is not the case, the average Hamiltonian still furnishes a good approximation of the effective Hamiltonian $\mathscr{H}_{\text{eff}}$ if $\tau_{\text{tot}} << 2\pi\|\mathscr{H}\|^{-1}$, where $\|\mathscr{H}\|$ is the characteristic strength of the pulse Hamiltonian [72, 74]. In practice, this approximation can often not be applied [74], as it is the case for the pulse sequences introduced in Section 3.4. An elegant solution to overcome this issue is provided by the interaction representation (toggling frame) of the experiment considered.

The toggling frame point of view is based on the possibility to change the frame of reference in which a physical system is looked at, as long as all the physical quantities of the system change accordingly. In the toggling frame point of view, the hard pulses are seen as acting on the internal Hamiltonian $\mathscr{H}_0$. This contrasts with the fixed reference frame, in which the internal Hamiltonian $\mathscr{H}_0$ remains constant and the pulses are viewed as acting on the state of the system. Since the global transformation performed on the system at final time should be independent of the frame of reference in which the system is looked at during the sequence, it is important when working with the toggling frame to make sure that at final time, the frames for each linear droplet of $\mathscr{H}_0$ are rotated back to be aligned with the fixed reference frame.

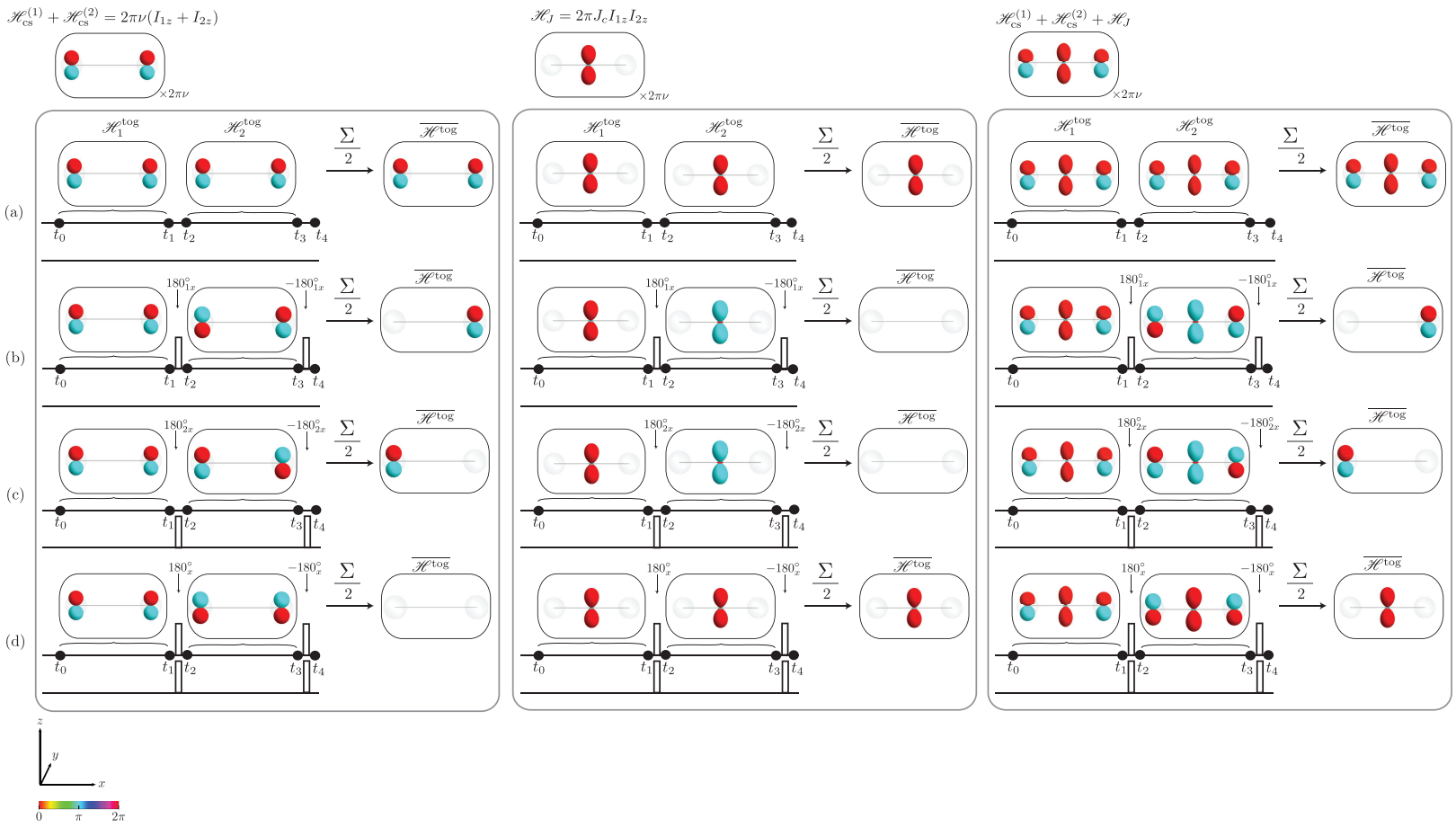

Figure 3.12: DROPS visualization of the Hamiltonian in the toggling frame for the (d) refocusing, (c) decoupling, (b) superposition pulse sequences and (a) the free evolving system, as designed for $\rho(t_0) = I_{1x}$. The time evolution of I_{1x} under these sequences can be found in Fig. 3.8.

3.5.4 Illustration 1: Decoupling and refocusing pulse sequences

In the description of the refocusing and decoupling pulses made in Section 3.4, we explained that the undesired terms created during the first delay and pulse in these sequences were canceled during the second delay and pulse. If the effective Hamiltonian theory is particularly suitable to understand the *global* effect of a pulse sequence, it does not explain the mechanism by which the undesired terms cancel each other. In this regard, the concept of toggling frame provides a suitable tool to understand and illustrate these mechanisms.

The pulse sequences of Fig. 3.8 (refocusing, decoupling and free evolution) are summarized in Fig. 3.12 in which the toggling frame Hamiltonians during the first ($\mathscr{H}_1^{\text{tog}}$) and second ($\mathscr{H}_2^{\text{tog}}$) delays are illustrated.

In addition, the average Hamiltonian in the toggling frame $\overline{\mathscr{H}^{\text{tog}}}$ has been depicted. Using the DROPS representation of these Hamiltonians in the toggling frame point of view, we can now study these sequences with a new eye.

In (d) the refocusing pulse sequence, the bilinear droplet remains intact all along the sequence. The linear droplets however both change signs after the global 180° pulse. On the time evolution of operators, this translates as follows: terms created before the pulse by the linear terms in the Hamiltonian (*i.e.* by the chemical shift Hamiltonian) are also created after the pulse, but with opposite sign. That is, these terms cancel.

In the decoupling pulse sequences (b) and (c), the bilinear droplet changes its sign after the pulse. We now *see* why the terms created by the bilinear part of the Hamiltonian (*i.e.* the coupling term) before the first pulse are canceled by those created afterwards. When the pulses are applied on spin k, the droplet corresponding to this particle also changes its sign after the first pulse and illustrates how the effect of $\mathscr{H}_{\text{cs}}^{(k)}$ is canceled over the whole pulse sequence.

Note that the average Hamiltonians $\overline{\mathscr{H}^{\text{tog}}}$ deduced in the toggling frame are identical to the effective Hamiltonians previously computed.

3.5.5 Illustration 2: Understanding the TOCSY experiment

The TOCSY (TOtal Correlation SpectroscopY) experiment is designed to detect the correlation between all spins of a coupled network [74]. The total Hamiltonian of the system is

$$\mathscr{H} = \mathscr{H}_{\text{cs}} + \mathscr{H}_J, \tag{3.11}$$

where the coupling Hamiltonian $\mathscr{H}_J = \mathscr{H}_{\text{iso}} = 2\pi J(I_{1x}I_{2x} + I_{1y}I_{2y} + I_{1z}I_{2z})$ corresponds to isotropic couplings between the connected spins. The time evolution of the initial state $\rho(t_0) = I_{1x}$ under the isotropic coupling Hamiltonian alone is found in Fig. 3.5 (b) and is the mechanism we seek to exploit to detect the correlation between the coupled spins. We see indeed that there is magnetization transfer between the linear droplets which are coupled together. However, since $\mathscr{H}_{\text{cs}}$ and $\mathscr{H}_J$ do not commute, the chemical shift Hamiltonian interferes with the process we are interested in, *i.e.* maximizing the magnetization transfer between coupled spins. To address this issue, a simplified version of the TOCSY experiment is implemented by juxtaposing many refocusing pulse sequences, as illustrated in Fig. 3.13. For short[1] durations τ, the chemical shift Hamiltonian $\mathscr{H}_{\text{cs}}$ has

[1] if $2\tau << \|\mathscr{H}_{\text{cs}} + \mathscr{H}_J\|^{-1}$

then a negligible effect on the time evolution of the system and the effective Hamiltonian $\mathscr{H}_{\text{eff}}$ corresponding to the sequence is to a good precision approximated by $\mathscr{H}_{\text{eff}} \cong \mathscr{H}_{\text{iso}}$.

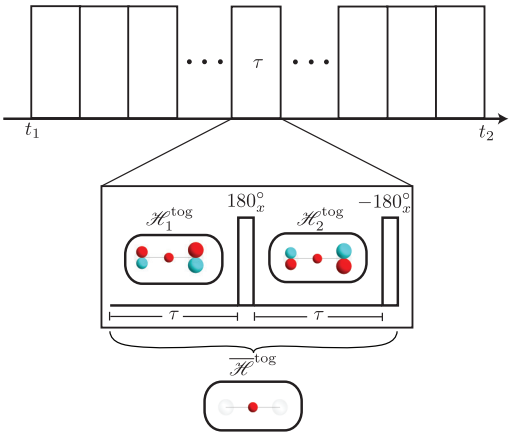

Figure 3.13: Visualization of a simplified version of the TOCSY experiment implemented as a succession of refocusing pulse sequences. Here, a second 180° pulse has been added in the refocusing sequence to make sure that the toggling frames are aligned with the fixed reference frame after each refocusing sequence.

3.6 Coherence order, phase cycling and gradient pulses

3.6.1 Coherences

Multiple quantum coherences play an important role in NMR spectroscopy. Aside from their physical interpretation [68], their periodicity properties make them tractable and easy to select as measurable information in experiments. As already stated in Section 2.5.5 of Chapter 2, operators A_p of multiple quantum coherence order $p \in \mathbb{N}$ are invariant under global z rotations up to a phase factor: [8]

$$\mathrm{e}^{-i\alpha\mathcal{R}_z} A_p \, \mathrm{e}^{i\alpha\mathcal{R}_z} = \mathrm{e}^{-ip\alpha} A_p, \tag{3.12}$$

where $\mathcal{R}_z := \sum_{k=1}^{n} I_{kz}$. This periodicity property is nicely captured in their corresponding DROPS representation, as illustrated in Fig. 2.5 (of Chapter 2) and Fig. 3.14 below. Each droplet of a coherence A_p is symmetric with respect to *any* z rotation and thus has the shape of a solid of revolution about the z axis. Then, for each layer corresponding to a fixed z value, the phase is uniformly distributed about the z axis with periodicity p, *i.e.* all the phase values from 0 to 2π are scanned exactly $|p|$ times, anti-clockwise if $p > 0$ and clockwise if $p < 0$ (when looking toward the $-z$ direction).

Multiple quantum coherences are then good candidates concerning signal manipulation in experiments, since we do have the possibility to influence the phase of operators over the course of a given experiment. A fundamental example which bears witness to the need of coherence manipulation comes about from a limitation inherent to NMR spectroscopy. Spectrometers detect the presence of linear pure quantum coherences of order $p = -1$ only. Accordingly, if we are interested in measuring the presence of a coherence operator $A'_{p'}$ of order $p' \neq -1$, the experiment must be designed such that the operators $A'_{p'}$ get fully or partly *transferred* in a measurable pure quantum operator

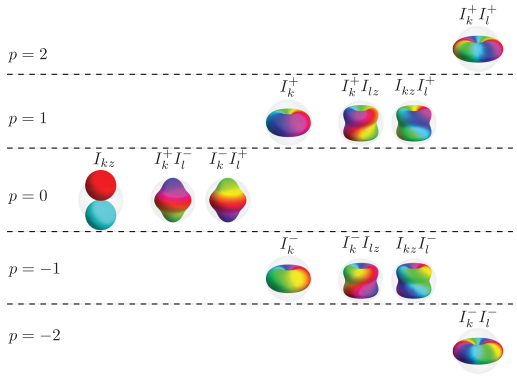

Figure 3.14: DROPS visualization of the characteristic droplets for multiple quantum operators in a system of two spin-1/2 particles.

A_{-1}. Moreover, the experiment should ideally be designed such that only the signal coming from $A'_{p'}$ is measured, and not that from other operators.

Coherence transfer pathways

The coherences which are created at each step of a pulse sequence can be represented by a coherence pathway diagram as in Fig. 3.15. We see with such a diagram that one pulse may convert, or *transfer*, one coherence A_p into a linear combination of many other coherences $A'_{p_1}, A'_{p_2}, \cdots$.

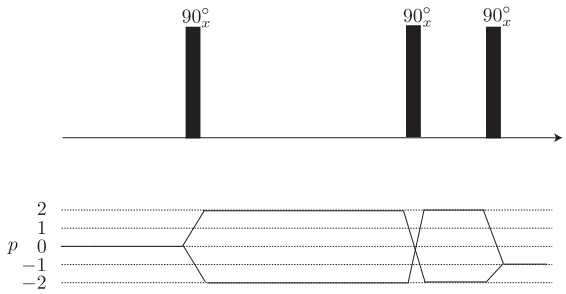

Figure 3.15: Coherence transfer pathways generated by the DQF COSY experiment (Figure borrowed from [68]).

As discussed above, in many experiments we are interested in selecting one specific transfer, *e.g.* $A_p \longrightarrow A'_{p_2}$, and the signals coming from the other coherences $A'_{p'}$ are undesirable. The challenge is then to design experiments which preserve the signals resulting from a defined coherence transfer pathway, and average out the signals generated by all other pathways. We present now two principal concepts arising in the design of such experiments, the phase cycling and the gradient pulse strategies, which both rely on a clever phase manipulation of coherences to take advantage of their periodicity.

3.6.2 Phase cycling

A phase cycling experiment is defined by a family of pulse sequences $\mathrm{P}_0, \mathrm{P}_1, \ldots$, which differ from one another by the phase of some pulses in the sequences and/or the phase of the receiver. The phase changes in the pulses (or the change of the receiver phase) are chosen such that the coherence transfer we wish to observe is preserved whereas all the other coherences are dephased. To illustrate the situation, let P_0 be an initial pulse and A_p be a coherence of order p. Under the pulse P_0, A_p is transformed as

$$A_p \xrightarrow{\mathrm{P}_0} A'_{p'} + A'',$$

where $A'_{p'}$ is the coherence we aim at preserving and A'' is the linear combination of all the other undesired created coherences. The coherence transfer to be selected is $A_p \longrightarrow A'_{p'}$. To select $A'_{p'}$, the phase cycle should be designed such that each pulse $\mathrm{P}_0, \mathrm{P}_1, \ldots$ in the cycle preserves $A'_{p'}$ whereas the undesired coherences in A'' experience phase changes. As a result, when all the data are summed up, all the undesired coherences should be dephased and cancel out and the ones associated with A_p should sum up.

Let us derive the appropriate phase cycling pattern which suits our needs. The transformation of A_p under the first pulse P_0 satisfies

$$A_p \longrightarrow U_0 A_p U_0^{-1} = A'_{p'} + A'',$$

where U_0 is the propagator associated with P_0. Consider now the effect of the same pulse, the phase of which is shifted by an angle α. The corresponding propagator is $U_\alpha = \mathrm{e}^{-i\alpha\mathcal{R}_z} U_0 \mathrm{e}^{i\alpha\mathcal{R}_z}$ and has the following effect on A_p:

$$\begin{aligned} A_p \xrightarrow{\mathrm{P}_1} U_\alpha A_p U_\alpha^{-1} &= \mathrm{e}^{-i\alpha\mathcal{R}_z} U_0 \cdot \mathrm{e}^{i\alpha\mathcal{R}_z} A_p \exp^{-i\alpha\mathcal{R}_z} \cdot U_0^{-1} \mathrm{e}^{i\alpha\mathcal{R}_z} \\ &= \mathrm{e}^{ip\alpha} \times \mathrm{e}^{-i\alpha\mathcal{R}_z} \cdot U_0 A_p U_0^{-1} \cdot \mathrm{e}^{-i\alpha\mathcal{R}_z} \\ &= \mathrm{e}^{ip\alpha} \times \mathrm{e}^{-i\alpha\mathcal{R}_z} (A'_{p'} + A'') \mathrm{e}^{-i\alpha\mathcal{R}_z} \\ &= \mathrm{e}^{ip\alpha} \times \left(\mathrm{e}^{-ip'\alpha} A'_{p'} + A''' \right) \\ &= \mathrm{e}^{-i(p'-p)\alpha} A'_{p'} + \mathrm{e}^{ip\alpha} A''', \end{aligned} \tag{3.13}$$

where the periodicity property (Eq. (3.12)) of the quantum operators A_p and $A'_{p'}$ has been exploited to obtain the second and last equalities respectively.

We can now modify the phase of operators present after a pulse by shifting by an angle φ_{rec} the phase of the receiver. We can schematically represent the receiver phase change as a multiplication of the operators by $\mathrm{e}^{-i\varphi_{\mathrm{rec}}}$. That is, the change of the receiver phase after the above pulse P_1 (see Eq. (3.13)) results in

$$A_p \xrightarrow{\mathrm{e}^{-i\varphi_{\mathrm{rec}}}\mathrm{P}_1} \mathrm{e}^{-i[\varphi_{\mathrm{rec}} + \Delta p\alpha]} A'_{p'} + \mathrm{e}^{i(-\varphi_{\mathrm{rec}} + p\alpha)} A''', \tag{3.14}$$

where $\Delta p = p' - p$ denotes the coherence difference. We then see that to preserve the coherence transfer $A_p \longrightarrow A'_{p'}$, the receiver phase should be set to [68]

$$\varphi_{\mathrm{rec}} = -\Delta p \alpha.$$

It is actually known [68] that phase cycles which consist of N evenly distributed angles

$$\alpha_k := k\frac{2\pi}{N}, \quad k = 0, 1, \ldots, N-1, \tag{3.15}$$

together with the phase cycle pattern

$$\varphi_{\text{rec}}^{(k)} = -m\alpha_k \tag{3.16}$$

exactly preserve the coherence transfers $A_p \longrightarrow A'_{p'}$ satisfying

$$\Delta p = m + Nx, \qquad x = 0, \pm 1, \pm 2, ... \tag{3.17}$$

and average out all the other coherence transfers. We can interpret the roles of the phase cycle and the receiver phase pattern as follows: the phase cycle in Eq. (3.15) is characterized by its number of steps and defines the *distance* between the selected coherence differences, whereas the receiver phase determines which Δp in particular has to be selected. The case where the receiver phase is not modified corresponds to $m = 0$ in Eq. (3.16). In this case, the coherence differences which are selected are $\Delta p = Nx$, $x = 0, \pm 1, \pm 2$,... In particular, we see that $\Delta p = 0$ is always selected by such a phase cycle and that if Δp is selected then so is $-\Delta p$.

Illustrations

The previous reasoning can be visualized using the DROPS visualization of coherences as in Fig. 3.16. In this figure, the DROPS visualization of coherence operators A_p for $p = 1, 0, -1$ is plotted in column (a). The operators resulting in 45°_α pulses about the $x, y, -x$ and $-y$ axes on the A_p operators are plotted in column (b) and their decomposition in terms of coherences is illustrated in the tables of column (c). In particular, column (c) corresponds to the decomposition appearing on the right-hand side of Eq. (3.13). The four rotations correspond to a phase cycle as in Eq. (3.15) with $N = 4$, *i.e.* $\alpha = 0, \frac{\pi}{2}, \pi$ and $\frac{3\pi}{2}$ respectively. Columns (d) and (e) show the effect of an additional receiver shift pattern equal to $\varphi_{\text{rec}} = 0, \pi, 0, \pi$ (from top to bottom) on operators in columns (b) and (c) respectively. On the bottom row, the result of averaging the operators obtained by the phase cycle is shown.

Given a coherence transfer $A_p \longrightarrow A'_{p'}$, the average effect of the above phase cycle $A'_{p'}$, without a receiver phase change, corresponds to the selection Eq. 3.17 where $m = 0$ and $n = 4$. Explicitly,

$$\frac{1}{4}\left(\mathrm{e}^{-i\Delta p 0} + \mathrm{e}^{-i\Delta p \frac{\pi}{2}} + \mathrm{e}^{-i\Delta p \pi} + \mathrm{e}^{-i\Delta p \frac{3\pi}{2}}\right) A'_{p'},$$

where we used Eq. (3.13) four times, for the four values of α. It is readily verified that the possible coherence differences are $\Delta p = 0, \pm 1, \pm 2$ and that the result of the above equation is different from zero only for $\Delta p = 0$. This can be seen in Fig.3.16, on the last row of column (c). The coherence terms which did not cancel over the cycle are A'_1 obtained from A_1, A'_0 from A_0 and A'_{-1} from A_{-1}.

Considering now the phase cycle with the receiver phase shifts $\varphi_{\text{rec}} = 0, \pi, p, \pi$, we see with Eq. (3.16) that $\varphi_{\text{rec}}^{(k)} = 2\alpha_k$ and the coherence differences selected should be of the form $\Delta p = -2 \pm 4x$, $x = 0, \pm 1, \pm 2, \ldots$ Explicitly, we deduce from Eq. (3.14) that the average effect of the four-step cycle on $A'_{p'}$ is now

$$\frac{1}{4}\left(\mathrm{e}^{-i[\Delta p 0 - 0]} + \mathrm{e}^{-i[\Delta p \frac{\pi}{2} - \pi]} + \mathrm{e}^{-i[\Delta p \pi - 0]} + \mathrm{e}^{-i[\Delta p \frac{3\pi}{2} - \pi]}\right) A'_{p'}.$$

We verify that, as expected, the only values of Δp for which this expression is not zero are $\Delta p = \pm 2$, which can be seen on the last row of column (e) in Fig. 3.16. The coherence

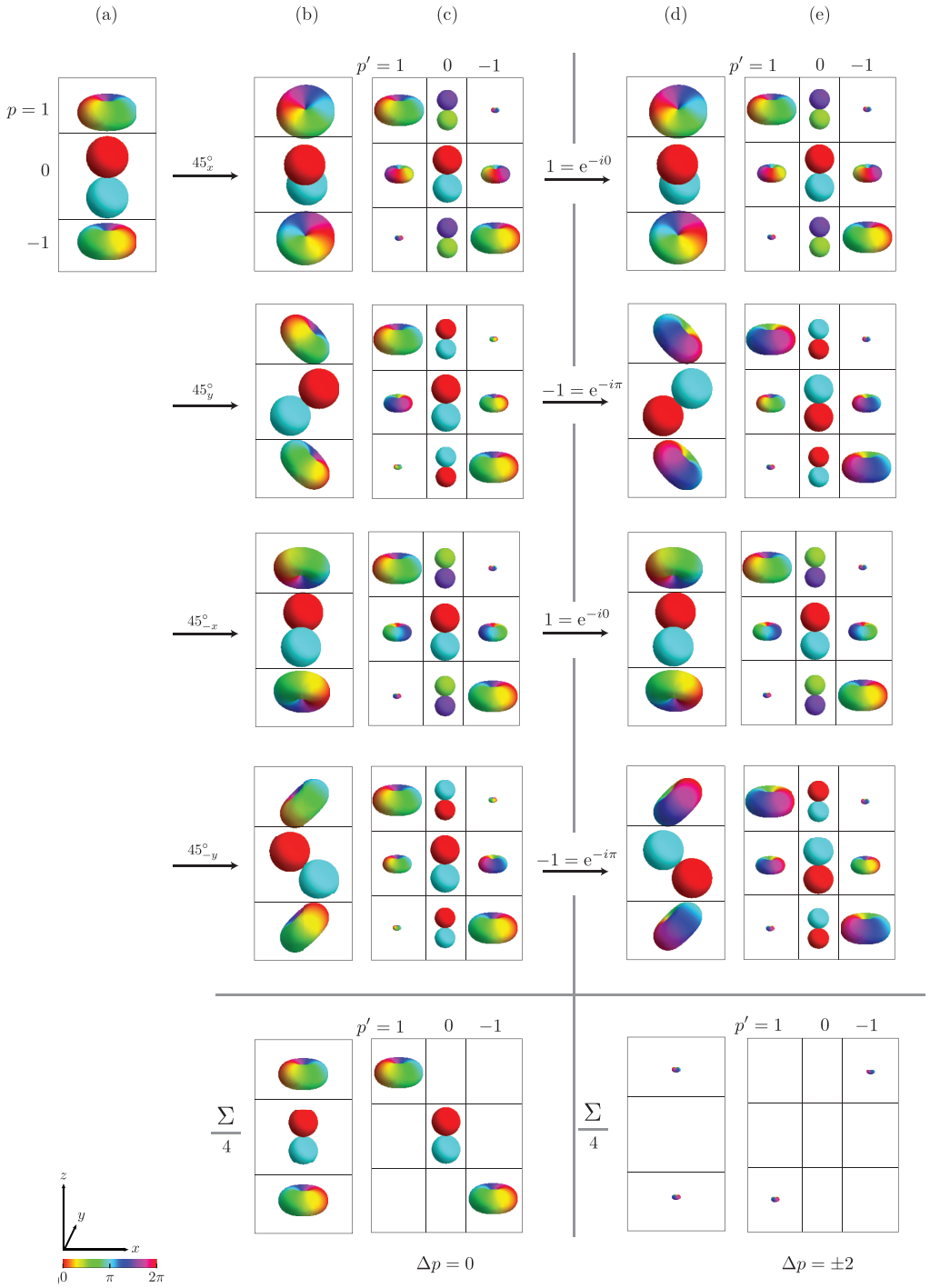

Figure 3.16: (Caption next page.)

Figure 3.16: (Previous page.) Illustration of a phase cycling sequence over a 45°_α pulse the phase of which is taken to be $\alpha = 0, \frac{\pi}{2}, \pi$ and $\frac{3\pi}{2}$. Column (a) shows the DROPS representation of coherences A_p with $p = 1, 0, -1$. In the case of a single-spin system for instance, these coherences correspond to the operators $A_1 = I^+$, $A_0 = I_z$ and $A_-1 = I^-$. Column (b) shows the effect of the four 45°_α pulses on the operators A_p and column (c) shows their decomposition in terms of coherences $A'_{p'}$ for $p' = 1, 0, -1$. The average operators obtained over the cycle appear on the bottom row. Likewise, column (d) shows the effect of the four 45°_α pulses together with receiver phase shifts $\varphi_{\rm rec} = 0, \pi, 0, \pi$ (rows one to four) and their decomposition in terms of coherences appears in column (e). The average operators obtained over the full cycle appear on the bottom row.

terms which are not canceled by the phase cycle are A'_1 obtained from A_{-1} and A'_{-1} from A_1.

The effect of this phase cycle, with and without receiver phase shifts, is also illustrated in Fig. 3.17 and Fig. 3.18 in which the cycle is considered for a 90° and a 180° pulse respectively. These figures differ from Fig. 3.16 presented above by the amount of transfer from A_p to $A'_{p'}$ before and after the pulse. For the 90° pulse (Fig. 3.17), there is no transfer $A_0 \longrightarrow A'_0$ whereas only transfers from A_p to A'_{-p} are created by the 180° pulse (Fig. 3.18). The coherence transfers which are selected by the phase cycle are then subsets of those for the 45° pulses.

Another example of phase cycling is illustrated in Fig. 3.19, in which the coherence operators take the values $p = -2, -1, 0, 1, 2$. The structure of this figure is similar to the previous one and the reader is invited to refer to the above discussion for explanations of the figure configuration. The phase cycle affects 45°_α pulses, the phases of which are taken as before to be $\alpha = 0, \frac{\pi}{2}, \pi$ and $\frac{3\pi}{2}$ (corresponding to $x, y, -x, -y$ rotation axes respectively). The average effect of this sequence, without receiver shifts, was presented in Eq. (3.6.2). In this case, Δp can take the values $0, \pm1, \pm2, \pm3, \pm4$ and we verified with Eq. (3.17) that coherence transfers with $\Delta p = 0$ and $\Delta p \pm 4$ are preserved by this sequence, which is what is actually seen on the bottom row of Fig. 3.19.

This time, the receiver phase pattern is taken to be $\varphi_{\rm rec} = 0, \frac{\pi}{2}, \pi, \frac{3\pi}{2}$, which corresponds to $m = -1$ in Eq. (3.16). Accordingly, the phase cycle selects coherence transfers satisfying $\Delta p = -1 \pm 4x$, $x = 0, \pm1, \pm2, \ldots$, where $4 = N$ is the number of steps in the cycle. When we explicitly compute the average effect of the four-step phase cycle on $A'_{p'}$ using Eq. (3.14), we find

$$\frac{1}{4}\left(\mathrm{e}^{-i[\Delta p 0 + 0]} + \mathrm{e}^{-i[\Delta p \frac{\pi}{2} + \frac{\pi}{2}]} + \mathrm{e}^{-i[\Delta p \pi + \pi]} + \mathrm{e}^{-i[\Delta p \frac{3\pi}{2} + \frac{3\pi}{2}]}\right) A'_{p'}.$$

As expected, coherence transfers selected by the phase cycle together with this receiver shift pattern are those for which $\Delta p = -1$ and $\Delta p = -1 + 4 = 3$.

Finally, note that phase cycling can be considered as a filtering technique for coherences. That is, the coherences $A'_{p'}$ which are selected by a phase cycle from the coherence A_p are present in each individual experiment (including the receiver phase) in the cycle. On Figs. 3.16, 3.17, 3.18 and 3.19, this amounts to say that the operators in the last rows of columns (c) and (d) are present in each individual step (row) of the corresponding column, where A_p are the operators in column (I).

3.6.3 Gradient pulses

Coherence order selection, or coherence transfer selection, can also be achieved using gradient pulses. Like for the rf-pulses, gradient pulses are created by the application

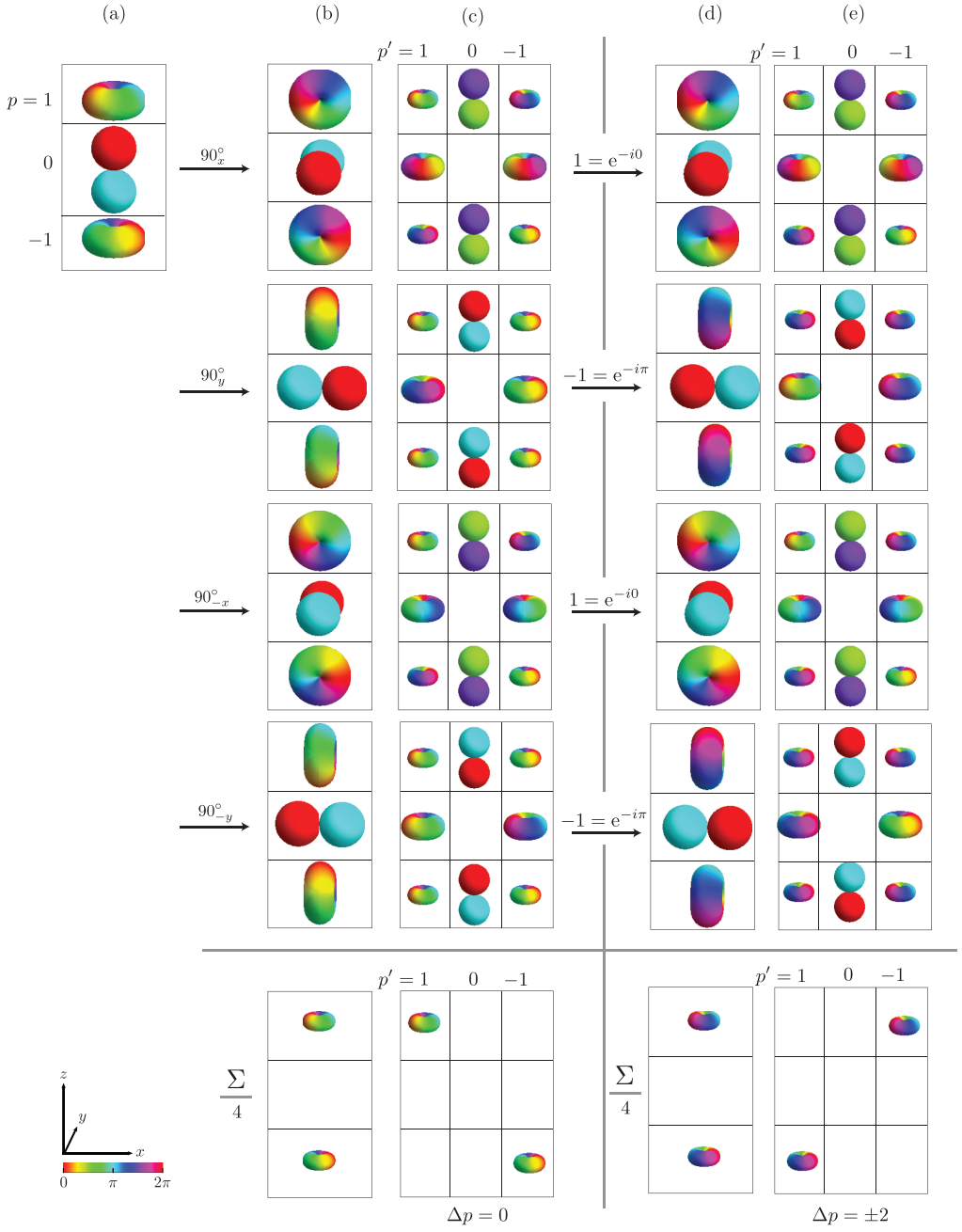

Figure 3.17: Illustration of a phase cycling sequence over a 90°_α pulse the phase of which is taken to be $\alpha = 0, \frac{\pi}{2}, \pi$ and $\frac{3\pi}{2}$. See the caption of Fig. 3.16 for the details on the structure of this figure.

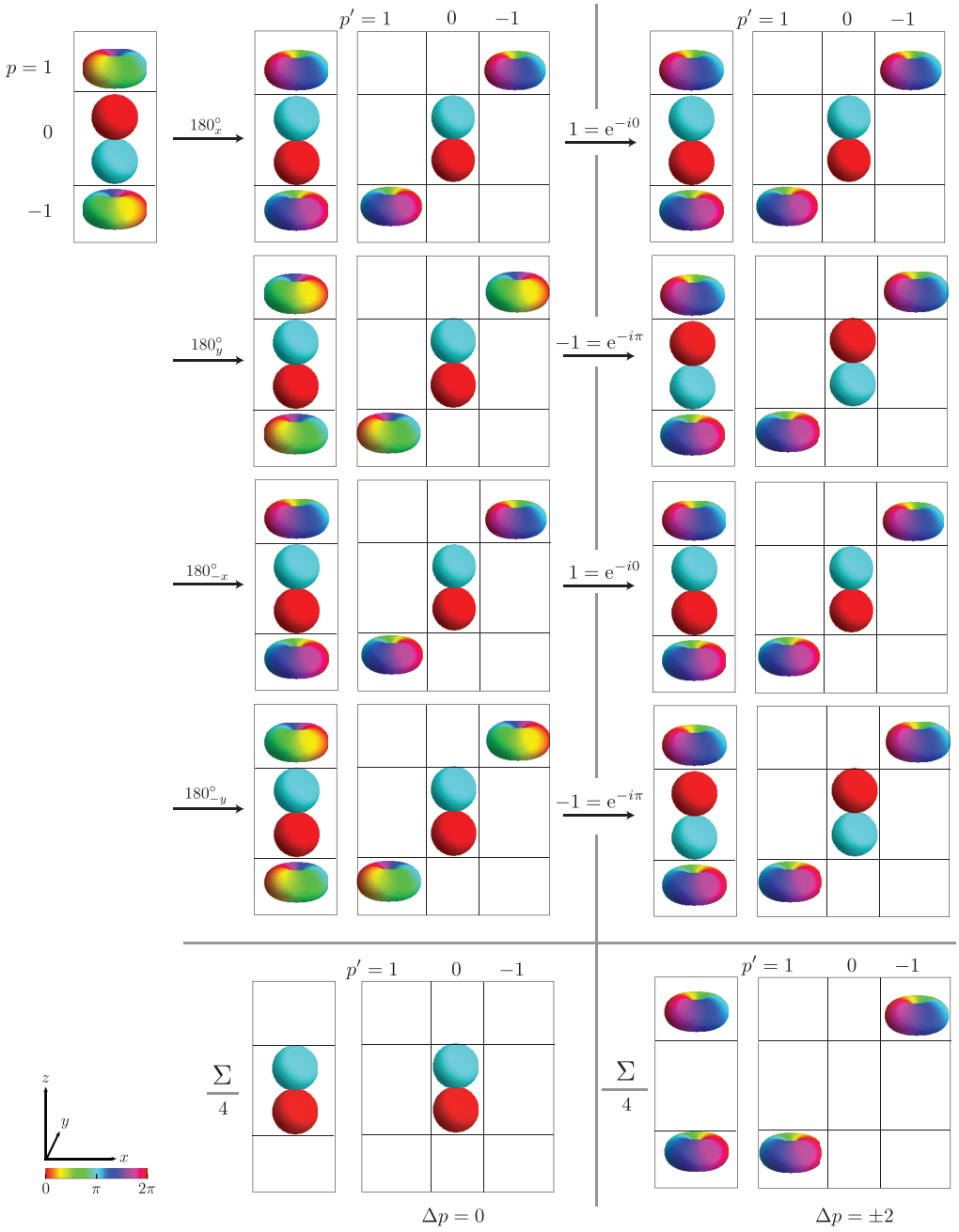

Figure 3.18: Illustration of a phase cycling sequence over a 180°_α pulse the phase of which is taken to be $\alpha = 0, \frac{\pi}{2}, \pi$ and $\frac{3\pi}{2}$. See the caption of Fig. 3.16 for the details on the structure of this figure.

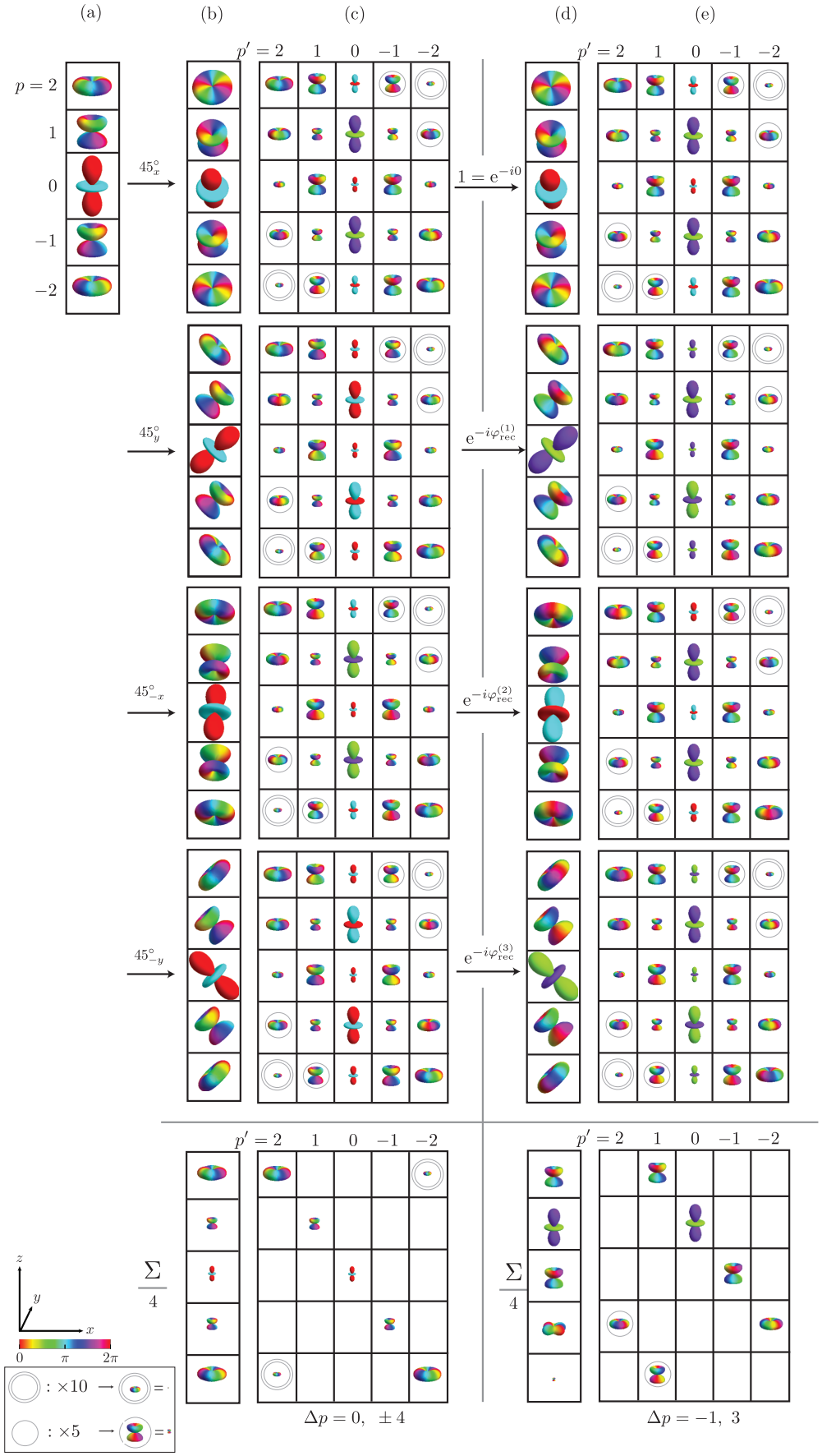

Figure 3.19: (Caption next page.)

Figure 3.19: (Previous page.) Illustration of a phase cycling sequence over a 45°_α pulse the phase of which is taken to be $\alpha = 0, \frac{\pi}{2}, \pi$ and $\frac{3\pi}{2}$. Column (a) shows the DROPS representation of coherences A_p with $p = 2, 1, 0, -1, -2$ from top to bottom. Column (b) shows the effect of the four 45°_α pulses on the operators A_p and column (c) shows their decomposition in terms of coherences $A'_{p'}$ for $p' = 2, 1, 0, -1, -2$ (from left to right respectively). The average operators obtained over the cycle appear on the bottom row. Likewise, column (d) shows the effect of the four 45°_α pulses together with receiver phase shifts $\varphi_{\text{rec}} = 0, \frac{\pi}{2}, pi, \frac{3\pi}{2}$ (rows one to four) and their decomposition in terms of coherences appears in column (e). The average operators obtained over the full cycle appear on the bottom row.

of an external magnetic field $\vec{B}_{\text{grad}}$ to steer the system. However, the usefulness of the latter for coherence order selection comes from two major differences with normal rf-pulses: (1) Gradient pulses are oriented along the z axis and (2) are inhomogeneous in space. That is, the magnetic field has the form

$$\vec{B}_{\text{grad}}(x) = Gx\vec{1}_z,$$

where G is the (constant) gradient strength. The amplitude of the field Gx then depends on the position x (distance to the origin) of the particle in the sample, where the origin of the z axis is taken to be at the center of the sample. From point (1), we understand that the effect of a gradient pulse on an operator $\rho(x) = \sum_p c_p A_p$ is to dephase all its coherence components A_p individually, according to the strength of the field at position x. After a time t, coherences with different orders p are dephased by a different z rotation angle

$$\boldsymbol{\phi}(x) = -p \cdot 2\pi\nu_{\text{G}}(x)t, \tag{3.18}$$

where $2\pi\nu_{\text{G}}(x) := -\gamma Gx$. The inhomogeneity of the field (2) is used to average the signal. Its effect is similar to the previously encountered action of phase cycling and averaging the signals, the difference being that all the signals are generated at the same time at different positions x in the sample. Nevertheless, the coherence transfer pathways selected by gradient pulses generally differ from those created by phase cycling.

The only coherence order transitions selected by a single gradient pulse $\mathbf{G}$ are those of the form $A_p \longrightarrow A'_{p'}$ with $p = 0$. To select any other pathway, two gradient pulses $(\mathbf{G}_1, \mathbf{G}_2)$ are required. Indeed, the first pulse $\mathbf{G}_1$ dephases all coherences A_p with $p \neq 0$ initially present in an operator. A second gradient pulse $\mathbf{G}_2$ is then applied after a pulse (or a plus sequence) to rephase the coherences corresponding to the desired transfer.

To understand how $\mathbf{G}_2$ should be defined to select a given coherence transfer from A_p (before the pulse) to $A'_{p'}$ (after the pulse), consider the effect of the first gradient field on the sample. The phase shift experienced by the quantum coherence $A_p(x)$ after the application of $\mathbf{G}_1$ is

$$A_p(x) \overset{\mathbf{G}_1}{\longrightarrow} \mathrm{e}^{i\boldsymbol{\phi}_1(x)} A_p(x). \tag{3.19}$$

Denoting by τ_1 the duration of the pulse and by G_1 its gradient strength, the phase shift $\boldsymbol{\phi}_1(x) := -p \cdot 2\pi\nu_{\mathbf{G}_1}(x)\tau_1 = p\gamma G_1 x\tau_1$ (see Eq. (3.18)) experienced by A_p depends on its coherence order p and its position x. Let now a pulse be applied:

$$\mathrm{e}^{i\boldsymbol{\phi}_1(x)} A_p(x) \overset{\mathscr{H}t}{\longrightarrow} \mathrm{e}^{i\boldsymbol{\phi}_1(x)} \left(A'_{p'}(x) + A''(x) \right), \tag{3.20}$$

where $A'_{p'}$ is the coherence operator we wish to preserve. An important point to underline here is that the presence of the coherence $A'_{p'}$ can be the result of the first gradient pulse, that is, it could be that $A'_{p'}$ is not created from A_p by the rectangular pulse only. Now,

in order to rephase the coherence $A'_{p'}(x)$, we apply a second gradient pulse $\mathbf{G}_2$:

$$\mathrm{e}^{i\boldsymbol{\phi}_1(x)}\left(A'_{p'}(x)+A''(x)\right) \overset{\mathbf{G}_2}{\longrightarrow} \mathrm{e}^{i\boldsymbol{\phi}_1(x)}\left(\mathrm{e}^{i\boldsymbol{\phi}_2(x)}A'_{p'}(x)+A'''(x)\right),$$

where τ_2 is the duration of the second gradient pulse and we used a relation similar to Eq. (3.19). The phase shift introduced by $\mathbf{G}_2$ on $A'_{p'}$ is $\boldsymbol{\phi}_2(x) := p'\gamma G_2 x\tau_2$ and the operators in $A''(x)$ are all further dephased to give $A'''(x)$. We then see that to rephase $A'_{p'}$ (which amount to measuring the coherence transfer $A_p \longrightarrow A'_{p'}$), the two gradient pulses must satisfy

$$\boldsymbol{\phi}_1(x) = -\boldsymbol{\phi}_2(x) \quad \overset{p\neq 0}{\Longrightarrow} \quad \frac{-p'}{p} = \frac{G_1\tau_1}{G_2\tau_2}. \tag{3.21}$$

Note that all coherence transfers $A_{p_1} \longrightarrow A_{p_2}$, $p_1 \neq 0$, satisfying $\frac{-p_2}{p_1} = \frac{-p'}{p}$ are selected by the gradient pair $(\mathbf{G}_1, \mathbf{G}_2)$ according to relation (3.21). Note also that $\mathbf{G}_1$ and $\mathbf{G}_2$ are designed regardless of the pulse applied between them.

The case $p = p' = 0$ is particular. Indeed, in this case, $A_p = A_0$ is invariant (*i.e.* not dephased) under *any* gradient pulse $\mathbf{G}_1$ and similarly, $A'_{p'} = A'_0$ is invariant under *any* gradient pulse $\mathbf{G}_2$. Consequently, coherence transfers $A_0 \longrightarrow A'_0$ are always preserved under any gradient pulse.

Illustration

The action of gradient pulses and the above steps in the design of the gradient pulses $\mathbf{G}_1$ and $\mathbf{G}_2$ can be well visualized through the DROPS representation of operators at each step, as illustrated in Figure 3.20.

In this figure, the two gradient fields $\mathbf{G}_1$ and $\mathbf{G}_2$ considered are identical. Such a pair $(\mathbf{G}_1, \mathbf{G}_2)$ forms a crusher gradient [7]. Columns one and two (resp. three and four) in the figure compare the effect of a 90°_x (resp. 180°_x) pulse without and with crusher gradients on different operators. Rows (a-c) show the effect of the above sequences on pure coherences $A_{-1} := I^-$, $A_0 := I_z$ and $A_{+1} := I^+$ respectively. Rows (d-e) show their effect on operators $I_x := \frac{I^+ + I^-}{2}$ and $I_y := \frac{I^+ - I^-}{2i}$, which are a mix of coherence operators A_1 and A_{-1}. The points in space x where the effects of $\mathbf{G}_1$ and $\mathbf{G}_2$ are illustrated are chosen such that the operators undergo a total global rotation of $\pi/2, \pi, \frac{3\pi}{2}$ and 2π at these positions in the sample.

According to Eq. (3.21), coherence transfers which are selected by crusher gradients are $A_p \longrightarrow A'_{p'}$ with $p' = -p$. In the present case, these correspond to the transfers

p	p'
$+1$	-1
-1	$+1$
0	0.

(3.22)

Figure 3.20: (Next page.) Illustration of coherence transfer selection by means of gradient fields. The first and second columns compare the averaged signals of an experiment consisting of a 180°_x pulse, without and with gradient fields respectively. The third and fourth columns compare the averaged signals of an experiment consisting of a 90°_x pulse, without and with gradient fields respectively. The effect of each of these pulse sequences is illustrated by plotting the time evolution of the initial operators $\rho(t_0) =$ (a) I^-, (b) I^+, (c) I_z, (d) I_x and (e) I_y at key times. Here, ρ denotes the density operator terms. The initial and final operators are marked with gray boxes.

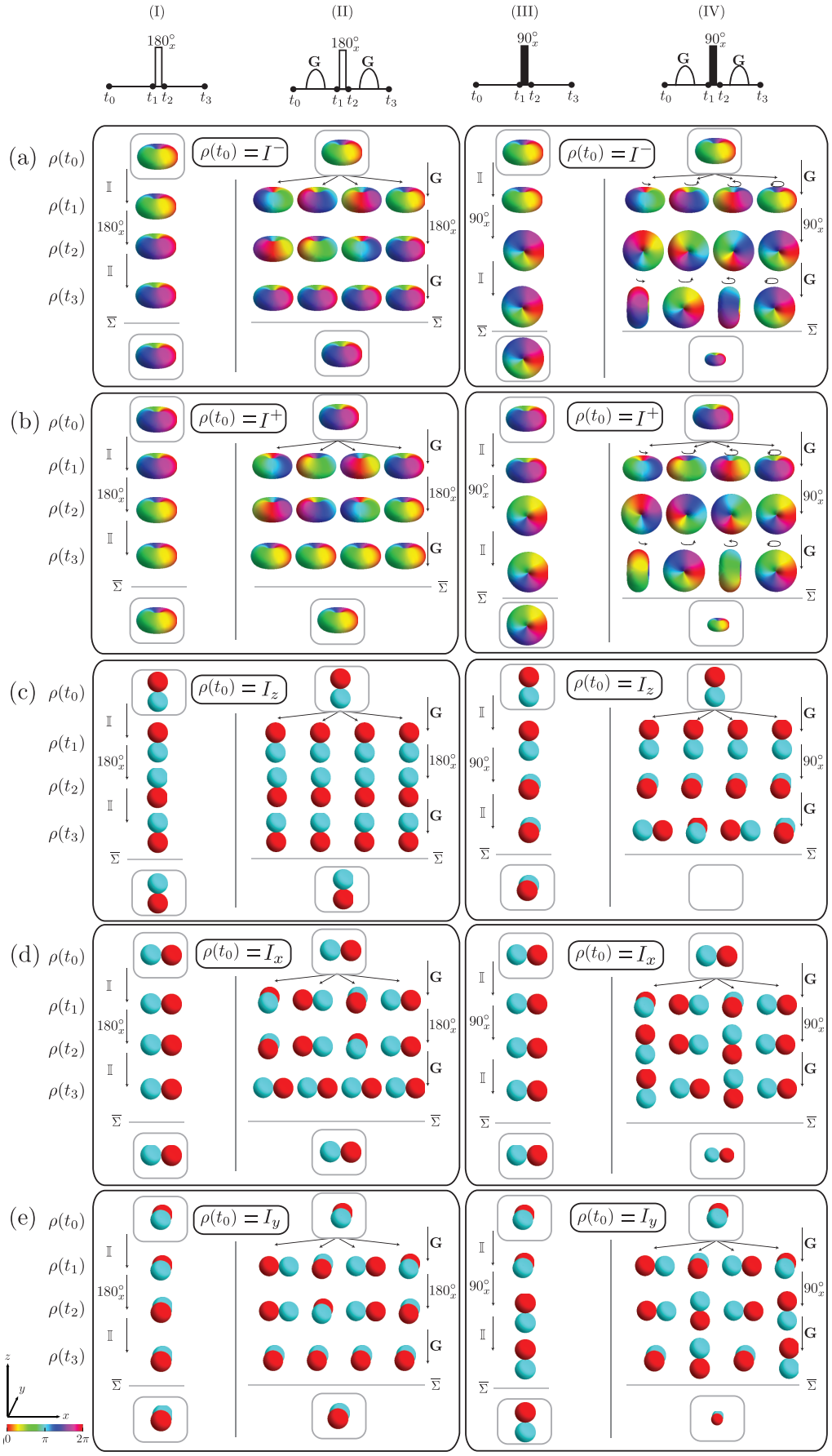

Figure 3.20: (Caption previous page.)

In the case of the 180°_x pulse, we see in Fig. 3.20 (first column) that the pulse itself selects the coherence transfers of Table (3.22) and the presence of the gradient fields (second column) does not affect the result of the experiment. Nevertheless, column two furnishes good examples to understand the effect of gradients on operators and how they work together to build the final desired coherence.

In the case of the 90°_x pulse, the presence of the crusher gradients (last column) makes a notable difference in the averaged signal in comparison to the pulse without gradients (column three). As expected, regardless of the operator obtained without gradients, the averaged operator with gradients does result in a desired transfer in Table (3.22).

We discussed earlier in the text (below Eq. (3.20)) the fact that the presence of the first gradient pulse $\mathbf{G}_1$ may be responsible for the creation of coherence transfers which would not have been created otherwise. This point is illustrated with the 90°_x pulse on the operator I_y (row (e)). Without gradients (column three), the coherence transfers created by the pulse are $A_{\pm 1} \longrightarrow A_0$, none of which corresponds to a transfer in Table (3.22). Nevertheless, in the presence of crusher gradients, the transfers $A_{\pm 1} \longrightarrow A_{\mp 1}$ are created. This example illustrates the importance of not seeing the action of gradients as a simple filter, but as a mechanism in itself to create and select the desired coherence transfers. Other insightful examples of this are those corresponding to the initial operators (c) $\rho_(t_0) = I_z$ and (d) $\rho(t_0) = I_x$. In the case (c) $I_z = A_0$, the coherence transfer $A_0 \longrightarrow A'_0$ in Table (3.22) is not created by the single 90°_x pulse (column three) but cannot be created by using the gradients either, resulting in a vanishing average signal (column four). In the case (d) $\rho_(t_0) = I_x = A_{+1} + A_{-1}$, the coherence transfers $A_{\pm 1} \longrightarrow A_{\mp 1}$ is maximal in the pulse without gradients (column three) and the presence of the gradients reduces the signal to half of what it was without them. The desired coherence transfer in Eq. (3.22) are nevertheless selected.

3.6.4 Phase cycling *versus* gradient pulses

The phase cycling and gradient pulse techniques to select coherence transfers obviously present similarities. The two methods exploit the same idea of manipulating the phase of coherences, either by changing the pulses and receiver phases in a phase cycle or by using a field oriented along the z-axis in the case of the gradient pulses. Furthemore, both tools rely on signal averaging, either on a cycle of pulses or on the different signals created in the sample respectively, to select the desired coherence transfers. Nevertheless, the two approaches do not select the same families of coherence transfers. That is, if $A_p \longrightarrow A'_{p'}$ is selected by both methods, phase cycling will select the family of transfers $A_{p_1} \longrightarrow A'_{p_2}$ for which $p_2 - p_1 = p' - p$ whereas gradient pulses will select the family for which $\frac{-p_2}{p_1} = \frac{-p'}{p}$.

The coherence transfers selected by each method can be summarized by a simple rule in terms of the coherence difference Δp. In the case of phase cycling, we already discussed the fact that as N-step cycle $\{\alpha_k\}$ defined as in Eq. (3.15) selects coherence transfers satisfying $\Delta p = m + Nx$, $x = 0, \pm 1, \pm 2, \ldots$, where m is defined by the receiver phase when set to $\varphi^{(k)}_{\text{rec}} = -m\alpha_k$. On the other hand, gradient pulses $(\mathbf{G}_1, \mathbf{G}_2)$ select coherence transfers $\Delta p = (r-1)p$, where $r = \frac{p'}{p} = -\frac{G_1}{G_2}$.[2] The difference between the coherence transfers selected by four-step phase cycles and gradient pulses for $p, p' \in$

[2] $\frac{-p'}{p} = \frac{G_1}{G_2} \Longrightarrow p' = -\frac{G_1}{G_2} p \Longrightarrow p' - p = p(-\frac{G_1}{G_2} - 1) = p(r-1)$.

$\{-2,-1,0,1,2\}$ is illustrated in Fig. 3.21.

In Figs. 3.22 and 3.23, we take advantage of the DROPS visualization of operators to compare both methods. Figure 3.22 compares the two methods for an initial state $\rho(t_0) = I^+$ and a 90° pulse. In row (a), each step is mathematically indicated and schematically represented, whereas row (b) of this figure compares the two methods using the symbolical representation of the steps only. In Fig. 3.23, 90° and 180° pulses are considered, in columns (I-II) and (III-IV) respectively. Columns (II) and (IV), representing the gradient pulses, are identical to those of Fig. 3.20. Columns (I) and (III), representing the phase cycling, show the effect of the phase change in the pulse and the phase change of the receiver.

Since the possible coherences are $p = 0, \pm 1$, the two methods almost select the same family of transfers. The phase cycle selects the transfers $A_p \longrightarrow A'_{p'}$ for $\Delta p = \pm 2$ whereas the crusher gradients select transfers satisfying $\Delta p = -2p$. The difference between the two families is visible for the 90° pulse applied on $\rho(t_0) = I_{1z}$ (row (c), columns (I) and (II)). In this case, the phase cycle cannot select the transfer $A_0 \longrightarrow A'_0$ since $\Delta p \neq \pm 1$, which results in a signal averaging to zero (in column (I)). On the other hand, since $p = p' = 0$ satisfies $\Delta p = -2p = -2 \cdot 0$, there is selection of this pathway and the averaged signal using the crusher gradients does not cancel (column (II)). The selection of the other pathways is identical, but the steps by which the operator phases are altered differ.

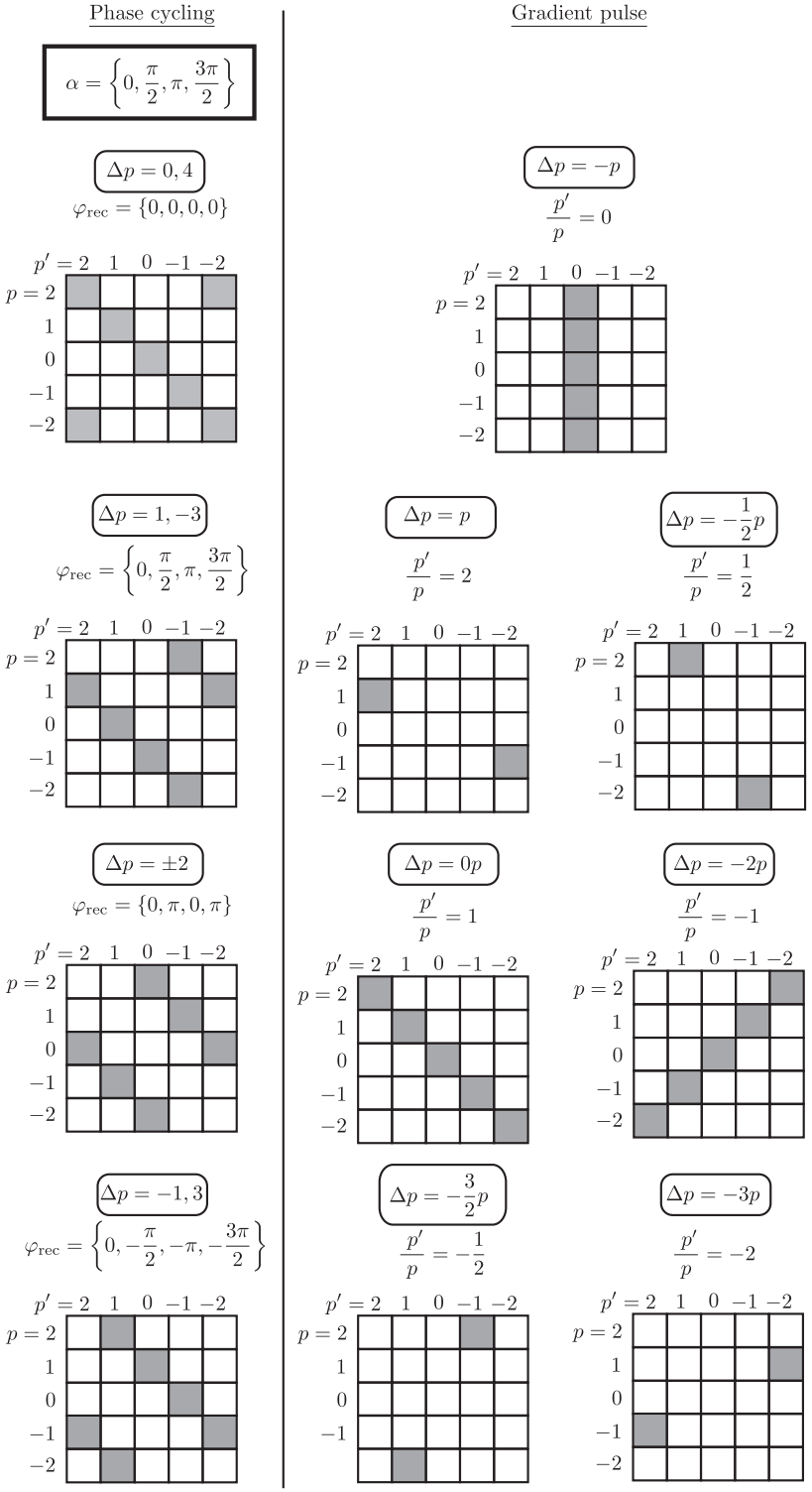

Figure 3.21: Comparison of the transfer pathways selected by a four-step phase cycle (on the left) and gradient pulses (on the right).

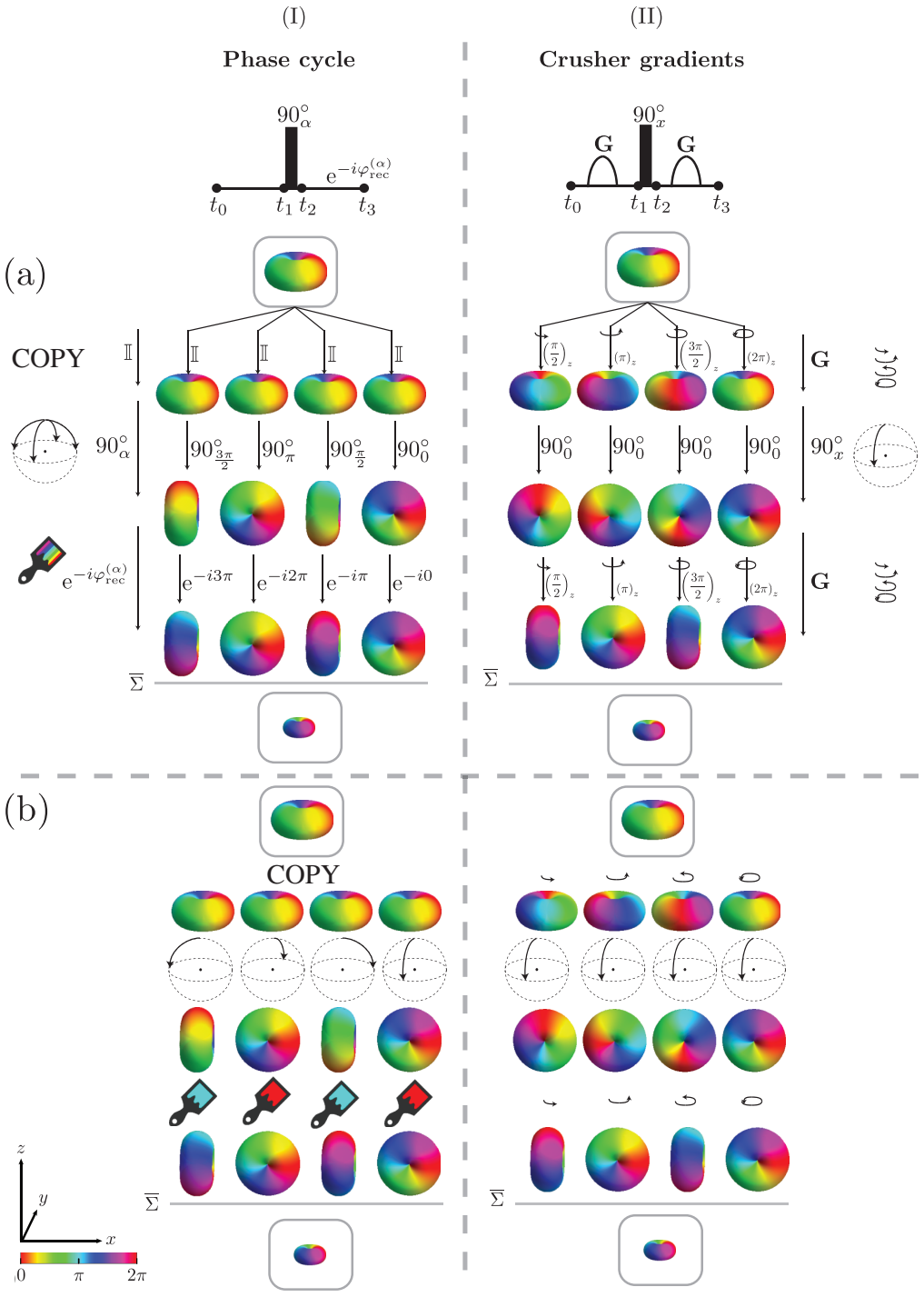

Figure 3.22: Comparison of the different steps taken in a phase cycle (column (I)) and in a pulse gradient experiment (column (II)). On row (a), the steps are explicitly indicated for the two methods and are additionally represented by a symbol in the margins. On row (b), the different steps are schematically illustrated by their symbolical representation only.

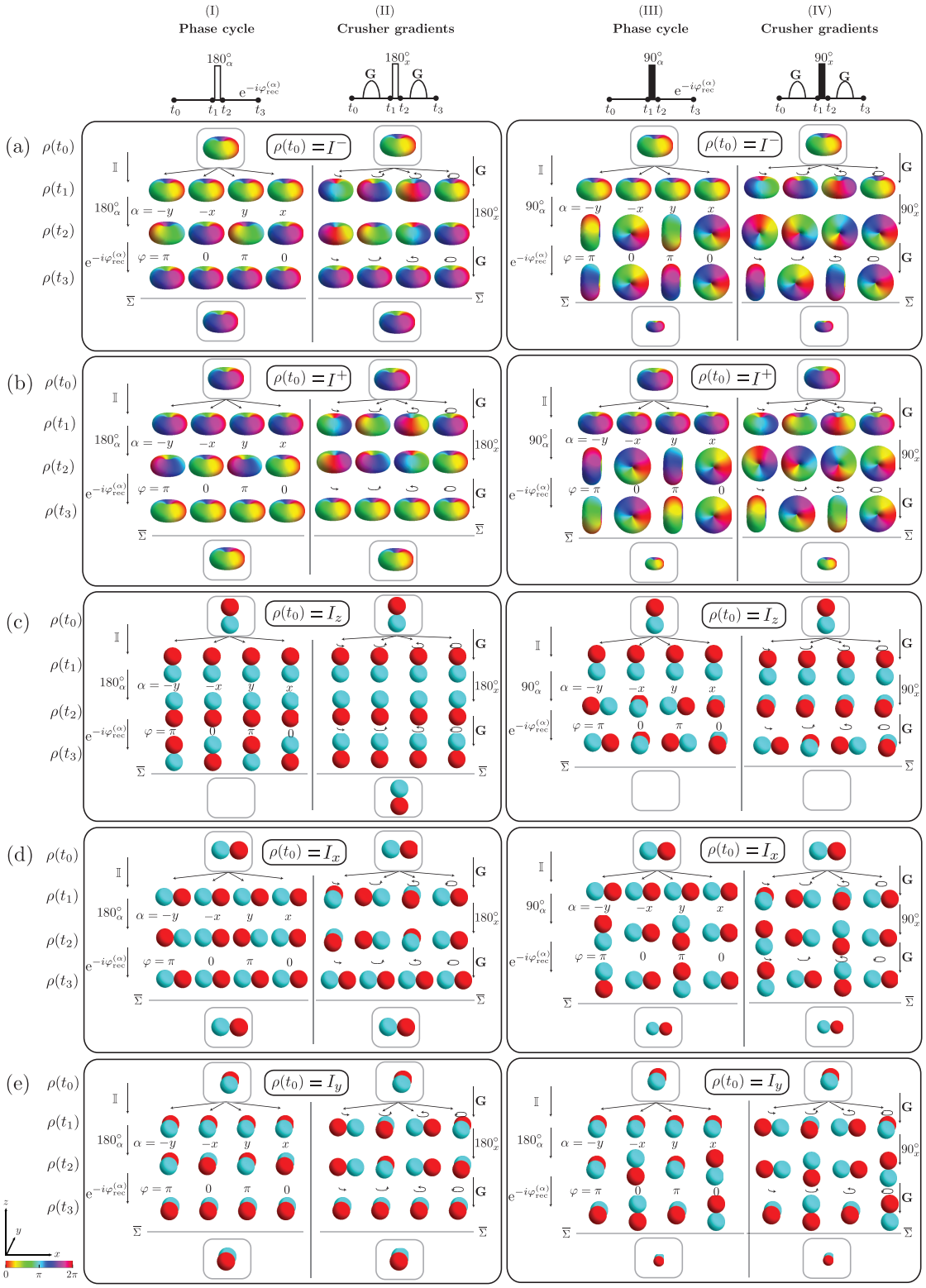

Figure 3.23: (Caption next page.)

Figure 3.23: (Previous page.) Comparison of the transfer pathways selected by the phase cycle presented in Figs. 3.17 and 3.18 with those selected by means of crusher gradients, for 180° (first two columns) and 90° pulses (last two columns). The effect of each method is illustrated at four key times. The initial operator and the final averaged operator are highlighted with gray rounded boxes. Operators considered are $\rho(t_0) =$ (a) $A_{-1} = I^-$, (b) $A_1 = I^+$, (c) $A_0 = I_z$, (d) $\frac{I^+ + I^-}{2} = I_x$ and (e) $\frac{I^+ - I^-}{2i} = I_y$.

3.7 Conclusion

In this chapter, we made use of the DROPS visualization of operators to present and explain fundamental concepts of NMR spectroscopy. In most of the cases, using the DROPS visualization made possible a discussion on the ideas involved without going too deeply into technical details. This underlines the potential of this visualization technique as an effective communication tool, which despite its apparent simplicity, transmits essential information and does so in a completely rigorous framework. An interesting extension of this work would be to use the DROPS visualization to deduce transformation rules of operators under certain Hamiltonians which would only rely on the geometric properties of the DROPS visualization of the operators involved. Another extension of this work would be to adapt the above presentation in the framework of three-spin-1/2 systems and systems involving particles with spin number $I > 1/2$.

3.8 Appendix

3.8.1 Time evolution of $\rho(0) = I_{1x}$ under different coupling Hamiltonians

We consider the time evolution of $\rho(0) = I_{1x}$ under the different coupling Hamiltonians introduced in Section 3.3.2. We first express the decomposition of $\rho(t)$ in terms of Cartesian operators by multiple applications of the sandwich formula given in Eq. 3.4. This successive evaluation is valid since the Cartesian operators in the coupling Hamiltonians commute with each other [8]. For each coupling Hamiltonian, the decomposition of $\rho(t)$ is graphically represented and the explicit form of $\rho(t)$ at times $t = \frac{1}{4J}, \frac{1}{2J}$ is given. These two time values correspond respectively to $t = 2\tau$ and $t = 4\tau$ in Fig. 3.5.

Evolution under $\mathscr{H}_{\text{long}} = 2\pi J I_{1z} I_{2z}$

$$I_{1x} \xrightarrow{2\pi J I_{1z} I_{2z}\, t} \begin{array}{l} I_{1x}\cos(\pi J t) \\ 2I_{1y} I_{2z}\sin(\pi J t) \end{array}$$

$$\begin{array}{lll} \rho(2\tau) & = \rho(\frac{1}{4J}) & = \frac{1}{\sqrt{2}}(I_{1x} + 2I_{1y} I_{2z}), \\ \rho(4\tau) & = \rho(\frac{1}{2J}) & = 2I_{1y} I_{2z}. \end{array}$$

Evolution under $\mathscr{H}_{\text{iso}} = 2\pi J(I_{1x} I_{2x} + I_{1y} I_{2y} + I_{1z} I_{2z})$

$$I_{1x} \xrightarrow{2\pi J I_{1x} I_{2x}\, t} I_{1x} \xrightarrow{2\pi J I_{1y} I_{2y}\, t} \begin{array}{l} I_{1x}\cos(\pi J t) \xrightarrow{2\pi J I_{1z} I_{2z}\, t} \begin{array}{l} I_{1x}\cos^2(\pi J t) \\ 2I_{1y} I_{2z}\cos(\pi J t)\sin(\pi J t) \end{array} \\ -2I_{1z} I_{2y}\sin(\pi J t) \longrightarrow \begin{array}{l} -2I_{1z} I_{2y}\sin(\pi J t)\cos(\pi J t) \\ I_{2x}\sin^2(\pi J t) \end{array} \end{array}$$

$$\begin{array}{lll} \rho(2\tau) & = \rho(\frac{1}{4J}) & = \frac{1}{2}(I_{1x} + 2I_{1y} I_{2z} - 2I_{1z} I_{2y} + I_{2x}), \\ \rho(4\tau) & = \rho(\frac{1}{2J}) & = I_{2x}. \end{array}$$

Evolution under $\mathscr{H}_{\text{plan}} = 2\pi J(I_{1x} I_{2x} + I_{1y} I_{2y})$

$$I_{1x} \xrightarrow{2\pi J I_{1x} I_{2x}\, t} I_{1x} \xrightarrow{2\pi J I_{1y} I_{2y}\, t} \begin{array}{l} I_{1x}\cos(\pi J t) \\ -2I_{1z} I_{2y}\sin(\pi J t) \end{array}$$

$$\begin{array}{lll} \rho(2\tau) & = \rho(\frac{1}{4J}) & = \frac{1}{\sqrt{2}}(I_{1x} - 2I_{1z} I_{2y}), \\ \rho(4\tau) & = \rho(\frac{1}{2J}) & = -2I_{1z} I_{2y}. \end{array}$$

Evolution under $\mathscr{H}_{\text{dip}} = 2\pi J(I_{1x}I_{2x} + I_{1y}I_{2y} - 2I_{1z}I_{2z})$

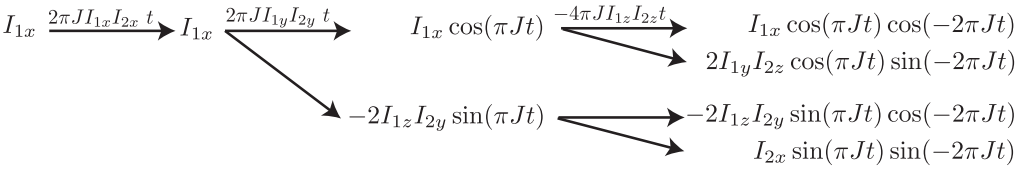

$$\begin{aligned}\rho(2\tau) &= \rho(\tfrac{1}{4J}) &&= \tfrac{1}{\sqrt{2}}(-2I_{1y}I_{2z} - I_{2x}),\\ \rho(4\tau) &= \rho(\tfrac{1}{2J}) &&= 2I_{1z}I_{2y}.\end{aligned}$$

Time-optimal control of quantum gates

This chapter is an adaptation of [75].

4.1 Introduction

Manipulating a quantum system by an external field to achieve a given task remains a primary goal of various areas [23] extending from atomic and molecular physics [76–79], nuclear magnetic resonance spectroscopy [8, 70], and quantum computing [80] to solid state physics. One of the most general and versatile procedures to tackle such control problems is optimal control theory [81, 82]. This technique designs a field able to steer the quantum system to the target state while maximizing or minimizing a given cost functional.

In our setting, an optimal control problem can be treated by two different types of approaches, geometric [83–91] and numerical methods [92–96] for quantum systems of low and high dimension, respectively. In addition to the problem of steering the density operator of the system to the target state, the creation of desired unitary operators plays a key role in both spectroscopy and quantum information processing. Various approaches to construct a desired unitary transformation have been proposed. One of them is based on the combination of simple pulses according to general symmetry principles [8, 70, 97–99] but the control fields constructed with this method generally present the drawback of having long durations. Time-optimal solutions can be determined using numerical optimal control methods [92, 100–105] as well as using geometrical principles [89,106]. Note that related problems can also be solved by the use of Lie group techniques [25]. This work uses geometric principles to address one of the basic and fundamental questions in quantum computation: the optimal control of a single-qubit gate. This well-known control problem has been the subject of a series of works both in mathematics [25,30] and in physics [26–29], to cite a few. Here, we propose to revisit this question by giving an explicit coordinate parametrization of the optimal trajectories. This leads to a complete, analytical and straightforward resolution of the control problem. We also discuss the influence of a detuning term on the optimal pulse sequence.

We consider a spin-$\frac{1}{2}$ particle interacting with a constant magnetic field $\vec{\mathrm{B}}_0$ along the z direction. The control of the spin is performed through the variation of an external transverse magnetic field $\vec{\mathrm{B}}_1(t)$. We place ourselves in the framework of the rotating-wave approximation, for which $|\vec{\mathrm{B}}_1| << |\vec{\mathrm{B}}_0|$, and the frequency of the transverse magnetic field is close to the Larmor frequency of the spin [8, 70, 107, 108].

To simplify the discussion, we consider in this work only gates on SU(2) and not on U(2). We recall that the elements of SU(2) are the matrices of U(2) with determinant

equal to one, *i.e.* the elements for which a global phase factor has been removed. The formalism introduced below can be straightforwardly extended to the unitary group U(2). For a given target state belonging to SU(2), we determine the control fields which minimize the total time of the process by applying the Pontryagin maximum principle. Note that a similar control problem has been recently treated in Ref. [29] in which a different parameterization of the optimal trajectories was used. Our work complements this first study by addressing related questions such as the optimization on SO(3) as well as the computation of trajectories when a detuning term is taken into account.

The remainder of the chapter is organized as follows. The model of the system is presented in Sec. 4.2 and the different choices of coordinates to parametrize SU(2) are discussed. In Sec. 4.3, we show how to apply the Pontryagin maximum principle to this quantum system. Sections 4.4 and 4.5 are devoted to the computation of the optimal trajectories with and without detuning. Special attention is paid to two specific examples: the rotations about the z axis and the rotations about axes in the (x, y) plane. Explicit optimal solutions are given for these two quantum operations. In Section 4.6, we apply the results to work out equivalent time-optimal control problem on the group of rotations SO(3). A conclusion and prospective problems are given in Sec. 4.7. Finally, technical proofs and further explanations are reported in the appendices, Sec. 4.8.

4.2 The model system

This section is dedicated to presenting the general problem studied throughout the chapter. After introducing the system under concern, we describe the problem mathematically and translate it in different coordinate systems in order to get several points of view, which are used for the analysis of the optimal control problem.

4.2.1 Spin systems

We consider a one spin-$\frac{1}{2}$ closed system on which a constant magnetic field $\vec{\mathrm{B}}_0$ aligned in the z direction is applied. In addition, the system can be acted upon by a controlled transverse magnetic field $\vec{\mathrm{B}}_1(t)$ of bounded strength [8, 70]. As mentioned in the introduction of the chapter, we assume that $|\vec{\mathrm{B}}_1|$ is much smaller than $|\vec{\mathrm{B}}_0|$ and that this field oscillates at a frequency close to the Larmor frequency of the spin. Under this hypothesis, we can place ourselves in a given rotating frame and use the rotating-wave approximation in order to simplify the description of the problem. In this framework, the time-dependant quantum Hamiltonian of the system takes the form

$$\mathrm{H} = \omega_x(t)\frac{\sigma_x}{2} + \omega_y(t)\frac{\sigma_y}{2} + \omega\frac{\sigma_z}{2},$$

where ω_x, ω_y are the control fields, which satisfy $\omega_x^2 + \omega_y^2 \leq \omega_{\max}^2$.

The constant ω is the *detuning* term and corresponds (up to a constant factor) to the frequency difference between the frequency of the control field $\vec{\mathrm{B}}_1(t)$ and the Larmor frequency. In particular, ω is zero in the resonant case where the two frequencies are equal. The σ_i's denote the Pauli matrices. [1] In order to treat the problem in its most general context, we use the normalized variables $v_i = \omega_i/\omega_{\max}$ where $v = (v_x, v_y)$ satisfies $\|v(t)\| \leq 1$ for $t \in [0, T(v)]$ ($T(v)$ being the control duration) and $\Delta := \omega/\omega_{\max}$.

[1] The Pauli matrices are $\sigma_x = \left(\begin{smallmatrix} 0 & 1 \\ 1 & 0 \end{smallmatrix}\right)$, $\sigma_y = \left(\begin{smallmatrix} 0 & -i \\ i & 0 \end{smallmatrix}\right)$ and $\sigma_z = \left(\begin{smallmatrix} 1 & 0 \\ 0 & -1 \end{smallmatrix}\right)$.

Such a transformation corresponds to a renormalization of the time by $\tau := \frac{\omega_{\max}}{2} t$. For the sake of notation simplicity, we keep t instead of τ in the remainder of the text, although it is to be understood that the renormalization holds implicitly. The quantum Hamiltonian of the system now takes the form:

$$\mathrm{H} = v_x(t)\sigma_x + v_y(t)\sigma_y + \Delta\sigma_z. \tag{4.1}$$

The angular part of v is be denoted $\mu(t)$ such that

$$\begin{aligned} v_x(t) &= v_0(t)\cos\mu(t), \\ v_y(t) &= v_0(t)\sin\mu(t), \end{aligned} \tag{4.2}$$

v_0 being the amplitude of the control field. Note that the time dependance of most of the dynamical variables is dropped throughout the text in order to simplify the notation. Writing the state of the system at time t in the density matrix formalism $\rho(t)$, the time evolution is given by the von Neumann equation

$$i\partial_t \rho(t) = [\mathrm{H}, \rho(t)],$$

where one is working in a system of units such that $\hbar = 1$. Since the system is closed, the states $\rho(t)$ are linked to the initial one ρ_0 by a unitary matrix $U(t) \in \mathrm{SU}(2)$ via the relation $\rho(t) = U(t)\rho_0 U(t)^\dagger$. Note that $U(t)$ belongs to SU(2) and not U(2), because the quantum Hamiltonian $\mathrm{H}(t)$ is an element of the Lie algebra $su(2)$. The question of controlling the quantum system from a given initial state ρ_0 can then be translated to a control problem on SU(2), which is exactly the objective of the present work. More precisely, one investigates the problem of finding the optimal control v^* (the $*$ sign indicates the optimal solutions in the remainder of this document), steering the system from the identity matrix $U(0) = I \in \mathrm{SU}(2)$ to a target state $U^* \in \mathrm{SU}(2)$ while minimizing the time $T(v)$ to get there. The time duration of v^* is also denoted $t^* := T(v^*)$. The dynamics governing the system for this *time-optimal* control problem is given by the Schrödinger equation:

$$i\partial_t U(t) = \mathrm{H}(t)U(t). \tag{4.3}$$

4.2.2 Choice of coordinates

Let us recall some characteristics of the group SU(2), which is at the core of our control problem. Elements $U \in \mathrm{SU}(2)$ are the 2×2 matrices with complex entries satisfying $\det(U) = 1$. Defining $\mathbf{i} = i\sigma_z$, $\mathbf{j} = i\sigma_y$ and $\mathbf{k} = i\sigma_x$, a possible parametrization of U is

$$U = \begin{pmatrix} x_1 + ix_2 & x_3 + ix_4 \\ -x_3 + ix_4 & x_1 - ix_2 \end{pmatrix} = x_1 \mathbb{1} + x_2\mathbf{i} + x_3\mathbf{j} + x_4\mathbf{k} \tag{4.4}$$

where the x_i's are real. This is the quaternion representation of U and is related to the group of rotations SO(3). Indeed, there exists $\alpha \in [0, 4\pi]$ and $\vec{n} \in S^2(0,1)$ (the unit sphere centered at the origin) such that

$$\begin{aligned} x_1 &= \cos(\alpha/2), \\ x_2 &= \sin(\alpha/2)n_z, \\ x_3 &= \sin(\alpha/2)n_y, \\ x_4 &= \sin(\alpha/2)n_x, \end{aligned} \tag{4.5}$$

and that U represents a rotation of angle α about the unit axis $\vec{n}$. However, since $\det(U) = 1$, the x_i's satisfy the relation $\sum_{i=1}^4 x_i^2 = 1$ and the quaternion parametrization

uses one parameter more than needed. This remark partly motivates our choice of considering the Hopf parametrization instead. In terms of the Hopf variables $\{\theta_1, \theta_2, \theta_3\}$, U can be written as

$$U(\theta_1, \theta_2, \theta_3) = \begin{pmatrix} \cos\theta_1 e^{i\theta_2} & \sin\theta_1 e^{i\theta_3} \\ -\sin\theta_1 e^{-i\theta_3} & \cos\theta_1 e^{-i\theta_2} \end{pmatrix} \tag{4.6}$$

where the domain of definition is be defined below. The main advantage of the Hopf parametrization is that Eq. (4.3) translates nicely in its variables, which give the simple form

$$\begin{pmatrix} \dot{\theta}_1 \\ \dot{\theta}_2 \\ \dot{\theta}_3 \end{pmatrix} = \begin{pmatrix} u_1 \\ -\tan\theta_1 \; u_2 - \Delta \\ \cot\theta_1 \; u_2 - \Delta \end{pmatrix}, \tag{4.7}$$

where the normalized "rotated" controls

$$\begin{aligned} u_1 &:= -v_0 \sin(\mu + \theta_2 + \theta_3), \\ u_2 &:= -v_0 \cos(\mu + \theta_2 + \theta_3), \end{aligned} \tag{4.8}$$

have been used and satisfy $\|u\| \leq 1$. The explicit calculations for obtaining equations (4.7) can be found in Appendix 4.8.1. The control problem now reads as follows: *Given a target state* $(\theta_1^*, \theta_2^*, \theta_3^*)$, *find the control* u^* *steering* $\theta_i(0) \mapsto \theta_i^*$ *while minimizing the control duration* $T(u)$.
Note that the condition $U(0) = I$ translates in terms of Hopf variables as

$$\begin{aligned} &\theta_1(0) = 0, \\ &\theta_2(0) = 0, \\ &\theta_3(0) = \text{undefined}. \end{aligned} \tag{4.9}$$

In later parts of the chapter, we also make use of the Euler parametrization $U(\psi, \theta, \phi)$, which allows to easily visualize rotations. The Euler variables are related to the Hopf variables by

$$\begin{aligned} \psi &= \theta_2 + \theta_3, \\ \theta &= 2\theta_1, \\ \phi &= \theta_2 - \theta_3. \end{aligned} \tag{4.10}$$

Recalling the close relation between elements of SU(2) and rotations $\mathcal{R}(\psi, \theta, \phi) \in \mathrm{SO}(3)$, in terms of Euler coordinates, unitary matrices can be decomposed as $U(\psi, \theta, \phi) = \mathrm{e}^{i\psi\frac{\sigma_z}{2}} \cdot \mathrm{e}^{i\theta\frac{\sigma_y}{2}} \cdot \mathrm{e}^{i\phi\frac{\sigma_z}{2}}$. The Euler variables are taken to be in the domains $\phi \in [-\pi, \pi)$, $\psi \in [-2\pi, +2\pi)$ and $\theta \in [0, \pi]$. The domains of the θ_i variables can then be deduced directly from Eqs. (4.10).

4.3 The Pontryagin maximum principle

The problem of finding the time-optimal control for steering the system from an initial state to a fixed target can be decomposed into three steps, each of which brings its own considerations and particular methodology. First, one must find the optimal candidates for the control functions. We can have two types of controls: regular type or singular type. The second step consists in computing the trajectories associated with the different controls. Finally, one has to determine the right trajectory to reach the desired target state. While the first two steps are treated through the Pontryagin maximum principle

(PMP) [81], depending on the optimal problem considered the last step may require numerical methods.

The present section is intended to expose the main features of the PMP and to apply it to our particular problem.

4.3.1 Theory

This section aims at presenting the elements of the theory of PMP used to solve our control problem. In order to be as pedagogical as possible, the general equations arising from the theory [81, 82] is followed by their translation in our particular context.

Consider a controlled system

$$\dot{x} = f(t, x(t), u(t)) \tag{4.11}$$

where $x(t) = (x_1, x_2, \cdots, x_n) \in \mathbb{R}^n$, $u(t) \in \Omega \subset \mathbb{R}^m$ for $t \in [0, T]$, where $T := T(u)$ as before. Let $x_u(\cdot)$ denote the trajectory associated with the control u. Given two points $x_0, x^* \in \mathbb{R}^n$, one aims at finding u such that $x_u(0) = x_0$, $x_u(T) = x^*$, and minimizing (or eventually optimizing) the cost functional,

$$c(T, u) = g(T, x_u(T)) + \int_0^T f^0(t, x_u(t), u(t))\ dt. \tag{4.12}$$

The function f^0 is the *running cost* which depends on the whole trajectory $x_u(\cdot)$, whereas g is the final cost which depends only on the final time and state. The *Hamiltonian* of the system driven by u is also called PMP *pseudo-Hamiltonian* and is denoted

$$H(t, x, p, \mathrm{p}^0, u) = p \cdot \dot{x} + \mathrm{p}^0 f^0. \tag{4.13}$$

The term $p \cdot \dot{x}$ denotes the scalar product between the derivative of the state vector x and a vector $p(t) \in \mathbb{R}^n$ called the *adjoint state*, which is required to be continuous all along an optimal trajectory. The constant p^0 is taken to be negative (for a maximum principle) and should be such that p^0 and p never simultaneously vanish. Note that the overall vector $(p, \mathrm{p}^0) \in \mathbb{R}^{n+1}$ is defined up to a positive constant factor.

At this stage, we express our problem in this formalism. First, Eq. (4.11) corresponds to our system given in Eq. (4.7) with $x_i := \theta_i$. The norm of the controls $u(t)$ is bounded to $\|u\| \leq 1$. Since the goal is to minimize the control time, the cost function is $c(T, u) = T$ and one can consider $g \equiv 0$ and $f^0 \equiv 1$ in Eq. (4.12). Finally, after factorizing the two control components, the PMP pseudo-Hamiltonian takes the form

$$\begin{aligned} &H(t, \vec{\theta}, p, \mathrm{p}^0, u) = \\ &u_1 p_1 + u_2(-p_2 \tan\theta_1 + p_3 \cot\theta_1) - (p_2 + p_3)\Delta + \mathrm{p}^0, \end{aligned} \tag{4.14}$$

where $\vec{\theta} := (\theta_1, \theta_2, \theta_3)$. The PMP suggests that a *necessary* condition for a control $u^*(t)$ to optimize (minimize in our case) the cost functional is to maximize the PMP pseudo-Hamiltonian $H(t)$ at any time. This leads to the PMP Hamiltonian $\mathscr{H}_{u^*}(t, x, p, \mathrm{p}^0)$, denoted with a script letter, which is free of an explicit control dependence and which satisfies

$$\mathscr{H}_{u^*}(t, x, p, \mathrm{p}^0) = \max_{u \in \Omega} H(t, x, p, \mathrm{p}^0, u), \quad \forall\ t \in [0, T].$$

Due to the fact that u_1 and u_2 can be factorized in the pseudo-Hamiltonian H [see Eq. (4.14)], we find that the controls are given by

$$\begin{aligned} u_1(t) &= \tfrac{p_1}{N}, \\ u_2(t) &= \tfrac{-p_2 \tan\theta_1 + p_3 \cot\theta_1}{N}, \end{aligned} \tag{4.15}$$

where

$$N = \sqrt{p_1^2 + [-p_2 \tan\theta_1 + p_3 \cot\theta_1]^2} \tag{4.16}$$

is such that $u_1^2 + u_2^2 = 1$ [82,87]. Such controls, which are well defined when $N \neq 0$ only, are said to be *normal* and the associated trajectories $\vec{\theta}(\cdot)$ are called *regular*. When $N = 0$, computational analysis (detailed below) reveals that the controls, said to be *singular*, must vanish. The associated trajectories are also called *singular* and are non-trivial only when $\Delta \neq 0$. Singular controls are briefly discussed in Appendix 4.8.3. However, for both $\Delta = 0$ and $\Delta \neq 0$, we show in Appendix 4.8.6 that singular trajectories as well as mixtures of regular and singular trajectories are *never* optimal. In other words, the time-optimal controls for our problem are necessarily normal and consequently, we restrict our study to only these. In addition, the PMP states that the final PMP Hamiltonian must satisfy

$$\mathscr{H}_{u^*}(T) = -\mathrm{p}^0 \frac{\partial g}{\partial t}(T), \tag{4.17}$$

$$\frac{\partial \mathscr{H}_{u^*}}{\partial t} = \frac{d\mathscr{H}_{u^*}}{dt}, \tag{4.18}$$

for almost all $t \in [0, T]$. Equation (4.17) is called the *transversality* condition and takes the above form when we apply the PMP formalism to our problem for some non-fixed final time T. Equation (4.18) is derived from the fact that the PMP pseudo-Hamiltonian does not depend explicitly on time. Note that in our case, since $g \equiv 0$, those two relations merge into the relation

$$\mathscr{H}_{u^*}(\vec{\theta}, p, \mathrm{p}^0) = 0. \tag{4.19}$$

In the following, the constant p^0 is normalized to -1. Finally, the PMP ensures that the dynamics along an optimal trajectory is given by the Hamilton set of $2n$ differential equations

$$\frac{\partial \mathscr{H}_{u^*}}{\partial p} = \dot{x},$$
$$-\frac{\partial \mathscr{H}_{u^*}}{\partial x} = \dot{p}.$$

When normal controls are considered, this system takes the form

$$\begin{cases} \begin{pmatrix} \dot{\theta}_1 \\ \dot{\theta}_2 \\ \dot{\theta}_3 \end{pmatrix} = \begin{pmatrix} p_1 \\ \mathrm{p}_2 \tan^2\theta_1 - \Delta \\ -\mathrm{p}_2 - \Delta \end{pmatrix}, \\ \begin{pmatrix} \dot{p}_1 \\ \dot{p}_2 \\ \dot{p}_3 \end{pmatrix} = \begin{pmatrix} -\mathrm{p}_2^2 \tan\theta_1 \sec^2\theta_1 \\ 0 \\ 0 \end{pmatrix}, \end{cases} \tag{4.20}$$

where the adjoint variables have been normalized to $p_i' := \frac{p_i}{N}$, the prime has been dropped to simplify the notations, and we used the constants of motion

$$p_2(t) \equiv \mathrm{p}_2,$$
$$p_3(t) \equiv 0,$$

to simplify the equations. The relation $p_3(t) \equiv 0$ is deduced from the expression of $u_2(0)$ in Eqs. (4.15). Since $\theta_1(0) = 0$, the $p_3 \cot\theta_1$ term would be infinite in $t = 0$ if $p_3(0) \neq 0$,

which cannot be the case since the controls have finite intensity. Using this condition, it is also straightforward to check that singular controls are null. The term $N(t)$ is equal to zero on a given time interval only if $p_1(t) = 0$. The associated singular trajectories correspond to a freely evolving system whose dynamics is governed by the detuning term Δ (see Appendix 4.8.3 for more details about the singular controls).

4.4 Optimal trajectories without detuning

We recall that the case without detuning corresponds to $\Delta = 0$. As already mentioned, the only controls to consider are the normal controls. In particular, since such controls satisfy $\|u\| = 1$, the controls are uniquely characterized (modulo 2π) by the angular parameter (see Eqs. (4.8))

$$\beta(t) := \mu(t) + \psi(t). \tag{4.22}$$

In this section, we explicitly write the solutions of the system of dynamical equations (4.20) in terms of the Euler angle parametrization (ψ, θ, ϕ). The full problem is solved for some typical targets frequently encountered in quantum computing [80].

4.4.1 The general case

Using Eqs. (4.10) and setting $\Delta = 0$, the dynamics satisfied by the regular extremals can be written in terms of the Euler parameters as

$$\begin{pmatrix} \dot{\psi} \\ \dot{\theta} \\ \dot{\phi} \end{pmatrix} = \begin{pmatrix} \mathrm{p}_2(\tan^2 \frac{\theta}{2} - 1) \\ 2p_1 \\ \mathrm{p}_2 \sec^2 \frac{\theta}{2} \end{pmatrix}. \tag{4.23}$$

Using the two definitions of the controls given in Eqs. (4.8) and Eqs. (4.15) as well as the dynamics described by Eq. (4.23), we get two relations between the variables $\psi(t)$, $\phi(t)$ and $\mu(t)$:

$$\dot{\mu} = 2\mathrm{p}_2 \quad \text{and} \quad \dot{\mu} + \dot{\psi} - \dot{\phi} = 0. \tag{4.24}$$

The interested reader will find in Appendix 4.8.2 the proofs of these relations. Since p_2 is constant, the first of these two equations implies that the real angular control is a linear function of the time

$$\mu(t) = \mu(0) + 2\mathrm{p}_2 t.$$

We show in Appendix 4.8.5 that $\beta(0) = -\frac{\pi}{2}$ and from this relation together with the fact that $\phi(0) = -\psi(0)$ (since $\theta_2(0) = 0$), we directly compute $\mu(0) = \phi(0) - \frac{\pi}{2}$ by using the definition of $\beta(t)$.

Equations (4.24) also provide the main tool needed to visualize the extremals as their projection on the sphere S^2. Indeed, given an extremal $(\psi(t), \theta(t), \phi(t))$ associated with the regular control $u(t)$ for $t \in [0, T(u)]$, let $\gamma(t) := (\theta(t), \phi(t))$ be the projection of this extremal on the sphere. The variable $\theta(t)$ gives the vertical inclination and $\phi(t)$ the azimuthal angle with respect to the x axis. We assume that $\phi(0)$ and p_2, which define a particular trajectory, are known. We then have the following property (see Appendix 4.8.4 for the proof) which has been also established in Ref. [29].

Proposition 1 *Let $\bar{\theta} = \arctan(\frac{1}{\mathrm{p}_2})$ and $\bar{\phi} = \phi(0) + \frac{\pi}{2}$. The projected trajectory $\gamma(t) = (\theta(t), \phi(t))$ defines a circle around the fixed axis $\vec{n} = (\bar{\theta}, \bar{\phi})$. Moreover, $\gamma(t)$ is traveled with constant speed $\|\dot{\gamma}(t)\| = 2$. The final time t^* is equal to $\frac{1}{2}$ the arc length of $\gamma(t)$.*

Note that the factor $+\frac{\pi}{2}$ appearing in the definition of $\bar{\phi}$ comes from the relation $\beta(0) = -\frac{\pi}{2}$ previously established.

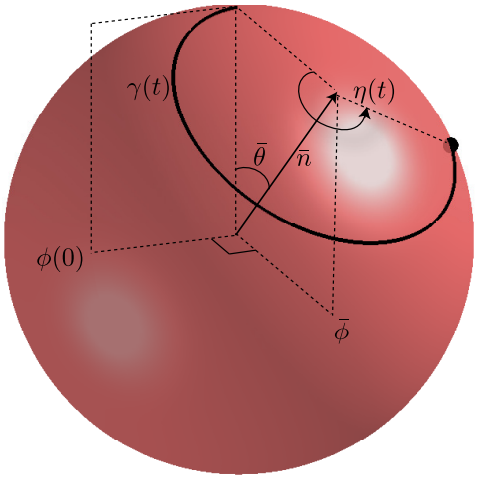

Figure 4.1: Illustration of the different angular parameters used in Proposition 1 to characterize a projected trajectory $\gamma(t)$.

Examples of such projected trajectories are illustrated in Fig. 4.2. In the situation where $\mathrm{p}_2 = 0$, Eqs. (4.20) are directly integrable and hence we obtain that $\gamma(t)$ describes a great circle, which is the limit case of Proposition 1.

Using Eqs. (4.24), we deduce the explicit expression for the time evolution of Euler parameters:

$$\begin{aligned} \theta(t) &= \cos^{-1}(1 + \sin^2\bar{\theta}(\cos\eta(t) - 1)), \\ \phi(t) &= \phi(0) + \mathrm{sign}(\mathrm{p}_2)\tfrac{\pi}{2} + \tan^{-1}\left(\tfrac{\sin\eta(t)}{\cos\bar{\theta}(\cos\eta(t)-1)}\right), \\ \psi(t) &= -2\phi(0) + \phi - 2\mathrm{p}_2 t, \end{aligned} \tag{4.25}$$

where

$$\eta(t) := \frac{2t}{\sin\bar{\theta}} \tag{4.26}$$

is the angular parametrization of the circle section drawn by $\gamma(t)$ around its axis $\bar{n}$ illustrated on Fig. 4.1. The calculations leading to these equations can be found in Appendix 4.8.4. In particular, the time t for which $\gamma(t)$ traces out a complete circle on the sphere corresponds to an angle of $\eta(t) = \mathrm{sign}(\mathrm{p}_2)2\pi$. In the limiting case where $\mathrm{p}_2 = 0$, the equation for $\phi(t)$ given in Eqs. (4.25) takes the simple form $\phi(t) \equiv \phi(0)$.

4.4.2 Time-optimal controls

We can show that all unitary matrices $U^* \in \mathrm{SU}(2)$ are reached by a unique regular control $u : [0, t^*] \mapsto \mathrm{SU}(2)$ with $|\eta(t^*)| < 2\pi$ for all unitary matrices which do not correspond to z rotations. Moreover, these controls are precisely the time-optimal controls. The condition $|\eta(t^*)| < 2\pi$ implies that time-optimal trajectories necessarily trace out circular arcs of angle $|\eta(t^*)| < 2\pi$ and hence, they turn less than once around their axis

$\bar{n}$. All regular controls satisfying $|\eta(T)| < 2\pi$ ($T = T(u)$) are then uniquely denoted u_U where $U \in \mathrm{SU}(2)$ is the target unitary they optimally generate. The case $|\eta(T)| = 2\pi$ corresponds to rotations along the z axis and, in this case, all the trajectories corresponding to the same inclination angle $\bar{\theta}$ will generate the same unitary matrix in the same time. This special case is discussed in the next section.

To completely solve the problem at hand, it remains to find the explicit parameters p_2 and $\phi(0)$ (defining any regular controls up to the final time), which steer the system to the desired target. In fact, we show in Appendix 4.8.5 that

$$\mathrm{p}_2 = \frac{\sin(\phi^* - \phi(0))}{\tan(\frac{\theta^*}{2})}, \tag{4.27}$$

and hence we need to only consider the single parameter $\phi(0)$. Consequently, Eqs. (4.25) form a system of three equations of two variables $\phi(0)$ and t^* and the solution for a general $U^* = (\psi^*, \theta^*, \phi^*)$ can be found numerically.

Some cases are of particular practical interest: the unitary matrices describing rotations about the z axis or about any axis in the (x, y) plane. The full solution for each of these two classes of targets is presented in the next sections. For both cases, the initial parameter $\phi(0)$ can be found analytically. Interestingly, an analytical formula for the optimal time t^* is found as a function of the target U^*. The general case is then briefly discussed.

4.4.3 Rotation about the z axis

Consider the problem of reaching a target of the form $U^* = e^{i\lambda^* \frac{\sigma_z}{2}}$ where $\lambda^* \in [-2\pi, 2\pi]$. The final state is characterized by any pair (λ^*, ϕ^*), *i.e.* $(\psi^*, \theta^*, \phi^*) = (\lambda^* - \phi^*, 0, \phi^*)$. Since the definition of U^* depends only on λ^*, the time-optimal trajectories associated with any value of ϕ^* should not influence the final time t^* taken to reach the target. Note that the projected trajectory $\gamma(t) := (\theta(t), \phi(t))$ starts and ends at the North Pole of the sphere, since $\theta(0) = \theta^* = 0$. As a consequence of this remark together with Proposition 1, $\gamma : [0, t^*] \to S^2$ describes a complete circle and direct computation detailed in Appendix 4.8.7 shows that the initial parameters leading to the target are given by

$$\begin{array}{rcl} \mathrm{p}_2 & = & \mathrm{sign}(\lambda^*) \cot\left(\cos^{-1}\left(1 - \frac{|\lambda^*|}{2\pi}\right)\right) \\ & \text{and} & \\ t^* & = & \frac{1}{2}\sqrt{4\pi|\lambda^*| - |\lambda^*|^2}, \end{array} \tag{4.28}$$

from which we can explicitly write the time-optimal trajectory given by Eqs. (4.25). Examples of projected trajectories for four different z-rotation unitary matrices are shown on the left sphere of Fig. 4.2. Note that equations similar to Eqs. (4.28) have been encountered in [89] for the time-optimal control on three coupled spins.

4.4.4 Rotation in the (x, y) plane

Now, we consider a target corresponding to a rotation in the (x, y) plane given by $U^* = e^{i(-a)\frac{\sigma_z}{2}} \cdot e^{ib\frac{\sigma_y}{2}} \cdot e^{ia\frac{\sigma_z}{2}}$, which is defined by the Euler variables $(\psi^*, \theta^*, \phi^*) = (-a, b, a)$ with $b \in [0, 2\pi)$. This special choice for the domain $[0, 2\pi)$ of b find its motivation later when we consider the opposite rotation $-U$.

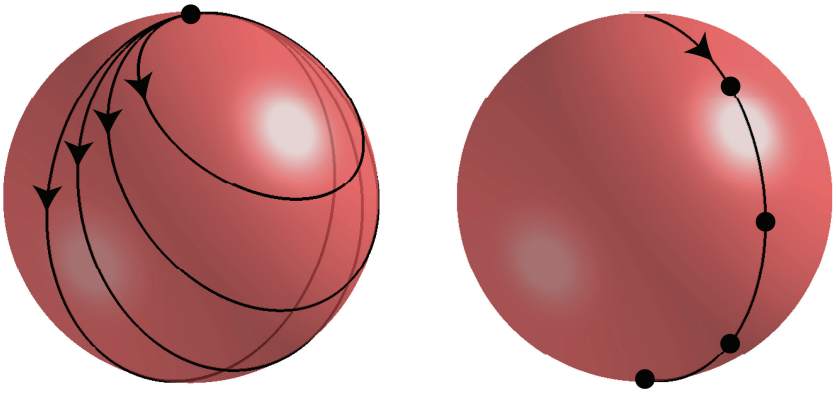

Figure 4.2: On the left, the projected trajectories for the optimal synthesis of $U^* = e^{i\lambda\frac{\sigma_z}{2}}$ with $\lambda = \frac{\pi}{2}, \pi, \frac{3\pi}{2}, 2\pi$. On the right, the projection of the optimal trajectories of $U^* = e^{-ia\frac{\sigma_z}{2}} e^{ib\frac{\sigma_y}{2}} e^{ia\frac{\sigma_z}{2}}$ with $(a, b) = (0, \frac{k\pi}{4})$ where $k = 1, 2, 3, 4$. The dots indicate the position of the target states.

At this point, a remark about the behaviour of the Hopf variable θ_2 should be made. We can show (see Appendix 4.8.8) that $\theta_2(t)$ is monotonic along a time-optimal trajectory, meaning that it must either strictly increase or strictly decrease, otherwise it is equal to zero all along the trajectory. In the present case, since $\theta_2(0) = \theta_2^* = 0$, the third situation applies which implies that $\dot{\theta}_2 = 0$ and $\theta_2(t) = 0$ along the complete trajectory. By comparing this equality with Eqs. (4.20), it becomes clear that we are in the very special case where $\mathrm{p}_2 = 0$ and that the only variable among Hopf angles and adjoint state variables which *is not* constant is θ_1. All the equations among Eqs. (4.23) are directly integrable, and hence we obtain that $\gamma(t)$ must follow a great circle. The initial conditions and the final time for reaching the target can then be written as

$$\mathrm{p}_2 = 0, \quad \phi(0) = a \quad \text{and} \quad t^* = \tfrac{b}{2}. \tag{4.29}$$

The interested reader can find in Appendix 4.8.8 a formal proof of these equalities. Examples of projected trajectories for four different unitary matrices corresponding to rotations in the transverse plane are shown on the right sphere of Fig. 4.2.

4.5 Optimal trajectories with detuning

In this section, we consider the case where the frequency of the transverse magnetic field $\vec{\mathrm{B}}_1$ is not on resonance with the Larmor frequency. In the rotating frame, the system is subject to a z magnetic field proportional to $\Delta \neq 0$. In this case, both regular and singular controls lead to non-trivial trajectories but, as already discussed in Sec. 4.3.1, the time-optimal ones are necessarily regular, that is, time-optimal controls are never vanishing.

In the following, we discuss the shape of the regular trajectories and the set of the time-optimal ones is given as a function of Δ. Note that the analysis is completely general and applies to any possible value of Δ, as long as the rotating wave approximation is valid.

4.5.1 The general case

Let $\Delta \neq 0$ and consider the dynamics of the system given by Eqs. (4.7) in terms of the Euler parameters:

$$\begin{pmatrix} \dot{\psi} \\ \dot{\theta} \\ \dot{\phi} \end{pmatrix} = \begin{pmatrix} u_2(-\tan\theta_1 + \cot\theta_1) - 2\Delta \\ 2u_1 \\ u_2(-\tan\theta_1 - \cot\theta_1) \end{pmatrix}.$$

Replacing the control values (see Eqs. (4.15)) in these equations, the dynamics of the system governed by the associated regular control is then

$$\begin{pmatrix} \dot{\psi} \\ \dot{\theta} \\ \dot{\phi} \end{pmatrix} = \begin{pmatrix} \mathrm{p}_2(\tan^2\theta_1 - 1) - 2\Delta \\ 2p_1 \\ \mathrm{p}_2 \sec^2\theta_1 \end{pmatrix}. \tag{4.30}$$

Equations (4.24) generalize in a straightforward way to the case with a detuning term as follows:

$$\dot{\mu} = 2\mathrm{p}_2 + 2\Delta \quad \text{and} \quad \dot{\mu} + \dot{\psi} - \dot{\phi} = 0 \tag{4.31}$$

and we recall that the proof of these equations can be found in the Proof section 4.8.2. More generally, when comparing dynamics of Eqs. (4.30) with the dynamics without detuning given by Eqs. (4.23), we note that the only variable being influenced by the detuning Δ is $\psi(t)$. In particular, the projected trajectories $\gamma(t) = (\phi(t), \theta(t))$ are of the same shape as the ones without detuning, *i.e.* they describe circles on the sphere. More precisely, Proposition 1 still holds with the same definition for the rotation axis $\bar{n} = (\bar{\theta}, \bar{\phi})$. The time-evolution of the Euler-variables is then given by

$$\begin{aligned} &\theta(t) = \cos^{-1}(1 + \sin^2\bar{\theta}(\cos\eta(t) - 1)), \\ &\phi(t) = \phi(0) + \mathrm{sign}(\mathrm{p}_2)\tfrac{\pi}{2} + \tan^{-1}\left(\tfrac{\sin\eta(t)}{\cos\bar{\theta}(\cos\eta(t)-1)}\right), \\ &\psi(t) = -2\phi(0) + \phi - 2(\mathrm{p}_2 + \Delta)t, \end{aligned} \tag{4.32}$$

as established in Appendix 4.8.4.

4.5.2 Time-optimal controls

In order to be as general as possible and include rotations about the z axis in our study, every unitary matrix $U^* = e^{i\lambda^* \frac{\sigma_z}{2}}$ corresponding to a z rotation will be characterized by $\phi^* = 0$, that is $U^* = (\psi^*, \theta^*, \phi^*) = (\lambda^*, 0, 0)$. To avoid confusion, targets $\mathbf{U} = (\boldsymbol{\psi}, \boldsymbol{\theta}, \boldsymbol{\phi})$ and $U^* = (\psi^*, \theta^*, \phi^*)$ will correspond to targets which are reached without and with detuning respectively.

As opposed to the case without detuning, when $\Delta \neq 0$, there may be more than one regular control u reaching a target $U^* \in \mathrm{SU}(2)$ with $|\eta(T(u))| \leq 2\pi$. We are then interested in finding which regular controls correspond to the time-optimal controls. Recall that the regular controls are uniquely denoted $u_{\mathbf{U}}$ where $\mathbf{U} \in \mathrm{SU}(2)$ is the unitary matrix being generated by the regular control $u_{\mathbf{U}}$ *without detuning*. We consider the well-known end-point mapping [82]:

$$\mathrm{End}_\Delta : u_{\mathbf{U}} \mapsto (\boldsymbol{\psi} - 2\Delta T(u_{\mathbf{U}}), \boldsymbol{\theta}, \boldsymbol{\phi}) \tag{4.33}$$

mapping any regular control on its target in the presence of a detuning term Δ. In general, for a given control u, $\mathrm{End}_\Delta(u) \neq \mathrm{End}_{\Delta'}(u)$ for $\Delta \neq \Delta'$. We verify directly that

when there is no detuning, this function maps a control $u_{\mathbf{U}}$ on $\mathbf{U}$, that is $\mathrm{End}_0(u_{\mathbf{U}}) = \mathbf{U}$. We can also check the validity of the mapping by noting (1) that the dynamical variables $\theta(t)$ and $\phi(t)$ are unaffected by the detuning and (2) that $\psi^* = \boldsymbol{\psi} - 2\Delta T(u_{\mathbf{U}})$ by simply comparing the equations for $\dot{\psi}$ given in Eqs. (4.23) and (4.30).

Clearly, the regular controls $u_{\mathbf{U}}$ reaching a desired target $U^* = (\psi^*, \theta^*, \phi^*)$ are the ones for which $\boldsymbol{\theta} = \theta^*$, $\boldsymbol{\phi} = \phi^*$ and $\boldsymbol{\psi} - 2\Delta T(u_{\mathbf{U}}) = \psi^* \mod 4\pi$. Since the first two relations are trivial to satisfy, we can then focus on the variable $\boldsymbol{\psi}$ only and consider the restriction (denoted f_Δ) of the end-point mapping End_Δ to the controls $u_{\mathbf{U}}$ satisfying $\boldsymbol{\theta} = \theta^*$ and $\boldsymbol{\phi} = \phi^*$. These controls are then uniquely denoted $u_{\boldsymbol{\psi}}$. The function f_Δ takes the form:

$$f_\Delta : u_{\boldsymbol{\psi}} \mapsto \boldsymbol{\psi} - 2\Delta T(u_{\boldsymbol{\psi}}). \tag{4.34}$$

As expected, we have $f_0(u_{\boldsymbol{\psi}}) = \boldsymbol{\psi}$ and the end-point mapping can be rewritten as $\mathrm{End}_\Delta(u_{\boldsymbol{\psi}}) = (f_\Delta(u_{\boldsymbol{\psi}}), \boldsymbol{\theta}, \boldsymbol{\phi})$. Examples of graphs for f_Δ are illustrated in Fig. 4.3 (b) and (c). With these tools available, we obtain the set of controls $u_{\boldsymbol{\psi}}$ corresponding to

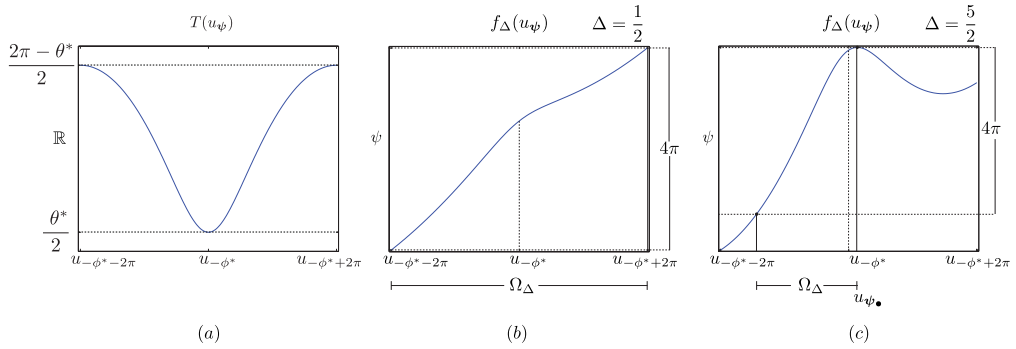

Figure 4.3: (a) Time taken by the regular controls $u_{\mathbf{U}}$ where $\boldsymbol{\theta} = 2.2689$, $\boldsymbol{\psi} = 0$ are fixed and $\boldsymbol{\psi}$ vary in the domain $[-\boldsymbol{\psi} - 2\pi, -\boldsymbol{\psi} + 2\pi]$. (b,c) Plots of the restriction f_Δ of the end-point mapping for detuning values $\Delta = \frac{1}{2}$ and $\frac{3}{2}$ respectively. Plot (b) illustrates the case $\Delta \leq |\tan(\frac{\theta^*}{2})|$ where $\Omega_\Delta = \Omega_0$. Plot (c) illustrates the case $\Delta > |\tan(\frac{\theta^*}{2})|$ where the optimal domain $\Omega_\Delta \subset \Omega_0$.

time-optimal controls under a detuning term $\Delta \neq 0$. This set, denoted $\Omega_\Delta^{(\theta^*,\phi^*)}$ or simply Ω_Δ (for θ^* and ϕ^* fixed), is given in the following Proposition:

Proposition 2 *Let θ^* and ϕ^* be fixed. If $|\Delta| \leq |\tan(\frac{\theta^*}{2})|$, then $\Omega_\Delta = \Omega_0$. Otherwise, $\Omega_\Delta = \left[u_{\boldsymbol{\psi}_\bullet}, f_\Delta^{-1}\left(f_\Delta(u_{\boldsymbol{\psi}_\bullet}) \pm 4\pi\right)\right]$ where $\pm$ is the sign of $-\Delta$.*

Here, $[u_{\boldsymbol{\psi}_{\min}}, u_{\boldsymbol{\psi}_{\max}}] := \{u_{\boldsymbol{\psi}} | \boldsymbol{\psi} \in [\boldsymbol{\psi}_{\min}, \boldsymbol{\psi}_{\max}]\}$. In particular, the time-optimal domain $\{u_{\boldsymbol{\psi}}\} \in \Omega_\Delta$ is such that $\boldsymbol{\psi} \in [\boldsymbol{\psi}_{\min}, \boldsymbol{\psi}_{\max}]$. The angle $\boldsymbol{\psi}_\bullet$ is chosen such that the adjoint variable p_2 characterizing $u_{\boldsymbol{\psi}_\bullet}$ satisfies $\mathrm{p}_2 = \frac{1}{\Delta}$ and depends on Δ. The interested reader will find further explanations about the interpretation of this result as well as an idea of the proof in Appendix 4.8.6.

Any target $U^* = (\psi^*, \theta^*, \phi^*)$ is reached by one and only one time-optimal control in Ω_Δ. In other words, the function f_Δ is bijective on Ω_Δ. The time-optimal control

generating U^* is the unique control $u_{\boldsymbol{\psi}}$ solution of the equation

$$u_{\boldsymbol{\psi}} = f_\Delta^{-1}(\psi^* + n \cdot 4\pi) \cap \Omega_\Delta \tag{4.35}$$

for a certain $n \in \mathbb{Z}$. Examples of the projected trajectories for two targets $U^* = e^{i\frac{\pi}{2}\frac{\sigma_z}{2}}$ and $U^* = e^{i\frac{\pi}{4}\frac{\sigma_y}{2}}$ under different detuning values $\Delta = 0, \frac{1}{2}, \frac{3}{2}, \frac{5}{2}$ are depicted in Fig. 4.4.

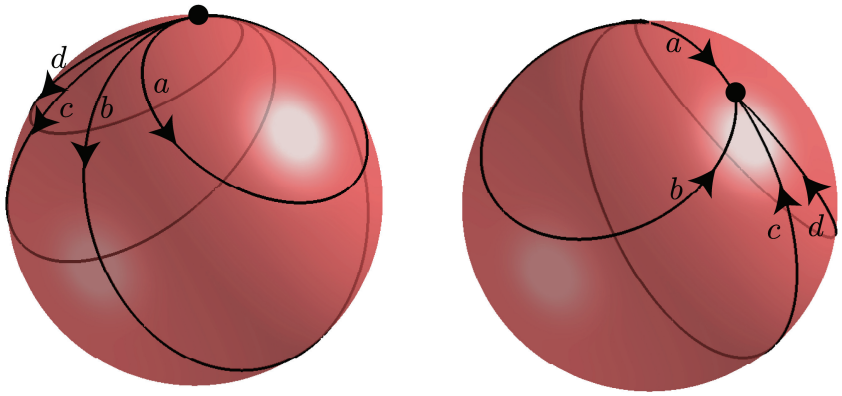

Figure 4.4: Projected trajectories for the optimal synthesis of $U^* \in \mathrm{SU}(2)$ subjected to a detuning field of intensity $\Delta = 0, \frac{1}{2}, \frac{3}{2}, \frac{5}{2}$ (trajectories a, b, c, d respectively). On the left, $U^* = e^{i\frac{\pi}{2}\frac{\sigma_z}{2}}$ corresponds to a rotation about the z axis. On the right, $U^* = e^{i\frac{\pi}{4}\frac{\sigma_y}{2}}$ corresponds to a rotation about the y-axis.

Given a propagator $U(\psi^*, \theta^*, \phi^*) \in \mathrm{SU}(2)$, we can use the following algorithm to find the time-optimal control u^* generating U^*.

Algorithm 1 *To find the time-optimal control $u^* = u_{\boldsymbol{\psi}}$ generating $U(\psi^*, \theta^*, \phi^*)$ under a detuning term Δ:*

1. *For $\boldsymbol{\psi} \in [-\phi^* - 2\pi, -\phi^* + 2\pi]$, compute $\mathrm{p}_2(u_{\boldsymbol{\psi}})$ by inverting Eqs. (4.25) for the target $U(\boldsymbol{\psi}, \theta^*, \psi^*)$.*
2. *Compute the time optimal domain $\Omega_\Delta^{\theta^*,\phi^*}$ using Proposition 13.*
3. *Find the unique $u_{\boldsymbol{\psi}} \in \Omega_\Delta$ such that $f_\Delta(u_{\boldsymbol{\psi}}) = \psi^* \bmod 4\pi$ by simply inverting the function f_Δ (defined in Eq. (4.34)) on Ω_Δ.*

4.6 Application: Optimal control on SO(3)

In the context of many experiments (in NMR or quantum gate generation, for instance), the global phase of a unitary matrix U is not relevant, in the sense that the action of two opposite evolution operators U and $-U$ on an identical initial state ρ_0 results in identical states which are experimentally undistinguishable. The global phase issue has been discussed in [101, 102, 104]. In Ref. [101], the authors point out that the time to optimally generate U differs from that for $-U$. The control problem on SU(2) in this experimental context then translates as a control problem on the group of rotations SO(3).

The time-optimal control problem on SO(3) can be reformulated as follows: *Given two opposite unitary matrices U and $-U$, which one of U or $-U$ is the fastest to generate in the context of time-optimal control on* SU(2)*?* If $U^* \in \{U, -U\}$ denotes the answer to this question, then the time-optimal control $u(t)$ for generating U^* also corresponds to the time-optimal control for generating the associated rotation $\mathcal{R}^* \in \mathrm{SO}(3)$. In the following, we aim at answering the above question for any pair of unitary matrices U and $-U$. After considering the two classes of unitary matrices studied in Sec. 4.4.3 and 4.4.4 in the case without detuning, we finally find the class of $U \in \mathrm{SU}(2)$ such that U and $-U$ are optimally reached in the same time in both cases with and without detuning. In order to simplify the notations, the variables related to $-U$ will be denoted with the symbol $\widetilde{\cdot}$.

4.6.1 Case without detuning $\Delta = 0$

Rotation about the z axis.

Let $U = e^{i\lambda\frac{\sigma_z}{2}}$ as before and $-U = e^{i\widetilde{\lambda}\frac{\sigma_z}{2}}$. The parameter $\widetilde{\lambda} = \lambda - \mathrm{sign}(\lambda)\cdot 2\pi$ is chosen to be in the domain $\widetilde{\lambda} \in [-2\pi, 2\pi]$. Note that λ and $\widetilde{\lambda}$ have opposite signs. Using the equations for the final time given in Eq. (4.28), we deduce that:

Proposition 3 *The rotation $\mathcal{R}^* = \mathcal{R}(\lambda - \phi^*, 0, \phi^*)$ is optimally generated by U if $|\lambda| < \pi$ and by $-U$ otherwise. The time for generating U and that for $-U$ are the same when $|\lambda| = \pi$.*

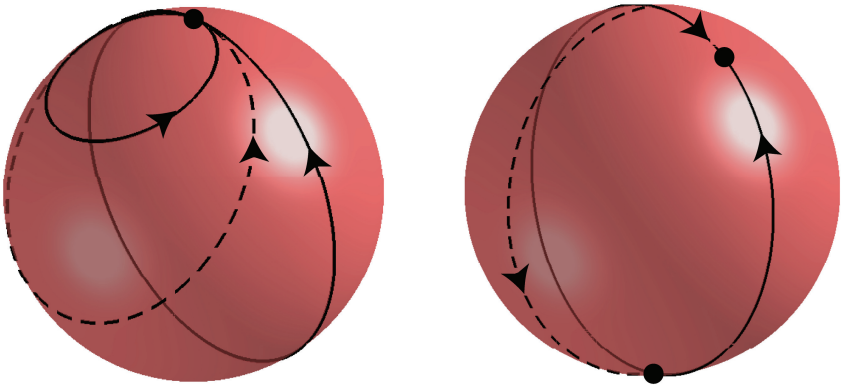

Figure 4.5: On both figures, the two full lines correspond to the trajectories for U^* and $-U^*$, where the dots correspond to the end points of the trajectories and the arrows to the travel direction. On the left, we see the projected trajectory of a z rotation where $U^* = e^{i\frac{\pi}{4}\frac{\sigma_z}{2}}$. On the right, the figure displays the projected trajectory of a rotation on the (x, y) plane where $U^* = e^{i\frac{\pi}{5}\frac{\sigma_y}{2}}$. The dashed lines are the trajectories for the limit case U such that $t^*(U) = t^*(-U)$.

Rotation in the (x, y) plane.

Let $U = e^{-ia\frac{\sigma_z}{2}} e^{ib\frac{\sigma_y}{2}} e^{ia\frac{\sigma_z}{2}}$ be a unitary matrix where the domains of definition are $a \in [-\pi, \pi]$ and $b \in (0, 2\pi)$. Let $-U = e^{-i\widetilde{a}\frac{\sigma_z}{2}} e^{i\widetilde{b}\frac{\sigma_y}{2}} e^{i\widetilde{a}\frac{\sigma_z}{2}}$ be the unitary matrix opposite

to U. In order to remain in the prescribed domain, $-U$ is characterized by $\widetilde{a} = a \pm \pi$ and $\widetilde{b} = 2\pi - b$ where the sign $\pm$ is chosen such that a and $\widetilde{a}$ have opposite signs. Using the equation for the final time given in Eqs. (4.29), we deduce that:

Proposition 4 *The rotation $\mathcal{R}^* := \mathcal{R}(-a, b, a)$ is optimally generated by U if $b < \pi$ and by $-U$ if $b > \pi$. The time for generating U and that for $-U$ are the same when $b = \pi$.*

In other words, for a rotation about any axis in the transverse plane, $t^* = \widetilde{t^*}$ if and only if U describes a π rotation about this axis.

General case.

In order to find which one of U and $-U$ is the fastest to generate in the most general case, we proceed as before by first finding the class of unitary matrices satisfying $t^* = \widetilde{t^*}$. We have already seen that $\pm\pi$ rotations about the z axis or any axis in the transverse plane are such that the associated U and $-U$ matrices are optimally reached in the same time. Let us now consider a general rotation $\mathcal{R}(\psi^*, \theta^*, \phi^*)$ about any axis which is not included in the two families already treated and let U and $-U$ be the two unitary matrices generating this rotation. We aim at finding the criterion that should be filled by $\mathcal{R}$ in order to have $t^* = \widetilde{t^*}$.

First, we know from Proposition 1 that the final time t^* for reaching U is equal to half of the length of the projected trajectory γ. Consequently, since $t^* = \widetilde{t^*}$, γ and $\widetilde{\gamma}$ have the same length. Coming back to the Hopf parametrization, and writing the parameters for $-U$ as a function of U, we get:

$$\widetilde{\theta_1^*} = \theta_1^* \quad \text{and} \quad \widetilde{\theta_2^*} = \theta_2^* - \text{sign}(\theta_2^*)\pi. \tag{4.36}$$

In particular, the Euler variables θ^* and $\widetilde{\theta^*}$ are equal. Summarizing what has been deduced so far, γ and $\widetilde{\gamma}$ have the same length and end up at the same inclination angle θ^* while describing a circle on the sphere starting at the North Pole. The only possibility is that γ and $\widetilde{\gamma}$ describe a circle of identical radius, but one clockwise and the other anti-clockwise since θ_2^* and $\widetilde{\theta_2^*}$ have opposite signs. In fact, we can deduce that $\theta_2^* = -\widetilde{\theta_2^*}$ and inserting this relation in Eq. (4.36), the condition for U such that $t^* = \widetilde{t^*}$ is

$$\theta_2^* = \pm\frac{\pi}{2}. \tag{4.37}$$

In other words, the unitary matrices corresponding to π-rotations ($\mathcal{R}$) about *any* axis are the ones which take as much time to generate as their opposite. This can be seen using the quaternion parametrization introduced in Sec. 4.2. Indeed, $\theta_2^* = \pm\frac{\pi}{2}$ implies that $x_1 = 0$ in Eq. (4.6). In terms of quaternions, this leads to $x_1 = \cos(\alpha/2)$ from which we deduce that $\alpha = \pm\pi$. Recalling that α denotes the rotation angle of U about a given axis, the rotation associated with $\theta_2^* = \pm\frac{\pi}{2}$ is a $\pm\pi$-rotation about this axis (see Fig. 4.6). Finally, we deduce:

Proposition 5 *Let $U \in \text{SU}(2)$ and θ_2^* be the corresponding Hopf parameter. Then $t^* < \widetilde{t^*} \iff |\theta_2^*| < \frac{\pi}{2}$. In particular, $t^* = \widetilde{t^*} \iff |\theta_2| = \frac{\pi}{2}$.*

Figure 4.6 shows the optimal time to generate unitary matrices defined according to their quaternion's definition given in Eq. (4.5). Three axes $\vec{n}_y$, $\frac{1}{\sqrt{2}}(\vec{n}_y + \vec{n}_z)$ and $\vec{n}_z$ are

considered, corresponding to an axis progressively tilted from the (x, y) plane to the z axis. Note the monotonic evolution of the time function on the intervals $[0, 2\pi]$ and $[2\pi, 4\pi]$ in Fig. 4.6. As expected, the matrices satisfying $t^* = \widetilde{t^*}$ (intersection of the solid and dashed lines) are exactly the ones for which $\alpha = \pi + k \cdot 2\pi$. At these points (black dots), the corresponding rotations for $\vec{n} = \vec{n}_y$ and $\vec{n} = \frac{1}{\sqrt{2}}(\vec{n}_y + \vec{n}_z)$ are the well-known refocusing [8, 70] and Hadamard gates [80], respectively.

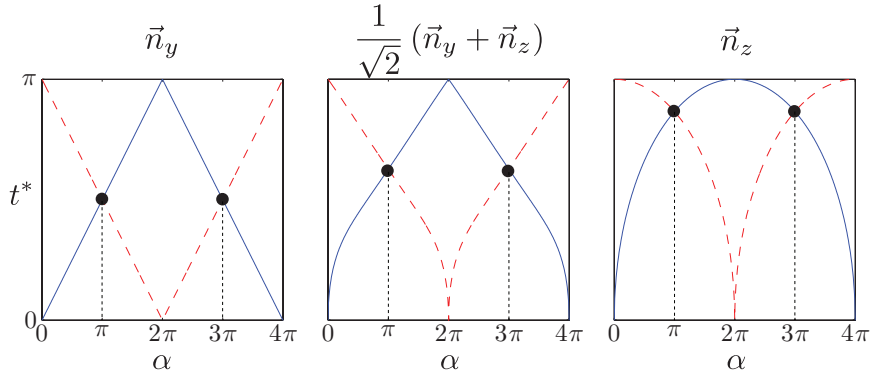

Figure 4.6: Plot of the minimum time t^* to generate the rotations around the $\vec{n}_y$, $\frac{1}{\sqrt{2}}(\vec{n}_y + \vec{n}_z)$ and $\vec{n}_z$ axes as a function of the rotation angle α. The blue (solid) and red (dashed) curves represent the time to generate U and $-U$ respectively. The black dots and vertical dotted lines underline the angles α for which $t^* = \widetilde{t^*}$. These angles are $\alpha = \pi, 3\pi$, as expected (see Eq. (4.37)).

4.6.2 With detuning

Let us consider a target of the form $U = (\psi^*, \theta^*, \phi^*)$. Recall that we are interested in answering the question: *Given $\Delta \neq 0$, which target among U and $-U$ is the fastest to generate?* Or equivalently, if $\mathrm{T}_{\mathrm{diff}}(\Delta) := T(U, \Delta) - T(-U, \Delta)$ is the "difference time" function, *for which values Δ does the $\mathrm{T}_{\mathrm{diff}}$ function change sign?* Here, $T(U, \Delta)$ denotes the duration of the time-optimal control generating U under a detuning term Δ. In order to answer the question, we can of course proceed algorithmically by finding the time-optimal controls for U and $-U$ respectively using the results of Section 4.5.2 and then comparing the duration of the two corresponding controls. But here, we aim at understanding under which conditions the function $\mathrm{T}_{\mathrm{diff}}$ changes sign at a specific value of Δ.

There are two controls of particular interest denoted by $u_{\boldsymbol{\psi}_+}$ and $u_{\boldsymbol{\psi}_-}$, where $\boldsymbol{\psi}_\pm := -\phi^* \pm \pi$. They are special since they correspond to the only two controls (θ^*, ϕ^* being fixed) which generate two opposite matrices $U := (\boldsymbol{\psi}_+, \theta^*, \phi^*)$ and $-U := (\boldsymbol{\psi}_-, \theta^*, \phi^*)$ in the same time $T(u_{\boldsymbol{\psi}_+}) = T(u_{\boldsymbol{\psi}_-})$. Let us split the full detuning domain $\mathbb{R}$ into two regions, X and $\mathbb{R}/X$, where $X := \{\Delta \mid \text{both } u_{\boldsymbol{\psi}_+}, u_{\boldsymbol{\psi}_-} \in \Omega_\Delta\}$.

When $\Delta \in X$, we can show that $u_{\boldsymbol{\psi}_+}$ is the optimal control generating U^* if and only if $u_{\boldsymbol{\psi}_-}$ is the optimal control generating $-U^*$ or vice-versa. In particular, the values of Δ for which $u_{\boldsymbol{\psi}_+}$ and $u_{\boldsymbol{\psi}_-}$ are the optimal controls of U^* and $-U^*$ are the ones for which the time difference function $\mathrm{T}_{\mathrm{diff}}$ is equal to zero since $T(u_{\boldsymbol{\psi}_+}) = T(u_{\boldsymbol{\psi}_-})$. These values of Δ are easily found to be $\Delta = -\frac{\phi^* + \psi^* \pm \pi + n \cdot 4\pi}{2T(u_{\boldsymbol{\psi}_\pm})}$ for a certain $n \in \mathbb{Z}$.

When $\Delta \notin X$, at least one of the two controls $u_{\boldsymbol{\psi}_\pm}$ is not time-optimal such that the

time difference function $\mathrm{T_{diff}}$ is never zero on the set $\mathbb{R}/X$. Since the time-optimal control domain Ω_Δ as well as the optimal control $u_{\boldsymbol{\psi}}$ of U^* (or of $-U^*$) vary smoothly with Δ (this means that the angle $\boldsymbol{\psi}$ defining $u_{\boldsymbol{\psi}}$ is smooth), the function $\mathrm{T_{diff}}$ also varies smoothly with respect to Δ except when the time-optimal control jumps between extremities of Ω_Δ. This occurs when the optimal control for one of two unitary matrices U or $-U$ jumps between $u_{\boldsymbol{\psi}_{\min}}$ and $u_{\boldsymbol{\psi}_{\max}}$ for an infinitesimal variation of Δ. We can summarize the previous discussion by the following Proposition.

Proposition 6 *For $\Delta \in X$, the function $\mathrm{T_{diff}}$ changes sign $\iff$ $\Delta = -\frac{\phi^*+\psi^* \pm \pi + n\cdot 4\pi}{2T(u_{\boldsymbol{\psi}_\pm})}$ for a certain $n \in \mathbb{Z}$. Moreover, $\mathrm{T_{diff}} = 0$ at these points. For $\Delta \in \mathbb{R}/X$, the function $\mathrm{T_{diff}}$ changes sign if and only if the time-optimal control for U or $-U$ is $u_{\boldsymbol{\psi}_{min/max}}$.*

An example of application of Proposition 6 is depicted in Fig. 4.7 for the unitary matrices $U = (\psi^*, \theta^*, \phi^*) = (0, 1.9897, 0)$ and $-U$. The upper graph shows the optimal time for generating unitaries U and $-U$ as a function of Δ. For each value of Δ, the time-optimal domain Ω_Δ is given by the two enveloping black curves on the lower graph. As long as both $u_{\boldsymbol{\psi}_\pm} \in \Omega_\Delta$ (region X), the optimal times $T(U, \Delta)$ and $T(-U, \Delta)$ vary continuously between the shortest and longest times and the two curves meet (black dots on Fig.4.7 (a)) when their two time-optimal controls are exactly $u_{\boldsymbol{\psi}_\pm}$ (black dots on Fig.4.7 (b)). As soon as one of $u_{\boldsymbol{\psi}_\pm}$ is not in Ω_Δ anymore ($\Delta \in \mathbb{R}/X$), the time functions stop crossing but jump one above the other when the optimal controls (curves of the lower graph) reach the limits of Ω_Δ. Three other examples are given in Fig. 4.8.

The detailed derivation of the results summarized above is presented in Appendix 4.8.9.

4.7 Conclusion

In this work, we have investigated the time-optimal control of SU(2) quantum operations by a bounded external field with two components along the x and y directions. We have analyzed a control problem where the rotating wave approximation provides a valid simplification of the dynamics of the system. We have considered two different situations, with and without a constant detuning term. We have shown that geometric optimal control techniques provide a systematic way to attack such control problems, leading to the complete description of the pulse sequences. Furthemore, we have studied the basic model of a two-level quantum system in order to highlight the geometric structure of the control. Such results could be applied to more complicated systems such as the one presented in Ref. [88], where the control of three coupled spins can be reduced to SU(2) operations.

4.8 Appendices

This section is dedicated to giving most of the details which have been left aside to seamlessly present the main results and ideas. The reader will find here the technical proofs of the main results as well as preliminary results on which they are based. For more complicated results, additional information and explanations support the proofs and in order to ease the legibility of these explanations for the reader seeking for an overview of the ideas only, the proofs are delimited in grey areas in the whole section.

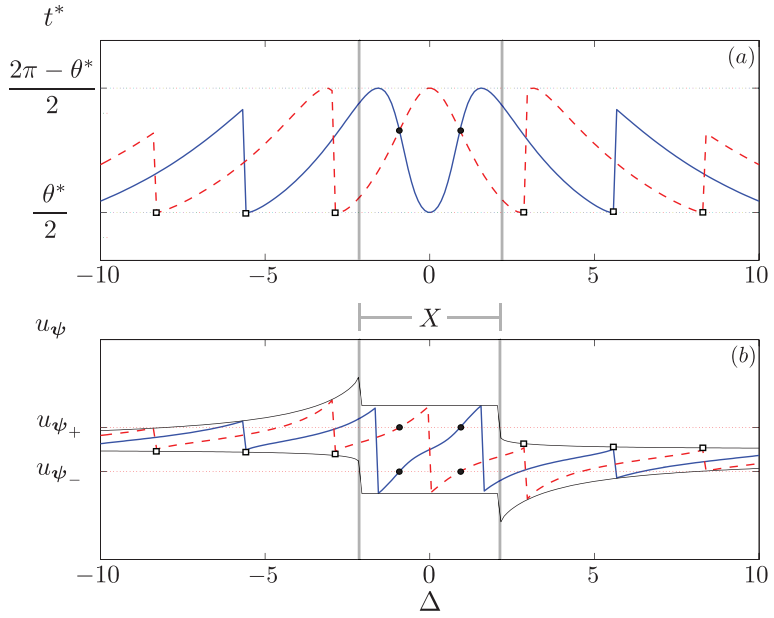

Figure 4.7: (a) Time-optimal durations $T(U, \Delta)$ and $T(-U, \Delta)$ to generate $U = (0, 2.2689, 0)$ (blue/solid line) and $-U$ (red/dashed line) as a function of the detuning Δ. (b) Time-optimal controls u_ψ of U (blue/solid line) and $-U$ (red/dashed line) respectively as a function of the detuning Δ. The region defined by the two black curves represents the time-optimal domain Ω_Δ for each value of Δ. The time difference function $\mathrm{T_{diff}}$ stops being continuous when both u_{ψ_+} and u_{ψ_-} do not belong to Ω_Δ (domain X defined by the two vertical lines). The black dots and the white squares represent the values of Δ for which $\mathrm{T_{diff}}$ changes sign for $\Delta \in X$ and $\Delta \in \mathbb{R}/X$ respectively.

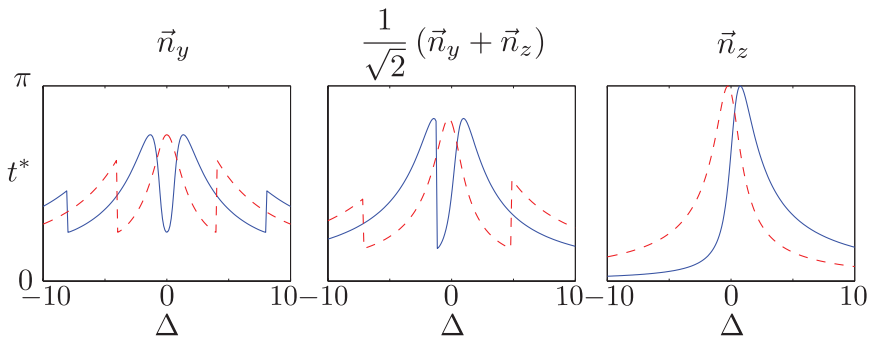

Figure 4.8: Evolution of the minimum time t^* as a function of Δ for rotations around the three axes $\vec{n}_y$, $\frac{1}{\sqrt{2}}(\vec{n}_y + \vec{n}_z)$ and $\vec{n}_z$. The rotation angle is fixed to $\alpha = \pi/2$.

4.8.1 Derivation of the dynamical Equations (4.7)

Proposition 7 *The translation of the Schrödinger equation* (4.3) *in terms of Hopf variables gives rise to the following system of three equations:*

$$\begin{pmatrix} \dot{\theta}_1 \\ \dot{\theta}_2 \\ \dot{\theta}_3 \end{pmatrix} = \begin{pmatrix} u_1 \\ -\tan\theta_1 \; u_2 - \Delta \\ \cot\theta_1 \; u_2 - \Delta \end{pmatrix}.$$

Proof. Let us write the quantum Hamiltonian (4.1) in terms of the normalized variables $v_i := \frac{\omega_i}{\omega_{\max}}$ and $\Delta = \frac{\omega}{\omega_{\max}}$ using the Quaternions notation introduced in Section 4.2.2 [a] :

$$\mathrm{H} = v_x\sigma_x + v_y\sigma_y + \Delta\sigma_z = -i(v_x\mathbf{k} + v_y\mathbf{j} + \Delta\mathbf{i}).$$

Using the definition of $U = x_1\mathbb{1} + x_2\mathbf{i} + x_3\mathbf{j} + x_4\mathbf{k}$ given in Eq. (4.4), the Schrödinger equation (4.3) translates into

$$\begin{array}{rcl} i\partial_t U(t) & = & \mathrm{H}(t)U(t) \\ & \Longleftrightarrow & \\ \partial_t U(t) & = & -i\mathrm{H}(t)U(t) \\ & \Longleftrightarrow & \\ \dot{x}_1 + \dot{x}_2\mathbf{i} + \dot{x}_3\mathbf{j} + \dot{x}_4\mathbf{k} & = & -(\Delta\mathbf{i} + v_y\mathbf{j} + v_x\mathbf{k}) \cdot (x_1\mathbb{1} + x_2\mathbf{i} + x_3\mathbf{j} + x_4\mathbf{k}) \\ & \Longleftrightarrow & \\ \begin{pmatrix} \dot{x_1} \\ \dot{x_2} \\ \dot{x_3} \\ \dot{x_4} \end{pmatrix} & = & L_{iH} \begin{pmatrix} x_1 \\ x_2 \\ x_3 \\ x_4 \end{pmatrix} \end{array}$$

where

$$L_{iH} = \begin{pmatrix} 0 & \Delta & v_y & v_x \\ -\Delta & 0 & v_x & -v_y \\ -v_y & -v_x & 0 & \Delta \\ -v_x & v_y & -\Delta & 0 \end{pmatrix}.$$

Now, noticing that the coordinates x_i can be written in terms of the Hopf parameters as

$$\begin{array}{rl} x_1 & = \cos\theta_1 \cos\theta_2, \\ x_2 & = \cos\theta_1 \sin\theta_2, \\ x_3 & = \sin\theta_1 \cos\theta_3, \\ x_4 & = \sin\theta_1 \sin\theta_3, \end{array}$$

where we set the variable $r = 1$, we deduce by straightforward calculations that

$$\begin{pmatrix} \dot{x}_1 \\ \dot{x}_2 \\ \dot{x}_3 \\ \dot{x}_4 \end{pmatrix} = T \begin{pmatrix} \dot{r} \\ \dot{\theta}_1 \\ \dot{\theta}_2 \\ \dot{\theta}_3 \end{pmatrix}$$

where

$$T = \begin{pmatrix} \cos\theta_1\cos\theta_2 & -\sin\theta_1\cos\theta_2 & -\cos\theta_1\sin\theta_2 & 0 \\ \cos\theta_1\sin\theta_2 & -\sin\theta_1\sin\theta_2 & \cos\theta_1\cos\theta_2 & 0 \\ \sin\theta_1\cos\theta_3 & \cos\theta_1\cos\theta_3 & 0 & -\sin\theta_1\sin\theta_3 \\ \sin\theta_1\sin\theta_3 & \cos\theta_1\sin\theta_3 & 0 & \sin\theta_1\cos\theta_3 \end{pmatrix}.$$

The matrix T is invertible when $\theta_1 \neq \frac{n\pi}{2}$ for $n \in \mathbb{N}$ with inverse

$$T^{-1} = \begin{pmatrix} \cos\theta_1\cos\theta_2 & \cos\theta_1\sin\theta_2 & \sin\theta_1\cos\theta_3 & \sin\theta_1\sin\theta_3 \\ -\sin\theta_1\cos\theta_2 & -\sin\theta_1\sin\theta_2 & \cos\theta_1\cos\theta_3 & \cos\theta_1\sin\theta_3 \\ -\sec\theta_1\sin\theta_2 & \sec\theta_1\cos\theta_2 & 0 & 0 \\ 0 & 0 & -\csc\theta_1\sin\theta_3 & \csc\theta_1\cos\theta_3 \end{pmatrix}.$$

The dynamics of the system can now be described in terms of the Hopf variables:

$$\begin{pmatrix} \dot{r} \\ \dot{\theta}_1 \\ \dot{\theta}_2 \\ \dot{\theta}_3 \end{pmatrix} = T^{-1} L_{iH} \begin{pmatrix} \cos\theta_1 \cos\theta_2 \\ \cos\theta_1 \sin\theta_2 \\ \sin\theta_1 \cos\theta_3 \\ \sin\theta_1 \sin\theta_3 \end{pmatrix}.$$

Knowing that $\dot{r} = 0$, the remaining above equality reduces to

$$\begin{pmatrix} \dot{\theta}_1 \\ \dot{\theta}_2 \\ \dot{\theta}_3 \end{pmatrix} = \begin{pmatrix} -v_x \sin(\theta_2+\theta_3) - v_y \cos(\theta_2+\theta_3) \\ \tan\theta_1 [\ v_x \cos(\theta_2+\theta_3) - v_y \sin(\theta_2+\theta_3)] - \Delta \\ \cot\theta_1 [-v_x \cos(\theta_2+\theta_3) + v_y \sin(\theta_2+\theta_3)] - \Delta \end{pmatrix}.$$

Finally, using the transformation (4.8) defining the "rotated controls"

$$\begin{aligned} u_1 &= -v_0 \sin(\mu+\theta_2+\theta_3) \\ &= -v_x \sin(\theta_2+\theta_3) - v_y \cos(\theta_2+\theta_3), \\ u_2 &= -v_0 \cos(\mu+\theta_2+\theta_3) \\ &= -v_x \cos(\theta_2+\theta_3) + v_y \sin(\theta_2+\theta_3), \end{aligned}$$

where one used the definition of the control v given in Eq. (4.2), we finally get the dynamical equations (4.7):

$$\begin{pmatrix} \dot{\theta}_1 \\ \dot{\theta}_2 \\ \dot{\theta}_3 \end{pmatrix} = \begin{pmatrix} u_1 \\ -\tan\theta_1\ u_2 - \Delta \\ \cot\theta_1\ u_2 - \Delta \end{pmatrix}.$$

[a] We recall that the basis elements of the quaternion field are taken to be $\mathbb{1} = \left(\begin{smallmatrix} 1 & 0 \\ 0 & 1 \end{smallmatrix}\right)$, $\mathbf{i} = i\sigma_z$, $\mathbf{j} = i\sigma_y$ and $\mathbf{k} = i\sigma_x$.

4.8.2 Constants of motion and linear evolution of the regular controls

We recall here the definition of β given in Eq. (4.22) ,

$$\beta(t) := [\mu(t) + \psi(t)],$$

which denotes the angular parametrization of the rotated controls controls $u(t)$ such that they take the form (see (4.8))

$$\begin{aligned} u_1(t) &= -\sin\beta(t), \\ u_2(t) &= -\cos\beta(t). \end{aligned} \tag{4.38}$$

Recall that the adjoint variable p_3 is zero on extremal trajectories, as explained in the last paragraph of Section 4.3.1.

Lemma 1 *The angular parameter β satisfies $\dot{\beta} = \mathrm{p}_2 \sec^2\theta_1$.*

Proof. $\dot{\beta} \overset{(4.38)}{=} \frac{\dot{u}_1}{u_2} \overset{(4.15)}{=} \frac{\dot{p}_1}{-\mathrm{p}_2 \tan\theta_1} \overset{(4.20)}{=} \frac{-\mathrm{p}_2^2 \tan\theta_1 \sec^2\theta_1}{-\mathrm{p}_2 \tan\theta_1} = \mathrm{p}_2 \sec^2\theta_1$. ■

As a corollary, we find that the phase $\mu(t)$ of the regular controls $v(t)$, defined in Eq. (4.2), evolves linearly in time.

Corollary 1 $\mu(t) = \mu(0) + 2(\mathrm{p}_2 + \Delta)t$.

Proof. $\dot{\mu} \overset{(4.22)}{=} \dot{\beta} - \dot{\psi} \overset{(4.10)}{=} \dot{\beta} - \dot{\theta}_2 - \dot{\theta}_3 \overset{(4.20),Lem.\ 1}{=} 2(\mathrm{p}_2 + \Delta)$. ∎

Corollary 2 $\dot{\mu} + \dot{\psi} - \dot{\phi} = 0$.

Proof. $\dot{\mu} + \dot{\psi} - \dot{\phi} \overset{(4.22)}{=} \dot{\beta} - \dot{\phi} \overset{(4.10)}{=} \dot{\beta} - \dot{\theta}_2 + \dot{\theta}_3 \overset{(4.20),Lem.\ 1}{=} 0$. ∎

4.8.3 Singular controls and their associated trajectories

Let us express the dynamics (4.7) in terms of the Euler parameters using Eqs. (4.10):

$$\begin{pmatrix} \dot{\psi} \\ \dot{\theta} \\ \dot{\phi} \end{pmatrix} = \begin{pmatrix} u_2(-\tan\theta_1 + \cot\theta_1) - 2\Delta \\ 2u_1 \\ u_2(-\tan\theta_1 - \cot\theta_1) \end{pmatrix}. \tag{4.39}$$

Recall that singular controls correspond to controls for which $N = 0$, *i.e.* to controls vanishing a.e. [25]. We can see it by noticing that N is proportional to $\sqrt{u_1^2 + u_2^2}$ (see Eqs. (4.15) and (4.16)). After setting $u_1 = u_2 = 0$ in Eqs. (4.39), the differential equations simply become

$$\begin{pmatrix} \dot{\psi} \\ \dot{\theta} \\ \dot{\phi} \end{pmatrix} = \begin{pmatrix} -2\Delta \\ 0 \\ 0 \end{pmatrix},$$

and are directly integrable. On the time interval $[t_0, t_1]$, the trajectory at time $t \in [t_0, t_1]$ is then given by

$$\psi(t) = \psi(t_0) - 2\Delta(t - t_0), \tag{4.40a}$$
$$\theta(t) \equiv \theta(t_0), \tag{4.40b}$$
$$\phi(t) \equiv \phi(t_0). \tag{4.40c}$$

The projected trajectory $\gamma(t) := (\theta(t), \phi(t))$ (see the statement of Proposition 1) associated with a singular control is then reduced to the point $\gamma(t) = (\theta_0, \phi_0)$ while the remaining parameter $\psi(t)$ evolves with constant velocity $\dot{\psi} = -2\Delta$.

We conclude this section devoted to singular controls and trajectories with a direct Corollary of the above Eqs. (4.40) that is later needed to determine the time-optimal controls.

Corollary 3 *Let $U^* = e^{i\lambda^* \frac{\sigma_z}{2}}$ be a target propagator such that $\lambda^* \in [0, 4\pi \cdot \mathrm{sign}(-\Delta)]$ and consider the singular control generating U^* after a time t_{sing} starting at $t_0 = 0$ from the identity. Then*

(i) $t_{\mathrm{sing}} = -\frac{\lambda^*}{2\Delta}$;

(ii) $\phi(0) = \lambda^* - \psi^*$.

Proof. Using the hypothesis $t_0 = 0$, the first relation is a direct consequence of the equalities:
$t_{\mathrm{sing}} \overset{Eq.\ (4.40a)}{=} \frac{\psi(t)-\psi(0)}{-2\Delta} \overset{Eq.\ (4.40c)}{=} \frac{\psi(t)+\phi(t)-\phi(0)-\psi(0))}{-2\Delta} \overset{\theta_2(0)=0}{=} \frac{\psi(t)+\phi(t)}{-2\Delta} = \frac{\lambda^*}{-2\Delta}$.

The second relation follows directly from Eq. (4.40c) together with the definition of $\lambda^* := \phi^* + \psi^* = \phi(0) + \psi^*$. ∎

4.8.4 Regular controls and their associated trajectories

The proof of the main result about the shape of regular trajectories requires the use of the following Lemma, which links the phase of the rotated control β to the Euler parameter ϕ.

Lemma 2 $\dot{\beta} = \dot{\phi}$.

Proof. $\dot{\beta} - \dot{\phi} \overset{(4.10)}{=} \dot{\beta} - \dot{\theta}_2 + \dot{\theta}_3 \overset{(4.20),Lem.\ 1}{=} 0$. ∎

We now have everything in hand to prove Proposition 1, that we recall here.

Proposition 1 *Let* $\bar{\theta} = \arctan(\frac{1}{\mathrm{p}_2})$ *and* $\bar{\phi} = \phi(0) - \beta(0)$. *The projected trajectory* $\gamma(t) = (\theta(t), \phi(t))$ *defines a circle around the fixed axis* $\vec{n} = (\bar{\theta}, \bar{\phi})$. *Moreover,* $\gamma(t)$ *is traveled with constant speed* $\|\dot{\gamma}(t)\| = 2$. *The final time* $T(u)$ *is equal to* $\frac{1}{2}$ *the arc length of* $\gamma(t)$.

The reader is directed to Fig. 4.1 for a visual representation of the different variables encountered in the proof.

Proof. Let $\gamma : [0, t^*] \longrightarrow S^2$ be the path on the sphere described by the Euler angles $\theta(t)$ and $\phi(t)$ and let $\vec{\gamma}(t) := (\sin\theta(t)\cos\phi(t), \sin\theta(t)\sin\phi(t), \cos\theta(t))$ denote the vector in $\mathbb{R}^3$ defined by the point $\gamma(t)$. We first show that $\vec{\gamma}(t) \cdot \vec{n} \equiv \cos\bar{\theta}$ for all t proving that $\gamma(t)$ lies in a plane orthogonal to $\vec{n}$. As $\vec{\gamma}(t)$ also lies on a sphere and since the intersection of a plane and a sphere is a circle, this then proves that the projected trajectory $\gamma(t)$ lies on a circle.

Dropping some trivial manipulations, we have:

$$\begin{aligned}\vec{\gamma}(t) \cdot \vec{n} &= \sin\theta\sin\bar{\theta}(\cos\phi\cos\bar{\phi} + \sin\phi\sin\bar{\phi}) + \cos\theta\cos\bar{\theta} \\ &= \sin\theta\sin\bar{\theta}\cos(\phi - \bar{\phi}) + \cos\theta\cos\bar{\theta} \\ &= \sin\theta\sin\bar{\theta}\cos\beta + \cos\theta\cos\bar{\theta}\end{aligned}$$

where we have used the definition of $\bar{\phi}$ and Lemma 2 to write $\phi - \bar{\phi} = \beta$. Factorizing by $\cos\bar{\theta}$ and using $\bar{\theta} := \arctan(\frac{1}{\mathrm{p}_2})$, the precedent equality becomes

$$\begin{aligned}\vec{\gamma}(t) \cdot \vec{n} &= \cos\bar{\theta}(\tan\bar{\theta}\sin\theta\cos\beta + \cos\theta) \\ &= \cos\bar{\theta}(\sin\theta\tan\theta_1 + \cos\theta)\end{aligned}$$

where we used $\cos\beta \overset{(4.38)}{=} -u_2 \overset{(4.15)}{=} \mathrm{p}_2\tan\theta_1$ to deduce the last equality. As $\theta_1 = \frac{\theta}{2}$, we finally conclude that

$$\begin{aligned}\vec{\gamma}(t) \cdot \vec{n} &= \cos\bar{\theta}(\sin\theta\tan\tfrac{\theta}{2} + \cos\theta) \\ &= \cos\bar{\theta}.\end{aligned}$$

It remains to show that the trajectory runs with a constant speed 2 on the circle. We use the two relations $\dot{\theta} = 2\dot{\theta}_1 = 2u_1$ and $\dot{\phi} = -u_2(\tan\theta_1 + \cot\theta_1)$ obtained from

Eq. (4.7) and the definition of $\dot{\phi} := \dot{\theta}_2 - \dot{\theta}_3$. After some simplifications, we obtain:

$$\begin{aligned} \|\vec{\dot{\gamma}}(t)\|^2 &= [\dot{\theta}\cos\theta]^2 + [\dot{\phi}\sin\theta]^2 + [\dot{\theta}\sin\theta]^2 \\ &= [\dot{\theta}]^2 + [\dot{\phi}\sin\theta]^2 \\ &= [2u_1]^2 + [-u_2(\tan\theta_1 + \cot\theta_1)\sin 2\theta_1]^2 \\ &= [2u_1]^2 + [-2u_2]^2 \\ &= 4\|u\|^2 \\ &= 4. \ \blacksquare \end{aligned}$$

Proposition 1 contains all the information needed to write the time-evolution of a propagator $U \in \mathrm{SU}(2)$ governed by a regular control u. In terms of Euler parameters, the trajectory $U(t)$ is given by

$$\begin{aligned} &\theta(t) = \cos^{-1}(1 + \sin^2\bar{\theta}(\cos\eta(t) - 1)), \\ &\phi(t) = \phi(0) + \mathrm{sign}(\mathrm{p}_2)\tfrac{\pi}{2} + \tan^{-1}\left(\tfrac{\sin\eta(t)}{\cos\bar{\theta}(\cos\eta(t)-1)}\right), \\ &\psi(t) = -2\phi(0) + \phi(t) - 2(\mathrm{p}_2 + \Delta)t, \end{aligned}$$

where $\eta(t) := \frac{2t}{\sin\bar{\theta}}$ is the angular parametrization of the circle section drawn by $\gamma(t)$ around its axis $\bar{n}$ (see Fig. 4.1).
We now show how to derive the three above equations.

Given p_2 and $\phi(0)$, we know that the projected trajectory $\gamma(t) = (\theta(t), \phi(t))$ traces out a circle on the sphere about the axis defined by $\bar{\theta} = \arctan(\frac{1}{\mathrm{p}_2})$ and $\bar{\phi} = \phi(0) - \beta(0)$. As a first step to deduce the trajectory of regular controls, let us first derive the trajectory of the two Euler variables $\theta(t)$ and $\phi(t)$. To do so, we have to find the parametrization of a circle starting at the North Pole and evolving linearly about the axis $\bar{n}$ given above. Let $\eta(t) = \frac{2t}{\sin\bar{\theta}}$ the parametrization of the circle relative to the axis $\bar{n}$. The radius r of the circle is $r = \sin\bar{\theta}$.

Starting with a circle of radius r in the xy plane with $\eta(0)$ in position $(-r, 0, 0)$, this circle is parametrized by $\gamma_1 = (x_1, y_1, z_1)$ where

$$\begin{bmatrix} x_1 \\ y_1 \\ z_1 \end{bmatrix} = \begin{bmatrix} -r\cos\eta \\ -r\sin\eta \\ 0 \end{bmatrix}.$$

In particular, at time $t = 0$, $\gamma_1(0) = (x_1, y_1, z_1)|_{t=0} = (-r, 0, 0)$. Then applying the rotation $R_y(\bar{\theta})$ to this circle gives it its final inclination with respect to the z axis. The resulting tilted circle $\gamma_2(t) = (x_2, y_2, z_2)$ is obtained from the previous one by

$$\begin{bmatrix} x_2 \\ y_2 \\ z_2 \end{bmatrix} = \begin{bmatrix} \cos\bar{\theta} & & \sin\bar{\theta} \\ & 1 & \\ -\sin\bar{\theta} & & \cos\bar{\theta} \end{bmatrix} \begin{bmatrix} x_1 \\ y_1 \\ z_1 \end{bmatrix}.$$

Now, at time $t = 0$, the initial position is $\gamma_2(0) = (x_2, y_2, z_2)|_{t=0} = (-r\cos\bar{\theta}, 0, r\sin\bar{\theta})$. We now translate the circle upward and forward such that the initial point $\gamma_3(0)$ lies at the North pole. That is, the translated tilted circle γ_3 should satisfy $\gamma_3(0) = (x_3, y_3, z_3)|_{t=0} = (0, 0, 1)$. The translation of γ_2 by the vector $[r\cos\bar{\theta}, 0, 1 - r\sin\bar{\theta}]^t$ gives:

$$\begin{bmatrix} x_3 \\ y_3 \\ z_3 \end{bmatrix} = \begin{bmatrix} x_2 \\ y_2 \\ z_2 \end{bmatrix} + \begin{bmatrix} r\cos\bar{\theta} \\ 0 \\ 1 - r\sin\bar{\theta} \end{bmatrix}.$$

The parametric variables for the *actual* trajectory $\gamma_3(t)$ is then

$$\begin{aligned}
\begin{bmatrix} x_3 \\ y_3 \\ z_3 \end{bmatrix} &= \begin{bmatrix} x_2 \\ y_2 \\ z_2 \end{bmatrix} + \begin{bmatrix} r\cos\bar{\theta} \\ 0 \\ 1 - r\sin\bar{\theta} \end{bmatrix} \\
&= \begin{bmatrix} \cos\bar{\theta} & & \sin\bar{\theta} \\ & 1 & \\ -\sin\bar{\theta} & & \cos\bar{\theta} \end{bmatrix} \begin{bmatrix} x_1 \\ y_1 \\ z_1 \end{bmatrix} + \begin{bmatrix} r\cos\bar{\theta} \\ 0 \\ 1 - r\sin\bar{\theta} \end{bmatrix} \\
&= \begin{bmatrix} \cos\bar{\theta} & & \sin\bar{\theta} \\ & 1 & \\ -\sin\bar{\theta} & & \cos\bar{\theta} \end{bmatrix} \begin{bmatrix} -r\cos\eta \\ -r\sin\eta \\ 0 \end{bmatrix} + \begin{bmatrix} r\cos\bar{\theta} \\ 0 \\ 1 - r\sin\bar{\theta} \end{bmatrix} \\
&= \begin{bmatrix} -r\cos\bar{\theta}\cos\eta \\ -r\sin\eta \\ r\sin\bar{\theta}\cos\eta \end{bmatrix} + \begin{bmatrix} r\cos\bar{\theta} \\ 0 \\ 1 - r\sin\bar{\theta}) \end{bmatrix} \\
&= \begin{bmatrix} -r\cos\bar{\theta}\cos\eta + r\cos\bar{\theta} \\ -r\sin\eta \\ r\sin\bar{\theta}\cos\eta + 1 - r\sin\bar{\theta} \end{bmatrix} \\
&= \begin{bmatrix} -\sin\bar{\theta}\cos\bar{\theta}\cos\eta + \sin\bar{\theta}\cos\bar{\theta} \\ -\sin\bar{\theta}\sin\eta \\ \sin\bar{\theta}\sin\bar{\theta}\cos\eta + 1 - \sin\bar{\theta}\sin\bar{\theta} \end{bmatrix}
\end{aligned}$$

where r has been replaced by its value $r = \sin\bar{\theta}$ to write the last equality. Factorizing some of the terms, the cartesian parametrization of γ_3 becomes

$$\begin{aligned}
x_3(t) &= -\sin\bar{\theta}\cos\bar{\theta}(\cos\eta - 1), \\
y_3(t) &= -\sin\bar{\theta}\sin\eta, \\
z_3(t) &= 1 + \sin^2\bar{\theta}(\cos\eta - 1),
\end{aligned}$$

and converting them into the spherical parameters, we obtain

$$\begin{aligned}
\theta_3(t) &= \cos^{-1}(z_3) \ = \cos^{-1}(1 + \sin^2\bar{\theta}(\cos\eta - 1)), \\
\phi_3(t) &= \tan^{-1}(\tfrac{y_3}{x_3}) = \tan^{-1}(\tfrac{\sin\eta}{\cos\bar{\theta}(\cos\eta - 1)})).
\end{aligned}$$

Now, γ_3 has been defined such that $\phi_3(0) = -\frac{\pi}{2}$ when η goes anti-clockwise and $\phi_3(0) = \frac{\pi}{2}$ when η goes clockwise, *i.e.* $\phi_3(0) = -\text{sign}(\mathrm{p}_2)\frac{\pi}{2}$ from the Lemma 3 below. The final trajectory, corresponding to the appropriate initial value of $\phi(0)$ is given by $\theta(t) := \theta_3(t)$ and $\phi(t) := \phi_3(t) + \epsilon\frac{\pi}{2} + \phi(0)$, that is:

$$\begin{aligned}
\theta(t) &= \cos^{-1}(1 + \sin^2\bar{\theta}(\cos\eta - 1)) \\
\phi(t) &= \phi(0) + \epsilon\tfrac{\pi}{2} + \tan^{-1}\left(\tfrac{\sin\eta}{\cos\bar{\theta}(\cos\eta - 1)}\right).
\end{aligned}$$

Finally, the time evolution of the variable ψ is deduced from the following series of equalities:

$$\begin{aligned}
\psi(t) - \psi(0) &\overset{Cor.\ 2}{=} \phi(t) - \phi(0) - [\mu(t) - \mu(0)] \\
&\overset{Cor.\ 1}{=} \phi(t) - \phi(0) - 2(\mathrm{p}_2 + \Delta)t \\
&\iff \\
\psi(t) &= \psi(0) - \phi(0) + \phi(t) - 2(\mathrm{p}_2 + \Delta)t
\end{aligned}$$

$\overset{\theta_2(0)=0}{=} -2\phi(0) + \phi(t) - 2(\mathrm{p}_2 + \Delta)t.$ ■

Use of the following Lemma has been made in the above proof.

Lemma 3 *$\gamma(t)$ goes anti-clockwise* $\iff \mathrm{p}_2 > 0$.

Proof. The projected trajectory $\gamma(t)$ runs anti-clockwise $\iff \dot{\phi} > 0 \overset{Lemma\ 2}{\iff} \dot{\beta} = \mathrm{p}_2 \sec^2\theta_1 > 0 \iff \mathrm{p}_2 > 0$. ■

4.8.5 Some initial conditions and relation between $\phi(0)$ and p_2

The initial values $\beta(0)$ and $\mu(0)$ of the angular controls are given by the following lemma.

Lemma 4 *At time $t = 0$, we have:*

(i) $p_1(0) = 1$;

(ii) $\beta(0) = -\frac{\pi}{2}$;

(iii) $\mu(0) = \phi(0) - \frac{\pi}{2}$.

Proof.

(i) At $t = 0$, $\theta_1(0) \overset{\text{Eq. (4.9)}}{=} 0 \implies \tan\theta_1(0) = 0 \overset{\text{Eq. (4.15)}}{\implies} u_2 = 0$. Since the control has maximum amplitude, this implies that $u_1 = \pm 1$. But as $\theta_1(0) = 0$ and $\theta_1(t) > 0$, $\dot{\theta}_1$ must satisfy $\dot{\theta}_1(0) = u_1(0) \geq 0$, *i.e.* $u_1(0) = p_1(0) = 1$.

(ii) The double equality $u_1(t) \overset{\text{Eq. (4.38)}}{=} -\sin\beta(t) \overset{\text{Eq. (4.15)}}{=} p_1(t)$ being satisfied for all $t \in [0, T(u)]$, it is also satisfied in $t = 0$ such that $-\sin\beta(0) = p_1(0) = 1$ from (i) such that $\beta = -\frac{\pi}{2}$.

(iii) $\mu(0) \overset{\text{Eq. (4.22)}}{=} \beta(0) - \psi(0) \overset{\text{(ii)}}{=} -\frac{\pi}{2} + \phi(0)$ where the last equality is deduced using Eq. (4.10) and the fact (see Eq. (4.9)) that $\theta_2(0) = 0$. ■

Given a regular control u and a (possibly null) detuning term Δ, the time evolution of the Euler variables given by Eqs. (4.32) corresponds to a set of three equations with two unknown parameters p_2 and $\phi(0)$. These two parameters are however related by the following equality.

Proposition 8 $\mathrm{p}_2 = \frac{\sin(\phi^* - \phi(0))}{\tan\frac{\theta^*}{2}}$.

Proof. Consider the double equality for the control component $-u_2 \overset{\text{Eq. (4.38)}}{=} \cos\beta \overset{\text{Eq. (4.15)}}{=} \mathrm{p}_2 \tan\frac{\theta}{2}$ where $\theta_1 \overset{\text{Eq. (4.10)}}{=} \frac{\theta}{2}$ has been used. When the target is reached, we then have $\cos\beta^* = \mathrm{p}_2 \tan\frac{\theta^*}{2}$. Now, a direct corollary of Lemma 2 is that $\beta^* = \beta(0) + \phi^* - \phi(0) \overset{\text{Lemma 4 (ii)}}{=} -\frac{\pi}{2} + \phi^* - \phi(0)$. We finally get

$\cos\beta^* = \cos(-\frac{\pi}{2} + \phi^* - \phi(0)) \equiv \sin(\phi^* - \phi(0)) = \mathrm{p}_2 \tan\frac{\theta^*}{2}$. ■

For a given target U^*, the value $\phi(0)$ can then be found at least numerically from the trajectory Eqs. (4.32). As discussed in the main text, the initial value $\phi(0)$ (and consequently all the other parameters) can be found analytically for the two particular classes of target propagators $U^* = e^{i\lambda\frac{\sigma_z}{2}}$ and $U^* = e^{-ia\frac{\sigma_z}{2}}e^{ib\frac{\sigma_y}{2}}e^{ia\frac{\sigma_z}{2}}$, which correspond respectively to "rotations" around the z axis and around an axis lying in the (x, y) plane.

4.8.6 Time-optimal controls

Using the PMP, we found (see Eq. 4.15) that time-optimal regular controls ($N \neq 0$) must *necessarily* have the form

$$u_1(t) = \frac{p_1}{N},$$
$$u_2(t) = \frac{-p_2\tan\theta_1 + p_3\cot\theta_1}{N},$$

Their associated trajectories have been derived in Appendix 4.8.4. When $N = 0$, we found that the singular controls vanish and their associated trajectories have been derived in Appendix 4.8.3. The two classes of controls, singular and regular, are said to be *extremal* controls as they satisfy Pontryagin's necessary condition of being potentially time-optimal. These two sets of controls, together with all their possible combinations, constitute the set of controls among which we have to find the time-optimal controls. The aim of the present section is to find the set of time-optimal controls, denoted Ω_Δ, for a system undergoing a drift term Δ. To do so, we first find the set Ω_0 of time-optimal controls without detuning. We then prove that the time-optimal controls Ω_Δ when $\Delta \neq 0$ is a subset of Ω_0 to finally characterize the controls in Ω_0 which remain time-optimal when varying the drift value Δ.

Case Δ=0

When $\Delta = 0$, the trajectory associated with singular controls is trivial and consists of a fixed point (see Eq. 4.40). In particular, given a target $U^* \neq \mathrm{Id}$, the time-optimal control generating U^* cannot be singular. Since mixing singular and regular controls is equivalent to only considering the regular controls (as the singular control has no effect), we then conclude that time-optimal controls are necessarily regular.

The following proposition states that time-optimal regular controls consist of those for which the associated projected trajectories $\gamma(t)$ draw circle arcs of angle $|\eta^*| \leq 2\pi$. Recall that the "projected trajectory" is defined in the statement of the Proposition 1 and is illustrated in Fig. 4.1.

Proposition 9 *The regular time-optimal controls u^* correspond to regular controls for which the regular trajectories draw circle arcs of total rotation angle $\eta(T(u^*)) \leq 2\pi$.*

As a consequence, all regular controls with $|\eta^*| \leq 2\pi$ can be uniquely denoted $u_{\psi,\theta,\phi}$ where $U(\psi, \theta, \phi)$ is the propagator time-optimally generated by $u_{\psi,\theta,\phi}$.

Note that the regular controls $u_{(\lambda-\phi),0,\phi}$, for $\phi \in [-\pi, \pi)$, generate the same propagator $U = e^{i\lambda\frac{\sigma_z}{2}}$. The phase $\mu(t)$ of controls corresponding to different values of ϕ only differ by a constant and the controls themselves have the same duration

$$T(u_\lambda) := T(u_{(\lambda-\phi),0,\phi}) = \frac{1}{2}\sqrt{4\pi|\lambda| - |\lambda|^2}.$$

To summarize, the set Ω_0 of time-optimal controls without a drift term is the set of all regular controls satisfying $|\eta(T(u))| \leq 2\pi$ and has the form:

$$\Omega_0 = \{u_{\psi,\theta,\phi}\}.$$

Case $\Delta \neq 0$.

To better understand what follows, the reader should quickly skim through Section 4.5.2 of the main text, if not already done.

We are interested in finding the set of all the time-optimal controls Ω_Δ for $\Delta \neq 0$. *A priori*, this set Ω_Δ potentially contains singular and regular controls and even combinations of these two types of controls. Our first main result shows that the time-optimal controls consist of the regular controls only. We then see that the set of regular controls Ω_0 covers SU(2) from which $\Omega_\Delta \subseteq \Omega_0$. We finally find an expression for the set $\Omega_\Delta^{\theta,\phi}$ of all the time-optimal controls generating propagators of the form $U(\psi,\theta,\phi)$ where (θ,ϕ) are fixed and $\psi \in [-2\pi, 2\pi)$. Ω_Δ is then defined as

$$\Omega_\Delta = \bigcup_{\theta,\phi} \Omega_\Delta^{\theta,\phi}.$$

Recall that in order not to get confused with the controls notation (defined in the $\Delta = 0$ section), bold characters $\{\boldsymbol{\psi}, \boldsymbol{\theta}, \boldsymbol{\phi}\}$ refer to regular controls $u_{\mathbf{U}} = u_{\boldsymbol{\psi},\boldsymbol{\theta},\boldsymbol{\phi}}$ and the targets $\mathbf{U}(\boldsymbol{\psi}, \boldsymbol{\theta}, \boldsymbol{\phi})$ they generate *without detuning*. Unbold symbols $\{U, \psi, \theta, \phi\}$ refer to variables in the actual problem, in which $\Delta \neq 0$.

Before proving the main results, some properties about the time duration of regular controls $T : u_{\boldsymbol{\psi}} \mapsto T(u_{\boldsymbol{\psi}})$ should be underlined.

Proposition 10 *The time function $T : u_{\boldsymbol{\psi}} \mapsto T(u_{\boldsymbol{\psi}})$ satisfies the following properties:*

(i) *$T(u_{\boldsymbol{\psi}})$ is continuous in $\boldsymbol{\psi}$;*

(ii) *$T(u_{\boldsymbol{\psi}})$ is concave, symmetric in its minimum $\boldsymbol{\psi} = -\phi^*$, and reaches its maxima at $\boldsymbol{\psi} = -\phi^* \pm 2\pi$;*

(iii) $\frac{dT(u_{\boldsymbol{\psi}})}{d\boldsymbol{\psi}} = \frac{\mathrm{p}_2(u_{\boldsymbol{\psi}})}{2}$;

where $\mathrm{p}_2(u_{\boldsymbol{\psi}})$ is the value of the adjoint variable p_2 along the trajectory corresponding to the regular control $u_{\boldsymbol{\psi}}$.

Points (i) and (ii) are illustrated in Figure 4.3 (a) and point (iii) is proved now.

Proof. Let $u_{\boldsymbol{\psi}}$ be a regular control and $\bar{\theta}$ the inclination angle of the axis $\bar{n}$ about which the projected trajectory governed by $u_{\boldsymbol{\psi}}$ is evolving (see Fig. 4.1). Without loss of generality, suppose $\bar{\theta} \geq 0$. Let $\eta := \eta(T(u_{\boldsymbol{\psi}}))$ denote the final rotation angle about $\bar{n}$ which corresponds to $u_{\boldsymbol{\psi}}$.

The radius of the circle is $\sin\bar{\theta}$ such that the time to make the complete circle would be $T_{\max} = \frac{1}{2} \cdot 2\pi \sin\bar{\theta} = \pi \sin\bar{\theta}$ according to Proposition 1. The duration $T(u_{\boldsymbol{\psi}})$ is then $T(u_{\boldsymbol{\psi}}) = \frac{\eta}{2\pi} T_{\max} = \frac{\eta}{2\pi} \pi \sqrt{1 - \cos^2\bar{\theta}}$ from which we compute $\frac{dT(u_{\boldsymbol{\psi}})}{d\cos\bar{\theta}} = -\frac{\eta}{2}\mathrm{p}_2$ (using the equality $\bar{\theta} = \frac{1}{\mathrm{p}_2}$ from Prop. 1). We also know from Eqs. (4.25) that $\boldsymbol{\psi}(t) = -2\boldsymbol{\phi}(0) + \boldsymbol{\phi}(t) - 2\mathrm{p}_2 t \equiv -2\boldsymbol{\phi}(0) + \boldsymbol{\phi}(t) - \eta(t)\cos\bar{\theta}$ where the last equality comes from the definitions of $\eta(t)$ (see Eq. 4.26) and $\bar{\theta}$. Isolating

$\cos\bar{\theta}$ in this equality, we get $\frac{d\cos\bar{\theta}}{d\psi} = \frac{d(\frac{-2\phi(0)+\phi-\psi}{\eta})}{d\psi} = \frac{-1}{\eta}$. We finally compute

$$\frac{dT(u_\psi)}{d\psi} = \frac{dT(u_\psi)}{d\cos\bar{\theta}} \cdot \frac{d\cos\bar{\theta}}{d\psi} = \frac{-\eta}{2}\mathrm{p}_2 \cdot \frac{-1}{\eta} = \frac{\mathrm{p}_2}{2}. \blacksquare$$

We are now ready to prove the first important result of this section.

Proposition 11 *Time-optimal controls are regular.*

Proof. Without loss of generality, suppose that $\Delta > 0$. From Eqs. (4.40), we have $\theta_1 \equiv 0$ along a singular trajectory such that the only propagators generated by a singular control are of the form $U^* = e^{i\lambda^*\frac{\sigma_z}{2}}$ corresponding to "rotations" about the z axis. Let us consider $\lambda^* \in [-4\pi, 0]$. We know from Corollary 3 (ii) that the singular control of shortest duration generating U^* satisfies

$$t_{\mathrm{sing}} = -\frac{\lambda^*}{2\Delta}.$$

By continuity of the time function T (Prop. 10 (i)), the function f_Δ is also continuous and there exists $\boldsymbol{\lambda} \in [-2\pi, 2\pi]$ such that $\lambda^* = f_\Delta(u_{\boldsymbol{\lambda}}) + n\cdot 4\pi = \boldsymbol{\lambda} - 2\Delta T(u_{\boldsymbol{\lambda}}) + n\cdot 4\pi$. Let us consider $\boldsymbol{\lambda}$ *with the shortest duration.* There are two cases defined by $\boldsymbol{\lambda} \in [-2\pi, 0]$ or $\boldsymbol{\lambda} \in [0, 2\pi)$, for which $n = 0$ and $n = -1$, respectively. In both cases, we have:

$$t_{\mathrm{sing}} = -\frac{\lambda^*}{2\Delta} = -\frac{\boldsymbol{\lambda} - 2\Delta T(u_{\boldsymbol{\lambda}}) + n\cdot 4\pi}{2\Delta} = -\frac{\boldsymbol{\lambda} + n\cdot 4\pi}{2\Delta} + T(u_{\boldsymbol{\lambda}}) > T(u_{\boldsymbol{\lambda}})$$

proving that the singular control is never optimal.

The last part of the proof is to show that combination of regular controls and combination of singular and regular controls are never optimal. To do so, consider the most general control which can possibly be time-optimal, *i.e.* a control mixing regular and singular controls, and let us show that in order to be optimal, this mixed control has to be a single regular control. The proof of this result relies on two key arguments. The first one is based on the continuity of the adjoint vector $\vec{p}$ along a time-optimal trajectory insured by the PMPs. Since the adjoint variable p_2 is a constant, the combination of two regular controls, if optimal, must by continuity have the same p_2 variable and hence describe a single regular control. In other words, the time-optimal combination of two regular controls is equivalent to a single regular control. The other key argument is to note that regular and singular controls commute since singular controls just contribute for an additional shift on the variable ψ. We can then always decompose the time-optimal trajectory as a regular control followed by a singular one. Finally, since singular controls are never optimal, they can always be replaced by a regular one and the new control, of shorter duration, is a combination of two regular controls, which have to define the same regular control to be time-optimal according to our first key argument. Time-optimal controls are then regular ones. ∎

We can further restrict the class of controls which can potentially be the time-optimal ones by noting that the regular controls $u_\psi \in \Omega_0$ (for which the projected trajectories

without detuning correspond to circle arcs of angle $|\eta^*| \leq 2\pi$) are sufficient to cover SU(2):

Proposition 12 $\Omega_\Delta \subseteq \Omega_0$.

Proof. We show that for all $\psi^* \in [-2\pi, 2\pi)$ there exists $u_{\boldsymbol{\psi}} \in \Omega_0$ such that $f_\Delta(u_{\boldsymbol{\psi}}) = \psi^*$. To do so, we consider $\boldsymbol{\psi}_{\min} = -\phi^* - 2\pi$ and $\boldsymbol{\psi}_{\max} = -\phi^* + 2\pi$ where $[\boldsymbol{\psi}_{\min}, \boldsymbol{\psi}_{\max}]$ covers the full domain of length 4π. By Proposition 10 (ii), the durations for the two associated controls are identical: $T(u_{\boldsymbol{\psi}_{\min}}) = T(u_{\boldsymbol{\psi}_{\max}}) = T$, which implies that $f_\Delta(u_{\boldsymbol{\psi}_{\max}}) - f_\Delta(u_{\boldsymbol{\psi}_{\min}}) = \boldsymbol{\psi}_{\max} - \boldsymbol{\psi}_{\min} = 4\pi$. By continuity of f_Δ in the variable $\boldsymbol{\psi}$ (see Proposition 10 (i)), the full range of values for ψ^* is then covered by $f_\Delta(u_{\boldsymbol{\psi}})$ for $u_{\boldsymbol{\psi}} \in \Omega_0$. The proof is completed by noting that controls in Ω_0 actually are the regular ones with the shortest durations. ∎

The above proposition expresses the fact that the function f_Δ is surjective on Ω_0. We now aim at finding the set $\Omega_\Delta \subseteq \Omega_0$ on which f_Δ is *bijective* and for which each control is time-optimal. Information on the injectivity of f_Δ is obtained by studying its derivative with respect to $\boldsymbol{\psi}$:

$$\frac{df_\Delta(u_{\boldsymbol{\psi}})}{d\boldsymbol{\psi}} = \frac{d(\boldsymbol{\psi} - 2\Delta\, T(u_{\boldsymbol{\psi}}))}{d\boldsymbol{\psi}} = 1 - 2\Delta \frac{T(u_{\boldsymbol{\psi}})}{d\boldsymbol{\psi}} \overset{\text{Prop. 10 (iii)}}{=} 1 - \Delta\ \mathrm{p}_2(u_{\boldsymbol{\psi}}).$$

In particular, $\frac{df_\Delta(u_{\boldsymbol{\psi}})}{d\boldsymbol{\psi}} = 0$ on controls $u_{\boldsymbol{\psi}}$ satisfying $\mathrm{p}_2(u_{\boldsymbol{\psi}}) = \frac{1}{\Delta}$. From Lemma 8, we know that $|\mathrm{p}_2(u_{\boldsymbol{\psi}})| \leq \cot(\frac{\theta^*}{2})$ such that for $|\Delta| < |\tan(\frac{\theta^*}{2})|$, the function f_Δ is monotonic on $u_{\boldsymbol{\psi}} \in \Omega_0$ (*i.e.* its derivative never vanishes). In this case, we conclude that $\Omega_\Delta = \Omega_0$. An example of this case is illustrated in Fig. 4.3 (b).

The case $|\Delta| > |\tan(\frac{\theta^*}{2})|$ is illustrated in Fig. 4.3 (c). Let $\boldsymbol{\psi}_\bullet$ denote the point (among possibly two) the closest to $-\phi^*$ satisfying $\mathrm{p}_2(u_{\boldsymbol{\psi}_\bullet}) = \frac{1}{\Delta}$ or equivalently $\frac{df_\Delta(u_{\boldsymbol{\psi}_\bullet})}{d\boldsymbol{\psi}} = 0$. We show that $\Omega_\Delta = [f_\Delta^{-1}(f_\Delta(u_{\boldsymbol{\psi}_\bullet}) \pm 4\pi), u_{\boldsymbol{\psi}_\bullet}]$, where $\pm 1 = \mathrm{sign}(-\Delta)$.

The possible forms of the optimal domain Ω_Δ are illustrated in Fig. 4.9.

Proposition 13 *Let θ^* and ϕ^* be fixed. If $|\Delta| \leq |\tan(\frac{\theta^*}{2})|$, then $\Omega_\Delta = \Omega_0$. Otherwise, $\Omega_\Delta = \left[u_{\boldsymbol{\psi}_\bullet}, f_\Delta^{-1}\left(f_\Delta(u_{\boldsymbol{\psi}_\bullet}) \pm 4\pi\right)\right]$ where $\pm$ is the sign of $-\Delta$.*

Proof. It remains to consider the case where $|\Delta| > |\tan(\frac{\theta^*}{2})|$ in which case the function f_Δ is not monotonic. In these cases, there exist some values of ψ which are created by more that one regular control $u_{\boldsymbol{\psi}}$ and we have to determine which of these controls have the shortest duration. We can assume without loss of generality that $\Delta > 0$ and consider $\Omega_\Delta = \left[f_\Delta^{-1}\left(f_\Delta(u_{\boldsymbol{\psi}_\bullet}) - 4\pi\right), u_{\boldsymbol{\psi}_\bullet}\right]$ defined as in the statement of the proposition. The function f_Δ is monotonic and bijective on this set. To prove the time-optimality of the controls in Ω_Δ so defined, we have to show that if $u_{\boldsymbol{\psi}_1} \in \Omega_\Delta$ and $u_{\boldsymbol{\psi}_2} \notin \Omega_\Delta$ are such that $f_\Delta(u_{\boldsymbol{\psi}_1}) = f_\Delta(u_{\boldsymbol{\psi}_2})$, then $T(u_{\boldsymbol{\psi}_1}) < T(u_{\boldsymbol{\psi}_2})$.

Notice that $u_{-\phi^*} \in \Omega_\Delta$. Indeed, let $\overline{\boldsymbol{\psi}}_\bullet := -2\phi^* - \boldsymbol{\psi}_\bullet$ define the control which is symmetric to $u_{\boldsymbol{\psi}_\bullet}$ with respect to $-\phi^*$. Then both $u_{\boldsymbol{\psi}_\bullet}$ and $u_{\overline{\boldsymbol{\psi}}_\bullet}$ are in Ω_Δ since $f_\Delta(u_{\boldsymbol{\psi}_\bullet}) - f_\Delta(u_{\overline{\boldsymbol{\psi}}_\bullet}) \overset{\text{Prop. 10 (ii)}}{=} \boldsymbol{\psi}_\bullet - \overline{\boldsymbol{\psi}}_\bullet = 2(\boldsymbol{\psi}_\bullet + \phi^*) < 2 \cdot 2\pi$ and $\psi_\bullet \in [-\phi^* - 2\pi, -\phi^* + 2\pi]$. Consequently, all the controls $u_{\boldsymbol{\psi}}$ with $\boldsymbol{\psi} \in [\overline{\boldsymbol{\psi}}_\bullet, \boldsymbol{\psi}_\bullet]$ are in Ω_Δ, including $u_{-\phi^*}$.

Let $u_{\boldsymbol{\psi}_1} \in \Omega_\Delta$ and $u_{\boldsymbol{\psi}_2} \notin \Omega_\Delta$ be such that $f_\Delta(u_{\boldsymbol{\psi}_1}) = f_\Delta(u_{\boldsymbol{\psi}_2})$. This implies that

$$\boldsymbol{\psi}_2 = \boldsymbol{\psi}_1 + 2\Delta(T(u_{\boldsymbol{\psi}_2}) - T(u_{\boldsymbol{\psi}_1})) \tag{4.41}$$

where the definition of f_Δ has been used only. (A) If $\boldsymbol{\psi}_1$ and $\boldsymbol{\psi}_2$ are of the same side of $-\phi^*$, then $T(\boldsymbol{\psi}_2) > T(\boldsymbol{\psi}_1)$ since Ω_Δ is centered in $-\phi^*$ and the time of the controls increases as we move away from $-\phi^*$ (Proposition 10 (ii)). Otherwise, (B) if $\boldsymbol{\psi}_1 > -\phi^*$ and $\boldsymbol{\psi}_2 < -\phi^*$, then $\boldsymbol{\psi}_2 < \overline{\boldsymbol{\psi}}_\bullet$ since $\overline{\boldsymbol{\psi}}_\bullet \in \Omega_\Delta$ and $T(u_{\boldsymbol{\psi}_2}) > T(u_{\overline{\boldsymbol{\psi}}_\bullet}) = T(u_{\boldsymbol{\psi}_\bullet}) > T(u_{\boldsymbol{\psi}_1})$. There remains the case (C) where $\boldsymbol{\psi}_1 < -\phi^*$ and $\boldsymbol{\psi}_2 > -\phi^*$. We have $\boldsymbol{\psi}_2 > \boldsymbol{\psi}_1$ such that the term $T(u_{\boldsymbol{\psi}_2}) - T(u_{\boldsymbol{\psi}_1})$ has to be positive in Eq. (4.41). That is, $T(u_{\boldsymbol{\psi}_2}) > T(u_{\boldsymbol{\psi}_1})$. ■

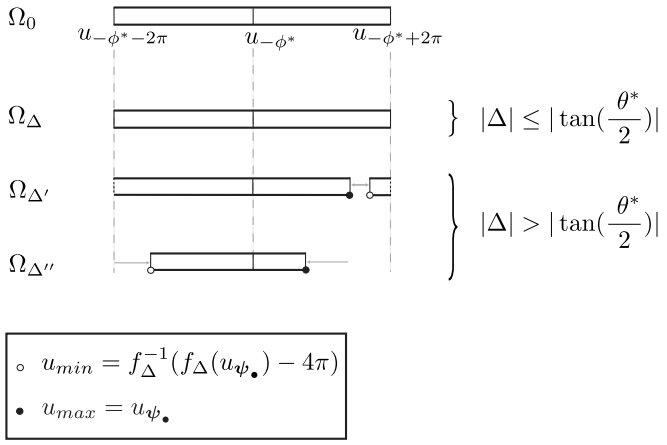

Figure 4.9: Possible structures of the time-optimal domain Ω_Δ which, we recall, is the set of all the time-optimal controls $u_{\boldsymbol{\psi}}$ generating targets of the form $U(\psi^*, \theta^*, \phi^*)$ for fixed θ^*, ϕ^*. The set Ω_0 consists in the complete set of regular controls $u_{\boldsymbol{\psi}}$. When $|\Delta| \leq |\tan(\frac{\theta^*}{2})|$, all the controls in Ω_0 remain time-optimal. When $|\Delta| > |\tan(\frac{\theta^*}{2})|$, some of the controls in Ω_0 lose their optimality and in these cases, $\Omega_\Delta \subset \Omega_0$.

4.8.7 Creation of z rotations when $\Delta = 0$.

Consider a target of the form $U^* = e^{i\lambda^* \frac{\sigma_z}{2}}$ where $\lambda^* \in [-2\pi, 2\pi]$. We are interested in finding the analytical form of the time-optimal control creating this propagator which amounts to finding the Hopf variable p_2 and the control duration t^*. We need the following lemma to find these parameters.

Lemma 5 *Let $\gamma(t)$ denote a projected trajectory on the sphere corresponding to the Hopf adjoint variable $\mathrm{p}_2 \neq 0$ and let $t_{\max}$ be the time at which a complete circle has been traced out. Then for all $t \in [0, t_{\max}]$, the Hopf variable θ_2 satisfies*

$$\theta_2(t) + \theta_2(t_{\max} - t) = \mathrm{sign}(\mathrm{p}_2)\pi(1 - \cos\bar{\theta}).$$

Proof. Let us denote $t' = t_{\max} - t$ and $\eta' := \eta(t') = \text{sign}(\text{p}_2)2\pi - \eta$. Note that completing a full circle takes the time

$$t_{\max} = \text{sign}(\text{p}_2)\pi \sin\bar{\theta}$$

which is directly deduced from looking at $\eta(t_{\max}) = \frac{2t_{\max}}{\sin\bar{\theta}} = \text{sign}(\text{p}_2)2\pi$.

Using the definition of $\theta_2 := \frac{\psi+\phi}{2}$ and the time evolution of Euler parameters given by Eqs. (4.25), we can write the time evolution of the variable θ_2 as (using the above equality)

$$\theta_2(t) = \text{sign}(\text{p}_2)\frac{\pi}{2} + \tan^{-1}\left(\frac{\sin\eta}{\cos\bar{\theta}(\cos\eta - 1)}\right) - \text{p}_2 t.$$

We then deduce the result from the equalities:

$$\begin{aligned}
\theta_2(t) + \theta_2(t') &= \text{sign}(\text{p}_2)\pi + \tan^{-1}\left(\tfrac{\sin\eta}{\cos\bar{\theta}(\cos\eta-1)}\right) + \tan^{-1}\left(\tfrac{\sin\eta'}{\cos\bar{\theta}(\cos\eta'-1)}\right) \\
&\qquad -\text{p}_2(t+t') \\
&= \text{sign}(\text{p}_2)\pi + \tan^{-1}\left(\tfrac{\sin\eta}{\cos\bar{\theta}(\cos\eta-1)}\right) + \tan^{-1}\left(\tfrac{-\sin\eta}{\cos\bar{\theta}(\cos\eta-1)}\right) \\
&\qquad -\text{p}_2 t_{\max} \\
&= \text{sign}(\text{p}_2)\pi - \text{p}_2 t_{\max} \\
&= \text{sign}(\text{p}_2)(\pi - \text{p}_2 \sin\bar{\theta}) \qquad (\leftarrow \text{def. of } t_{\max}) \\
&= \text{sign}(\text{p}_2)\pi(1 - \cos\bar{\theta}). \blacksquare \qquad (\leftarrow \text{def. of } \bar{\theta})
\end{aligned}$$

As discussed in the main text, the projected trajectory $\gamma(t)$ for a control creating a z rotation is a closed circle on the sphere, starting and ending at the North Pole (the point corresponding to $\theta_1 = 0$). Examples of such trajectories are illustrated on the left sphere of Fig. 4.2. We prove here the exactness of the equalities given in Eq. (4.28) for the parameters p_2 and t^* characterizing the shortest regular control generating U^*.

Proposition 14 *Let $U^* = e^{i\lambda^* \frac{\sigma_z}{2}}$ where $\lambda^* \in [-2\pi, 2\pi]$. Then*

(i) $\text{p}_2 = sgn(\lambda^*)\cot\left(\cos^{-1}\left(1 - \frac{|\lambda^*|}{2\pi}\right)\right)$,

(ii) $t^* = \frac{1}{2}\sqrt{4\pi|\lambda^*| - |\lambda^*|^2}$.

Proof.

(i) Using the above lemma, we know at final time t^* (which corresponds to $t_{\max}$ in the Lemma) that (a) $\theta_2^* = \text{sign}(\text{p}_2)\pi(1-\cos\bar{\theta})$. We also have by the definition of the target operator U^* that (b) $\theta_2^* = \frac{\psi^*+\phi^*}{2} = \frac{\lambda^*}{2}$. By comparing equations (a) and (b), we directly find that $\bar{\theta} = \text{sign}(\text{p}_2)\cos^{-1}(1 - \frac{|\lambda^*|}{2\pi})$. The result follows from the definition of $\bar{\theta}$ as $\cot(\bar{\theta}) = \text{p}_2$ (see Prop. 1). The fact that $\text{sign}(\text{p}_2) = \text{sign}(\lambda^*)$ follows from the sign comparison of both equalities (a) and (b).

(ii) The radius of the circle traced out by γ is $r_\gamma = |\sin\bar{\theta}| = \text{sign}(\text{p}_2)\sin\bar{\theta}$. Consequently, the total length of $\|\gamma\| = 2\pi r_\gamma = 2\pi\text{sign}(\text{p}_2)\sin\bar{\theta}$. But we know from Proposition 1 that $t^* = \frac{\|\gamma\|}{2} = \text{sign}(\text{p}_2)\pi\sin\bar{\theta}$. By replacing $\bar{\theta}$ by its

value found in (ii), we finally deduce:

$$\begin{aligned} t^* &= \mathrm{sign}(\mathrm{p}_2)\pi \sin\left(\mathrm{sign}(\mathrm{p}_2)\cos^{-1}(1-\frac{|\lambda|}{2\pi})\right) \\ &= \pi \sin\left(\cos^{-1}(1-\frac{|\lambda|}{2\pi})\right) \\ &= \pi\sqrt{1-\left(1-\frac{|\lambda|}{2\pi}\right)^2} \\ &= \frac{1}{2}\sqrt{4\pi|\lambda|-|\lambda|^2}. \ \blacksquare \end{aligned}$$

4.8.8 Creation of rotations in the (x, y) plane when $\Delta = 0$.

Consider unitary transformations having the form $U = e^{i(-a)\frac{\sigma_z}{2}} \cdot e^{ib\frac{\sigma_y}{2}} \cdot e^{a\frac{\sigma_z}{2}}$. These transformations correspond to rotations in the (x, y) plane. Like for the z rotations, the time-optimal controls to generate a rotation in the transverse plane can be analytically deduced from the variables defining the target, here a and b. The equations of the three parameters defining the control, which are p_2, $\phi(0)$ and t^*, are summarized in the Proposition 15. Prior to present this proposition, we need to prove a Lemma about the behavior of the Hopf variables θ_2 and θ_3 along a regular trajectory. Recall that a function on one variable is monotonic on a domain if its derivative doesn't change sign on this domain. The concept of monotonicity is then closely related to our understanding of what "increasing" or "decreasing" means.

Lemma 6 *The Hopf variables θ_2 and θ_3 are monotonic along optimal solutions. Moreover, they have an opposite behavior. When $\mathrm{p}_2 >$, θ_2 increases and θ_3 decreases. The converse holds in the case where $\mathrm{p}_2 < 0$.*

Proof. One first shows that θ_2 is monotonic. Suppose that there is $t' \in [0, t^*]$ such that $\dot{\theta}_2(t') = 0$. Then by the definition of the rotated control u_2 given in Eq. (4.15), this implies that $\mathrm{p}_2 \tan^2\theta_1 = 0$, which is verified if either $\mathrm{p}_2 = 0$ or $\theta_1 = \mathrm{n}\pi$ with $\mathrm{n} \in \mathbb{N}$. The second possibility forces $\theta_1(t') = 0$ since $|\theta_1| \leq \frac{\pi}{2}$ and in this case, the only possibility is that $t' = 0$ which means that $\dot{\theta}_2 = 0$ only at initial time. The first case $\mathrm{p}_2 = 0$ implies that $u_2 = 0$ all along the trajectory and since $\dot{\theta}_2 = -\tan\theta_1 u_2$ (see Eq. 4.7), we have that $\dot{\theta}_2 \equiv 0$ all along the trajectory and θ_2 is monotonic. Similar arguments hold for proving the monotonicity of θ_3. Finally, their opposite behavior is deduced from the sign difference of $\dot{\theta}_2$ and $\dot{\theta}_3$ in Eq. (4.7). Note that since $\dot{\theta}_2 = \mathrm{p}_2 \tan^2\theta_1$, the variable θ_2 increases when $\mathrm{sign}(\mathrm{p}_2) = 1$ and decreases when $\mathrm{sign}(\mathrm{p}_2) = -1$. ∎

Proposition 15 *Let $U = e^{i(-a)\frac{\sigma_z}{2}} \cdot e^{ib\frac{\sigma_y}{2}} \cdot e^{a\frac{\sigma_z}{2}}$. Then the variables defining the optimal trajectory satisfy*

(i) $\mathrm{p}_2 = 0$;

(ii) $\phi(0) = a$;

(iii) $t^* = \frac{b}{2}$.

Proof.

(i) Since $\theta_2(t)$ is monotonic (Lemma 6), the initial and final conditions $\theta_2(0) = \theta_2^* = 0$ imply that $\theta_2(t) \equiv 0\ \forall t$. In particular, $\dot{\theta}_2 \equiv 0$. But $\dot{\theta}_2 = \mathrm{p}_2 \tan^2\theta_1$ and $\tan^2\theta_1$ do not vanish a.e. (since $\tan^2\theta_1(0) = 1$). Consequently, we must have $\mathrm{p}_2 = 0$.

(ii) Since $p_2 = 0$, the dynamical equation for ϕ given in Eqs. (4.23) takes the trivial form $\dot{\phi} = 0$. That is, the variable ϕ is a constant of motion and $\phi(0) = \phi^* = a$ by the definition of the target U^*.

(iii) From Eqs. 4.20 we have that $\ddot{\theta}_1 = \dot{\mathrm{p}}_1 = 0$ since $\mathrm{p}_2 = 0$. That is, θ_1 evolves linearly in time with velocity $p_1 \equiv 1$ since $\mathrm{p}_1(0) = 1$ (see Lemma 4). Consequently, as $\theta_1(0) = 0$ and $\theta_1^* = \frac{\theta^*}{2} = \frac{b}{2}$, we have that $t^* = \frac{b}{2}$. ∎

4.8.9 Time-optimal control over SO(3): the complete reasoning

We recall first the question we are interested to answer: *Given $\Delta \neq 0$, which one among U and $= -U$ is the fastest to generate?* Or equivalently, if $T(U, \Delta)$ denotes the duration of the time-optimal control generating U in the presence of a detuning Δ, *for which values of Δ does the "time difference" function*

$$\mathrm{T}_{\mathrm{diff}} : \Delta \mapsto T(U, \Delta) - T(-U, \Delta) \tag{4.42}$$

change sign? Since $U = (\psi, \theta, \phi)$ and $-U := (\widetilde{\psi}, \widetilde{\theta}, \widetilde{\phi}) = (\psi \pm 2\pi, \theta, \phi)$ have the same two Euler angles θ and ϕ, the time-optimal controls generating U and $-U$ are denoted as u_{ψ} and $u_{\widetilde{\psi}}$ respectively. To simplify the arguments used to answer the above question, we introduce the notion of Δ-predecessor.

Definition 1 *Considering θ and ϕ to be fixed, a control u_{ψ} is said to be a Δ-predecessor of U, or simply of ψ^*, if $f_{\Delta}(u_{\psi}) = \psi^* \mod 4\pi$.*

That is, a Δ-predecessor u_{ψ} of U is any control (and thus not necessary optimal) which will create U in the presence of a detuning term Δ. In particular, Δ-predecessors of U generally differ from Δ'-predecessors of U when $\Delta \neq \Delta'$. The *time-optimal* Δ-predecessor for ψ^* is naturally defined to be the one with shortest duration, *i.e.* the time-optimal control creating U in the presence of the detuning Δ.

Let us now come back to the problem of finding the values of Δ for which the time difference function $\mathrm{T}_{\mathrm{diff}}$ changes sign. There are two types of detuning values to consider, which can be categorized by the following two sets:

$$\begin{aligned} \mathrm{A} := &\ \{\Delta \mid \mathrm{T}_{\mathrm{diff}}(\Delta) = 0\}, \\ \mathrm{B} := &\ \{\Delta \mid \mathrm{sign}(\mathrm{T}_{\mathrm{diff}}(\Delta)) \neq \mathrm{sign}(\mathrm{T}_{\mathrm{diff}}(\Delta + \delta))\}, \end{aligned}$$

where the sign difference in B occurs when $\delta \to 0$. Set A corresponds to the detuning values for which the function $\mathrm{T}_{\mathrm{diff}}$ varies smoothly with Δ and thus equals zero for some values of Δ. Set B corresponds to detuning values for which the function $\mathrm{T}_{\mathrm{diff}}$ abruptly jumps from positive to negative values (or *vice-versa*). We shall first study the two sets separately before grouping them into the main proposition (Proposition 6) of the section.

Characterization of the detuning set A**.**

The structure of the set A falls down as a corollary of the following lemma, which relates the pair of controls $u_{-\phi^*\pm\xi}$ to the propagator they generate.

Lemma 7 *Let $\xi \in [-2\pi, 2\pi]$. Then $u_{-\phi^*+\xi}$ is a Δ-predecessor of ψ^* $\iff$ $u_{-\phi^*-\xi}$ is a Δ-predecessor of $\psi^* - 2\xi$.*

Proof. Since $u_{-\phi^*+\xi}$ is a predecessor of ψ^*, by definition

$$f_\Delta(u_{-\phi^*+\xi}) := (-\phi^* + \xi) - 2\Delta T(u_{-\phi^*+\xi}) = \psi^* + n \cdot 4\pi.$$

By symmetry of the time function T with respect to $u_{-\phi^*}$ (Prop. 10 (ii)), we see that $T(u_{-\phi^*+\xi}) = T(u_{-\phi^*-\xi})$ such that

$$\begin{aligned} f_\Delta(u_{-\phi^*-\xi}) &= (-\phi^* - \xi) - 2\Delta T(u_{-\phi^*-\xi}) \\ &= [(-\phi^* + \xi) - 2\Delta T(u_{-\phi^*+\xi})] - 2\xi \\ &= [f_\Delta(u_{-\phi^*+\xi})] - 2\xi \\ &= [\psi^* + n \cdot 4\pi] - 2\xi \end{aligned}$$

and $u_{-\phi^*-\xi}$ is a Δ-predecessor of $\psi^* - 2\xi$. ∎

This Lemma can be translated into the following diagram:

$$\begin{array}{ccc} u_{-\phi^*+\xi} & & u_{-\phi^*-\xi} \\ \downarrow f_\Delta & \iff & \downarrow f_\Delta \\ \psi^* & & \psi^* - 2\xi \end{array} .$$

We are interested in the particular case of this lemma for which $\xi = \pm\pi$. In this case, the above lemma asserts that the special controls $u_{-\phi^*\pm\pi}$ are such that they *always* create opposite targets regardless of the presence or absence of a detuning term. These special controls are worth giving a special name, namely

$$u_{\boldsymbol{\psi}_\pm} := u_{-\phi^*\pm\pi},$$

and the previous remark is worth writing into a formal corollary.

Corollary 4 *The special controls $u_{\boldsymbol{\psi}_\pm}$ are such that they always create opposite targets whatever the detuning value Δ is.*

The interesting point is that these special controls also have the same duration by symmetry of the time function T with respect to $u_{-\phi^*}$ (Proposition 10 (i)). If $u_{\boldsymbol{\psi}_\pm}$ both are time-optimal controls (*i.e.* are in Ω_Δ), then they optimally create two opposite unitary transformations *in the same amount of time* and the values of Δ for which these two opposite matrices correspond to our two targets U and $-U$ are exactly the values for which $\mathrm{T_{diff}} = 0$. This discussion is summarized by the following proposition.

Proposition 16 $\mathrm{T_{diff}}(\Delta) = 0$ *if and only if $u_{\boldsymbol{\psi}_\pm}$ correspond to the time-optimal Δ-predecessors of U and $-U$.*

Proof. Let us write $u_{-\phi^*+\xi_1}$ the optimal predecessor of ψ^* and $u_{-\phi^*+\xi_2}$ the optimal predecessor of $\psi^* \pm 2\pi$. Since $T(U,\Delta) = T(-U,\Delta)$, $-\phi^*+\xi_1$ and $-\phi^*+\xi_2$ have to be symmetric with respect to $-\phi^*$ and $\xi_2 = -\xi_1$. But by the previous lemma, $u_{-\phi^*-\xi_1}$ is also the Δ-predecessor of $\psi^* - 2\xi_1$. We then conclude that $\xi_1 = \pm\pi$ and the result follows. ∎

To have the explicit form of set A, we simply have to find the values of Δ for which $f_\Delta(u_{\psi_\pm}) = \psi^*$ and $f_\Delta(u_{\psi_\mp}) = \psi^* \pm 2\pi$. Assuming that we found the duration of the time-optimal controls $u_{\boldsymbol{\psi}_\pm}$ by inverting the dynamic Equations (4.32), the structure of the set A is given by the following proposition.

Proposition 17 *The function* $\mathrm{T_{diff}}(\Delta)$ *is zero for a certain* Δ *if and only if* $\Delta = -\frac{\phi^*+\psi^*\pm\pi+n\cdot 4\pi}{2T(u_{\psi\pm})}$ *for a certain* $n \in \mathbb{Z}$ *and both* $u_{\boldsymbol{\psi}_\pm} \in \Omega_\Delta$.

Proof. Suppose $\Delta = -\frac{\phi^*+\psi^*+\pi+n\cdot 4\pi}{2T(u_{\psi\pm})}$. Then

$$\begin{aligned} f_\Delta(u_{\boldsymbol{\psi}_\pm}) &= -\phi^* \pm \pi - 2\Delta T(u_{\boldsymbol{\psi}_\pm}) \\ &= -\phi^* \pm \pi + 2\cdot\tfrac{\phi^*+\psi^*+\pi+n\cdot 4\pi}{2T(u_{\boldsymbol{\psi}_\pm})}\cdot T(u_{\boldsymbol{\psi}_\pm}) \\ &= -\phi^* \pm \pi + \phi^* + \psi^* + \pi + n\cdot 4\pi \\ &= \psi^* \pm \pi + \pi + n\cdot 4\pi \\ &= \psi^*, \widetilde{\psi}^* \bmod 4\pi. \end{aligned}$$

The arguments are the same for $\Delta = -\frac{\phi^*+\psi^*-\pi+n\cdot 4\pi}{2T(u_{\psi\pm})}$. ∎

We can finally summarize in the following algorithm the procedure to find the values of Δ in the set A:

Algorithm 2 *To find the set* A *of detuning values satisfying* $\mathrm{T_{diff}} = 0$*:*

1. *Compute* $T(u_{\boldsymbol{\psi}_\pm})$ *by inverting the Equations* (4.32).
2. *Compute the values* $\Delta = -\frac{\phi^*+\psi^*\pm\pi+n\cdot 4\pi}{2T(u_{\psi\pm})}$ *given in Prop.17.*
3. *For the values of* Δ *computed in 2., verify that* $u_{\boldsymbol{\psi}_\pm} \in \Omega_\Delta$.

It is straightforward to show that $\Omega_{\Delta+d} \subseteq \Omega_\Delta$ for any value of d with $\mathrm{sign}(d) = \mathrm{sign}(\Delta)$ by adapting the arguments used in Prop. 12. Consequently, the above algorithm stops at the first values of Δ found in 2. for which condition 3. is not satisfied.

Characterization of the set B

We are now interested in the detuning values such that the "time difference" function $\mathrm{T_{diff}}(\Delta)$ discontinuously changes sign. One key argument is to note that the time-optimal control $u_{\boldsymbol{\psi}}$ generating U varies continuously in Ω_Δ when Δ varies, noting that Ω_Δ also varies continuously with Δ. In particular, $T(U,\Delta)$ also varies continuously with Δ and so must the time difference function $\mathrm{T_{diff}}$. All of this is true, of course, when $u_{\boldsymbol{\psi}}$ is in the interior of the time-optimal domain Ω_Δ. A direct implication of the previous discussion is that the values of the detuning for which $\mathrm{T_{diff}}$ experiences a discontinuous

sign change have to be such that the time-optimal control $u_{\boldsymbol{\psi}}$ generating U suddenly jumps from one extremity of Ω_Δ to the other extremity, *i.e.* when $u_{\boldsymbol{\psi}}$ is not in the interior of Ω_Δ. The above condition is a necessary condition for $\mathrm{T}_{\mathrm{diff}}$ to change sign, but it is not a sufficient one. That is, the jump from one extremity of Ω_Δ to the other may not result in a sign change in $\mathrm{T}_{\mathrm{diff}}$ even if creating a discontinuity. Clearly, if $\Omega_\Delta = \Omega_0$, no sign change can occur since in this case, the two controls at the extremity of Ω_Δ are $u_{-\phi^*-2\pi}$ and $u_{-\phi^*+2\pi}$ and have the same duration. So an abrupt sign change can only occur when the time-optimal domain has the form $\Omega_\Delta = \left[u_{\boldsymbol{\psi}_\bullet}, f_\Delta^{-1}\left(f_\Delta(u_{\boldsymbol{\psi}_\bullet}) \pm 4\pi\right)\right]$ (see Fig. 4.9).

The additional necessary condition which has to be fulfilled for $\mathrm{T}_{\mathrm{diff}}$ to experience a sign change is expressed in point (ii) of following the proposition.

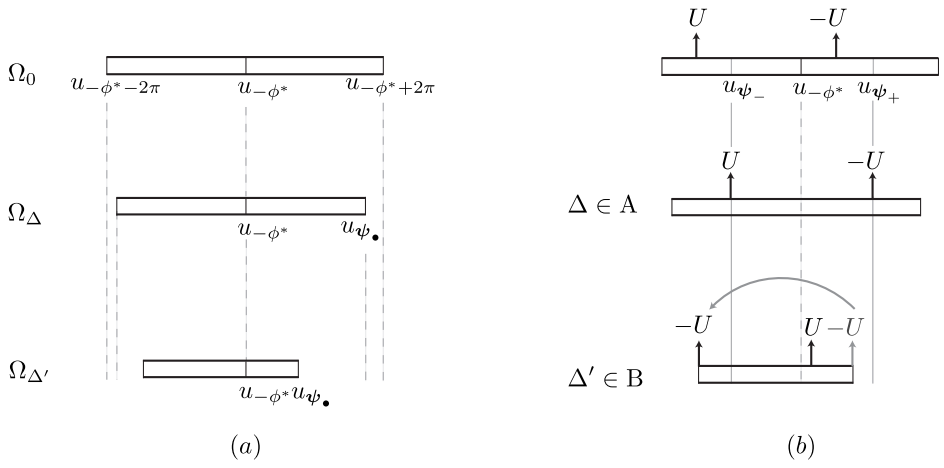

Figure 4.10: Illustration of the values of Δ for which $\mathrm{T}_{\mathrm{diff}}$ experiences a sign change. (a) Characteristic forms of the optimal domain Ω_Δ. The largest possible domain, and the characteristic domains for $\Delta \in \mathrm{A}$ and $\Delta \in \mathrm{B}$, are depicted from top to bottom respectively. (b) Illustration of the time-optimal controls (in the corresponding domain Ω_Δ) generating $\pm U$. The first row shows the time-optimal controls (the arrows) generating $\pm U$ in a general context and in which case $\mathrm{T}_{\mathrm{diff}}$ does not experience a sign change. When $\Delta \in \mathrm{A}$ (second row), the sign changes when the time-optimal controls generating $\pm U$ (the arrows) are exactly $u_{\pm\boldsymbol{\psi}}$. When $\Delta \in \mathrm{B}$, the sign change occurs when the time-optimal control of one of the propagators (here $-U$) jumps from one extremity of Ω_Δ to the other.

Proposition 18 *Let $\Delta \neq 0$. The function $\mathrm{T}_{\mathrm{diff}}$ experiences a discontinuous sign change in Δ if and only if the three following conditions are satisfied:*

(i) $\Omega_\Delta \neq \Omega_0$,

(ii) *one of the time-optimal controls generating U or $-U$ jumps from one extremity of Ω_Δ to the other,*

(iii) *at least one of $u_{\boldsymbol{\psi}_\pm}$ is not in Ω_Δ.*

Proof. Without loss of generality, suppose $\Delta > 0$. In particular, the time-optimal domain takes the form $\Omega_\Delta = \left[f_\Delta^{-1}\left(f_\Delta(u_{\boldsymbol{\psi}_\bullet}) - 4\pi\right), u_{\boldsymbol{\psi}_\bullet}\right]$ that we denote $\left[u_{\boldsymbol{\psi}_{\min}}, u_{\boldsymbol{\psi}_\bullet}\right]$ for short. We consider a variation of Δ in the positive direction and as doing so, the parameter $\boldsymbol{\psi}$ which characterizes the time-optimal control $u_{\boldsymbol{\psi}}$ generating U (or $-U$) shift in the positive direction (see Fig. 4.10, third row). The validity of the points (i) and (ii) has been discussed at the beginning of this subsection such that only the point (iii) has to be proved.

($\Longrightarrow$) Showing the converse, suppose that $u_{\boldsymbol{\psi}_\pm}$ both belong to the optimal domain Ω_Δ. The main argument comes from the fact that when both $u_{\boldsymbol{\psi}_\pm} := u_{-\phi^* \pm \pi}$ are in Ω_Δ, the optimal predecessors of U and $-U$ can be written as

$$u_{\boldsymbol{\psi}} = u_{\boldsymbol{\psi}_- + \xi_1(\Delta)} \text{ and } \widetilde{u}_\psi = u_{\boldsymbol{\psi}_+ + \xi_2(\Delta)}$$

respectively, where $\xi_1(\Delta) = 0 \iff \xi_2(\Delta) = 0$ since $u_{\boldsymbol{\psi}_+}$ and $u_{\boldsymbol{\psi}_-}$ have to be optimal predecessors for U and $-U$ exactly at the same time (see Cor. 4). Moreover, $\text{sign}(\xi_1(\Delta)) = \text{sign}(\xi_2(\Delta))$ by continuity of the time-optimal predecessors with respect to variations of Δ in the interior of the domain Ω_Δ as illustrated in the third row of Fig. 4.10 (b). Without loss of generality, in order to follow the third configuration of Fig. 4.10 (b), let us suppose that the time-optimal control for $-U$ is the one jumping between the extremities of Ω_Δ. Recalling that $u_{\boldsymbol{\psi}}$ denotes the time-optimal Δ-predecessor of U, we want to show that

$$\text{sign}(T(u_{\boldsymbol{\psi}_\bullet}) - T(u_{\boldsymbol{\psi}})) = \text{sign}(T(u_{\boldsymbol{\psi}_{\min}}) - T(u_{\boldsymbol{\psi}})).$$

To do so, consider the following sequence of inequalities:

$$u_{\boldsymbol{\psi}_{\min}} < u_{\boldsymbol{\psi}_-} < u_{\boldsymbol{\psi}_- + \xi_1(\Delta)} < u_{\boldsymbol{\psi}_+} < u_{\boldsymbol{\psi}_\bullet}.$$

The relation $u_{\boldsymbol{\psi}_{\min}} < u_{\boldsymbol{\psi}_-}$ implies that $T(u_{\boldsymbol{\psi}_{\min}}) > T(u_{\boldsymbol{\psi}_\pm})$ and the relation $u_{\boldsymbol{\psi}_+} < u_{\boldsymbol{\psi}_\bullet}$ that $T(u_{\boldsymbol{\psi}_\bullet}) > T(u_{\boldsymbol{\psi}_\pm})$, using the symmetry of the time duration of the regular controls with respect to $u_{-\phi^*}$ (Prop. 10 (ii)). The middle inequality $u_{\boldsymbol{\psi}_-} < u_{\boldsymbol{\psi}_- + \xi_1(\Delta)} < u_{\boldsymbol{\psi}_+}$ implies that $T(u_{\boldsymbol{\psi}_- + \xi_1(\Delta)}) < T(u_{\boldsymbol{\psi}_\pm})$. Recalling that $u_{\boldsymbol{\psi}_- + \xi_1(\Delta)} = u_{\boldsymbol{\psi}}$ is the time-optimal control for U and that $u_{\boldsymbol{\psi}_\bullet}$ and $u_{\boldsymbol{\psi}_{\min}}$ are the time-optimal controls generating $-U$ with detuning $\Delta - \varepsilon$ and Δ, we finally conclude that the time taken to generate $-U$ remains greater than the time taken to generate U when the time-optimal control for $-U$ jumps from $u_\bullet$ to $u_{\min}$.

($\Longleftarrow$) The arguments are similar to prove the converse, using the above series of inequalities. ■

Grouping of sets A **and** B

To summarize Propositions 17 and 18, the values of the detuning Δ for which the time difference function T_{diff} changes sign are differently defined, weather both $u_{\boldsymbol{\psi}_\pm}$ are time-optimal (in which case we have to consider the set A) or not (in which case we have to consider the set B). We already expressed the fact that $\Omega_{\Delta+d} \subseteq \Omega_\Delta$ for any value of d with $\text{sign}(d) = \text{sign}(\Delta)$ such that if one of $\boldsymbol{\psi}_\pm$ does not belong to Ω_Δ, then so is the case for the detuning values $\Delta + d$.

We can then split the full detuning domain $\mathbb{R}$ into two regions, X and $\mathbb{R}/X$, where $X := \{\Delta \mid \text{both } u_{\boldsymbol{\psi}_+}, u_{\boldsymbol{\psi}_-} \in \Omega_\Delta\}$. Propositions 17 and 18 are merged into

the Proposition 6 which was presented in the Section 4.6.2. Recalling that we denoted by $[u_{\boldsymbol{\psi}_{\min}}, u_{\boldsymbol{\psi}_{\max}}]$ the time-optimal domain $\Omega_\Delta = \left[f_\Delta^{-1}\left(f_\Delta(u_{\boldsymbol{\psi}_\bullet}) - 4\pi\right), u_{\boldsymbol{\psi}_\bullet}\right] \neq \Omega_0$, we finally have:

Proposition 6 *For $\Delta \in X$, the function $\mathrm{T}_{\mathrm{diff}}$ changes sign if and only if $\Delta = -\frac{\phi^* + \psi^* \pm \pi + n\cdot 4\pi}{2T(u_{\boldsymbol{\psi}_\pm})}$ for a certain $n \in \mathbb{Z}$. Moreover, $\mathrm{T}_{\mathrm{diff}} = 0$ at these points. For $\Delta \in \mathbb{R}/X$, the function $\mathrm{T}_{\mathrm{diff}}$ changes sign if and only if the time-optimal control for U or $-U$ is $u_{\boldsymbol{\psi}_{\min/\max}}$.*

Conclusion

We presented in this thesis two general problems of quantum mechanics, each of which finds applications in various fields of physics and chemistry. In Chapter 2, we first presented a general method to visualize any operator in any quantum system by laying down a generalization of Wigner representations. These representations are the groundwork of the DROPS visualization of operators. For each system under concern, we pointed out that there exists many possible DROPS representations for a given system and that the choice of a DROPS visualization may advantageously be adapted to the processes to be visualized. We derived a special DROPS representation, named LiSA visualization, for systems of identical particles and explicitly showed the result in the case of systems with three spin-1/2 particles.

In Chapter 3, the insightful nature of the LiSA DROPS visualization was demonstrated by illustrating fundamental concepts of NMR spectroscopy on spin-1/2 particles, from Cartesian operators to coherence transfer pathway selections, through average Hamiltonian theory.

In the second part of the thesis, consisting in Chapter 4, we presented a solution to the problem of creating in a time-optimal fashion a propagator in a closed system. Our approach using Pontryagin's maximum principle led to explicit parametrization to the trajectories un terms of both Hopf and Euler parameters. In particular, we paid attention to the role of singular controls and trajectories in the optimal solutions, which lacked in the previous works on the topic. We finally applied our results to solve the similar time-optimal control problem for creating rotations.

Bibliography

[1] J. G. Cramer, "The Transactional Interpretation of Quantum Mechanics," *Rev. Mod. Phys.*, vol. 58, no. 647, 1986.

[2] L. De Broglie, *Recherches sur la théorie des Quanta*. PhD thesis, Paris, 1924.

[3] P. of the American Philosophical Society, ed., *The Present Situation in Quantum Mechanics*, no. 124.

[4] A. Einstein, B. Podolsky, and N. Rosen, "Can Quantum-Mechanical Description of Physical Reality Be Considered Complete?," *Phys. Rev.*, vol. 47, no. 777, 1935.

[5] U. Fano, "Description of states in quantum mechanics by density matrix and operator techniques," *Reviews of Modern Physics*, vol. 29, pp. 74–93, Jan. 1957.

[6] R. P. Feynman, J. F. L. Vernon, and R. W. Hellwarth, "Geometrical Representation of the Schrödinger Equation for Solving Maser Problems," *J. Appl. Phys.*, vol. 28, pp. 49–52, 1957.

[7] M. A. Bernstein, K. F. King, and X. J. Zhou, *Handbook of MRI Pulse Sequences*. Elsevier, Burlington-San Diego-London, 2004.

[8] R. R. Ernst, G. Bodenhausen, and A. Wokaun, *Principles of Nuclear Magnetic Resonance in One and Two Dimensions*. Clarendon Press, Oxford, 1987.

[9] W. P. Schleich, *Quantum Optics in Phase Space*. Wiley-VCH, 2001.

[10] G. Hoatson and K. Packer, "The creation, interconversion and observation of states of zero-, single- and double-quantum order in the N.M.R. spectroscopy of spin-1 nuclei using non-selective r.f. pulses," *Molecular Physics*, vol. 40, no. 5, pp. 1153–1175, 1980.

[11] T. K. Halstead and P. A. Osment, "Multipole nmr. ix. polar graphical representation of nuclear spin polarizations," *Magnetic Resonance*, vol. 60, pp. 382–396, 1984.

[12] D. J. Philip and P. W. Kuchel, "A Way of Visualizing NMR Experiments on Quadrupolar Nuclei," *Concepts Magn. Reso. A*, vol. 25A, pp. 40–52, 2005.

[13] G. S. Agarwal, "Relation between atomic coherent-state representation, state multipoles, and generalized phase-space distributions," *Phys. Rev. A*, vol. 24, pp. 2889–2896, 1981.

[14] J. P. Dowling, G. S. Agarwal, and W. P. Schleich, "Wigner distribution of a general angular-momentum state: Applications to a collection of two-level atoms," *Phys. Rev. A*, vol. 49, pp. 4101–4109, May 1994.

[15] S. T. Merkel, P. S. Jessen, and I. H. Deutsch, "Quantum control of the hyperfine-coupled electron and nuclear spins in alkali-metal atoms," *Phys. Rev. A*, vol. 78, no. 023404, 2008.

[16] P. S. Jessen, D. L. Haycock, G. Klose, G. A. Smith, I. H. Deutsch, and G. K. Brennen, "Quantum control and information processing in optical lattices," *Quant. Inf. Computation*, vol. 1, pp. 20–32, 2001.

[17] G. Colangelo, R. J. Sewell, N. Behbood, F. M. Ciuraa, G. Triginer, and M. W. Mitchell, "Quantum atom-light interfaces in the Gaussian description for 1-spin systems," *New J. Phys.*, vol. 15, no. 103007, 2013.

[18] B. C. Sanctuary, "Multipole N.M.R. XI. Scalar spin coupling," *Mol. Phys.*, vol. 55, pp. 1017–1031, 1985.

[19] B. C. Sanctuary and F. P. Temme, "Multipole N.M.R. XIII. Multispin interactions and symmetry in Liouville space," *Mol. Phys.*, vol. 55, pp. 1049–1062, 1985.

[20] M. E. Rose, *Elementary theory of angular momentum.* Structure of matter series, Wiley, 1957.

[21] A. R. Edmonds, *Angular momentum in quantum mechanics.* Investigations in Physics Series, Princeton University Press, 1957.

[22] D. D. M. Brink and G. G. R. Satchler, *Angular Momentum.* Oxford Science Publications, Clarendon Press, Oxford, 1993.

[23] C. Brif, R. Chakrabarti, and H. Rabitz, "Control of quantum phenomena: past, present and future," *New. J. Phys.*, vol. 12, no. 075008, 2010.

[24] N. C. Nielsen, T. Schulte-Herbrüggen, and O. W. Sørensen, "Bounds on spin dynamics tightened by permutation symmetry Application to coherence transfer I_2S and I_3S spin systems ," *Mol. Phys.*, vol. 85, no. 6, pp. 1205–1216, 1995.

[25] U. Boscain and Y. Chitour, "Time-optimal synthesis for left-invariant control systems on SO(3)," *SIAM J. Control Optim.*, vol. 44, pp. 111–139, 2005.

[26] K. M. F. Romero, G. U. Laverde, and F. T. Ardila, "Optimal control of one-qubit gates," *J. Phys. A*, vol. 36, p. 841, 2003.

[27] M. Wenin and W. Pötz, "Optimal control of a single qubit by direct inversion," *Phys. Rev. A*, vol. 74, no. 022319, 2006.

[28] R. Wu, C. Li, and Y. Wang, "Explicitly solvable extremals of time optimal control for 2-level quantum systems," *Phys. Lett. A*, vol. 295, no. 20, 2002.

[29] A. D. Boozer, "Time-optimal synthesis of su(2) transformations for a spin-1/2 system," *Phys. Rev. A*, vol. 85, no. 012317, 2012.

[30] T. H. E. Kirillova and K. Spindler, "Optimal Control on Lie Groups: Theory and Applications," *WSEAS trans. Math.*, vol. 7, p. 687, 2008.

[31] M. A. Nielsen and I. L. Chuang, *Quantum Computation and Quantum Information*. Cambridge University Press, Cambridge (UK), 2000.

[32] O. W. Sørensen, "Polarization Transfer Experiments in High-Resolution NMR Spectroscopy," *Prog. NMR Spectrosc.*, vol. 21, pp. 503–569, 1989.

[33] A. Pines, S. Vega, D. J. Ruben, T. W. Shattuck, and D. E. Wemmer, *Magnetic Resonance in Condensed Matter - Recent Developments, Proceedings of the IVth Ampere International Summer School, Pula, Yugoslavia*, ch. "Double quantum NMR in solids", pp. 127–179. University of Ljubljana, 1976.

[34] D. Harland, M. J. Everitt, K. Nemoto, T. Tilma, and T. P. Spiller, "Towards a complete and continious Wigner function for an ensamble of spins or qubits," *Phys. Rev. A*, vol. 86, no. 062117, 2012.

[35] R. L. Stratonovich, "On distributions in Representation Space," *J. Exptl. Theoret. Phys. (U.S.S.R.)*, vol. 31, pp. 1012–1020, December 1956.

[36] C. Brif and A. Mann, "A general theory of phase-space quasiprobability distributions," *J. Phys. A: Math. Gen.*, vol. 31, pp. L9–L17, 1997.

[37] M. Hamermesh, *Group Theory*. Addison-Wesley, Reading, MA, 1962.

[38] J. Listerud, S. J. Glaser, and G. P. Drobny, "Symmetry and Isotropic Coherence Transfer. II. Three Spin Calculations Using a Young Tableaux Formulation," *Mol. Phys.*, vol. 78, pp. 629–658, 1993.

[39] J. Listerud, *Techniques in Solid State NMR*. PhD thesis, University of Washington, 1987.

[40] W. K. Tung, *Group Theory in Physics*. World Scientific Publishing Company, Incorporated, 1985.

[41] E. P. Wigner, "On Matrices which Reduce the Kronecker Products of Representations of S.R. Groups," in *Quantum Theory of Angular Momentum* (L. C. Biedenharn and H. van Dam, eds.), pp. 87–133, Academic Press, New York, 1965.

[42] J. Schwinger, "On Angular Momentum," U.S. Atomic Energy Commission, Technical report NYO-3071, 1952.

[43] J. Keeler, *Understanding NMR Spectroscopy*. John Wiley & Sons, Chichester, United Kingdom, 2nd ed., 2010.

[44] E. Ising, "Beitrag zur Theorie des Ferromagnetismus," *Z. Physik*, vol. 31, pp. 253–258, 1925.

[45] W. J. Caspers, *Spin systems*. Singapore: World Scientific, 1989.

[46] S. J. Glaser, "Coupling Topology Dependence of Polarization-Transfer Efficiency in TOCSY and TACSY Experiments," *J. Magn. Reson. A*, vol. 104, pp. 283–301, 1993.

[47] T. Schulte-Herbrüggen, Z. Mádi, O. W. Sørensen, and R. R. Ernst, "Reduction of Multiplet Complexity in COSY-Type NMR Spectra: the Bilinear and Planar COSY Experiments," *Molec. Phys.*, vol. 72, pp. 847–871, 1991.

[48] A. Kitaev, "Anyons in an exactly solved model and beyond," *Ann. Phys.*, vol. 321, pp. 2–111, 2005.

[49] W. K. Wootters, "Entanglement of formation of an arbitrary state of two qubits," *Phys. Rev. Lett.*, vol. 80, no. 10, pp. 2245–2248, 1998.

[50] S. Haroche and J.-M. Raimond, *Exploring the Quantum: Atoms, Cavities, and Photons*. Oxford University Press, New York, 2006.

[51] J. Stolze and D. Suter, *Quantum Computing: A Short Course from Theory to Experiment*. Wiley-VCH, Weinheim, 2004.

[52] B. C. Sanctuary, "Multipole operators for an arbitraty number of spins," *J. Chem. Phys.*, vol. 64, pp. 4352–4261, 1976.

[53] B. C. Sanctuary, "Multipole N.M.R. III. Multiplet spin theory," *Mol. Phys.*, vol. 48, pp. 1155–1176, 1983.

[54] B. C. Sanctuary, N. Lee, F. Commodari, G. Campolieti, M. S. Krishnan, and M. Lam, "Operator Space Quantum Numbers for Spin Systems," *J. Magn. Reson.*, vol. 84, pp. 323–332, 1989.

[55] D. H. Sattinger and O. L. Weaver, *Lie Groups and Algebras with Applications to Physics, Geometry, and Mechanics*. Springer, New York, 1986.

[56] L. C. Biedenharn and J. D. Louck, *Angular Momentum in Quantum Physics*. Addison-Wesley, Reading, MA, 1981.

[57] R. N. Zare, *Angular Momentum*. John Wiley & Sons, New York, 1988.

[58] W. J. Thompson, *Angular Momentum*. John Wiley & Sons, New York, 1994.

[59] J. D. Jackson, *Classical Electrodynamics*. John Wiley & Sons, New York, third ed., 1999.

[60] G. Racah, "Theory of Complex Spectra IV," *Phys. Rev.*, vol. 76, pp. 1353–1365, 1949.

[61] P. L. Corio, *Structure of High-Resolution NMR Spectra*. Academic Press, London, 1966.

[62] D. E. Littlewood, *The Theory of Group Characters and Matrix Representations of Groups*. Clarendon Press, Oxford, 2nd ed., 1958.

[63] D. E. Rutherford, *Substitutional Analysis*. Edinburgh University Press, Edinburgh, 1948.

[64] H. Boerner, *Darstellungen von Gruppen*. Springer, Berlin, 2nd ed., 1967.

[65] G. d. B. Robinson, *Representation Theory of the Symmetric Group*. University of Toronto Press, Toronto, 1961.

[66] G. James and A. Kerber, *The Representation Theory of the Symmetric Group*. Addison-Wesley, Reading, MA, 1981.

[67] B. E. Sagan, *The Symmetric Group*. Springer, New York, 2nd ed., 2001.

[68] J. Keeler, *Understanding NMR Spectroscopy.* Wiley, 2010.

[69] H. Breuer and F. Petruccione, *The Theory of Open Quantum Systems.* Oxford University Press, 2002.

[70] M. H. Levitt, *Spin dynamics: basics of nuclear magnetic resonance.* John Wiley and sons, New York-London-Sydney, 2008.

[71] S. Braun, H. Kalinowski, and S. Berger, *100 and more basic NMR experiments: a practical course.* VCH, 1996.

[72] U. Haeberlen and W. J. S., "Coherent averaging effects in magnetic resonance," *Phys. Rev.*, vol. 175, no. 453, 1968.

[73] A. Bielecki, A. C. Kolbert, H. J. M. de Groot, R. G. Griffin, and M. H. Levitt, "Frequency-Switched Lee—Goldburg Sequences in Solids," *Adv. Magn. Reson.*, vol. 14, no. 111, 1990.

[74] S. J. Glaser and J. J. Quant, "Homonuclear and heteronuclear hartmann—hahn transfer in isotropic liquids," vol. 19 of *Advances in Magnetic and Optical Resonance*, pp. 59 – II, Academic Press, 1996.

[75] A. Garon, S. J. Glaser, and D. Sugny, "Time-optimal control of SU(2) quantum operations," *Phys. Rev. A*, vol. 88, no. 043422, 2013.

[76] S. Rice and M. Zhao, *Optimal control of quantum dynamics.* John Wiley and Sons, Inc. New York, 2000.

[77] M. Shapiro and P. Brumer, *Principles of quantum control of molecular processes.* Wiley, New-York, 2003.

[78] D. J. Tannor, *Introduction to quantum mechanics: A time-dependent perspective.* University Science Books, Sausalito, 2007.

[79] T. Viellard, F. Chaussard, D. Sugny, B. Lavorel, and O. Faucher, "Fieldfree molecular alignment of co2 mixtures in presence of collisional relaxation," *J. Raman Spec.*, vol. 39, no. 6, pp. 694–699, 2008.

[80] M. A. Nielsen and I. L. Chuang, *Quantum computation and quantum information.* Cambridge, U. K.: Cambridge University Press, 2000.

[81] L. S. Pontryagin, V. G. Boltyanskii, R. V. Gamkrelidze, and E. F. Mishchenko, *The Mathematical Theory of Optimal Processes.* Mir, Moscow, 1974.

[82] B. Bonnard and M. Chyba, *Singular trajectories and their role in control theory*, vol. 40. Springer, New York, 2003.

[83] M. Lapert, Y. Zhang, M. Braun, S. J. Glaser, and D. Sugny, "Singular extremals for the time-optimal control of dissipative spin 1/2 particles," *Phys. Rev. Lett.*, vol. 104, no. 083001, 2010.

[84] E. Assémat, M. Lapert, Y. Zhang, M. Braun, S. J. Glaser, and D. Sugny, "Simultaneous time-optimal control of the inversion of two spin-1/2 particles," *Phys. Rev. A.*, vol. 82, no. 013415, 2010.

[85] U. Boscain and P. Mason, "Time minimal trajectories for a spin 1/2 particle in a magnetic field," *J. Math. Phys.*, vol. 47, no. 062101, 2006.

[86] D. D'Alessandro and M. Dahleh, "Optimal control of two-level quantum systems," *IEEE Trans. A. C.*, vol. 46, no. 866, 2001.

[87] D. Sugny and C. Kont, "Optimal control of a three-level quantum system by laser fields plus von neumann measurements," *Phys. Rev. A*, vol. 77, no. 063420, 2008.

[88] N. Khaneja, R. Brockett, and S. J. Glaser, "Time optimal control in spin systems," *Phys. Rev. A*, vol. 63, no. 032308, 2001.

[89] N. Khaneja, S. J. Glaser, and R. Brockett, "Sub-riemannian geometry and time optimal control of three spin systems: Quantum gates and coherence transfer," *Phys. Rev. A*, vol. 65, no. 032301, 2002.

[90] B. Bonnard and D. Sugny, "Time-minimal control of dissipative two-level quantum systems: The integrable case," *SIAM J. Control Opt.*, vol. 48, no. 3, pp. 1289–1308, 2009.

[91] B. Bonnard, M. Chyba, and D. Sugny, "Time-minimal control of dissipative two-level quantum systems: The generic case," *IEEE Trans. Autom. Control*, vol. 54, no. 2598, 2009.

[92] N. Khaneja, T. Reiss, C. Kehlet, T. Schulte-Herbrüggen, and S. J. Glaser, "Optimal control of coupled spin dynamics: design of nmr pulse sequences by gradient ascent algorithms," *J. Magn. Reson.*, vol. 172, no. 2, pp. 296–305, 2005.

[93] T. E. Skinner, T. O. Reiss, B. Luy, N. Khaneja, and S. J. Glaser, "Application of optimal control theory to the design of broadband excitation pulses for high-resolution nmr," *J. Magn. Reson.*, vol. 163, no. 1, pp. 8–15, 2003.

[94] D. M. Reich, M. Ndong, and C. P. Koch, "Monotonically convergent optimization in quantum control using Krotov's method," *J. Chem. Phys.*, vol. 136, no. 104103, 2012.

[95] J. Werschnik and E. K. U. Gross, "Quantum optimal control theory," *J. Phys. B*, vol. 40, no. 18, pp. 175–211, 2007.

[96] R. Kosloff, S. A. Rice, P. Gaspard, S. Tersigni, and D. Tannor, "Wavepacket dancing: Achieving chemical selectivity by shaping light pulses," *Chem. Phys.*, vol. 139, no. 1, pp. 201–220, 1989.

[97] R. Tycko, "Iterative methods in the design of pulse sequences for nmr excitation," *Adv. Magn. Reson.*, vol. 15, no. 1, pp. 1–49, 1990.

[98] M. H. Levitt, "Symmetry in the design of nmr multiple-pulse sequences," *J. Chem. Phys.*, vol. 128, no. 052205, 2008.

[99] B. Luy, K. Kozbar, T. E. Skinner, N. Kaneja, and S. J. Glaser, "Construction of universal rotations from point-to-point transformations," *J. Magn. Reson.*, vol. 176, no. 2, pp. 179–186, 2005.

[100] J. P. Palao and R. Kosloff, "Optimal control theory for unitary transformations," *Phys. Rev. A*, vol. 68, no. 062308, 2003.

[101] T. Schulte-Herbrüggen, A. Spörl, N. Khaneja, and S. J. Glaser, "Optimal control-based efficient synthesis of building blocks of quantum algorithms: A perspective from network complexity towards time complexity," *Phys. Rev. A*, vol. 72, no. 042331, 2005.

[102] M. A. Janich, R. F. Schulte, M. Schwaiger, and S. J. Glaser, "Robust slice-selective broadband refocusing pulses," *Journal of Magnetic Resonance*, vol. 213, no. 1, pp. 126 – 135, 2011.

[103] M. A. Janich, M. A. McLean, R. Noeske, S. J. Glaser, and R. F. Schulte, "Slice-selective broadband refocusing pulses for the robust generation of crushed spin-echoes," *J. Magn. Reson.*, vol. 223, pp. 129–137, 2012.

[104] K. Kobzar, S. Ehni, T. E. Skinner, S. J. Glaser, and B. Luy, "Exploring the limits of broadband 90 ° and 180 ° universal rotation pulses," *J. Magn. Reson.*, vol. 225, no. 142-160, 2012.

[105] M. Lapert, J. Salomon, and D. Sugny, "Time-optimal monotonically convergent algorithm with an application to the control of spin systems," *Phys. Rev. A*, vol. 225, no. 3, 2012.

[106] N. Khaneja, B. Heitmann, A. Spörl, H. Yuan, T. Schulte-Herbrüggen, and S. J. Glaser, "Shortest paths for efficient control of indirectly coupled qubits," *Phys. Rev. A*, vol. 75, no. 012322, 2007.

[107] I. I. Rabi, "On the process of space quantization," *Phys. Rev.*, vol. 49, pp. 324–328, Feb 1936.

[108] I. I. Rabi, "Space quantization in a gyrating magnetic field," *Phys. Rev.*, vol. 51, pp. 652–654, Apr 1937.